Quantum Magnetism in the Two-Dimensional Fermi-Hubbard Model and Beyond

Dissertation
zur
Erlangung des Doktorgrades (Dr. rer. nat.)
der
Mathematisch-Naturwissenschaftlichen Fakultät
der
Rheinischen Friedrich-Wilhelms-Universität Bonn

von
Nicola Camilla Wurz
aus
Baden-Baden

Bonn, 2021

Angefertigt mit Genehmigung der Mathematisch-Naturwissenschaftlichen Fakultät der Rheinischen Friedrich-Wilhelms-Universität Bonn

1. Gutachter:	Prof. Dr. Michael Köhl
2. Gutachter:	Prof. Dr. Martin Weitz
Tag der Promotion:	21.12.2021
Erscheinungsjahr:	2022

Abstract

Ultracold quantum gases in optical lattices serve as an analogue quantum simulator to investigate the physics of strongly correlated materials. With our quantum gas setup we investigate fermionic potassium atoms in a single layer of an anisotropic three-dimensional optical lattice configuration. The physics of this system is captured by the two-dimensional Fermi-Hubbard model, which includes only two elementary processes, namely tunnelling between neighbouring lattice sites with amplitude t and on-site interactions between opposite spins of strength U. The combination of high-resolution imaging and radio-frequency spectroscopy enables us to observe the in-situ density distribution of a single two-dimensional layer. We can either detect magnetic correlations by employing a spin-resolved imaging scheme or we can study the density sector by resolving the spatial distribution of singly and doubly occupied sites.

We have successfully employed a novel technique to coherently manipulate magnetic correlations. This allowed us to quantify the magnetic order of a two-dimensional layer in quasimomentum space and was furthermore used to perform thermometry at temperatures where charge excitations are mostly frozen out. In contrast to the temperature obtained from the global density profile, our spin thermometer represents a local probe, and combining both techniques enables us to study non-equilibrium properties of our system.

By implementing a superlattice along the vertical lattice direction, we can couple two horizontal layers in a controlled way. This allows us to study the bilayer Fermi-Hubbard model, which adds yet another energy scale, namely the vertical tunnel coupling, $t_\perp$. We have adapted a measurement scheme to access the magnetic correlations between neighbouring layers by inducing coherent singlet-triplet oscillations along the vertical bond and successively merging the double-well like potential into a single well. We have investigated the influence of the tunnel coupling between the two layers over a large parameter range of $0 \leq t_\perp \leq 5t$ and we have observed that the direction along which magnetic correlations predominantly form changes. Our results confirm the expectation of a crossover between the two low-temperature phases, i.e. a two-dimensional antiferromagnet within the layer and a band insulator of singlet pairs along the vertical direction for strong coupling between the layers. In addition, we have measured the compressibility of the bilayer system by applying an in-plane magnetic field gradient and thereby confirmed the strongly insulating nature of the bilayer band insulator.

Contents

CHAPTER 1

Introduction

One of the main goals of modern physics is to improve the understanding of strongly correlated quantum many-body systems [1]. These materials are governed by a subtle interplay of kinetic energy, interactions and dimensionality, and they have attracted a lot of interest over the past decades because they often exhibit macroscopic quantum phenomena such as colossal magnetoresistance [2], thermoelectricity [3] or high-temperature superconductivity [4].

Since the first experimental observation of high-temperature superconductivity in a Ba-La-Cu-O system in 1986 [5], many more superconducting copper oxide compounds have been identified. The common structural units shared by these compounds are CuO_2 layers, see Figure 1.1.

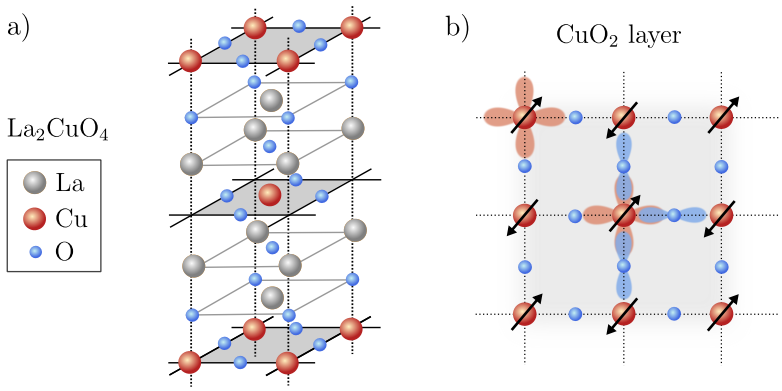

Figure 1.1: High-temperature superconductivity in copper oxides. a) Atomic structure of the insulating parent compound La_2CuO_4. The CuO_2 layers highlighted by the grey shaded areas become superconducting upon hole doping, for example by substituting La^{3+} with Sr^{2+}. b) Atomic structure of a CuO_2 layer, which is the common unit of high-temperature superconductors. The exemplary blue and red shaded areas represent the p and $d_{x^2-y^2}$ orbitals of oxygen and copper, respectively. In the undoped case the parent compound is a Mott insulator with antiferromagnetic correlations indicated by the black arrows. The dotted grid lines highlight the underlying square lattice structure. This figure was inspired by [6, 7].

When we consider the copper oxide compound La_2CuO_4, the valency of copper is given by Cu^{2+} resulting in a $3d^9$ electron configuration, where the energetically highest d orbital $d_{x^2-y^2}$ is only half-filled [6]. Band structure calculations predict a metallic behaviour but the presence of strong electron correlations leads to an antiferromagnetically ordered insulating

phase. When substituting lanthanum La^{3+} with strontium ions Sr^{2+}, the parent compound becomes effectively hole-doped, and as a consequence, the antiferromagnetic order vanishes and a superconducting gap with d-wave symmetry opens [8, 9]. While by now many new materials have been identified with transition temperatures of up to 133 K at ambient pressure [10], the research with solid-state materials is complicated by their limited tuning capabilities and the presence of impurities, which often impede a direct comparison to theory calculations. Even after decades of intensive research efforts the microscopic properties of high-temperature superconductivity, the key to pushing the critical temperature even further, are still not fully understood [11].

On the other hand, the theoretical models to describe copper oxides face the difficulty of strong electron correlations, which are responsible for the breakdown of band structure predictions. In addition, the exponential growth of the Hilbert space with system size restricts exact numerical simulations. Even for the two-dimensional Fermi-Hubbard model, a minimal microscopic Hamiltonian that is believed to describe high-temperature superconductivity, the ground-state phase diagram is not fully understood. Many approximate methods have been developed over the past decades including auxiliary-field quantum Monte Carlo [12, 13], density matrix renormalization group theory [14, 15] and dynamical cluster approximation [16]. By now it is for example well established that the Fermi-Hubbard model supports the (Mott) insulating behaviour with antiferromagnetic correlations at half-filling [17], while the existence of a d-wave superconducting phase at finite doping is still debated. In a recent publication, H.C. Jiang and T. P. Devereaux have described a large-scale density matrix renormalization group study to investigate the appearance of high-temperature superconductivity in a lightly doped Fermi-Hubbard model [18]. Their results indicate a delicate interplay between superconductivity and insulating charge stripes, which is tunable by additionally introducing a next-nearest neighbour tunnelling amplitude.

An overview of the progress on the strongly correlated phases of the Fermi-Hubbard model is presented in two very recent review articles [19, 20], including a discussion of relevant open questions in [20]. The Simons collaboration has presented numerical solutions to a large part of the phase space of the Fermi-Hubbard model obtained from a wide range of methods in the thermodynamic limit and the authors claim to provide reliable benchmark data [21]. Their approach of comparing several theoretical methods highlights the relevance of cross-validating numerical findings also by experimental means.

To improve the microscopic understanding of strongly correlated materials and in particular the Fermi-Hubbard model, we follow a complementary approach where we implement an enlarged model of a solid-state crystal with ultracold atoms in optical lattices. This approach is based on an idea proposed by Richard Feynman, one of the earliest pioneers of quantum computation. In 1982, he suggested using a highly controllable quantum system to simulate another quantum system that is interesting but more difficult to investigate by direct means [22]. His idea of *quantum simulation* circumvents the problem of the exponential increase in the required computation power by building a "machine", which employs quantum-mechanical elements as the logical units of computation. Since they can exist in a superposition of several states at the same time, the number of qubits that are required to simulate a quantum system only grows linearly with system size. Our experiment presents an analogue quantum simulator, which provides a clean and highly tunable implementation of the Fermi-Hubbard model.

Advanced laser technologies paired with research on light-matter interaction made it possible to refine our understanding of the quantum world using ultracold atoms and trapped ions [23]. For a gas at room temperature the thermal de Broglie wavelength of the atoms is on

the order of the Bohr radius. To access the regime of quantum degeneracy we need to reduce the thermal velocity to an equivalent of around 100 nK. For this purpose laser cooling [24] is typically employed as a first stage followed by a forced evaporation of the hottest atoms in a magnetic and an optical trap. Advances in these techniques have led to the first realizations of Bose-Einstein condensation in 1995 by Anderson et al. [25], Bradley et al. [26] and Davis et al. [27], followed by the first observation of a degenerate Fermi gas by DeMarco et al. [28] in 1999. Since then the field has evolved in several directions. Already today quantum gases serve as a basis for many applications ranging from atomic clocks providing the most accurate time standard to cold atom gravimeters [29]. Furthermore, companies and universities alike explore their potential to serve as a platform for quantum computing [30].

Apart from the metrological purposes, research with ultracold atoms improves our fundamental understanding of quantum many-body systems, because they enable full control over the microscopic system parameters. To confine neutral atoms in real space intense laser beams are routinely employed. The electric field of the laser light induces a dipole moment in the atoms, which in turn interacts with the electric field. The resulting potential landscape is proportional to the local light intensity. In particular optical lattices, i.e. standing waves of light that are generated by the interference of laser beams, allow us to implement lattice potentials, where particles can only move between the potential minima via the quantum-mechanical tunnelling effect. Ultracold gases of *fermionic* atoms loaded into such an artificial crystal made of light have attracted a lot of interest since they emulate condensed-matter materials. In the spirit of Feynman's quantum simulator these atoms mimic the behaviour of the valence electrons in crystal lattices. In contrast to their solid-state counterpart, ultracold atoms in optical lattices constitute a clean system without impurities, and the increased mass of the itinerant particles (atoms instead of electrons) facilitates the observation of dynamic effects. Furthermore, the large spacing between lattice sites, which is on the order of the laser wavelength, allows for an optical readout of the microscopic states using absorption or fluorescence imaging techniques, among others [31, 32].

To mimic the screened Coulomb repulsion between electrons in a condensed-matter material, we need to engineer short-range interactions between neutral atoms. The atomic species that we use is fermionic potassium ^{40}K, which belongs to the alkali metals, the first main group in the periodic table, whose electronic structure is similar to that of hydrogen. In contrast to lanthanides such as erbium or dysprosium, alkali atoms do not exhibit long-range dipole-dipole interactions since their magnetic moment is an order of magnitude smaller, and therefore they only interact via a short-range potential [33]. Intuitively speaking the ultracold potassium atoms experience the short-range potential when they collide with each other. By adjusting the magnetic field strength in the vicinity of a scattering resonance, one can tune the energy of a bound state into resonance with the kinetic energy of the scatterers. This allows us to realize a broad range of interaction strengths both in the repulsive and attractive regime. In an optical lattice these so-called Feshbach resonances result in a shift of the on-site energy by an amount U when two atoms with different internal states meet on a lattice site, see Figure 1.2. Therefore, ultracold atoms in optical lattices constitute an ideal platform to implement the Fermi-Hubbard model and allow for the investigation of the strongly interacting regime.

The current research with fermionic atoms in optical lattices mostly focusses on two-dimensional systems, for which the density equation of state reflecting the metal to insulator transition has been mapped out at finite temperature [34]. Furthermore, several characteristic features indicating the corresponding ground-state quantum phases such as the antiferromagnetic Mott insulator for repulsive interactions [35–38] and the charge-density wave for

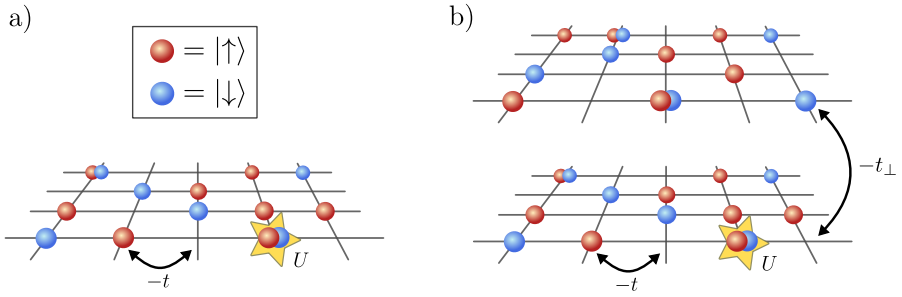

Figure 1.2: Two-dimensional and bilayer Fermi-Hubbard model. The Fermi-Hubbard model provides a simplified description of interacting spin-1/2 particles moving in a periodic lattice structure with amplitudes t and $t_\perp$. The interaction is quantified by an on-site energy shift U. Originally it was introduced to describe conduction electrons in narrow d-bands of transition metals. Inspired by the layered structure of the copper oxides, the two-dimensional Fermi-Hubbard model has received particular attention. We implement both the a) two-dimensional and the b) bilayer configuration using ultracold potassium atoms in optical (super)lattices. The two spin states are emulated by two distinct magnetic hyperfine states.

attractive interactions [39] have been observed. The characterization of magnetic order within a two-dimensional layer in terms of the magnetic structure factor and its potential for quantifying even out-of-equilibrium properties of the system by performing local thermometry are discussed in Chapter 5.

Real materials, however, are typically not strictly two-dimensional but often comprise several layers stacked on top of each other. For example, the copper-oxide compounds are classified by the number N of CuO_2 layers contained within a characteristic multilayer block [8, 9]. It was observed that the critical temperature T_c significantly increases with $N \leq 3$ and decreases thereafter [40, 41]. For these reasons there was a growing interest in understanding the physics of the bilayer Fermi-Hubbard model from a theoretical point of view [42–51]. It was found that the interlayer coupling strength, $t_\perp$, controls a transition from a Mott insulator to an unconventional band insulating phase at half-filling, and the insulator to insulator transition itself has recently received considerable attention [42, 43]. By implementing an optical superlattice we have extended our existing setup to allow for the investigation of coupled bilayer systems, depicted in Figure 1.2 b). Our results, including the characterization of the magnetic order both within and between the two-dimensional layers and the measurement of the compressibility quantifying the insulating nature of the system, are presented in Chapters 6 and 7.

Thesis Structure

In this thesis I report on the investigation of the Fermi-Hubbard model using fermionic potassium atoms in a three-dimensional optical lattice. The main focus is on the detection of magnetic correlations both within a single two-dimensional layer and between two coupled layers.

- In Chapter 2, I introduce the concept of optical lattices, which are the main tool for shaping the potential landscape experienced by ultracold atoms in order to emulate the periodic crystal structure of solids. After reviewing the quantum-mechanical description including the single-particle solutions called Bloch waves, I discuss the additional tuning options offered by bichromatic superlattices.

- In Chapter 3, I introduce the Fermi-Hubbard Hamiltonian, which describes interacting fermionic particles moving through a periodic lattice potential in a simplified version that is motivated by the tight-binding approximation. The main concepts of quantum magnetism and tunnel delocalization are reviewed for the minimal building block of the Hubbard model, i.e. a double-well. This serves as the basis to discuss both the two-dimensional and the bilayer Fermi-Hubbard model and their approximate phase diagrams.

- In the beginning of Chapter 4, I briefly explain the main parts of the experimental setup as well as the process of creating an ultracold Fermi gas. The following parts focus on the detection protocols that are employed to probe both the spin and density sector of a single two-dimensional layer as well as the recent adaptions that were implemented during the course of this thesis, including both an in-plane and out-of-plane superlattice as well as a digital-micromirror device (DMD) that allows for arbitrary potential shaping.

- In Chapter 5, I explain how we detect antiferromagnetic correlations in a two-dimensional layer even without single-site resolved imaging. A novel scheme that coherently manipulates spin correlations allows us to probe the magnetic structure factor in a momentum-resolved manner and we thereby overcome the optical resolution limitation. Furthermore, measuring magnetic correlations serves as a local probe of the temperature, which we combine with global density thermometry to optimize the lattice loading process and to ensure thermalization across the cloud.

- In Chapter 6, I present our results on magnetic correlations of the bilayer Fermi-Hubbard model. We have measured both intra- and interlayer spin-spin correlations and observed that the interlayer tunnelling amplitude drives a crossover from an anti-ferromagnetically ordered Mott insulator to a bilayer band insulator of vertical singlet bonds.

- In Chapter 7, I present the measurement of the compressibility in the bilayer Fermi-Hubbard model, which quantifies the insulating nature of the prepared state. We have observed that for an intermediate repulsive interaction strength, the compressibility is the lowest in the strong coupling regime and we have investigated the microscopic picture.

- In Chapter 8, I conclude this work with a summary of the main results followed by suggestions for further improvements and additional measurements to complement the findings presented in this thesis. Furthermore, I discuss possible future experiments that build on either of the two implemented superlattices.

List of Publications

The following publications originated during the course of this thesis. They are listed in chronological order.

- **Antiferromagnetic Correlations in Two-Dimensional Fermionic Mott-Insulating and Metallic Phases** J. H. Drewes, L. A. Miller, E. Cocchi, C. F. Chan, N. Wurz, M. Gall, D. Pertot, F. Brennecke and M. Köhl, Phys. Rev. Lett. **118**, 170401 (2017). https://doi.org/10.1103/PhysRevLett.118.170401
- **Coherent manipulation of spin correlations in the Hubbard model** N. Wurz, C. F. Chan, M. Gall, J. H. Drewes, E. Cocchi, L. A. Miller, D. Pertot, F. Brennecke and M. Köhl, Phys. Rev. A **97**, 051602 (2018). https://doi.org/10.1103/PhysRevA.97.051602
- **Simulating a Mott Insulator Using Attractive Interaction** M. Gall, C. F. Chan, N. Wurz and M. Köhl, Phys. Rev. Lett. **124**, 010403 (2020). https://doi.org/10.1103/PhysRevLett.124.010403
- **Pair correlations in the attractive Hubbard model** C. F. Chan, M. Gall, N. Wurz and M. Köhl, Phys. Rev. Research **2**, 023210 (2020). https://doi.org/10.1103/PhysRevResearch.2.023210
- **Competing magnetic orders in a bilayer Hubbard model with ultracold atoms** M. Gall*, N. Wurz*, J. Samland, C. F. Chan and M. Köhl, Nature **589**, 40–43 (2021). https://doi.org/10.1038/s41586-020-03058-x

*These authors contributed equally.

CHAPTER 2

Quantum Simulation of Solids using Optical Lattices

In the introduction I have motivated the use of ultracold atomic gases in optical lattices as a quantum-mechanical model system to simulate the behaviour of electrons in condensed-matter materials and to explore even their microscopic properties including magnetic correlations. To mimic the periodic potential landscape generated by the positively charged ions in a crystal lattice, we need to engineer a force, which acts on neutral particles and which is periodic in space. Laser beams that are far-detuned from the atomic resonance frequencies shift the energy levels of atoms, thereby creating a conservative potential, which is proportional to the local intensity of the electric field. Interfering two laser beams with exactly the same wavelength, for example by retro-reflecting one beam with a mirror, creates a standing-wave potential, i.e. a one-dimensional optical lattice. The benefit of using ultracold atoms in lattice potentials made of intense laser radiation is the increased lattice spacing, which is on the order of the laser wavelength and hence, around three orders of magnitude larger than in crystal lattices. The downside is that in order to observe quantum phenomena, we need to cool the atoms below the Fermi temperature, which is much lower in optical lattice systems. For more details concerning the comparison of solid-state materials and their quantum simulation using atoms see [32].

After briefly reviewing the interaction of neutral atoms with intense laser beams, this chapter will focus on the description of optical lattices including the eigenenergy spectrum, i.e. the band structure, which provides information on the mobility of the atoms. By adding a second lattice laser with a different wavelength we can realize bichromatic optical superlattices, which serve as a versatile toolbox that we employ both for the preparation and the detection of the atomic samples, see Sections 6.1.1, 6.1.2 and 6.4.1. Finally, we characterize the additional trapping potential generated by the finite waist of the Gaussian shaped laser beams, which is superimposed on the periodic lattice structure.

2.1 Atom-Light Interaction

This section is devoted to the interaction of neutral atoms with intense light fields and will focus in particular on how to confine atoms in space by employing laser beams. Since this technique is at the heart of many quantum gas experiments, it has been described in numerous places and I only want to highlight the review article by R. Grimm et al. [52], which was a source of inspiration for the following paragraph.

The trapping of neutral atoms in intense light fields relies on the electric dipole interaction

$$\hat{H}_{\mathrm{dip}} = -\boldsymbol{d} \cdot \boldsymbol{E}(\boldsymbol{r}, t). \tag{2.1}$$

Although neutral atoms in general do not possess a finite dipole moment $\boldsymbol{d}$, an oscillating electric field will induce a dipole moment that oscillates at the driving frequency ω

$$\boldsymbol{d}(\boldsymbol{r}, t) = \alpha(\omega)\boldsymbol{E}(\boldsymbol{r}, t), \tag{2.2}$$

where the complex polarisability $\alpha(\omega)$ determines not only the amplitude of the induced dipole moment, but also the phase relation between the electric driving field and the atomic response. The real part of the polarisability leads to a conservative trapping potential, which, in close analogy to the refractive index, is often called the dispersive part of the atom-light interaction

$$V_{\mathrm{dip}}(\boldsymbol{r}) = -\frac{1}{2\epsilon_0 c}\,\mathrm{Re}[\alpha] I(\boldsymbol{r}). \tag{2.3}$$

Even though the light field is far-detuned from all atomic transitions, an atom will absorb (and reemit) photons with a scattering rate given by

$$\Gamma_{\mathrm{sc}}(\boldsymbol{r}) = \frac{1}{\hbar\epsilon_0 c}\,\mathrm{Im}[\alpha] I(\boldsymbol{r}). \tag{2.4}$$

If we substitute the atomic polarisability with the result from the Lorentz oscillator model, we can express both the dipole potential as well as the scattering rate in terms of the detuning from the atomic resonance $\Delta = \omega - \omega_0$ and the damping rate Γ [52]

$$V_{\mathrm{dip}}(\boldsymbol{r}) = \frac{3\pi c^2}{2\omega_0^3}\frac{\Gamma}{\Delta} I(\boldsymbol{r}), \tag{2.5}$$

$$\Gamma_{\mathrm{sc}}(\boldsymbol{r}) = \frac{3\pi c^2}{2\hbar\omega_0^3}\left(\frac{\Gamma}{\Delta}\right)^2 I(\boldsymbol{r}). \tag{2.6}$$

The two expressions scale differently with the detuning Δ, which has two profound consequences: Firstly, in contrast to the scattering rate, Γ_{sc}, the dipole potential, V_{dip} depends on the sign of the detuning from the atomic resonance. Hence, we can realize both attractive and repulsive potentials by choosing either red- or blue-detuned laser beams, $\Delta < 0$ or $\Delta > 0$, respectively. Secondly, the dipole potential is proportional to $1/\Delta$, while the scattering rate scales as $1/\Delta^2$. As a consequence, we can reduce the amount of spontaneous scattering events which have an impact on the temperature of the atomic cloud, by choosing a large detuning from the resonance. To achieve reasonably strong potentials we increase the laser intensity. Another important benefit of choosing a large detuning is that the depth of the dipole potential is independent of the magnetic hyperfine state.

However, we should keep in mind, that the dipole potential is not an ideal conservative potential. Instead, the spontaneous emission of a photon in a random direction with rate Γ_{sc} heats the cloud as quantified by the increase in the mean kinetic energy, which is proportional to the scattering rate and the recoil energy, $E_{\mathrm{rec}} = \hbar^2 k_L^2/(2m)$, where $k_L = 2\pi/\lambda$ is the wavevector of the lattice laser with wavelength λ [53]. A thorough investigation of heating processes in far-detuned optical lattices was carried out by F. Gerbier et al. [54].

2.2 Optical Lattices and Bloch's Theorem

In the previous section we have seen that the dipole potential is proportional to the local intensity $I(\boldsymbol{r})$. An optical lattice is formed when two laser beams with the same frequency but opposite propagation direction interfere with each other. Assuming their electric field amplitude and polarization to be identical, the intensity distribution follows as

$$I(z) = \frac{\epsilon_0 c}{2} \left| \boldsymbol{E}_0 e^{ikz} + \boldsymbol{E}_0 e^{-i(kz+\varphi)} \right|^2 = 4 \left| \boldsymbol{E}_0 \right|^2 \frac{\epsilon_0 c}{2} \cos^2(kz + \varphi/2) \tag{2.7}$$

If we put an atom into a standing wave of light, it will interact with the laser radiation forming the optical lattice through virtual absorption and stimulated emission of photons with momentum $\pm\hbar k_L \boldsymbol{e}_z$, where $k_L = 2\pi/\lambda$ is the wavevector of the laser source with wavelength λ [55]. Each of these absorption and re-emission cycles transfers either $\pm 2\hbar k_L$ or zero net momentum to the atom. This becomes apparent if we express the cosine-squared potential in terms of exponential functions

$$V(z) = \pm V_{\text{latt}} \cos^2(k_L z) = \pm \frac{V_{\text{latt}}}{4} \left(e^{2ik_L \cdot z} + e^{-2ik_L \cdot z} + 2 \right), \tag{2.8}$$

where $V_{\text{latt}} = \left| \boldsymbol{E}_0 \right|^2 \left| \operatorname{Re}[\alpha] \right|$ and the potential is positive (negative) for a blue (red) detuned laser. In contrast to a free particle, whose momentum k is conserved due to the translation invariance of the corresponding Hamiltonian, the potential landscape in an optical lattice only possesses discrete translation symmetry. This leads to the conservation of quasimomentum, which is defined as the momentum modulo $2k_L$. If spontaneous emission is neglected, the atom's momentum only changes because of the interaction with the lattice potential that couples plane wave states with wavevectors differing by a multiple of $2k_L$, compare Equation 2.8. Therefore the lattice conserves quasimomentum [56]. This statement may also be recast by the Nyquist-Shannon sampling theorem according to which spatial frequency components above half the finite sampling rate cannot be distinguished from frequencies below. Hence, on a discrete lattice it is only sensible to define wavevectors up to $k_{\text{max}} = k_L = \pi/a$. In order to differentiate states with higher energy but the same quasimomentum, a second quantum number is introduced called the band index n. In the following I will discuss how the energy dispersion and the wavefunction of an atom in an optical (super)lattice are modified as compared to the case of a free particle, where $V(z) = 0$.

2.2.1 Monochromatic Optical Lattice

Since the lattice potential does not conserve momentum, the plane wave states e^{ikz}, which are the eigenstates of a free particle with dispersion relation $E_k = \hbar^2 k^2/(2m)$ cannot solve the eigenvalue problem of a particle in a periodic lattice. However, we can use them to construct a set of basis states

$$\phi_q^m(z) = e^{i(2mk_L + q)z}, \tag{2.9}$$

in a way that each two basis states for fixed q differ by a multiple of $2k_L$ in their momentum, which reflects the intrinsic coupling by the optical lattice potential. The kinetic energy operator $\hat{E}_{\text{kin}}$ is diagonal when expressed in the ϕ_m^q basis, which is not surprising since the basis states

are essentially plane waves:

$$\left\langle \phi_q^i \middle| \hat{H}_{\text{kin}} \middle| \phi_{q'}^j \right\rangle = \left\langle \phi_q^i \middle| \frac{-\hbar^2}{2m} \frac{\partial^2}{\partial z^2} \middle| \phi_{q'}^j \right\rangle = \frac{\hbar^2}{2m} \left(2jk_L + q\right)^2 \delta_{ij} \delta_{qq'}. \tag{2.10}$$

The potential term however mixes the basis states, as we have discussed before

$$\left\langle \phi_q^i \middle| V(z) \middle| \phi_{q'}^j \right\rangle = \delta_{qq'} \begin{cases} \frac{V_{\text{latt}}}{2} & \text{for } i = j, \\ \frac{V_{\text{latt}}}{4} & \text{for } i = j \pm 1, \\ 0 & \text{else.} \end{cases} \tag{2.11}$$

Since the basis states ϕ_q^m with different quasimomentum are not coupled by the lattice potential, we only have to solve the eigenvalue problem

$$\left(\hat{H}_{\text{kin}} + V(z)\right) \psi_q^n(z) = E_q^n \psi_q^n(z) \tag{2.12}$$

in the subspace of fixed q. The quasimomentum is not unique in labelling the eigenstate, therefore we need another quantum number, the band index n, which labels the energy eigenvalues in ascending order. This is in contrast to the description of a continuous system, where the kinetic energy $E = \hbar^2 k^2/(2m)$ directly follows from the momentum k and hence, specifying the momentum is enough to represent the state.

Note that the ability to separate the Hilbert space into subspaces with fixed q represents a huge simplification of the eigenvalue problem, since instead of solving for a continuous spectrum, we only have to obtain a discrete set of energy eigenvalues E_q^n for a continuous set of Hamiltonians. This simplification is nowadays best known in the form of the Bloch theorem, according to which the eigenstates of a single particle in an optical lattice are Bloch waves characterized by the quasimomentum q and the band index n,

$$\psi_q^n(z) = e^{iqz} u_q^n(z). \tag{2.13}$$

The amplitude function $u_q^n(z)$ inherits the periodicity of the optical lattice

$$u_q^n(z) = u_q^n(z + \pi/k_L), \tag{2.14}$$

which led Felix Bloch to the statement that *Bloch waves are plane de Broglie waves that are modulated in the rhythm of the lattice structure* [57].

Band Structure In Figure 2.1 we plot the spectrum of eigenenergies for different lattice depths. As the interaction between the atom and the optical lattice occurs through (virtual) absorption and emission of photons, we can identify the recoil energy E_{rec} as the relevant energy scale,

$$E_{\text{rec}} = \hbar^2 k_L^2/(2m). \tag{2.15}$$

This is the energy that is transferred to an atom of mass m when absorbing a photon from the lattice beam with wavelength $\lambda = 2\pi/k_L$. Throughout this thesis we will specify all lattice depths in units of their corresponding recoil energies.

For small lattice depths, the band structure as shown in Figure 2.1 a) still resembles the dispersion relation of a free particle $E = \frac{\hbar^2 k^2}{2m}$, however, folded into the first Brillouin zone,

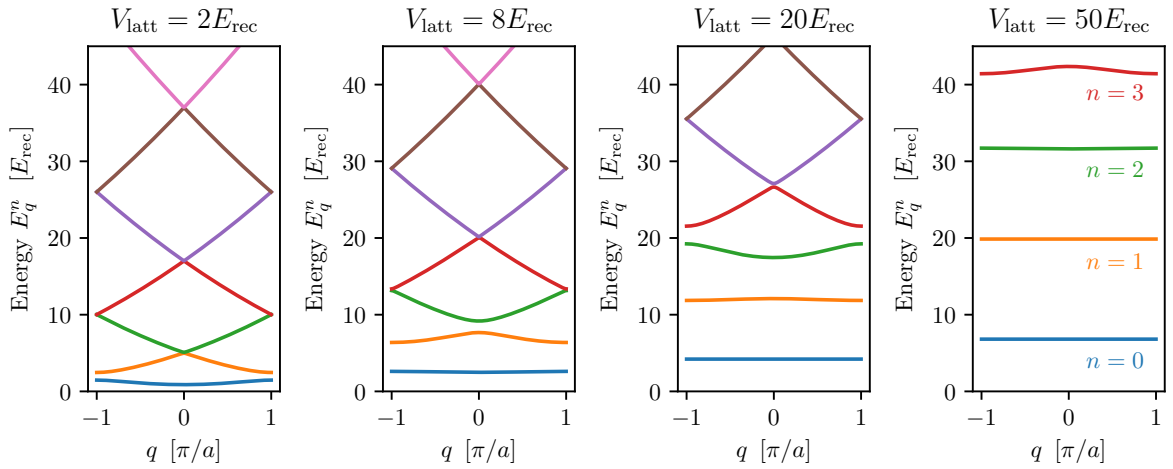

Figure 2.1: Band structure of a one-dimensional monochromatic optical lattice. The eigenenergies can be grouped into energy bands, where the index n labels the bands according to their energy in ascending order. For small lattice depth the bands resemble the parabolic free particle dispersion folded into the first Brillouin zone. For high lattice depths the energy bands become flat, since the lattice wells are mostly disconnected from each other and therefore resemble a harmonic oscillator potential.

$q \in [-\pi/a, \pi/a]$. Especially for energy bands whose energy is larger than the potential depth, we fully recover the parabolic dependence and consequently there are no gaps between these bands. In contrast, the lowest two Bloch bands are gapped at the band edge $q = \pi/a$ even for low lattice depths due to an avoided crossing. This has profound consequences, for example when we look at the group velocity $v_G(k) = \partial E/\partial k$. For a free particle $v_G(k)$ is proportional to k and we recover the intuitive picture that particles with higher momentum k possess a larger kinetic energy. However, in the periodic lattice potential the group velocity vanishes at the band edge $q = \pi/a$. Therefore when considering the lowest band only, eigenstates with the highest and lowest energy both feature a vanishing group velocity. This leads to the interesting effect that a cloud of fermionic atoms expands equally fast, whether the interactions are repulsive or attractive (same magnitude), which is completely different from the case of a free particle [58]. For large lattice depths the eigenenergy spectrum resembles the situation in a harmonic oscillator potential with equidistant eigenenergies and large band gaps.

Bloch Waves As discussed before, the eigensolutions of a single particle in a periodic lattice are Bloch waves. While in principle a particle is equally likely to be found at any lattice site, the phase relation between sites may differ. According to Bloch's theorem (see Equation 2.13) the amplitude functions $u_q^n(z)$ inherit the periodicity of the lattice and hence, $u_q^n(z) = u_q^n(z + a) = u_q^n(z + \pi/k_L)$. For the centre of the Brillouin zone, $q = 0$, the plane wave phase factor $e^{iqz} = 1$ for all z and hence the periodicity of the Bloch wave $\psi_{q=0}^n(z)$ has the same periodicity as the lattice itself. However at the band edge $q = \pi/a$, the sign of the Bloch wave alternates between neighbouring sites. In Figure 2.2 one can see how the quasimomentum determines the phase relation between neighbouring lattice sites.

In particular the Bloch wave $\psi_{q=0}^{n=0}(x)$ for $V_{\text{latt}} = 2E_{\text{rec}}$ still resembles a plane wave with a probability density that is only slightly modulated by the periodic lattice structure. Due to the large degree of delocalization the kinetic energy is low. In contrast, the Bloch wave

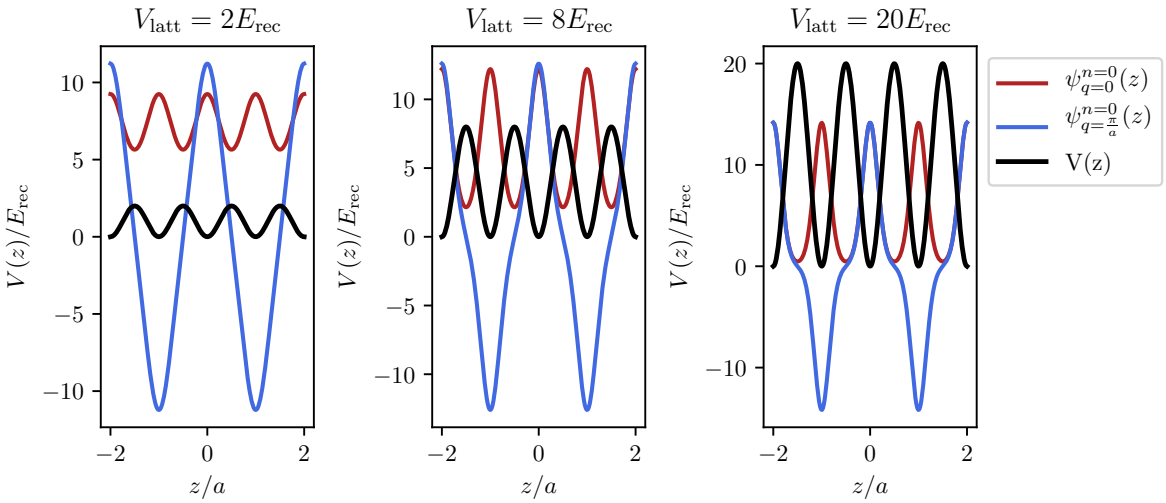

Figure 2.2: Bloch waves at $q = 0$ and $q = \pi/a$. The Bloch waves are plotted in arbitrary units for $q = 0$ (red) and $q = \pi/a$ (blue), to visualize the phase relation between neighbouring lattice sites. For increasing lattice depth V_{latt} the Bloch waves become more peaked around each lattice site.

with $q = \pi/a$ is forced to form a node where the optical lattice potential is maximum, and the corresponding kinetic energy is hence considerably larger. For increasing lattice depths all Bloch waves with arbitrary q become more strongly peaked around the centre of each lattice site, and the only difference that remains between the Bloch waves with $q = 0$ and $q = \pi/a$ is the phase relation of neighbouring lattice sites. As a consequence, the difference in the corresponding eigenenergies E_q^n decreases for deeper lattices and the energy band becomes more flat. Furthermore, the increasingly strong localization of the Bloch waves already provides an indication that for lattice depths $V_{\mathrm{latt}} \gg E_{\mathrm{rec}}$ a new set of localized states, the Wannier basis, will be more suitable.

Extension to Three Dimensions The extension of the description of the single-particle solution to the three-dimensional case is straightforward, if the lattice potential and therefore the Hamiltonian is separable, i.e. $V(\boldsymbol{r}) = V(x) + V(y) + V(z)$. In this case the full solution is simply given by the product state

$$\psi_{\boldsymbol{q}}^{\boldsymbol{n}}(\boldsymbol{r}) = \psi_{q_x}^{n_x}(x) \cdot \psi_{q_y}^{n_y}(y) \cdot \psi_{q_z}^{n_z}(z), \tag{2.16}$$

with the multi-band index $\boldsymbol{n} = (n_x, n_y, n_z)$. In our experiment the angle between the optical lattices in x and y direction deviates slightly from the right angle required for separability. While this can be neglected in most cases, it has to be considered when designing ramps in the lattice depth, as avoided crossings between the higher-band states of the different lattice directions might appear [59].

2.2.2 Bichromatic Superlattice

So far, we have discussed monochromatic optical lattices, where the lattice depth is the only relevant tuning parameter and we have seen that it determines the degree of localization of the Bloch waves. By adding a second optical lattice with a different, but commensurate

wavelength along the same spatial direction, we can create a so-called superlattice. The unit cell of the resulting lattice structure contains two sites and by tuning the wavelength of either optical lattice we can manipulate the potential landscape ranging from a lattice of separate double-wells to a potential with a staggered site offset. In the following we will mostly focus on a retro-reflecting lattice setup and discuss its tuning capabilities.

Manipulation of the Optical Lattice Landscape The full potential of an optical superlattice is given by the sum of the two individual lattices

$$V(z) = -V_r \cos^2(k_r \cdot z + \phi_r) + V_g \cos^2(k_g \cdot z + \phi_g), \tag{2.17}$$

where we have explicitly taken care of the sign, since we consider the short- (long-) wavelength lattice to be blue (red) detuned. In the experiment this is realized by employing a green ($\lambda_g = 532\,\mathrm{nm}$) and an infrared ($\lambda_r = 1064\,\mathrm{nm}$) lattice laser, which are both far-detuned from the atomic transitions of fermionic potassium at $\lambda_0 = 767\,\mathrm{nm}$.

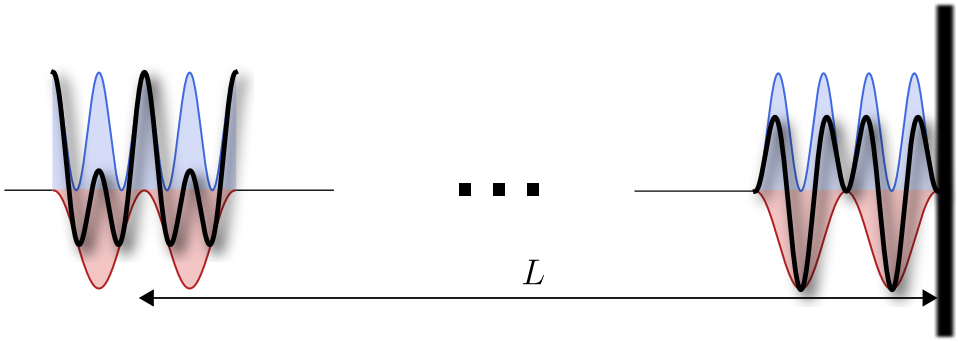

Figure 2.3: Superlattice potential for a retro-reflecting laser setup. Both individual optical lattices (red and blue lines) acquire a phase over the distance L between the retro-reflecting mirror and the position of the atoms. If the wavelengths are near-commensurate, the phase relation, which determines the superlattice potential shown in black changes with distance L.

The phases ϕ_r and ϕ_g are fixed at the position of the retro-reflecting mirror $z = 0$ (see Figure 2.3), where the total electric field of each optical lattice is bound to have a node due to the π-phase shift of the reflected beam. Therefore, an asymmetric double-well lattice with staggered site-offset forms at the position of the retro-reflecting mirror and if the two wavelengths were exact multiples of each other, the potential would not change as a function of the distance L. This is different, when we introduce a finite detuning from the commensurate case $k_g = 2k_r + \Delta k$. If the detuning of the frequency is small $\Delta\nu \ll \nu$, we can still assume the lattice periodicities to be multiples of each other $a_r = \lambda_r/2 = \lambda_g = 2a_g$. The effect of the slight detuning is, however, visible on the phase, which will be position-dependent $\phi_{\mathrm{tot}}(z) = \phi + \Delta\phi = \phi + \Delta k z$. At the position of the atomic cloud, the phase has advanced by

$$\Delta\phi = \Delta k L = \frac{2\pi\Delta\nu}{c} L, \tag{2.18}$$

which leads to a significant change in the superlattice potential if L is sufficiently large. For example, assuming a distance of $L = 0.5\,\mathrm{m}$ between the retro-reflecting mirror and the atoms, the frequency difference that is required to translate the optical lattice by one period, $\Delta\phi = \pi$,

is given by

$$\Delta\nu = \frac{c}{2L} = 300\,\mathrm{MHz}. \tag{2.19}$$

Note that this frequency difference is independent of the actual wavelength of the optical lattice. This means, that we have to shift either lattice by the same frequency in order to invoke a π phase shift, which translates the optical lattice by $\lambda/2 = \pi/k_L$. There are however some differences when tuning either the short or the long wavelength lattice, which I will discuss in the following.

In Figure 2.4 it is shown how the superlattice potential changes when tuning the frequency of the red-detuned long-wavelength lattice. Clearly the phase relation of the two individual

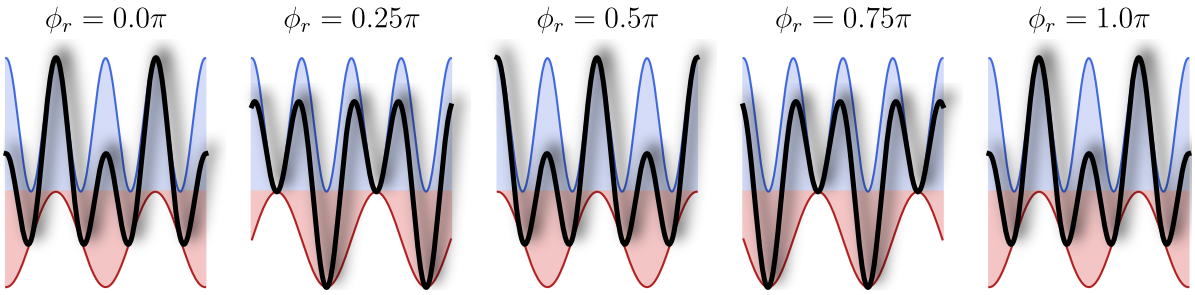

Figure 2.4: Superlattice potential when tuning the long lattice wavelength. Starting from a symmetric double-well configuration at $\phi_g = \phi_r = 0$ the potential gets more asymmetric when tuning the long-lattice wavelength, which changes the phase of the red lattice at the position of the atoms. At $\phi_r = \pi/4$ the completely asymmetric configuration is reached and the potential returns to a symmetric configuration at $\phi_r = \pi/2$. The absolute centre of the double-well is however shifted along the lattice direction with respect to the initial configuration at $\phi_r = 0$.

optical lattices at the position of the atoms changes. A benefit of tuning the frequency of the long-wavelength lattice is that the positions of the potential minima, which are mostly determined by the frequency of the short-wavelength lattice, are fixed in space. This enables us to tune the potential offset between lattice sites without additionally moving the atoms along the axis of the optical lattice. Another benefit is that the frequency difference required to change from a symmetric to an asymmetric double-well lattice is given by $\Delta\nu_r = c/8L$ only, corresponding to a phase difference of $\Delta\phi_r = \pi/4$. Since both lattices are translated in real space by one period $a_{g/r}$ along the propagation direction for a phase change of $\Delta\phi_{g/r} = \pi$, the impact of tuning the long-wavelength lattice frequency is stronger as a consequence of the wavelength being twice as large, compare Figures 2.4 and 2.5. Therefore, the frequency difference required to change from a symmetric to an asymmetric double-well lattice is a factor of two larger, $\Delta\nu_g = c/4L = 2\Delta\nu_r$, when tuning the short-wavelength lattice. This is visualized in Figure 2.5.

Estimate of the Potential Energy Offset For a bichromatic optical lattice generated by two laser sources with near-commensurate wavelengths $2k_r \approx k_g$, the resulting unit cell contains two lattice sites. Depending on the superlattice phase, these two sites may experience a potential energy offset, for which I want to derive an approximate formula in the following.

In the asymmetric case, the positions x_n of the lattice sites are directly determined by the

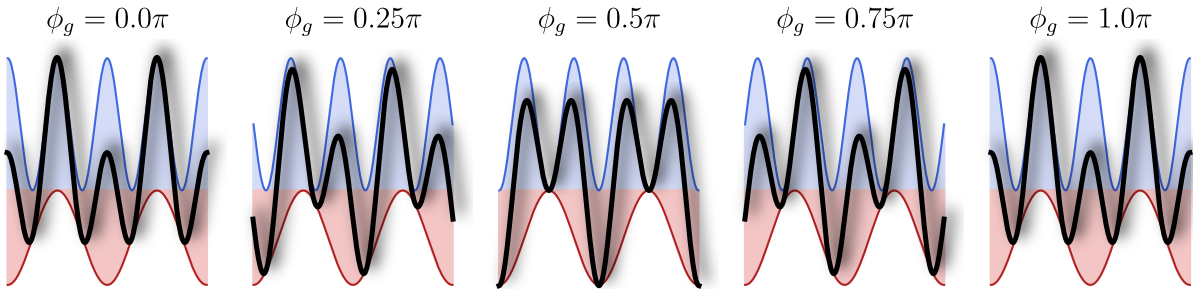

Figure 2.5: Superlattice potential when tuning the short lattice wavelength. The phase shift that is necessary to change between a symmetric and an anti-symmetric configuration is equal to $\Delta\phi_g = \pi/2$, which corresponds to a frequency difference of $\Delta\nu_g = c/(4L)$.

potential minima of the short-wavelength lattice,

$$V_g \cos^2(k_g \cdot x + \phi_g) \stackrel{!}{=} 0 \quad \rightarrow \quad k_g \cdot x_n = \frac{\pi}{2} \cdot (2n+1) - \phi_g \quad \forall n \in \mathbb{N}. \tag{2.20}$$

Near the symmetric case the lattice sites within a double-well move closer together when increasing the red lattice depth V_r. Therefore, the formula to determine the lattice site positions x_n given above only represents an approximation. Still, I will use it in the following to obtain an estimate of the potential tilt $V(x_1) - V(x_2) = 2\Delta$ between the two lattice sites of one unit cell,

$$V(x_1) - V(x_2) \approx \frac{V_r}{2}\left[\cos\left((3\pi - 2\phi_g)\cdot\frac{k_r}{k_g} + 2\phi_r\right) - \cos\left((\pi - 2\phi_g)\cdot\frac{k_r}{k_g} + 2\phi_r\right)\right] \tag{2.21}$$

$$\approx V_r \sin\left(2\phi_r - \phi_g\right). \tag{2.22}$$

From this approximate formula for the potential tilt, it is apparent once more that there is a difference when tuning the wavelength and hence the phase of either the short or the long wavelength optical lattice. When shifting the frequency of the long-wavelength laser the associated change in the superlattice configuration as quantified by the energy offset is approximately a factor of two larger.

2.3 Optical Potential Landscape

So far we have assumed an ideal optical lattice potential, which is infinitely extended and possesses a spatially constant lattice depth $V_{\text{latt}} \neq V_{\text{latt}}(\boldsymbol{r})$. However, the experimental implementation using laser beams deviates from this idealized description, as the intensity distribution orthogonal to the propagation direction of a laser beam in the $\text{TEM}_{0,0}$ mode is given by a Gaussian

$$I(x,y) = \frac{2P_0}{\pi\omega_x\omega_y} e^{-2\left[\left(\frac{x}{\omega_x}\right)^2 + \left(\frac{y}{\omega_y}\right)^2\right]} = \frac{\epsilon_0 c}{2}\left|\boldsymbol{E}_0(x,y)\right|^2. \tag{2.23}$$

Due to the finite waist in the x- and y-directions, the lattice depth reduces perpendicular to the propagation direction with the distance from the centre of the beam. The Rayleigh range is typically much larger than the cloud's extent and we will therefore neglect its influence in

the following by assuming the lattice depth to be constant along the axis of the optical lattice.

In our experiment, some of the optical lattices are created by retro-reflecting a laser beam and due to the imperfect reflection/transmission of optical elements, there will be an imbalance in the electric field amplitudes of the ingoing $\boldsymbol{E}_0^{\text{in}}(x,y)$ and the reflected beam $\boldsymbol{E}_0^{\text{re}}(x,y) = \sqrt{\gamma}\boldsymbol{E}_0^{\text{in}}(x,y)$ at the position of the atoms. The power imbalance is quantified by the reflection coefficient $\gamma \leq 1$ and it leads to a so-called running wave component, since not all the power in the lattice beam may be used to form the standing wave optical lattice. If we account for both, the locally varying electric field amplitude as well as the power imbalance in the two beams forming the optical lattice, Equation 2.8 modifies to [60]

$$V(\boldsymbol{r}) = \pm \underbrace{\sqrt{\gamma}\,|\mathrm{Re}[\alpha]|\left|\boldsymbol{E}_0^{\text{in}}(x,y)\right|^2}_{V_{\text{latt}}(x,y)} \left[\cos^2(kz) + \frac{(1-\sqrt{\gamma})^2}{4\sqrt{\gamma}}\right]. \tag{2.24}$$

With increasing power imbalance the lattice depth reduces according to $V_{\text{latt}} \propto \sqrt{\gamma}$. The offset term

$$R_- = \frac{(1-\sqrt{\gamma})^2}{4\sqrt{\gamma}} \tag{2.25}$$

quantifies the relevance of the running wave component with respect to the amplitude of the cosine-squared lattice potential, compare Figure 2.6.

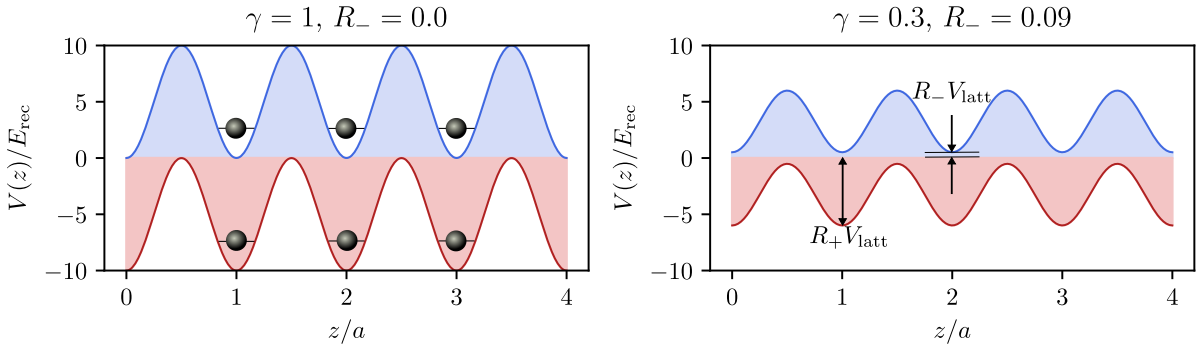

Figure 2.6: Running wave component. For $\gamma = 1$ there is no power imbalance between the two beams forming the optical lattice. In this case the maximum lattice depth is reached and there is no running wave component, i.e. the potential is not offset from $V(z) = 0$. In contrast, a finite power imbalance reduces the lattice depth by a factor of $\sqrt{\gamma}$, while increasing the offset $R_- V_{\text{latt}}$.

The amount of running wave component is independent of the detuning $\Delta = \omega - \omega_0$ of the lattice laser from the atomic resonance. There is, however, a major difference between red and blue detuned lattice lasers when considering their impact on the slowly-varying trapping potential, i.e. the part of the potential that remains after removing the cosine-squared term. Since the atoms always reside in the potential minima of the optical lattice, they experience a much higher laser intensity in the red-detuned case, see Figure 2.6, which is quantified by

$$R_+ = -(R_- + 1) = -\frac{(1+\sqrt{\gamma})^2}{4\sqrt{\gamma}}. \tag{2.26}$$

This is the relevant quantity when characterising the effect of a red-detuned laser on the slowly-varying part of the potential and its precise knowledge is crucial for analysing the inhomogeneous in-situ density distribution. There are two contributions to the overall trapping potential for any one-dimensional optical lattice. The first contribution arises as a direct consequence of the transverse intensity profile of the lattice laser beams, $V_{\mathrm{latt}}(x,y)R_{\mp}$, which is typically given by a Gaussian

$$V_{\mathrm{latt}}(x,y)R_{\mp} = V_{\mathrm{latt}}^{(0)} e^{-2\left[\left(\frac{x}{\omega_x}\right)^2+\left(\frac{y}{\omega_y}\right)^2\right]} R_{\mp}, \tag{2.27}$$

where $V_{\mathrm{latt}}^{(0)} = V_{\mathrm{latt}}(x=y=0)$ is the lattice depth in the centre of the trap. The first contribution to the trap potential is confining (deconfining) for red (blue) detuned light and its impact is much larger in the case of red detuning, as $R_- \approx 0 < |R_+| = 1 + R_-$ in the limit of small power imbalance, compare Figure 2.6.

The second contribution to the slowly varying trap potential indirectly follows from the lattice depth variation orthogonal to the beam propagation direction. It can be thought of as the quantum-mechanical correction to the classical expectation as it quantifies how the zero-point energy of each well increases with the local lattice depth. When Taylor expanding the cosine squared potential up to second order, the zero-point energy reproduces the result of an harmonic oscillator potential

$$\frac{\hbar\omega_{\mathrm{well}}}{2} = \sqrt{V_{\mathrm{latt}}(x,y)E_{\mathrm{rec}}}. \tag{2.28}$$

Note that this result is only valid for large lattice depths $V_{\mathrm{latt}} \gtrapprox 5E_{\mathrm{rec}}$. Combining these two terms yields the full trap potential of an optical lattice along the z-direction

$$V^{\mathrm{pot}}(x,y) = \pm e^{-2\left[\left(\frac{x}{\omega_x}\right)^2+\left(\frac{y}{\omega_y}\right)^2\right]} V_{\mathrm{latt}}^{(0)} R_{\mp} + \sqrt{V_{\mathrm{latt}}^{(0)} E_{\mathrm{rec}}}\, e^{-\left[\left(\frac{x}{\omega_x}\right)^2+\left(\frac{y}{\omega_y}\right)^2\right]}. \tag{2.29}$$

Note that the second term is always of deconfining nature, since the ground state energy of the harmonic oscillator approximation only depends on the lattice depth, which reduces from inside to outside, regardless of the sign of the detuning. In Section 4.3 we will use this formula to characterize the trap potential in the three-dimensional optical lattice configuration beyond the harmonic approximation.

CHAPTER 3

The Fermi-Hubbard Model

The Fermi-Hubbard model describes the behaviour of interacting spin-1/2 particles in a periodic potential landscape. Originally it was introduced to capture the physics of strongly correlated electrons in a crystal lattice structure [61, 62]. It presents a simplified version of the full many-body Hamiltonian by reducing both the kinetic and interaction energy to their most dominant contributions, i.e. tunnelling between adjacent lattice sites and on-site interactions. This simplification is valid for deep lattices, where the tight-binding approximation [63] holds, which assumes the atomic orbitals to be strongly localized to their respective lattice sites.

In this chapter I begin by introducing the Wannier basis which allows for a localized description of lattice physics. The double-well potential represents the fundamental building block of the Fermi-Hubbard model and is often employed to investigate the interplay of the kinetic and interaction energy with Pauli's exclusion principle. Even though the Hubbard Hamiltonian does not feature a direct spin-spin interaction, quantum magnetism already arises in the two-site implementation due to the superexchange mechanism, which is equivalent to a spin-flip process in the Heisenberg model. After reviewing the properties of the two-dimensional (2D) Hubbard model, where the motion is limited to a two-dimensional layer with square lattice structure, I will discuss an approximate phase diagram. Finally, I will introduce the bilayer Fermi-Hubbard model. In its two limiting cases of negligible and strong coupling between the two layers, we retrieve the behaviour of the 2D and double-well Fermi-Hubbard model, respectively.

For more information, the reader may refer to the review articles on the Fermi-Hubbard model and its implementation using ultracold fermions in optical lattices, [64–68]. The following section was mostly inspired by the review article by L. Tarruell [69].

3.1 Tight-Binding Approximation

The many-body Hamiltonian that will be considered in the following contains an interaction term, which introduces correlations between the spin-1/2 particles in addition to the single-particle term. The Coulomb repulsion that we intend to mimic with our quantum simulator is a long-range interaction that scales as $V_C \propto 1/r$. However, in solids it is mostly screened by the positive nuclei and therefore we will assume a regularized δ-potential instead [70]

$$U(\boldsymbol{r}) = g\delta(\boldsymbol{r})\frac{\partial}{\partial r}, \tag{3.1}$$

where g is the interaction strength and $\boldsymbol{r} = \boldsymbol{r}_2 - \boldsymbol{r}_1$ is the relative position of the two interacting particles. This assumption drastically simplifies the two-body interaction. For the description of an interacting quantum many-body system, it is useful to adopt the formalism of second quantization and the full Hamiltonian, including the single-particle kinetic energy, the lattice potential landscape $V(\boldsymbol{r})$ and the contact interaction $U(\boldsymbol{r})$ is given by

$$\hat{H} = \sum_{\sigma=\uparrow,\downarrow} \int \mathrm{d}^3\boldsymbol{r}\, \hat{\psi}_\sigma^\dagger(\boldsymbol{r}) \left[-\frac{\hbar^2\nabla^2}{2m} + V(\boldsymbol{r}) \right] \hat{\psi}_\sigma(\boldsymbol{r}) + g \int \mathrm{d}^3\boldsymbol{r}\, \hat{\psi}_\uparrow^\dagger(\boldsymbol{r}) \hat{\psi}_\downarrow^\dagger(\boldsymbol{r}) \hat{\psi}_\downarrow(\boldsymbol{r}) \hat{\psi}_\uparrow(\boldsymbol{r}), \tag{3.2}$$

where the field operator $\hat{\psi}_\sigma^\dagger(\boldsymbol{r})$ creates a particle with spin σ at position $\boldsymbol{r}$.

Note that we consider interactions between fermions of opposite spin only. For a short-range two-body interaction potential this is justified in the low-temperature limit, where only s-wave interactions are energetically possible, as for $l = 0$ the angular momentum barrier in the effective potential disappears [71]. Two fermions in the same spin state, or more generally speaking in a symmetric spin state, can never undergo s-wave collisions for which a spatially symmetric wavefunction is required. This is a very general statement and remains valid even when considering higher bands.

Wannier Basis

In the previous chapter we have found that for deep lattices, $V_{\mathrm{latt}} \gg E_{\mathrm{rec}}$, the lowest energy bands are essentially flat and the band gaps are large, similar to a harmonic oscillator potential. If the temperature is small compared to the band gap, we can restrict the description to the ground band. Since the Bloch functions of the lowest band strongly peak around each lattice site, a change of the basis to a set of localized states is reasonable. Furthermore, a two-body interaction that is purely local in real space will mix the Bloch waves at arbitrary momenta, which renders the Bloch basis impractical. This mixing of the q-states is circumvented in the Hubbard model by employing a set of basis states $w(\boldsymbol{r} - \boldsymbol{r}_j)$ called Wannier functions, which are exponentially localized around their respective lattice sites [72],

$$w(\boldsymbol{r} - \boldsymbol{r}_j) = \left(\frac{a}{2\pi}\right)^{3/2} \int \mathrm{d}^3\boldsymbol{q}\, \psi_{\boldsymbol{q}}^0(\boldsymbol{r}) e^{-i\boldsymbol{q}\cdot\boldsymbol{r}_j}. \tag{3.3}$$

For periodic potentials where the unit cell contains more than one lattice site the Wannier functions as defined in Equation 3.3 are not sensible as they would be centred with respect to the unit cell. For example in the case of bichromatic superlattices, introduced in Section 2.2.2, the unit cell contains two lattice sites. In order to obtain a wavefunction that is strongly localized around either of the sites, one may employ the definition of Wannier states by S. Kivelson [73] as eigenstates of the position operator projected onto a given energy band or band manifold. This method and its implementation are discussed in detail in [74–76]. Recently my colleague N. Klemmer implemented this method to obtain a faithful description of the Wannier functions of our optical superlattice configuration [77]. However, for the following discussion it suffices to concentrate on simple cubic lattice structures.

In second quantization the field operator $\hat{\psi}_\sigma(\boldsymbol{r})$ removing a particle with spin σ at position $\boldsymbol{r}$ may be expanded in the Wannier basis of the lowest energy band according to

$$\hat{\psi}_\sigma(\boldsymbol{r}) = \sum_j w(\boldsymbol{r} - \boldsymbol{r}_j) \hat{c}_{j,\sigma}, \tag{3.4}$$

where the fermionic operator $\hat{c}_{j,\sigma}$ annihilates a particle with spin σ in the Wannier function of the ground band that is centred around the lattice site j. If we insert this expression into the Hamiltonian defined in Equation 3.2, we obtain a description in the lattice site space. For deep lattices the Wannier functions are strongly localized around their respective lattice sites and the overlap between Wannier functions of neighbouring sites is small although not negligible. In this case, it is well justified to limit both the kinetic and interaction energy to their most dominant contribution each, i.e. nearest-neighbour tunnelling with amplitude t and on-site interactions of strength U, and we obtain the Fermi-Hubbard Hamiltonian in its standard form

$$\hat{H} = -t \sum_{\langle i,j \rangle, \sigma} \hat{c}^{\dagger}_{i,\sigma} \hat{c}_{j,\sigma} + U \sum_{i} \hat{n}_{i,\uparrow} \hat{n}_{i,\downarrow}, \tag{3.5}$$

where $\hat{n}_{i,\sigma} = \hat{c}^{\dagger}_{i,\sigma} \hat{c}_{i,\sigma}$ is the occupation number operator for particles with spin σ at site i. Both contributions will be discussed briefly in the following.

Tunneling Dynamics

The tunnelling amplitude between two arbitrary lattice sites i and j is given by

$$t_{ij} = -\int \mathrm{d}^3\boldsymbol{r}\, w^*(\boldsymbol{r} - \boldsymbol{r}_i) \left[-\frac{\hbar^2 \nabla^2}{2m} + V(\boldsymbol{r}) \right] w(\boldsymbol{r} - \boldsymbol{r}_j). \tag{3.6}$$

For the special case, where $i = j$, the matrix element corresponds to the on-site energy, which is a relevant term if the particles experience an additional trap confinement or for bichromatic optical lattices with differing site offsets. However, for homogeneous monochromatic lattices the on-site energy is a constant offset and is typically neglected. As the spatial overlap of the Wannier functions decreases quickly with distance $\boldsymbol{r}_j - \boldsymbol{r}_i$, the dominant contribution to the kinetic energy is given by the nearest-neighbour tunnelling with amplitude $t \equiv t_{ij}$, with the sites i and j being adjacent to one another.

Among other things the nearest-neighbour tunnelling amplitude t determines the relevant timescale for coherent Rabi oscillations, where a single particle oscillates between two lattice sites which are not offset in their potential energy. The oscillation frequency is given by $f_{\mathrm{Rabi}} = 2t/h$ and this simple formula may be used to calibrate the tunnelling amplitude as will be the topic of Section 6.2.1. In contrast, the expansion velocity of a Bloch wave with wavevector q is given by the group velocity, $v_{\mathrm{group}} = \partial E / (\hbar \partial q)$ [58].

Two-Body Interaction

For a pure contact interaction potential the dominant contribution is the on-site interaction, which shifts the energy of doubly occupied lattice sites by an amount

$$U = g \int \mathrm{d}^3\boldsymbol{r}\, |w(\boldsymbol{r} - \boldsymbol{r}_i)|^4 = \frac{4\pi\hbar^2 a_{\mathrm{sc}}}{m} \int \mathrm{d}^3\boldsymbol{r}\, |w(\boldsymbol{r} - \boldsymbol{r}_i)|^4. \tag{3.7}$$

Here, we have introduced the scattering length, a_{sc}, which is the only parameter that is required to fully characterize the spherically symmetric contact interaction potential. More details on the scattering length may be found in Section 4.1.1.

Note that the Wannier functions do not incorporate the effect of interactions, as they are

derived from the Bloch waves, which are the single-particle solutions of a periodic potential. Therefore, the (simple) Wannier basis is not a suitable basis to estimate the Hubbard parameters in the strongly interacting regime [78]. There has been considerable effort in determining the energy offset for two interacting particles in an isotropic and anisotropic harmonic potential [70, 79] and in optical lattices [78]. To obtain the interaction strength for our experimental implementation of the Hubbard model, we follow the approach by [70] where the interaction shift was calculated for an axially symmetric harmonic trap with ellipticity $\eta = \omega_{x,y}/\omega_z$. The approximation by a harmonic potential close to the centre of a lattice site,

$$V_{\text{well}}(x) \approx \frac{1}{2} m\omega_x^2 (x - x_i)^2 + \text{const.}, \tag{3.8}$$

is valid if the lattice is deep and the particles are closely localized around their respective lattice site minima [69]. Here we have introduced the harmonic oscillator frequency $\hbar\omega_x = 2\sqrt{s_x} E_{\text{rec}}$ that depends on the lattice depth $s_x = V_x/E_{\text{rec}}$.

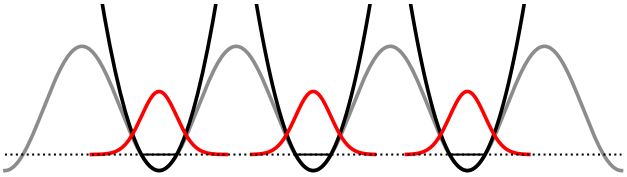

Figure 3.1: Harmonic approximation of an optical lattice potential. In a deep optical lattice, the sinusoidal potential (grey) may be approximated by a harmonic oscillator potential (black) with a Gaussian ground band wavefunction (red).

However, since the harmonic approximation overestimates the compression by the lattice potential as shown in Figure 3.1, the true interaction in an optical lattice will be smaller than the one given in [70]. This is accounted for by rescaling the result with the ratio of the interaction strengths calculated using the single-particle Wannier functions and the non-interacting solution of the harmonic oscillator potential [60, 80], which is a Gaussian,

$$g(x) = \frac{1}{\pi^{1/4} l_x^{1/2}} e^{-\frac{1}{2}\frac{(x-x_i)^2}{l_x^2}}, \tag{3.9}$$

where $l_x = \sqrt{\frac{\hbar}{m\omega_x}}$ is the harmonic oscillator length. In Figure 3.1 we plot the harmonic approximation of the lattice potential close to the centre of the lattice sites and the Gaussian eigenfunction of the harmonic well. In contrast to the Wannier functions, which constitute an orthonormal basis, the Gaussian solutions centred around different lattice sites are in general not orthogonal. Within the harmonic approximation, we may obtain an analytic expression for the on-site interaction as a function of the lattice depths s_i and the respective lattice spacings a_i,

$$U = \sqrt{\frac{\pi}{8}} a_{sc} h^2 \frac{(s_x s_y s_z)^{1/4}}{m a_x a_y a_z}, \tag{3.10}$$

which is used to calculate the rescale factor as discussed above.

According to [80] and [78] the true interaction strength deviates significantly from the non-interacting estimate, if $a_{sc}/l_i > 0.3$ for any of the harmonic oscillator lengths $l_{x,y,z}$. The absolute value of the interaction strength reduces with respect to the estimate using non-interacting Wannier functions independent of the sign of the scattering length, see [78] and [80]. Therefore, it seems that the Wannier functions broaden under the effect of very strong interactions whether they are repulsive [81, 82] or attractive in nature.

3.2 Two-Site Hubbard Model

In the following, I will discuss the fundamental building block of the Hubbard model. In a double-well potential two sites are coupled by quantum-mechanical tunnelling through a barrier. There is an introductory article by Foot and Shotter [83] reviewing the physics of the double-well, which apart from the mathematical derivations provides an intuitive understanding. The double-well is not only an instructive model system to understand the interplay of kinetic and interaction energy, it also constitutes one of the two limiting cases of the bilayer Fermi-Hubbard model, which is essential to this thesis.

3.2.1 Balanced Double-Well

I will start by investigating the properties of the balanced double-well system, i.e. there is no potential energy offset between the two sites.

A Single Particle in the Double-Well

If we only fill a single particle, either bosonic or fermionic, into a double-well potential, a possible basis is given by the Wannier states that are localized in either the left $|L\rangle$ or right $|R\rangle$ well, respectively. The only term in the Hamiltonian that gives a contribution in this case is the tunnelling, since there is no other particle to interact with. Furthermore, the spin property is irrelevant and therefore the spatial basis $\{|L\rangle, |R\rangle\}$ is sufficient to describe the system and we obtain

$$H_{N=1} = \begin{pmatrix} 0 & -t \\ -t & 0 \end{pmatrix}, \tag{3.11}$$

with eigenenergies $E_\pm = \mp t$ and eigenstates

$$|\phi_\pm\rangle = \frac{1}{\sqrt{2}} \left(|L\rangle \pm |R\rangle \right). \tag{3.12}$$

Note that we obtain the same ground state for fermions and bosons, since with just one particle in the system it is not possible to define an exchange symmetry. Both eigenstates are delocalized over the two lattice sites of the double-well potential, however only the symmetric superposition $|\phi_+\rangle$ lowers the energy of the system, since it does not have a node in the wavefunction.

Two Interacting Fermions in the Double-Well

If the double-well is occupied by two particles of opposite spin, the interaction energy adds flavour and will compete with the kinetic energy. We will start the discussion with the symmetric double-well potential. The single band approximation is still valid in the presence of interactions

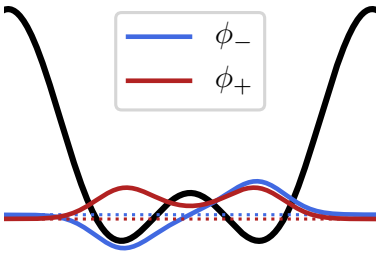

Figure 3.2: Eigenstates of a single-particle in the double-well potential. The symmetric spatial wavefunction ϕ_+ lowers its kinetic energy with respect to the antisymmetric wavefunction ϕ_- by delocalizing over the barrier. The difference in eigenenergies $E_\pm$, indicated by the blue and red dotted lines, respectively, decreases with barrier height, as the tunnelling is suppressed.

as long as $U \ll \hbar\omega$, where ω is the approximate harmonic oscillator frequency of the double-well potential.

With two interacting particles in the double-well potential we will have to consider the spin property of the particles. For the energy spectrum, however, the spin part of the wavefunction is not relevant since there is no spin-dependent term in the Hamiltonian. Therefore, it suffices to construct the two-particle basis $\{|LL\rangle, |LR\rangle, |RL\rangle, |RR\rangle\}$ in first quantization from the localized singe-particle states, where the first (second) entry determines the spatial wavefunction of the first (second) particle [84]. In this basis the Fermi-Hubbard Hamiltonian follows as

$$H_{N=2} = \begin{pmatrix} U & -t & -t & 0 \\ -t & 0 & 0 & -t \\ -t & 0 & 0 & -t \\ 0 & -t & -t & U \end{pmatrix}. \tag{3.13}$$

For the non-interacting case $U = 0$, the spatial part of the eigenstates corresponding to the lowest and highest energy, E_1 and E_4, are simply product states of the single-particle solutions $|\phi_\pm\rangle$:

$$|\phi_1(U=0)\rangle = \frac{1}{2}\left(|LL\rangle + |LR\rangle + |RL\rangle + |RR\rangle\right) = |\phi_+\rangle \otimes |\phi_+\rangle, \tag{3.14}$$

$$|\phi_4(U=0)\rangle = \frac{1}{2}\left(|LL\rangle - |LR\rangle - |RL\rangle + |RR\rangle\right) = |\phi_-\rangle \otimes |\phi_-\rangle. \tag{3.15}$$

Therefore, it is not surprising to find $E_1(U=0) = -2t\ (= 2E_+)$ and $E_4(U=0) = +2t\ (= 2E_-)$. In Figure 3.3 we can see that there is an avoided crossing at $U = 0$ between the eigenenergies E_1 and E_4. Depending on the sign of the interaction strength, the ground state is either dominated by singly or doubly occupied sites, which corresponds to a crossing of the bare states $1/\sqrt{2}\left(|LL\rangle + |RR\rangle\right)$ and $1/\sqrt{2}\left(|LR\rangle + |RL\rangle\right)$, which are coupled by quantum tunnelling.

The two states corresponding to the intermediate eigenenergies E_2 and E_3 cannot be expressed as a direct product of the single-particle states, since the exchange symmetry following from the spin statistics theorem would be violated. Their representation does not depend on the

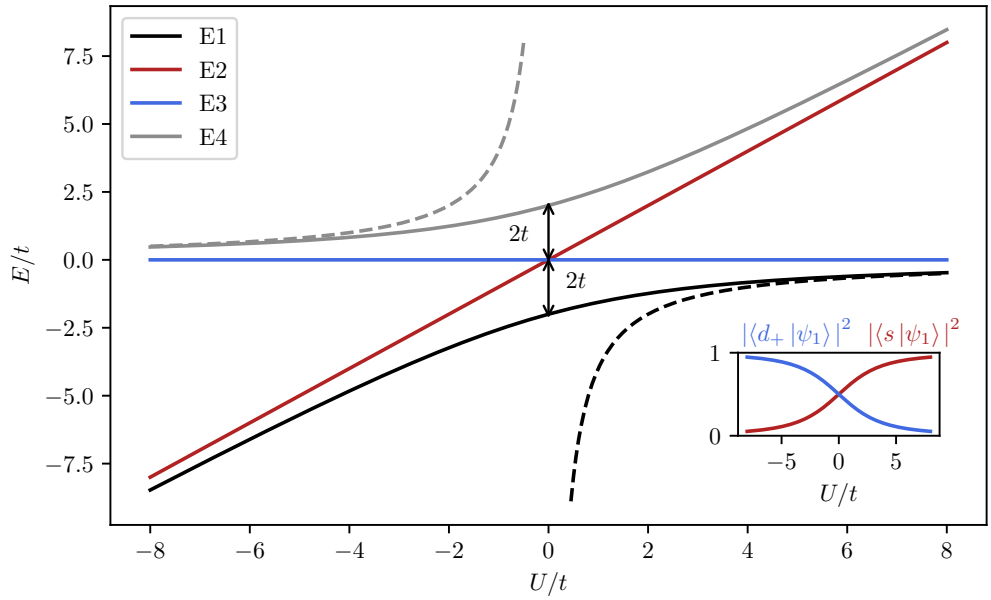

Figure 3.3: Energies of the eigenstates of two interacting fermions in a double-well potential. We obtain the eigenenergies E_i of two interacting fermions in a double-well by exact diagonalization of the Hamiltonian given in Equation 3.13. In the inset we show the two contributions $|s\rangle$ and $|d_+\rangle$, defined in Equations 3.27 and 3.28, to the full wavefunction of the ground state $|\psi_1\rangle$ as a function of the interaction strength. The inverse dependence is found for the excited state $|\psi_4\rangle$. For large repulsive interactions the ground state energy is well approximated by the superexchange constant $J = 4t^2/U$ (dashed black line). A similar observation holds for the excited state at strong attractive interactions. The eigenenergies E_i and their corresponding wavefunctions $|\psi_i\rangle$ are listed in Table 3.1.

interaction strength

$$|\phi_2(U)\rangle = |\phi_2\rangle = \frac{1}{\sqrt{2}}\left(|LL\rangle - |RR\rangle\right), \tag{3.16}$$

$$|\phi_3(U)\rangle = |\phi_3\rangle = \frac{1}{\sqrt{2}}\left(|LR\rangle - |RL\rangle\right). \tag{3.17}$$

The full eigenenergy spectrum of the double-well Hamiltonian is shown in Figure 3.3 and the corresponding eigenenergies are given in Table 3.1. Note that in contrast to the non-interacting case, the eigenenergies of two interacting spin-1/2 particles may not simply be inferred from the single-particle sector.

Spin Wavefunction With two indistinguishable particles in the double-well, we also have to take care of the proper symmetrization of the spin part of the wavefunction. Since the spin property does not appear in the Hamiltonian, the spin part separates from the spatial wavefunction, and is therefore not relevant for the eigenenergies. The full wavefunction is simply given by the product of the spatial and the spin part,

$$\psi_i\left(\boldsymbol{r}^{(1)}, m_S^{(1)}, \boldsymbol{r}^{(2)}, m_S^{(2)}\right) = \phi_i\left(\boldsymbol{r}^{(1)}, \boldsymbol{r}^{(2)}\right) \otimes \chi\left(m_S^{(1)}, m_S^{(2)}\right) \tag{3.18}$$

where the quantum number $m_S^{(1,2)}$ denotes the internal spin state of the first (second) particle. For fermions the total wavefunction must be antisymmetric under the exchange of two particles. Therefore, we have to assign a symmetric spin state to an antisymmetric spatial wavefunction and vice versa. These (anti)symmetric spin wavefunctions can be found by diagonalization of the total spin operator $\hat{\boldsymbol{S}} = \hat{\boldsymbol{S}}_1 + \hat{\boldsymbol{S}}_2$, which in the case of two interacting fermions in a double-well is a sum over the spin operators of both particles. The defining property of the spin operator, as for any other angular momentum operator, is the commutation relation that applies to the components of the vector operator $\hat{\boldsymbol{S}} = \left(\hat{S}^x, \hat{S}^y, \hat{S}^z\right)$,

$$\left[\hat{S}^x, \hat{S}^y\right] = i\hbar\hat{S}^z \tag{3.19}$$

and cyclic permutation of the indices x, y, z. For a spin-1/2 system the components of the spin operator can be represented using the Pauli matrices and in first quantization we obtain

$$\hat{S}^x = \frac{\hbar}{2}\sigma^x = \frac{\hbar}{2}\begin{pmatrix}0 & 1\\ 1 & 0\end{pmatrix}, \quad \hat{S}^y = \frac{\hbar}{2}\sigma^y = \frac{\hbar}{2}\begin{pmatrix}0 & -i\\ i & 0\end{pmatrix}, \quad \hat{S}^z = \frac{\hbar}{2}\sigma^z = \frac{\hbar}{2}\begin{pmatrix}1 & 0\\ 0 & -1\end{pmatrix}, \tag{3.20}$$

where the basis states $|\uparrow\rangle = \begin{pmatrix}1\\0\end{pmatrix}$ and $|\downarrow\rangle = \begin{pmatrix}0\\1\end{pmatrix}$ are the eigenstates of $\hat{S}^z$ and they correspond to the spin projection quantum numbers $m_S = \pm 1/2$, respectively.

Now, for the double-well we can express the total spin operator in matrix representation[1] by employing the two-particle basis $\{|\uparrow\uparrow\rangle, |\uparrow\downarrow\rangle, |\downarrow\uparrow\rangle, |\downarrow\downarrow\rangle\}$, where the first (second) entry specifies the spin projection quantum number of the first (second) particle and we obtain

$$\hat{\boldsymbol{S}}^2 = \hbar^2\begin{pmatrix}2 & 0 & 0 & 0\\ 0 & 1 & 1 & 0\\ 0 & 1 & 1 & 0\\ 0 & 0 & 0 & 2\end{pmatrix} \quad \text{and} \quad \hat{S}^z = \hbar\begin{pmatrix}1 & 0 & 0 & 0\\ 0 & 0 & 0 & 0\\ 0 & 0 & 0 & 0\\ 0 & 0 & 0 & -1\end{pmatrix}. \tag{3.21}$$

The symmetric and antisymmetric spin wavefunctions χ_{S,M_S} are found by solving the eigenvalue equations

$$\hat{\boldsymbol{S}}^2\chi_{S,M_S} = \hbar^2 S(S+1)\chi_{S,M_S} \quad \text{and} \quad \hat{S}^z\chi_{S,M_S} = \hbar M_S\chi_{S,M_S}. \tag{3.22}$$

From the matrix representation we can directly identify the two eigenstates $|\chi_{1,1}\rangle = |\uparrow\uparrow\rangle$ and $|\chi_{1,-1}\rangle = |\downarrow\downarrow\rangle$ with eigenvalue $S(S+1) = 2$. The other eigenstates are

$$|\chi_{0,0}\rangle = \frac{1}{\sqrt{2}}\left(|\uparrow\downarrow\rangle - |\downarrow\uparrow\rangle\right) \quad \text{and} \quad |\chi_{1,0}\rangle = \frac{1}{\sqrt{2}}\left(|\uparrow\downarrow\rangle + |\downarrow\uparrow\rangle\right). \tag{3.23}$$

Since there is no coupling between the spatial and spin degrees of freedom, the total wavefunction is simply given by the product of the spatial and the spin part $|\psi_i\rangle = |\phi_i\rangle \otimes |\chi\rangle$. Here, the spin part has to be chosen such that $|\psi_i\rangle$ is antisymmetric under particle exchange for fermionic particles. To simplify the description of the double-well, we will express the total wavefunction

[1] $S_1^x + S_2^x = \frac{\hbar}{2}\begin{pmatrix}0 & 1 & 1 & 0\\ 1 & 0 & 0 & 1\\ 1 & 0 & 0 & 1\\ 0 & 1 & 1 & 0\end{pmatrix}$, $S_1^y + S_2^y = \frac{\hbar}{2}\begin{pmatrix}0 & -i & -i & 0\\ i & 0 & 0 & -i\\ i & 0 & 0 & -i\\ 0 & i & i & 0\end{pmatrix}$, $S_1^z + S_2^z = \frac{\hbar}{2}\begin{pmatrix}2 & 0 & 0 & 0\\ 0 & 0 & 0 & 0\\ 0 & 0 & 0 & 0\\ 0 & 0 & 0 & -2\end{pmatrix}$

in the framework of second quantization by defining the Fock state basis

$$|\uparrow\downarrow,0\rangle = c^\dagger_{L\downarrow}c^\dagger_{L\uparrow}|0\rangle\,, \quad |\uparrow,\downarrow\rangle = c^\dagger_{R\downarrow}c^\dagger_{L\uparrow}|0\rangle\,, \quad |\downarrow,\uparrow\rangle = c^\dagger_{R\uparrow}c^\dagger_{L\downarrow}|0\rangle\,, \quad |0,\uparrow\downarrow\rangle = c^\dagger_{R\downarrow}c^\dagger_{R\uparrow}|0\rangle\,, \tag{3.24}$$

where we do not specify the state of each particle individually. Instead a state is determined merely by the number of particles in a certain spin state for both lattice sites. The anticommutation relations for the fermionic creation and annihilation operators

$$\{c^\dagger_{i\sigma}, c^\dagger_{j,\sigma'}\} = \{c_{i\sigma}, c_{j,\sigma'}\} = 0 \quad \text{and} \quad \{c_{i\sigma}, c^\dagger_{j,\sigma'}\} = \delta_{ij}\delta_{\sigma\sigma'} \tag{3.25}$$

take care of the proper symmetrization and normalization of the many-body state. In Table 3.1 we list the eigenenergies together with their corresponding total wavefunction $|\psi\rangle$ and the exchange symmetries that apply to the spatial and spin part.

Eigenenergy	$\|\phi\rangle$	$\|\chi_{S,M_S}\rangle$	$\|\psi\rangle$
$E_1 = \frac{U}{2}\left(1 - \sqrt{\frac{16t^2}{U^2}+1}\right)$	$\|\phi_1\rangle$ $(+)$	$\|\chi_{0,0}\rangle$ $(-)$	$\propto \frac{E_4}{2t}\|s\rangle + \|d_+\rangle$
$E_2 = U$	$\|\phi_2\rangle$ $(+)$	$\|\chi_{0,0}\rangle$ $(-)$	$\frac{1}{\sqrt{2}}(\|\uparrow\downarrow,0\rangle - \|0,\uparrow\downarrow\rangle) =: \|d_-\rangle$
$E_3 = 0$	$\|\phi_3\rangle$ $(-)$	$\|\chi_{1,-1}\rangle$ $(+)$ $\|\chi_{1,0}\rangle$ $(+)$ $\|\chi_{1,1}\rangle$ $(+)$	$\|\downarrow,\downarrow\rangle$ $\frac{1}{\sqrt{2}}(\|\uparrow,\downarrow\rangle + \|\downarrow,\uparrow\rangle) =: \|t_0\rangle$ $\|\uparrow,\uparrow\rangle$
$E_4 = \frac{U}{2}\left(1 + \sqrt{\frac{16t^2}{U^2}+1}\right)$	$\|\phi_4\rangle$ $(+)$	$\|\chi_{0,0}\rangle$ $(-)$	$\propto \frac{E_1}{2t}\|s\rangle + \|d_+\rangle$

Table 3.1: Eigenenergies and wavefunctions for two interacting fermions in a double-well. We obtain the eigenstates by exact diagonalization and specify both the spatial and the spin part of the wavefunction. The sign states whether the corresponding wavefunction is symmetric $(+)$ or antisymmetric $(-)$ under particle exchange.

Similar to the $|t_+\rangle$ and $|t_-\rangle$ states, which cannot lower their energy by tunnelling due to Pauli's exclusion principle, the triplet state $|t_0\rangle$ also has the same energy $E_3 = 0$. Even though the two particles delocalize over the double-well by realizing a superposition state, they do not build up coherence by quantum tunnelling since

$$\hat{H}_{\text{kin}}|t_0\rangle = -t|d_+\rangle + t|d_+\rangle = 0. \tag{3.26}$$

In contrast, note that the singlet state

$$|s\rangle = \frac{1}{\sqrt{2}}(|\uparrow,\downarrow\rangle - |\downarrow,\uparrow\rangle) \tag{3.27}$$

and the doublon state

$$|d_+\rangle = \frac{1}{\sqrt{2}} \left(|\uparrow\downarrow, 0\rangle + |0, \uparrow\downarrow\rangle \right) \tag{3.28}$$

are connected via quantum tunnelling through the barrier of the double-well, since

$$\langle d_+ | \hat{H}_{\text{kin}} | s \rangle = -2t. \tag{3.29}$$

Therefore, for non-interacting fermions the ground state is an equal mixture of both of these states. However, if we turn on strong interactions $|U| \gg t$ between particles with opposite spin, the ground state will favour either singly or doubly occupied sites. In the inset of Figure 3.3 we show that the imbalance between the singlet and doublon state increases with the interaction strength regardless of the sign. This is a clear indication that the delocalization energy is outweighed by the interaction energy. In this regime of strong on-site interactions, density fluctuations are suppressed and second-order tunnelling becomes the dominant process. In the following section we will investigate how the interplay of strong repulsive interactions and Pauli's exclusion principle will lead to antiferromagnetic ordering.

3.2.2 Quantum Magnetism in the Double-Well

For fermions, the ground state of the double-well features an antisymmetric spin singlet configuration for any interaction. However, only if particles with opposite spin strongly repel each other, the ground state is mostly composed of singly occupied sites, see Figure 3.3. For low enough temperatures they will order antiferromagnetically in spin space. In contrast, for attractive interactions the system favours doubly-occupied and empty sites and therefore we obtain ordering in the density sector (charge-density wave). In the following we want to investigate how the Hubbard model supports quantum magnetism even though it does not feature a direct spin-spin interaction term as the Heisenberg Hamiltonian does.

For the non-interacting case, the ground state minimizes its kinetic energy by delocalization to $E_1(U = 0) = -2t$. When introducing weak repulsive interactions the ground state energy increases according to

$$E_1(U) \approx -2t + \frac{U}{2}. \tag{3.30}$$

For strong repulsive interactions $U \gg t$, the single-particle tunnelling is strongly suppressed due to the energy gap $\Delta E = U$ between basis states containing only singly-occupied sites $\{|\uparrow, \downarrow\rangle, |\downarrow, \uparrow\rangle, |\uparrow, \uparrow\rangle, |\downarrow, \downarrow\rangle\}$ and those containing a doublon $\{|\uparrow\downarrow, 0\rangle, |0, \uparrow\downarrow\rangle\}$. In this case the approximate eigenstates of the low-energy sector $E \approx 0$ are given by $|s\rangle, |t_0\rangle, |t_+\rangle$ and $|t_-\rangle$, cf. Table 3.1. As the charge degree of freedom is frozen, we obtain an effective spin interaction. Employing second-order perturbation theory, we can compute the energy shift experienced by the singlet state by treating the tunnelling operator as a small perturbation [85]

$$\delta E^{(2)}_{|s\rangle} = \frac{\langle s | \hat{H}_{\text{kin}} | d_+ \rangle \langle d_+ | \hat{H}_{\text{kin}} | s \rangle}{E_{|s\rangle} - E_{|d_+\rangle}} \overset{\text{Eq. 3.29}}{=} -\frac{4t^2}{U}. \tag{3.31}$$

Therefore, in the limit of $U \gg t$ the energy of the ground state is reduced by the superexchange constant, $J = 4t^2/U$. Due to the fermionic anticommutation sign the first-order tunnelling

amplitudes interfere constructively for the singlet state (compare Equation 3.29) as visualized in Figure 3.4. The opposite applies to the triplet state $|t_0\rangle$ and indeed the energy shift according to second-order perturbation theory vanishes for all three triplet states

$$\delta E^{(2)}_{|t_0\rangle} = \delta E^{(2)}_{|t_+\rangle} = \delta E^{(2)}_{|t_-\rangle} = 0. \tag{3.32}$$

Physically this is linked to the fact that the triplet states are not able to tunnel. While for the state $|t_0\rangle$ the tunnelling amplitudes to the $|d_+\rangle$ state interfere destructively (see Equation 3.26), tunnelling is forbidden by Pauli's exclusion principle for the basis states $|t_+\rangle$ and $|t_-\rangle$ where neighbouring sites are occupied by the same spin state.

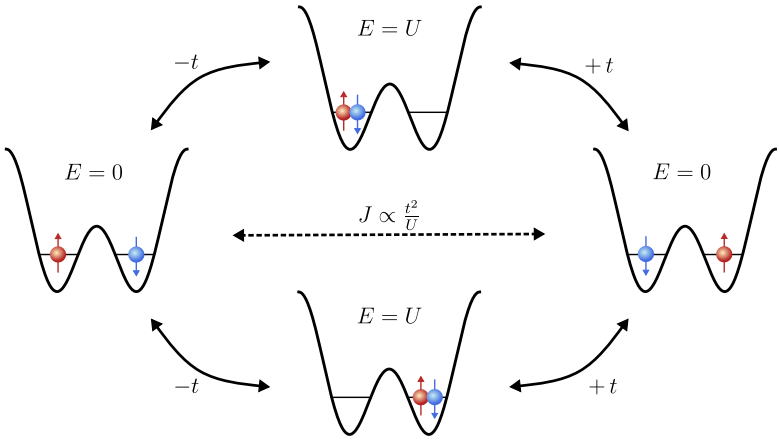

Figure 3.4: Superexchange mechanism in the double-well. In the strongly-interacting regime single-particle tunnelling is strongly suppressed due to the energy difference of $\Delta E = U$. The energy of the singlet is still lower compared to the triplet states, since second-order tunnelling leads to a virtual occupation of double occupancies. Therefore, this so-called superexchange process favours antiparallel alignment of spins. This figure was inspired by [84].

The energy gain of the singlet state that we obtained as an approximate result by treating the tunnelling as a perturbation matches the eigenenergy obtained by exact diagonalization of the double-well Hamiltonian for strong repulsive interactions $U \gg t$, where

$$E_1(U \gg t) \approx -\frac{4t^2}{U}. \tag{3.33}$$

The first-order correction to the bare singlet state $|s\rangle$ also reveals that a finite amount of double occupancies is necessary to lower the ground state energy

$$|s\rangle^{(1)} \propto |s\rangle + \frac{2t}{U}|d_+\rangle \approx |\psi_1(U \gg t)\rangle\,. \tag{3.34}$$

Therefore the term *virtual double occupancy* that is often used is sensible only in the context of perturbation theory.

Note that the antiferromagnetic alignment is favoured for fermions as a consequence of the anticommutation relations that apply to the creation and annihilation operators. Therefore, for bosons we obtain the opposite result and the spins experience an effective ferromagnetic interaction.

3.2.3 Tilted Double-Well

The implementation of the two-site system using optical superlattices allows us to modify the potential landscape including the energy offset 2Δ between the two coupled sites of a double-well potential, compare Figure 3.14. This site-offset is engineered by properly adjusting the wavelength of either lattice, as shown in Figures 2.4 and 2.5. In the following we will investigate the influence of this tilt onto the ground state wavefunction. The Hamiltonians describing the situation when only one atom or two atoms with opposite spin are present in a tilted double-well are given in Equation 3.35. For the matrix representation we employ the basis states $\{|\sigma,0\rangle\,,\ |0,\sigma\rangle\}$ and $\{|\uparrow\downarrow,0\rangle\,,\ |\uparrow,\downarrow\rangle\,,\ |\downarrow,\uparrow\rangle\,,\ |0,\uparrow\downarrow\rangle\}$, respectively, where the order of the fermionic creation operators $c^\dagger_{R\downarrow}c^\dagger_{R\uparrow}c^\dagger_{L\downarrow}c^\dagger_{L\uparrow}$ fixes the signs of the tunnelling matrix elements.

$$H_{N=1} = \begin{pmatrix} \Delta & -t \\ -t & -\Delta \end{pmatrix} \qquad H_{N=2} = \begin{pmatrix} U+2\Delta & -t & t & 0 \\ -t & 0 & 0 & -t \\ t & 0 & 0 & t \\ 0 & -t & t & U-2\Delta \end{pmatrix} \tag{3.35}$$

From an exact diagonalization in each of the sectors with fixed N we obtain the eigenenergies and corresponding eigenstates. In Figure 3.5 a) and b) we plot the ground state contributions for $U/t = 2$. For $N = 1$, the particle is predominantly localized in the left (right) well if Δ/t smaller (larger) than zero or in a symmetric superposition in case of a balanced double-well potential where $\Delta = 0$. With two particles, $N = 2$, we additionally have to consider double occupancies, which will dominate the ground state when the tilt is large, $|\Delta|/t \gg 1$. Following the definition of the basis, every single occupancy in the left well is accompanied by a single occupancy with opposite spin in the right well. Therefore, we find that $s^{\mathrm{L}}_\sigma = s^{\mathrm{R}}_{\bar{\sigma}}$. In addition the tilt is not spin-dependent, therefore the basis states $|\uparrow,\downarrow\rangle$ and $|\downarrow,\uparrow\rangle$ ought to be equally likely. To simulate the probabilities for singly and doubly occupied sites for an arbitrary total filling n per spin state we combine the two separate solutions with $n = 0.25$ for $N = 1$ and $n = 0.5$ for $N = 2$. The result for an average filling of $n = 0.43$ is shown in Figure 3.5 c) and we observe that the average singles filling is different in the two wells due to the finite contribution of the $N = 1$ sector. In Figure 6.8 we will compare our experimental data on the filling of both singly and doubly occupied sites obtained from a strongly coupled bilayer lattice system to this double-well calculation.

Introducing a tilt to the lattice structure has profound consequences on the single particle dynamics. I. Dimitrova and co-workers have shown that a potential energy offset 2Δ between neighbouring sites suppresses first-order tunnelling while the superexchange mechanism remains resonant [86]. However, the energy of the intermediate level is different for the two configurations corresponding to a particle that has to tunnel either "uphill" or "downhill" and the coupling constant modifies to [87]

$$J(\Delta) = \frac{1}{2}\left(\frac{4t^2}{U+2\Delta} + \frac{4t^2}{U-2\Delta}\right). \tag{3.36}$$

3.3 Two-Dimensional Hubbard Model

In the 1980s, high-temperature superconductivity was observed in doped metal-oxide compounds [5, 88, 89]. In conventional superconductors weak attractive interactions mediated by phonon

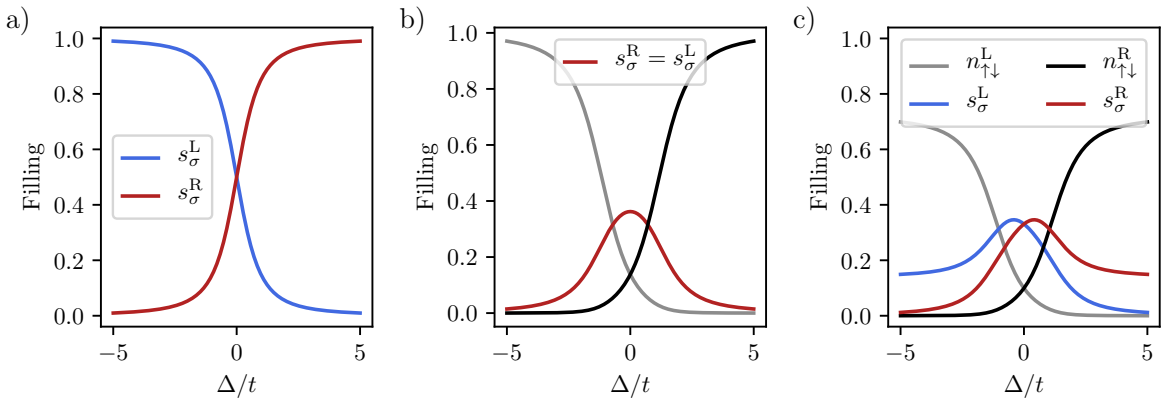

Figure 3.5: Ground state wavefunction in a tilted double-well. Shown are the contributions to the ground state $|\psi_0\rangle$ of the $N = 1$ (a) and $N = 2$ (b) Fermi-Hubbard Hamiltonian, given in Equation 3.35, with $U/t = 2$. For a single particle with spin σ there are only two basis states, namely a single occupancy in the left or right well and we identify $s_\sigma^{\mathrm{L}} = |\langle \sigma, 0|\psi_0\rangle|^2$. In the case where two particles with opposite spin occupy the double-well ($N = 2$) we additionally distinguish between single and double occupancies. The latter is given by $n_{\uparrow\downarrow}^{\mathrm{L}} = |\langle \uparrow\downarrow, 0|\psi_0\rangle|^2$. In order to simulate an intermediate filling, in between the $N = 1$ case with a total filling of $n = 0.25$ per spin state and the $N = 2$ case with $n = 0.5$, we combine the two solutions. In c) we have chosen an average total filling of $n = 0.43$.

modes couple electrons to Cooper pairs. In contrast, in materials with a high critical temperature the superconducting phase often appears in close proximity to a Mott insulating state with strong electron correlations [7, 90]. The conjecture by P. W. Anderson [91] that the main features of high-temperature superconductivity are captured by the two-dimensional (2D) Hubbard model has sparked an increasing interest in studying the properties of the 2D Hubbard model both with theoretical [17, 92–94] and experimental efforts [34, 38, 95–97]. An extensive overview about the realization of Fermi-Hubbard models in optical lattices is presented in [98].

In this section we will start with a close look at the individual terms that appear in the 2D Fermi-Hubbard model. This serves as the foundation to investigate both the symmetries and the (conjectured) properties of the phase diagram.

3.3.1 Fermi-Hubbard Hamiltonian

The 2D Fermi-Hubbard model describes spin-1/2 particles in a square lattice potential, where the mobility is restricted to a 2D layer. In the tight-binding approximation only two elementary processes are kept, i.e. nearest-neighbour tunnelling with amplitude t and an on-site interaction with strength U, which shifts the energy of doubly occupied lattice sites, see Figure 3.6.

The corresponding Hamiltonian in real space is given by

$$\hat{H} = -t \sum_{\langle i,j\rangle,\sigma} \hat{c}_{i,\sigma}^\dagger \hat{c}_{j,\sigma} + U \sum_i \hat{n}_{i\uparrow}\hat{n}_{i\downarrow}, \tag{3.37}$$

where $\hat{c}_{i,\sigma}$ ($\hat{c}_{i,\sigma}^\dagger$) denotes the annihilation (creation) operator of a fermion on lattice site i in spin state $\sigma = \{\uparrow, \downarrow\}$ and the bracket $\langle i, j\rangle$ indicates that the sum is restricted to nearest neighbours. In the non-interacting case, $U = 0$, the Hamiltonian is diagonal in momentum space. This can be seen by expressing the real space creation and annihilation operators as a Fourier transform

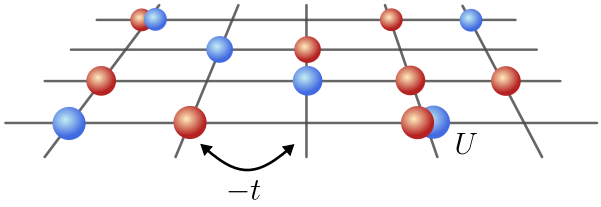

Figure 3.6: Sketch of the elementary processes in the two-dimensional Hubbard model. The Fermi-Hubbard model describes spin-1/2 particles, shown as red and blue spheres, which can tunnel to a neighbouring site, and thereby lower their kinetic energy. Interactions between opposite spin states are introduced by the on-site interaction with strength U.

over the momentum space operators $\hat{c}_{q,\sigma}$,[2]

$$\hat{c}_{j,\sigma} = \frac{1}{\sqrt{L}} \sum_{q} e^{iqr_j} \hat{c}_{q,\sigma}. \tag{3.38}$$

Consecutively, the diagonal form of the Hamiltonian is obtained by inserting this transformation into Equation 3.37

$$\hat{H} = -2t \sum_{q\sigma} \left[\cos(q_x a) + \cos(q_y a)\right] \hat{c}^{\dagger}_{q,\sigma} \hat{c}_{q,\sigma}, \tag{3.39}$$

from which the eigenenergy spectrum is directly read-off

$$E_{\sigma}(q) = -2t \left[\cos(q_x a) + \cos(q_y a)\right]. \tag{3.40}$$

From the definition of the Fourier transform it follows that for a finite system with L lattice sites there is also a finite number of momentum eigenstates. In the thermodynamic limit, however, they lie infinitely close together in an energy band of width $W = 8t$. We obtain two identical copies of the cosine shaped band, as we have not included the effect of interactions yet and hence the two spin components simply coexist in the lattice. Note that this result reproduces the true dispersion of the lowest band shown in Figure 2.1 in the limit of large lattice depths $V_0 \gg E_{\mathrm{rec}}$ where the tight-binding approximation is well justified. Therefore, the eigenstates of the non-interacting Fermi-Hubbard model are Bloch waves with wavevector q. For a fully filled lattice, we find that the kinetic energy, which is given by the sum over all occupied q-states, $E_{\mathrm{kin}} = \sum_q E_{\sigma}(q)$ vanishes. Intuitively speaking, the atoms are not able to move, as all lattice sites are occupied. At half-filling, when there is on average one particle per lattice site, the kinetic energy takes on its minimum value since all particles lower their energy by delocalizing over the lattice.

Introducing on-site interactions to the Fermi-Hubbard model restricts the mobility of the spin-1/2 particles by reducing the amount of density fluctuations in the ground state. The purely local interaction term couples all the different quasimomentum states and therefore the extended Bloch waves are not the eigenstates any more but are replaced by more localized states. In the case of strong attractive (repulsive) interactions, the system minimizes its total energy

[2] Note that due to the two-dimensional lattice geometry i, j and q are vectors comprising an x and y component: $i \equiv \begin{pmatrix} i_x \\ i_y \end{pmatrix}$ and $q \equiv \begin{pmatrix} q_x \\ q_y \end{pmatrix}$.

by increasing (decreasing) the occurrence of doubles and holes. The stronger the interaction the more classical is the behaviour of the spin-1/2 particles, i.e. the particle-character wins over the wave-like nature and the amount of superposition in the eigenstates reduces. For intermediate interaction strength, the competition of the kinetic and interaction energy terms often leads to strong correlations in the density and spin sectors, and as a consequence the 2D Fermi Hubbard model is not exactly solvable. Before discussing the different phases in more detail, I will introduce two additional terms to the Hamiltonian, namely the chemical potential, μ, which adjusts the average filling $n_\sigma = N_\sigma/L$ and an effective magnetic field, h, which couples to the imbalance in the spin densities $n_\uparrow - n_\downarrow$.

Chemical Potential For the discussion of the double-well Hamiltonian in the preceding chapter, we have treated the problem in the subspace of fixed particle number $N = 1$ and $N = 2$. It is however useful to solve the 2D Fermi-Hubbard model within the framework of the grand-canonical ensemble, and hence to specify the chemical potential μ instead of the total particle number N [99]. The role of the chemical potential μ is to adjust the average density in the system by allowing for exchange with a particle reservoir and we obtain

$$\hat{H} = -t \sum_{\langle i,j\rangle\sigma} (\hat{c}^\dagger_{i,\sigma}\hat{c}_{j,\sigma} + h.c.) + U \sum_i \hat{n}_{i\uparrow}\hat{n}_{i\downarrow} - \sum_i \mu_i(\hat{n}_{i\uparrow} + \hat{n}_{i\downarrow}). \tag{3.41}$$

The dependence of the average filling $n_\sigma = \langle \hat{n}_\sigma \rangle$ on the chemical potential μ is called the (density) equation of state, since we can derive thermodynamic variables such as the pressure and the entropy from it. We will revisit the equation of state $n_\sigma(\mu)$ throughout this thesis, for example in Figure 3.11 we investigate the effect of introducing repulsive on-site interactions to the equation of state of the 2D Fermi-Hubbard model. Note that for a spin-balanced system we have $n_\sigma(\mu) = n_{\bar{\sigma}}(\mu) \equiv n(\mu)$.

Unlike solid-state systems, ultracold atoms in optical lattices are usually confined by an additional slowly varying trapping potential $V(x, y)$, see Section 2.3. This leads to an inhomogeneous density distribution $n_\sigma(x, y)$ within the 2D layer. In Figure 3.7 we sketch the trap potential, which close to the centre may be approximated as a harmonic trap. If the potential

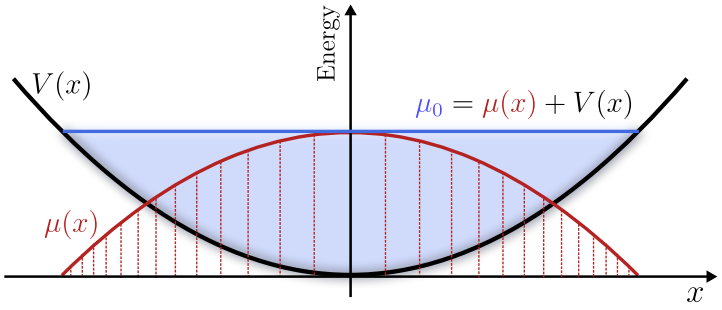

Figure 3.7: Sketch of the local density approximation. Due to the trap potential $V(x)$ the local chemical potential $\mu(x)$ varies throughout the trap and the maximum value μ_0 is realized in the trap centre. The red dotted lines schematically indicate the isopotential bins that we typically define for analysing the inhomogeneous density distribution.

varies slowly as compared to characteristic length scales of the system, e.g. the correlation length of spin correlations and if the chemical potential variation is negligible as compared to the smallest energy, we can adopt the local density approximation (LDA) [99]. According

to this approximation, the trapped system behaves locally like a homogeneous one with the chemical potential

$$\mu(x, y) = \mu_0 - V(x, y). \tag{3.42}$$

In order to analyse our experimental data, we typically group the density into isopotential bins as sketched in Figure 3.7. This requires an accurate calibration of the trap potential $V(x, y)$.

Spin Imbalance So far we have only assumed the chemical potential to vary locally within the trap. However, there was no dependence on the spin state included in the description above. In order to account for different total atom numbers of spin-up and -down atoms, we need to extend the Hamiltonian by introducing spin-dependent chemical potentials,

$$\hat{H}_\mu = -\sum_i (\mu_{i\uparrow}\hat{n}_{i\uparrow} + \mu_{i\downarrow}\hat{n}_{i\downarrow}) \tag{3.43}$$

$$= -\sum_i \underbrace{\frac{\mu_{i\uparrow} + \mu_{i\downarrow}}{2}}_{\mu_i}(\hat{n}_{i\uparrow} + \hat{n}_{i\downarrow}) - \sum_i \underbrace{\frac{\mu_{i\uparrow} - \mu_{i\downarrow}}{2}}_{h_i}(\hat{n}_{i\uparrow} - \hat{n}_{i\downarrow}). \tag{3.44}$$

Now, the mean chemical potential μ_i couples to the total density as before, while the difference in the chemical potentials leads to an imbalance of the spin densities. The latter term is often referred to as an effective magnetic field h, since a (real) magnetic field causes a mismatch in the Fermi surfaces for the two spin components of the electrons in the solid-state context [100]. For experiments using ultracold atoms however, the internal level structure is much more complicated and the spin property is emulated in the magnetic hyperfine state, thus realizing a so-called pseudo-spin system. Since the lowest magnetic hyperfine states are stable and only transferred into one another by driving radio-frequency transitions, a magnetic field would not unbalance the spin mixture. However, we can engineer an effective magnetic field term in the experiment by creating an imbalance in the populations of the two pseudo-spin components before loading them into the three-dimensional optical lattice configuration [101, 102]. In Figure 3.8 we sketch the impact of the effective magnetic field on the chemical potentials of both spin components within the LDA.

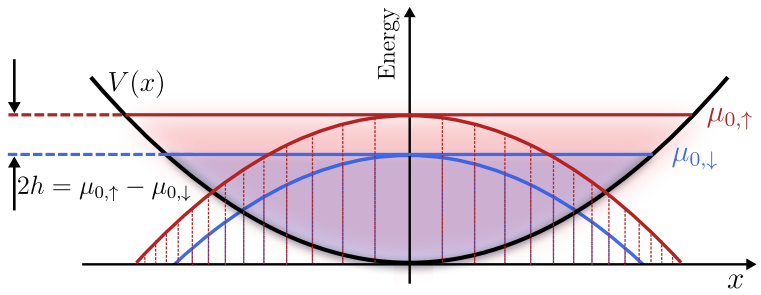

Figure 3.8: Sketch of the local density approximation with spin imbalance. In a system with an imbalance in the spin populations, the local chemical potentials $\mu_\uparrow(x)$ and $\mu_\downarrow(x)$ differ by twice the effective Zeeman field, $2h$, at any position.

There is a peculiarity about the effective magnetic field h. If the confining potential $V(x, y)$ is independent of the spin property, h is a global parameter describing the entire trapped

system. For far-detuned lattice beams this assumption is fulfilled to good approximation and hence the spatial dependence as introduced by the trapping potential cancels. This can be shown by employing the definition of the local chemical potential according to the LDA, given in Equation 3.42 and we indeed find that h is constant within the trap

$$2h = \mu_\uparrow(x,y) - \mu_\downarrow(x,y) = \mu_{0,\uparrow} - \mu_{0,\downarrow}. \tag{3.45}$$

3.3.2 Symmetries in the Fermi-Hubbard Model

Symmetry is a very general concept which finds application in all natural sciences and is often exploited in order to limit the parameter space that needs to be investigated. In particular, knowing the symmetry properties of the Hamiltonian of interest allows for choosing the parameter regime that is the most accessible in the experiment in order to probe a certain phase [102]. In the following I will discuss some of the symmetries of the Fermi-Hubbard model, including the (partial) particle-hole symmetry, which maps the spin onto the density sector for opposite interaction strengths and thereby provides a strong connection between the repulsive and the attractive Fermi-Hubbard model.

Discrete Translation Symmetry

The homogeneous Hubbard Hamiltonian is invariant under a discrete translation in real space by a multiple of the lattice spacing. The conserved quantity corresponding to this symmetry operation $j \to j+1$ is the quasimomentum q. Consequently, any change to the lattice potential that does not violate the discrete translation symmetry, e.g. the lattice depth modulation to excite transitions to higher bands, does not change the quasimomentum. However, if the harmonic confinement of the trap potential is too strong, different q-states will be coupled with a finite probability. Another way to (partially) break the discrete translation symmetry is by introducing disorder to the lattice potential [103].

Spin and Charge Symmetries

Another group of symmetries is found when considering the internal degrees of freedom, the spin and the charge. Note that within our experimental implementation of the Fermi-Hubbard model using optical lattices, the spin-1/2 particles are emulated by neutral atoms, which do not carry a charge. Still, the terminology from the solid-state community is often adopted, e.g. the term *charge sector* is used even though *density sector* would be more appropriate. In the following we will use these terms interchangeably. For the discussion of the spin and charge symmetries it is beneficial to bring the Fermi-Hubbard Hamiltonian into a more symmetric form. This is achieved by the transformation $\hat{n}_{i,\sigma} \to \hat{n}_{i,\sigma} - 1/2$, which shifts the chemical potential such that half-filling is obtained at $\mu = 0$ for all U [104]. The resulting Hamiltonian is given by

$$\begin{aligned}\hat{H} = &- t \sum_{\langle i,j\rangle,\sigma} \hat{c}^\dagger_{i,\sigma}\hat{c}_{j,\sigma} + U \sum_i \left(\hat{n}_{i,\uparrow} - 1/2\right)\left(\hat{n}_{i,\downarrow} - 1/2\right) \\ &- \sum_i \mu_i \left(\hat{n}_{i,\uparrow} + \hat{n}_{i,\downarrow} - 1\right) - h \sum_i \left(\hat{n}_{i,\uparrow} - \hat{n}_{i,\downarrow}\right)\end{aligned} \tag{3.46}$$

and from this symmetrized form we can read off that the chemical potential is connected to the density doping away from the special point of half-filling, where $\langle \hat{n}_{i,\uparrow} + \hat{n}_{i,\downarrow} \rangle = 1$. In a similar manner the effective Zeeman field h couples to an imbalance in the total spin densities. We can identify two distinct sectors by calculating the expectation values of the density imbalance $\langle \hat{n}_\uparrow - \hat{n}_\downarrow \rangle$ and the density doping $\langle \hat{n}_\uparrow + \hat{n}_\downarrow - 1 \rangle$ for the four possible states of a single lattice site. The result is given in Table 3.2. The spin sector is given by the single occupancies $|\uparrow\rangle$ and $|\downarrow\rangle$, while the doubles and the empty sites do not possess magnetization, i.e. spin. Conversely, the single occupancies do not contribute to the charge sector as quantified by the density doping since they represent a half-filled lattice site. Hence, the charge sector is spanned by the doubles and empty lattice sites. By defining the occupation number operators for doubly occupied and

	$\|\uparrow\rangle$	$\|\downarrow\rangle$	$\|\uparrow\downarrow\rangle$	$\|0\rangle$
$\langle \hat{n}_\uparrow - \hat{n}_\downarrow \rangle$	1	-1	0	0
$\langle \hat{n}_\uparrow + \hat{n}_\downarrow - 1 \rangle$	0	0	1	-1
E_{int}	$-U/4$	$-U/4$	$U/4$	$U/4$

Table 3.2: Identifying spin and density sector. Only the singly occupied lattice sites carry spin and hence magnetization. The charge or density doping sector, in contrast, is formed by the doubly occupied and empty sites as the expectation value $\langle \hat{n}_\uparrow + \hat{n}_\downarrow - 1 \rangle$ vanishes in the case of half-filling. Furthermore, the expectation value of the interaction energy, E_{int}, clearly shows that we have chosen a symmetric form of the Fermi-Hubbard Hamiltonian where not only the doubles experience an energy shift.

empty lattice sites,

$$\hat{n}_{i,\uparrow\downarrow} = \hat{n}_{i,\uparrow}\hat{n}_{i,\downarrow} \quad \text{and} \quad \hat{n}_{i,0} = (1 - \hat{n}_{i,\uparrow})(1 - \hat{n}_{i,\downarrow}) = \hat{n}_{i,\uparrow\downarrow} - (\hat{n}_{i,\uparrow} + \hat{n}_{i,\downarrow} - 1), \tag{3.47}$$

we can rewrite the density doping as the imbalance of doubles and empty sites $\langle \hat{n}_{i,\uparrow} + \hat{n}_{i,\downarrow} - 1 \rangle = \langle \hat{n}_{i,\uparrow\downarrow} - \hat{n}_{i,0} \rangle$. Furthermore, the occupation number operator for singly occupied sites $\hat{s}_{i,\sigma}$ follows from the total spin occupation by subtracting the occurrence of doubles,

$$\hat{s}_{i,\sigma} = \hat{n}_{i,\sigma} - \hat{n}_{i,\uparrow\downarrow}. \tag{3.48}$$

If we rewrite the Fermi-Hubbard Hamiltonian once more according to the Equations 3.47 and 3.48, we obtain

$$\begin{aligned} \hat{H} = &- t \sum_{\langle i,j \rangle, \sigma} \hat{c}^\dagger_{i,\sigma} \hat{c}_{j,\sigma} + U \sum_i \left(\hat{n}_{i,\uparrow} - 1/2 \right) \left(\hat{n}_{i,\downarrow} - 1/2 \right) \\ &- \sum_i \mu_i \left(\hat{n}_{i,\uparrow\downarrow} - \hat{n}_{i,0} \right) - h \sum_i \left(\hat{s}_{i,\uparrow} - \hat{s}_{i,\downarrow} \right), \end{aligned} \tag{3.49}$$

which further highlights the intricate connection between the spin and charge sectors that will be discussed further in the following paragraphs. In addition, we calculate the energy expectation value of the on-site interaction, E_{int}, which takes on distinct values in the spin and density sector, compare Table 3.2. Note that forming a double occupancy out of two singly occupied sites still requires adding a total energy of U, however it is now evenly distributed over the two processes of forming a double occupancy and a hole.

Spin-SU(2) Symmetry If we consider the spin-balanced Fermi-Hubbard model, $h = 0$, intuitively speaking it should not matter which of the two spin components we label as spin-up or -down. This argument can be extended further, as any arbitrary global rotation on the Bloch sphere would keep the Hamiltonian invariant. To see this we heave to properly define the spin operators in second quantization, which directly follow from their first quantized representation given by the Pauli matrices, see Equation 3.20,

$$\hat{S}_i^\alpha = \frac{\hbar}{2} \sum_{\sigma\sigma'} \hat{c}_{i\sigma}^\dagger \sigma_{\sigma\sigma'}^\alpha \hat{c}_{i\sigma'}, \quad \text{for } \alpha = x, y, z. \tag{3.50}$$

Typically the factor $\hbar$ is neglected in the description of the spin operators and we will follow this convention throughout the remainder of this thesis. The global spin operators are defined as a sum over all lattice sites,

$$\hat{S}^\alpha = \sum_i \hat{S}_i^\alpha, \tag{3.51}$$

and one can show that they commute with the Fermi-Hubbard Hamiltonian when there is no effective magnetic field h,

$$\left[\hat{H}, \hat{S}^\alpha\right] = 0. \tag{3.52}$$

This shows that the Fermi-Hubbard Hamiltonian possesses a spin-SU(2) symmetry if $h = 0$. In contrast, when introducing an effective magnetic field term, the two spin components are distinct, as we will obtain a minority and a majority component. Therefore, the Fermi-Hubbard Hamiltonian is not invariant when rotating the basis states and correspondingly the commutator does not vanish any more, $[\hat{H}, \hat{S}^{x,y}] \propto [\hat{S}^z, \hat{S}^{x,y}] \neq 0$.

There is a special case, namely when rotating the basis states on the Bloch sphere around the x-axis by an angle of π, we effectively transform

$$\hat{c}_{i,\sigma} \to -i\hat{c}_{i,\bar{\sigma}}. \tag{3.53}$$

This interchanges the spin-up with the spin-down component. Even though this transformation does not keep the Hamiltonian invariant, we recover the Fermi-Hubbard Hamiltonian when additionally flipping the sign of h. Intuitively speaking, if we exchange the minority and majority components by the transformation given above, the direction of the effective magnetic field has to be flipped in order to restore a physically reasonable scenario.

Pseudospin-SU(2) Symmetry There is another less known SU(2) symmetry of the Fermi-Hubbard model, which is generated by the pseudospin operators,

$$\hat{\eta}^\dagger = \sum_j (-1)^j \hat{c}_{j,\downarrow}^\dagger \hat{c}_{j,\uparrow}^\dagger = \hat{\eta}^x + i\hat{\eta}^y, \quad \hat{\eta} = \sum_j (-1)^j \hat{c}_{j,\uparrow} \hat{c}_{j,\downarrow}, \quad \hat{\eta}^z = \frac{1}{2} \sum_j \left(\hat{n}_{j,\uparrow\downarrow} - \hat{n}_{j,0}\right) \tag{3.54}$$

also referred to as η-pairing operators. These operators form an SU(2) algebra analogous to the one of the spin operators defined in Equation 3.51. As seen in Table 3.2, within the charge sector doubles and empty sites take on the role of spin-up and spin-down particles of the previously discussed spin sector. In particular, to obtain a better understanding of

the pseudospin symmetry we may think about a Bloch sphere defined by the basis states $|\uparrow\downarrow\rangle$ and $|0\rangle$. To highlight the close connection, the spin-balanced case at $h = 0$ is mirrored by equal probabilities for obtaining a doubly occupied or an empty site, which is fulfilled at half-filling, i.e. $\mu = 0$. Having drawn the close analogy to the spin sector, we can directly apply the conclusion obtained in the paragraph above. For a half-filled system where $\mu = 0$, the pseudospin operators commute with the Fermi-Hubbard Hamiltonian,

$$\left[\hat{H}, \hat{\eta}^{\alpha}\right] = 0. \tag{3.55}$$

Since the η-operators obey the same commutation relations as the spin operators, this leads to another SU(2) symmetry however in the charge sector of the Hubbard model, for which the terms superconducting [105] or pseudospin [106] SU(2) symmetry are used.

For a spin-balanced system at half-filling we have $\mu = h = 0$ and hence the Hubbard model possesses an SO(4)-symmetry [107]. At this point the probabilities of the four different occupations of a single site are equal $\langle \hat{s}_{\uparrow} \rangle = \langle \hat{s}_{\downarrow} \rangle = \langle \hat{n}_{\uparrow\downarrow} \rangle = \langle \hat{n}_0 \rangle = 0.25$, if $U = 0$.

Partial Particle-Hole Transformation The partial particle-hole transformation only affects the spin-down component[3] and is defined for bipartite lattices as

$$\hat{c}_{j,\downarrow} \leftrightarrow (-1)^{j_x + j_y} \hat{c}^{\dagger}_{j,\downarrow}, \qquad \hat{c}_{j,\uparrow} \leftrightarrow \hat{c}_{j,\uparrow}. \tag{3.56}$$

The definition in terms of the creation and annihilation operators is mostly relevant for the kinetic energy, which is invariant only due to the staggered sign. For all other terms in the Fermi-Hubbard Hamiltonian it suffices to know the transformation of the occupation number operator

$$\hat{n}_{i,\downarrow} \leftrightarrow (1 - \hat{n}_{i,\downarrow}). \tag{3.57}$$

In the left part of Figure 3.9 we show the mapping of the site occupancies under the partial particle-hole transformation (PHT), which maps the spin to the charge sector and vice versa. If we apply the transformation to the Hubbard Hamiltonian given in Equation 3.46, we realize

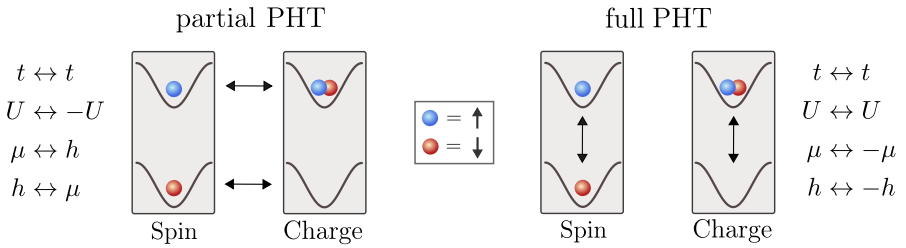

Figure 3.9: Particle-hole transformations in the Fermi-Hubbard model. There are two distinct particle-hole transformations (PHT) in the Fermi-Hubbard model. The partial PHT maps the spin onto the charge sector and vice versa. The roles of the effective Zeeman field h and the chemical potential μ are therefore interchanged. While the tunnelling term is left invariant, the sign of the interaction strength changes, compare Table 3.2. In contrast, the full PHT acts separately within both the spin and charge sector.

[3] In principle, transforming only the spin-up component is also a valid transformation, which is connected to the case presented here by the full particle-hole transformation.

that the effective Zeeman field, h, and the chemical potential, μ, exchange their roles while the interaction energy flips its sign, compare Table 3.2. Therefore, the partial PHT links the attractive to the repulsive Fermi-Hubbard model and we can conclude that there is an intricate connection which allows us to infer the properties on the attractive side from the repulsive case. In some sense the attractive and repulsive Fermi-Hubbard model are the exact opposite of each other and we will come back to this point when discussing the phase diagram of the 2D Fermi-Hubbard model shown in Figure 3.12. It is however important to note that the site occupancies also interchange, which is shown in Figure 3.10. Therefore, density correlations at $U < 0$ are mapped onto spin correlations at $U > 0$. In a recent publication [102], we have experimentally verified that even the thermodynamic variables are transformed into one another by comparing the compressibility $\kappa = \partial n/\partial \mu$ for $U > 0$ to the spin susceptibility $\chi_s = \partial m/\partial h$ for $U < 0$, where $m = \langle n_\uparrow - n_\downarrow \rangle$ is the magnetization of the system. Apart from the physical insight that one gains from the connection between the repulsive and attractive Hubbard model, the partial PHT has practical benefits as well since we can choose the experimental conditions to probe a certain phase. For example, preparing a homogeneous system is not easily achievable for quantum gas experiments. However, the partial PHT allows for a second level to quantum simulation, as we can simulate thy physics in a homogeneous lattice potential in a harmonic trap by inverting the sign of the interaction strength and transforming the physical observable under consideration. This is possible as the chemical potential μ, which varies throughout the trap is mapped onto the effective Zeeman field, which is a global parameter.

Full Particle-Hole Transformation The full particle-hole transformation (PHT) equally affects both spin components and is defined for bipartite lattices as

$$\hat{c}_{j,\downarrow} \leftrightarrow (-1)^{j_x+j_y} \hat{c}^\dagger_{j,\downarrow}, \qquad \hat{c}_{j,\uparrow} \leftrightarrow (-1)^{j_x+j_y} \hat{c}^\dagger_{j,\uparrow}. \tag{3.58}$$

Instead of providing a mapping between the spin and density sectors, the full PHT transforms spin-up into spin-down particles and doubles into empty sites, as shown on the right side of Figure 3.9. Therefore it acts only within each of the two sectors, and flips the sign of both h and μ while the interaction strength U and the tunnelling amplitude t are invariant. As a consequence we obtain a mirror symmetry in the expectation value of the occupation number operator around $\mu = 0$ and $h = 0$, as shown in Figure 3.10 a) and b), respectively.

We will first discuss the charge sector, which is slightly more intuitive. By tuning the chemical potential the total filling in the lattice changes. This can also be quantified by the imbalance of doubles and empty sites. At half-filling we find that $\langle \hat{n}_{\uparrow\downarrow} \rangle = \langle \hat{n}_0 \rangle$[4]. Increasing the chemical potential enhances the number of doubles, which is exactly mirrored by an increasing probability to obtain empty sites below half-filling. For a vanishing Zeeman field $h = 0$ the amount of spin-up $s_\uparrow$ and spin-down singles $s_\downarrow$ are equal for all μ. Consequently, the singles filling is mapped back onto itself by the full PHT,

$$s_{i,\uparrow}(\mu) = s_{i,\downarrow}(-\mu) = s_{i,\uparrow}(-\mu). \tag{3.59}$$

This is shown in Figure 3.10 a) and we obtain a maximum in the singles occupancy at the symmetry point, which is at half-filling, $\mu = 0$. This so-called *singles peak* provides an extremely important calibration point, which allows us to assign an *absolute* chemical potential to the

[4] At half-filling we have $2n_{\uparrow\downarrow} + s_\uparrow + s_\downarrow = 1$. In combination with the normalization condition $n_0 + n_{\uparrow\downarrow} + s_\uparrow + s_\downarrow = 1$, we obtain that the number of empty sites and doubles is equal at half-filling.

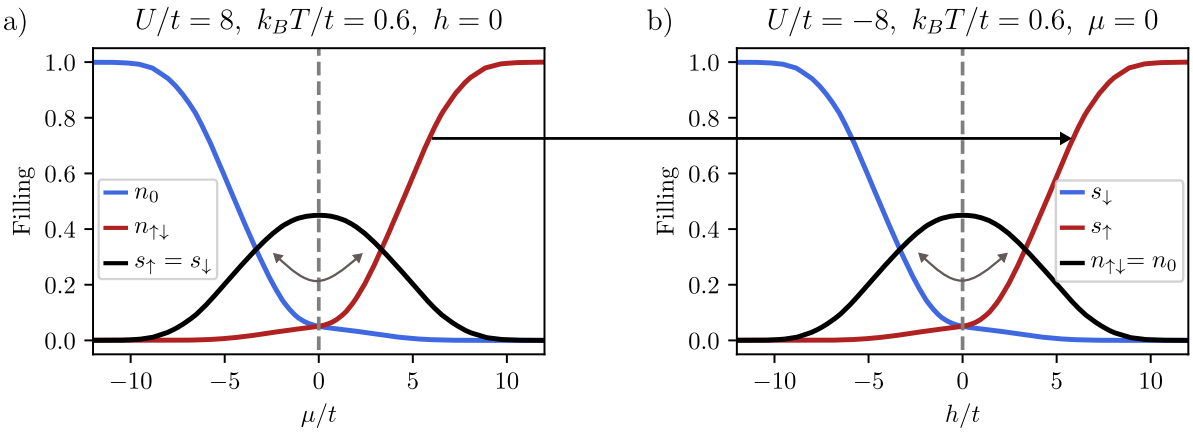

Figure 3.10: Mapping of site occupancies under the particle-hole transformation. We compare the expectation value of the site occupancies $n = \langle \hat{n} \rangle$ in the repulsive (a) and attractive (b) Fermi-Hubbard model, as determined by determinantal QMC (DQMC). The DQMC code is provided by the Quantum Electron Simulation Toolbox (QUEST) [17]. For more information on the DQMC simulations see Section 7.2 or [108]. The mirror symmetry around the $\mu = 0$ ($h = 0$) axis, indicated by the grey dashed line, is a consequence of the full particle-hole transformation (PHT). The partial PHT in contrast provides a mapping that interchanges the roles of the effective magnetic field, h, and the chemical potential, μ, which is accompanied by a flip in the sign of the interaction. While increasing the chemical potential enhances the number of doubles in the system, a larger Zeeman field implies a strong imbalance in the spin components. Hence, the partial PHT maps doubles onto spin-up singles, which is indicated by the black arrow.

local filling $n(x, y)$ which varies slowly within the xy-plane due to the harmonic confinement provided by the lattice laser beams. Since we obtain the filling of singly and doubly occupied sites only up to a constant scaling factor, the determination of this detection fudge relies on the knowledge of the absolute filling that we realize locally in addition to the theory comparison providing the equation of state $n(\mu)$.

When tuning the Zeeman field (Figure 3.10 b) instead of the chemical potential, we obtain the very same graph where only the legend has changed. This was to be expected, as the charge sector is mapped onto the spin sector by the partial PHT discussed above. The effective Zeeman field tunes the imbalance of the spin-up and spin-down components and similar to before we obtain an increase in the spin-up component for $h > 0$ which is exactly mirrored by an increase of the spin-down component for $h < 0$.

According to the full PHT is suffices to probe the Hubbard model only up to half-filling, which is a huge practical benefit. Furthermore, for spin-imbalanced systems, we observe the same physics whether the majority component is given by the spin-up or -down atoms.

Energy Inversion Symmetry The Fermi-Hubbard model possesses another symmetry which links the high-energy states of the attractive Hubbard model to the low-energy states of the repulsive Hubbard model if the momenta are shifted according to $k \to k + Q$, where $Q = \pi/a$ [109–111]. The underlying transformation that is responsible for this connection inverts the sign of both t and U. Consequently, also the sign of the full Hamiltonian changes $\hat{H} \to -\hat{H}$. The corresponding states are often referred to as negative temperature states, where the sign change effectively has been put into the temperature instead of the Hamiltonian.

3.3.3 Phase Diagram

The Fermi-Hubbard model includes strong correlations in the spin and density degree of freedom which arise due to the competition of kinetic and interaction energy as well as the dimensionality and the total filling. As a consequence, a reliable (ground state) phase diagram of the Fermi-Hubbard model in two and three dimensions remains elusive, while the one-dimensional case is solved by the Bethe ansatz. In the following, we will therefore only discuss an approximate phase diagram at half-filling, following the discussions in [67, 69].

For weak attractive or repulsive interactions or large temperatures the Fermi-Hubbard system is in a metallic state, which is characterized by (thermally induced) density fluctuations as the spin-1/2 particles have a large kinetic energy. Upon lowering the temperature, the relevance of the on-site interaction increases, which aims at localizing the particles to their respective lattice sites, either in the form of singles ($U > 0$) or doubles and empty sites ($U < 0$). An intuitive picture that explains the impact of the on-site interaction is provided by the concept of the *Hubbard bands*, see Figure 3.11. In Section 3.3.1 we have discussed the band structure of the non-interacting Fermi Hubbard model where we obtain separate bands for the two spin components with a bandwidth of W/t=8 each. For a finite interaction strength, the q-states get mixed and hence they can not be the eigenstates of the Fermi-Hubbard Hamiltonian. However, if U is much larger than t, the interacting spectral function separates into two Hubbard bands. In contrast to quasiparticles, which have a well defined quasimomentum corresponding to a certain energy, the Hubbard bands are incoherent, hence they describe localized particles that are smeared in q-space. The two Hubbard bands do not represent the two spin components

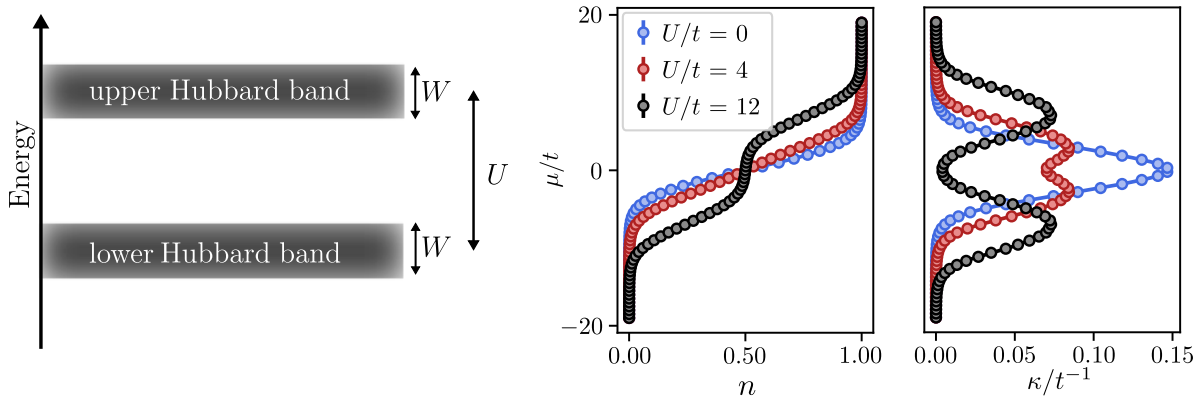

Figure 3.11: Hubbard bands and equation of state of the two-dimensional Fermi-Hubbard model. (Left) When increasing the interaction strength U, a charge gap opens for $U > W$. The insulating character of the Mott insulator is also apparent in the density equation of state $n(\mu)$, which features a plateau near half-filling, $\mu = 0$, and from the dip in the compressibility $\kappa(\mu)$. Both quantities are obtained using the DQMC code as provided by the Quantum Electron Simulation Toolbox (QUEST) [17] and we have chosen a temperature within our experimental capabilities, $k_B T/t = 1$. For more information on the DQMC simulations see Section 7.2.

as in the non-interacting case but singly and doubly occupied (+empty) sites, respectively. The gap to the upper Hubbard band is given by the on-site interaction which punishes the occurrence of doubles and empty sites (singles) in the repulsive (attractive) case. The concept of the Hubbard bands is useful for understanding the phase diagram of the Fermi-Hubbard model that is shown in Figure 3.12 and I will review some of the characteristics in the following.

Mott Insulator If the interaction strength is positive and exceeds the bandwidth of the interacting system, we obtain an insulating state at half-filling, the so-called Mott insulator. In Figure 3.11 we plot the density equation of state, $n(\mu)$, which develops a plateau around $\mu = 0$. This signals the insulating character as the system resists the addition of more particles. Consequently, the compressibility, which we define as $\partial n/\partial \mu$, shows a dip at half-filling. In contrast to a band insulator, adding more particles to the system is prohibited by the strong repulsive interaction. Therefore, the charge gap is a correlation gap and depends on the temperature. This is the reason why the compressibility at half-filling does not vanish even for $U/t = 12$. It is also noteworthy that the strong correlations induced by the on-site interaction will narrow the bandwidth to $W/t < 8$ [49] since the energy gain by delocalization is reduced. Therefore, the critical interaction strength to enter the Mott insulating regime will be smaller than the non-interacting bandwidth.

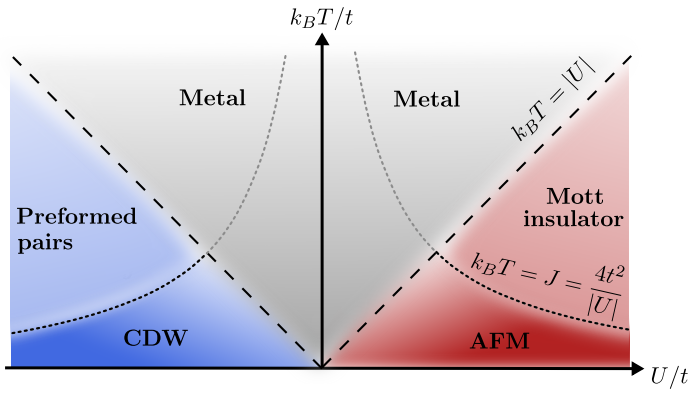

Figure 3.12: Phase diagram of the Fermi-Hubbard model at half-filling. Approximate scaling of the critical temperature to obtain order in the charge sector (dashed line), and the superexchange energy (dotted line) as a function of the Fermi-Hubbard parameters. In the repulsive case, the competition of quantum tunnelling, interactions and Pauli's exclusion principle drives a second-order phase transition from a disordered paramagnetic phase to a long-range ordered antiferromagnetic phase (AFM) with antiparallel spin alignment. According to the partial PHT, opposite behaviour is expected for the attractive Fermi-Hubbard model, where the charge order manifests itself in the reduction of single occupancies, in contrast to the Mott insulator. The normal fluid with preformed pairs and empty lattice sites becomes superfluid when lowering the temperature below the superexchange energy scale, $J = 4t^2/|U|$. In close analogy to the AFM, doubles and empty sites will order in a chequerboard fashion called the charge-density wave (CDW). This schematic is based on [67, 69].

Preformed Pairs For attractive interactions, it is energetically favourable for two fermions with opposite spin to form pairs, i.e. doubles and empty sites. Increasing the total filling is not prohibited as the state can adjust the probabilities of forming doubles and empty sites at no energy cost, see Table 3.2. Therefore, the preformed pairs phase is not a charge insulator. In contrast to the repulsive case, where the energy excitations on top of the Mott insulating ground state were given by particle-hole pairs, the low-energy excitations in the attractive case are single occupancies created out of a doublon and an empty site. A finite Zeeman field, h, introduces an imbalance of the two spin components, and consequently not all fermionic particles will find a partner to form a doubly occupied lattice site. The associated energy cost for the pair breaking induced by the Zeeman field is the on-site interaction. Hence, quantitatively we recover the result of the repulsive counterpart, the Mott insulator. However, the system

with attractive interactions resists the breaking of pairs as quantified by the spin susceptibility, which mirrors the meaning of the compressibility in the repulsive Fermi-Hubbard model [102].

Quasi-Long-Range Order at low Temperatures When the temperature is lowered below the superexchange scale, J, introduced in Section 3.2.2, the system develops (quasi-)long-range order[5] both in the attractive and repulsive Fermi-Hubbard model. Since first-order tunnelling processes are suppressed by the large interaction energy, the system is only able to lower its energy by the superexchange mechanism. On the repulsive side this leads to antiferromagnetic correlations in the spin sector. This will be investigated in detail in Chapter 5 for an elevated temperature $k_B T/J \approx 1.2$, where only short-ranged correlations are expected. On the attractive side, the doubles and the empty sites will order in a chequerboard fashion which is sometimes referred to as charge-density wave [104]. The quasi-long-range order that builds up in the transverse components of the pseudospin operators is linked to s-wave superfluidity.

3.4 Bilayer Fermi-Hubbard Model

The bilayer Fermi-Hubbard model is a natural extension of the two-dimensional version discussed above, where an additional parameter, $t_\perp$, is introduced that quantifies the tunnelling amplitude between a pair of horizontal layers, see Figure 3.13. I will start to analyse its properties by

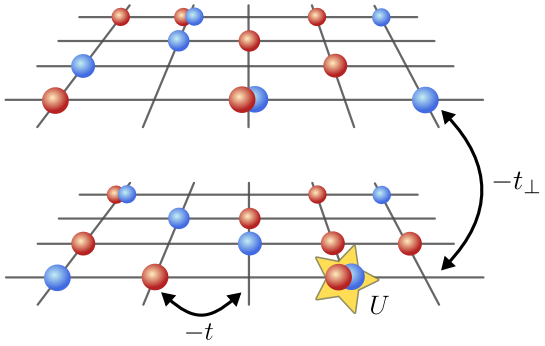

Figure 3.13: Sketch of the elementary processes in the bilayer Fermi-Hubbard model. In addition to the elementary processes within the two-dimensional Fermi-Hubbard model, namely the (intralayer) tunnelling amplitude t between adjacent lattice sites and the on-site interaction U, the bilayer Fermi-Hubbard model contains the interlayer tunnel coupling $t_\perp$ as an independent parameter.

deriving the single-particle dispersion in the non-interacting case, which reveals the opening of a band gap at half-filling in the strongly coupled regime, i.e. for $t_\perp \gg t$. When adding repulsive interactions to the model, even the ground state properties of the phase diagram at half-filling are extremely hard to predict. In the past years, several theory groups have studied the bilayer Fermi-Hubbard model with partially conflicting conclusions, which I will briefly mention in the second part. In order to reach the strongly coupled bilayer regime we reduce the barrier between the layers and thereby realize tunnelling amplitudes of up to $t_\perp/h = 1\,\mathrm{kHz}$. To evaluate whether the tight-binding approximation is still valid even for the low barrier heights, I will discuss the impact of higher-order interaction processes such as nearest-neighbour interactions and density-induced tunnelling in the last part of this section.

[5] The Mermin-Wagner theorem states that long-range order in two dimensions is only possible at zero temperature.

3.4.1 Band Structure of a Dimerized Lattice

In the experiment we realize the bilayer Fermi-Hubbard model by employing a superlattice along the z-direction. This creates a dimerized lattice structure as shown in Figure 3.14, where each unit cell labelled by an index j contains two lattice sites. If we follow the tight-binding approach as we did for the 2D Fermi-Hubbard model we can limit the relevant tunnelling processes to a coupling of nearest neighbours. Nevertheless, in general we obtain two distinct tunnelling amplitudes corresponding to a coupling within or between neighbouring unit cells. In order to

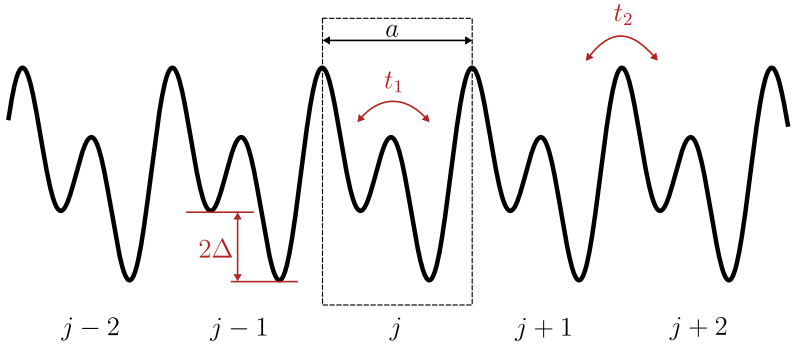

Figure 3.14: Dimerized lattice potential. With a bichromatic superlattice we can create dimerized lattice structures with a site offset of 2Δ. We restrict the elementary processes to nearest-neighbour tunnelling with an amplitude t_1 within a unit cell and a tunnelling amplitude t_2 between unit cells.

derive the band structure of this dimerized lattice structure, I will consider non-interacting particles and hence the spin index on the creation and annihilation operators may be dropped. The Hamiltonian, sometimes referred to as the Rice-Mele model, is then given by

$$\hat{H}_{\mathrm{SL}} = -\sum_j \left(t_1 \hat{a}_j^\dagger \hat{b}_j + t_2 \hat{a}_j^\dagger \hat{b}_{j-1} + h.c. \right) + \Delta \sum_j \left(\hat{a}_j^\dagger \hat{a}_j - \hat{b}_j^\dagger \hat{b}_j \right) \tag{3.60}$$

and its elementary processes are visualized in Figure 3.14. To account for the dimerized lattice structure we have introduced fermionic operators $\hat{a}_j^\dagger$ ($\hat{b}_j^\dagger$), which create a particle in unit cell j on the left (right) site, respectively. We obtain a diagonal representation by expressing the real space creation and annihilation operators using their momentum space analogues

$$\hat{a}_j = \frac{1}{\sqrt{L}} \sum_q e^{iqr_j} \hat{a}_q \tag{3.61}$$

and equivalently for sublattice B. Since the single-particle Hamiltonian is diagonal in momentum space, we can solve the eigenvalue problem for a fixed q. In the basis $\{\hat{a}_q^\dagger |0\rangle, \hat{b}_q^\dagger |0\rangle\}$ the Hamiltonian transforms to

$$\hat{H}_q = \begin{pmatrix} \Delta & -\left(t_1 + t_2 e^{-iqa}\right) \\ -\left(t_1 + t_2 e^{iqa}\right) & -\Delta \end{pmatrix} \tag{3.62}$$

and the eigenvalues follow from the exact diagonalization,

$$E_q^\pm = \pm\sqrt{t_1^2 + t_2^2 + 2t_1 t_2 \cos(qa) + \Delta^2}. \tag{3.63}$$

Here, a denotes the period of the superlattice (see Figure 3.14). For a dimerized lattice without tilt $\Delta = 0$ the band structure $E_q^{\pm}$ is shown in Figure 3.15 for different ratios of the tunnel couplings. For the special case where $t_1 = t_2 \equiv t$, we expect to recover the dispersion relation of a monochromatic one-dimensional optical lattice. However, the real-space unit cell of a dimerized lattice is larger by a factor of two and therefore we do not obtain the cosine band itself. Instead the band with a bandwidth of $W_{1D} = 4t$ is folded into the first Brillouin zone of the superlattice potential according to

$$E_q^{\pm} = \pm 2t|\cos(qa/2)| \quad \text{for } t_1 = t_2 \equiv t. \tag{3.64}$$

If the tunnel amplitudes t_1 and t_2 are different, a band gap opens at the edge of the Brillouin zone $q = \pm\pi/a$

$$\Delta_{\text{gap}} = 2|t_1 - t_2|. \tag{3.65}$$

The bandwidth of these so-called minibands reduces and vanishes completely when the lattice consists of individual uncoupled double-wells $t_2 = 0$. Hence, the tunnelling amplitude between different unit cells, t_2, takes over the role of the standard Hubbard tunnelling amplitude t and determines the bandwidth of the superlattice potential $W_{\text{SL}} = 2t_2$ which is, however, reduced by a factor of two compared to a one-dimensional monochromatic lattice, where $W_{1D} = 4t$.

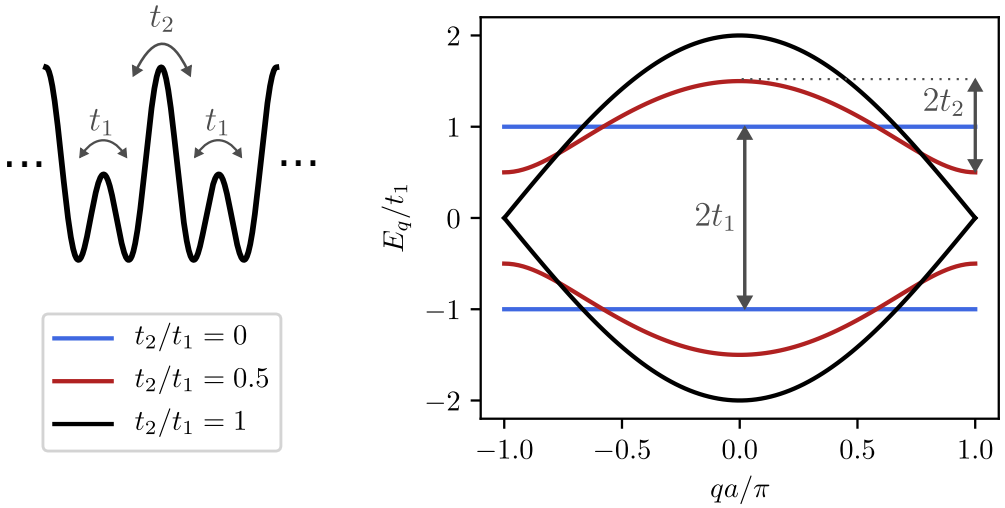

Figure 3.15: Band structure for a dimerized lattice potential without tilt. Band structure of the one-dimensional Fermi-Hubbard model in a dimerized lattice potential without tilt for various ratios of the tunnel couplings. The bandwidth of both minibands is determined by the amplitude t_2, while tunnelling within the double-well shifts the centres of the bands apart. An energy gap opens at the band edge whenever $t_1 \neq t_2$ or for a finite tilt $\Delta \neq 0$ (the latter is not shown).

The minibands are separated in energy by $2t_1$ and for $t_2 = 0$ we obtain flat bands at

$$E^{\pm} = \pm t_1, \tag{3.66}$$

which matches the result of a single particle in the double-well, compare Equation 3.11. Therefore, we can identify the lower miniband as the singlet band with a spatially symmetric wavefunction while the upper miniband contains the triplet states, as discussed in Section 3.2.1.

Therefore, in the bilayer Fermi-Hubbard model strong magnetic correlations may be observed along the double-well direction, even if the particles do not interact.

To realize the bilayer Fermi-Hubbard model with a superlattice potential along the z-direction, we have to make sure that tunnelling between different unit cells is strongly suppressed, i.e. $t_2 \ll t_1$. This guarantees that only two layers are coupled and consequently we obtain flat bands, as we will assume throughout this thesis. In this case, the band energy only depends on the intra-well tunnelling amplitude and we identify $t_1 \equiv t_\perp$.

For a separable three-dimensional lattice potential, the full band structure of the bilayer Fermi-Hubbard model simply follows as the sum of the dispersion of the 2D Fermi-Hubbard model $E(q_x, q_y) = -2t(\cos q_x a + \cos q_y a)$ with bandwidth $W = 8t$ and the eigenenergy spectrum of a double-well along the vertical z-direction

$$E^{\pm}(\boldsymbol{q}) = E(q_x, q_y) \pm t_\perp = -2t\left[\cos(q_x a) + \cos(q_y a)\right] \pm t_\perp. \tag{3.67}$$

As shown on the left side of Figure 3.16, the dimerized lattice structure along the vertical direction creates two copies of the Hubbard bands. In line with the terminology used in molecular physics, these two energy bands $E^{\pm}$ are referred to as bonding $(-)$ and antibonding $(+)$ band [42, 49], corresponding to the symmetric/antisymmetric superposition state of the left and right well. When increasing the interlayer coupling strength, the system transitions from a

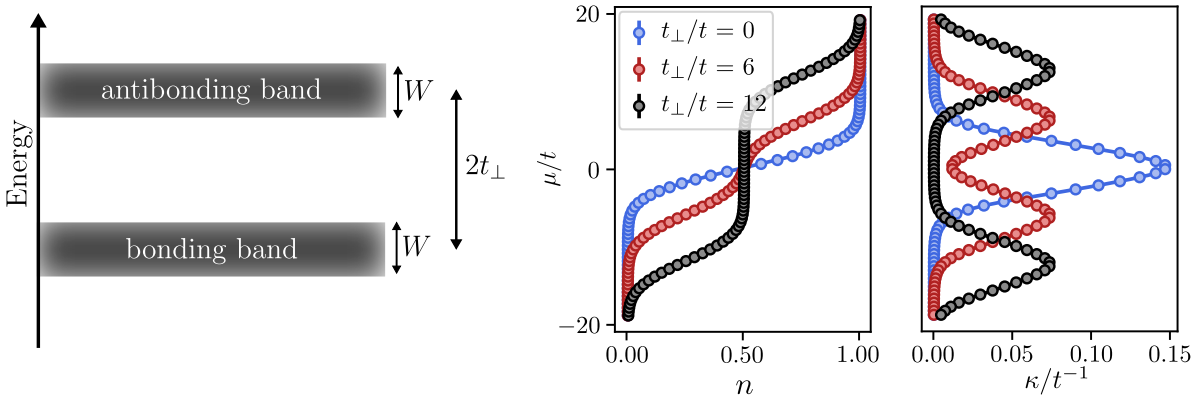

Figure 3.16: Band structure and equation of state of the non-interacting bilayer Fermi-Hubbard model. (Left) When increasing the tunnel coupling $t_\perp$ in the double-well direction a single-particle charge gap opens at $2t_\perp = W$. As for the Mott insulator, compare Figure 3.11, the insulating character can be quantified via the density equation of state $n(\mu)$ that is shown for $U = 0$ and $k_B T/t = 1$. Near half-filling it features a plateau if $t_\perp/t > 4$ and consequently the compressibility $\kappa(\mu)$ shows a minimum. Both quantities are obtained by using the DQMC code that is provided by the Quantum Electron Simulation Toolbox (QUEST) [17]. For more information on the DQMC simulations, see Section 7.2.

metallic state to a band insulator, since a gap opens between the bonding and antibonding band at half-filling if $2t_\perp > W$. Note that in contrast to the Mott insulating gap, which is a correlation gap, the charge gap responsible for the insulating nature of the non-interacting bilayer Fermi-Hubbard model is a single-particle gap and is therefore more robust since the non-interacting spectral function does not depend on the temperature.

3.4.2 Phase Diagram of the Bilayer Fermi-Hubbard Model

In the past years, several theory groups have studied the bilayer Fermi-Hubbard model employing different methods including dynamical mean field theory [42, 46] and its cluster extensions [43, 49] as well as variational Monte Carlo [50] and finite temperature determinantal quantum Monte Carlo (DQMC) studies [44, 48, 51, 112, 113], with partially conflicting conclusions. In the middle column of Figure 3.17, we show the phase diagram as put forward by M. Golor et al. [51], who have combined functional renormalization group calculations with projective determinantal quantum Monte Carlo simulations to estimate the phase boundaries over a broad range of interaction strengths. For the non-interacting square-lattice bilayer Fermi-Hubbard model, they predict a transition from a metallic state at low interlayer coupling strength to a band insulator at $t_\perp/t = 4$, which matches the prediction obtained from the single-particle dispersion shown above. While both cluster DMFT [43] and finite-temperature DQMC calculations [44] have found the paramagnetic metallic phase to persist at small on-site interactions and low interlayer coupling, Golor et al. predict that the metallic phase is restricted to $U = 0$. Instead, they argue that a Stoner instability, arising due to the perfect nesting property of the Fermi surfaces of the bonding and antibonding band at $\boldsymbol{q} = (\pi/a, \pi/a)$, is responsible for driving the system into an antiferromagnetic insulator. More insight into the underlying physics may be gained by combining these findings with the paper by R. Rüger et al. [50], where they have investigated both the magnetic and paramagnetic phase diagram with the variational Monte Carlo method by either allowing for or suppressing long-range magnetic order, respectively. They have found that only if magnetic order is allowed, the ground state of the square lattice bilayer Fermi-Hubbard model at $U > 0$ is an insulator with antiferromagnetic correlations instead of a paramagnetic metal as predicted by cluster DMFT calculations. As pointed out by Golor et al.,

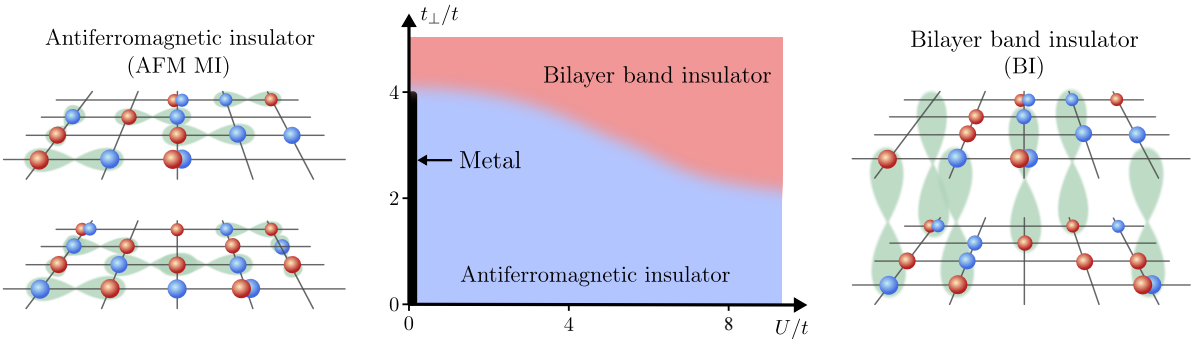

Figure 3.17: Band structure of the non-interacting bilayer system. (Middle) Schematic depiction of the ground state phase diagram of the bilayer Fermi-Hubbard model at half-filling, as obtained by M. Golor et al. [51]. They have employed functional renormalization group calculations (fRG) in combination with projective determinantal quantum Monte Carlo simulations (DQMC) and found that at a finite repulsive interaction strength the interlayer tunnelling amplitude controls a continuous transition from a Mott-insulator with antiferromagnetic correlations within the layers (left) to a band insulator with singlet bonds between the layers (right). The shaded areas illustrate the spin correlations between spin-up and -down particles, shown as red and blue spheres, respectively.

there are two regimes, which both show AFM order however with a different characteristic: For large U the well-known Mott insulator is obtained, which favours singly occupied lattice sites. Therefore, the local moment is large and spin correlations build up due to the superexchange mechanism [51]. In contrast, the AFM order found at small repulsive interactions is triggered

by the Fermi surface instability described above. Since the paramagnetic phase diagram by Rüger et al. predicts a metallic state at low U when suppressing long-range order, it suggests that the AFM correlations stabilise the insulating nature. At finite temperatures long-range order is absent in low-dimensional systems due to the Mermin-Wagner theorem, indicating the relevance of the paramagnetic phase diagram, which predicts a metallic state at low U [50].

While there are conflicting conclusions about the ground state in the low U and low $t_\perp$ regime, there is no doubt that at strong interlayer coupling $t_\perp/t > 4$ the bilayer system will be in a band insulating state independent of the strength of the repulsive on-site interaction. The insulating nature of this state is not connected to the repulsive interactions, instead the atoms reduce their kinetic energy by forming a symmetric superposition of the left and right layer [114]. A. Fuhrmann et al. have investigated the spectral density of the symmetric superposition state and found that for a pure band insulator the symmetric band is located entirely below the Fermi level and for a Mott insulator it is distributed equally over the upper and lower Hubbard bands [42]. Hence, the signature of the bilayer band insulator state for strong repulsive interactions are singlet bonds forming between the horizontal layers, see schematic in Figure 3.17. For low U we additionally expect to observe correlations between doubly occupied and empty sites, as the double-well ground state at $U = 0$ is a sum of the singlet state $|s\rangle$ and the doublon state $|d_+\rangle$, see Section 3.2. The critical tunnelling amplitude that is necessary to open the band gap between the bonding and antibonding band decreases, starting at $t_\perp/t = 4$ for the non-interacting system, since strong interactions reduce the bandwidth of the bonding and antibonding bands [49]. For $U/t \to \infty$ we approach the Heisenberg limit, where the Hubbard Hamiltonian reduces to an effective spin model and the transition to the dimerized phase with spin singlets forming between the horizontal layers occurs at $t_\perp/t \approx 1.59$ [115–118].

3.4.3 Extended Hubbard Parameters

So far for the description of the bilayer Fermi-Hubbard model we silently assumed the particles to be well localized to either site of the symmetric double-well potential along the vertical direction. However, if we want to realize strong tunnel couplings between the layers we need to reduce the barrier height. In this case the physics of the bilayer Fermi-Hubbard model is dominated by individual double-well potentials. In the following I want to investigate whether the tight-binding assumption is still well justified when reducing the height of the barrier or whether higher-order processes such as density-induced tunnelling or off-site interactions need to be included in the Hamiltonian description. Assuming a symmetric double-well, the on-site interaction U as previously defined does not distinguish whether two particle with opposite spin meet on the left or the right side of the double-well

$$U \propto \int dz\, w_L^*(z) w_L^*(z) w_L(z) w_L(z) = \int dz\, w_R^*(z) w_R^*(z) w_R(z) w_R(z). \tag{3.68}$$

Here, I deliberately ignored the Wannier functions $w(x)$ and $w(y)$ within the layer, since the tight-binding approximation is only likely to be unjustified along the z-direction. Starting from the Equations 3.2 and 3.4 we can group terms according to the value of the general interaction integral relative to the standard on-site interaction

$$\frac{U_{ijkl}}{U} = \frac{\int dz\, w_i^*(z) w_j^*(z) w_k(z) w_l(z)}{\int dz\, w_L^*(z) w_L^*(z) w_L(z) w_L(z)}, \tag{3.69}$$

where the indices i, j, k, l indicate either the left or the right well. Since there is a gauge freedom in the complex phase of the Bloch functions, it is always possible to define real-valued Wannier states and we may drop the complex conjugation. Higher-order interaction terms can be grouped according to the total occurrence of Wannier functions on the left and right well. There are two distinct groups that we need to distinguish including processes where two particles in the left well interact with two particles in the right well. They are quantified by the parameter

$$V := U_{LLRR} = U_{LRLR} = U_{RLRL} = U_{LRRL} = U_{RLLR} = U_{RRLL}. \tag{3.70}$$

The other group contains three Wannier states either on the right or the left well and corresponds to density-induced tunnelling with amplitude

$$\Delta t = U_{LLLR} = U_{LLRL} = U_{LRLL} = U_{RLLL} = U_{RRRL} = U_{RRLR} = U_{RLRR} = U_{LRRR}. \tag{3.71}$$

All possible higher-order processes are listed in Table 3.3.

V	$\hat{c}^\dagger_{L\uparrow}\hat{c}^\dagger_{R\downarrow}\hat{c}_{R\downarrow}\hat{c}_{L\uparrow} = \hat{n}_{L\uparrow}\hat{n}_{R\downarrow}$ $\hat{c}^\dagger_{R\uparrow}\hat{c}^\dagger_{L\downarrow}\hat{c}_{L\downarrow}\hat{c}_{R\uparrow} = \hat{n}_{R\uparrow}\hat{n}_{L\downarrow}$	nearest-neighbour interaction
V	$\hat{c}^\dagger_{L\uparrow}\hat{c}^\dagger_{L\downarrow}\hat{c}_{R\downarrow}\hat{c}_{R\uparrow}$ $\hat{c}^\dagger_{R\uparrow}\hat{c}^\dagger_{R\downarrow}\hat{c}_{L\downarrow}\hat{c}_{L\uparrow}$	pair hopping
V	$\hat{c}^\dagger_{L\uparrow}\hat{c}^\dagger_{R\downarrow}\hat{c}_{L\downarrow}\hat{c}_{R\uparrow}$ $\hat{c}^\dagger_{R\uparrow}\hat{c}^\dagger_{L\downarrow}\hat{c}_{R\downarrow}\hat{c}_{L\uparrow}$	spin-flip
Δt	$\hat{c}^\dagger_{L\uparrow}\hat{c}^\dagger_{L\downarrow}\hat{c}_{L\downarrow}\hat{c}_{R\uparrow} + \hat{c}^\dagger_{R\uparrow}\hat{c}^\dagger_{L\downarrow}\hat{c}_{L\downarrow}\hat{c}_{L\uparrow} = \hat{n}_{L\downarrow}\left(\hat{c}^\dagger_{L\uparrow}\hat{c}_{R\uparrow} + h.c.\right)$ $\hat{c}^\dagger_{R\uparrow}\hat{c}^\dagger_{R\downarrow}\hat{c}_{R\downarrow}\hat{c}_{L\uparrow} + \hat{c}^\dagger_{L\uparrow}\hat{c}^\dagger_{R\downarrow}\hat{c}_{R\downarrow}\hat{c}_{R\uparrow} = \hat{n}_{R\downarrow}\left(\hat{c}^\dagger_{R\uparrow}\hat{c}_{L\uparrow} + h.c.\right)$ $\hat{c}^\dagger_{L\uparrow}\hat{c}^\dagger_{L\downarrow}\hat{c}_{R\downarrow}\hat{c}_{L\uparrow} + \hat{c}^\dagger_{L\uparrow}\hat{c}^\dagger_{R\downarrow}\hat{c}_{L\downarrow}\hat{c}_{L\uparrow} = \hat{n}_{L\uparrow}\left(\hat{c}^\dagger_{L\downarrow}\hat{c}_{R\downarrow} + h.c.\right)$ $\hat{c}^\dagger_{R\uparrow}\hat{c}^\dagger_{R\downarrow}\hat{c}_{L\downarrow}\hat{c}_{R\uparrow} + \hat{c}^\dagger_{R\uparrow}\hat{c}^\dagger_{L\downarrow}\hat{c}_{R\downarrow}\hat{c}_{R\uparrow} = \hat{n}_{R\uparrow}\left(\hat{c}^\dagger_{R\downarrow}\hat{c}_{L\downarrow} + h.c.\right)$	density-induced tunnelling

Table 3.3: Off-site interaction processes in a double-well potential. We can group off-site interaction terms according to the total occurrence of Wannier functions on the left and right well [119].

Collecting the terms given in Table 3.3 the double-well Hamiltonian including off-site interactions is given by

$$\begin{aligned}\hat{H} = \sum_\sigma \left[-t\left(\hat{c}^\dagger_{L\sigma}\hat{c}_{R\sigma} + h.c.\right) + \Delta t\,\left(\hat{c}^\dagger_{L\bar{\sigma}}(\hat{n}_{L\sigma} + \hat{n}_{R\sigma})\hat{c}_{R\bar{\sigma}} + h.c.\right)\right] + U(\hat{n}_{L\uparrow}\hat{n}_{L\downarrow} + \hat{n}_{R\uparrow}\hat{n}_{R\downarrow}) \\ + V\left[\hat{n}_{L\uparrow}\hat{n}_{R\downarrow} + \hat{n}_{R\uparrow}\hat{n}_{L\downarrow} + \left(\hat{c}^\dagger_{L\uparrow}\hat{c}^\dagger_{L\downarrow}\hat{c}_{R\downarrow}\hat{c}_{R\uparrow} + h.c.\right) + \left(\hat{c}^\dagger_{L\uparrow}\hat{c}^\dagger_{R\downarrow}\hat{c}_{L\downarrow}\hat{c}_{R\uparrow} + h.c.\right)\right].\end{aligned} \tag{3.72}$$

When expanding the interaction in the Wannier basis, there is one term quantified by Δt that even though it derives from the interaction term indeed modifies the tunnelling. This can be intuitively understood by realizing that the on-site interaction effectively lowers or increases the barrier height that the atoms experience. In the basis of the singlet $|s\rangle$, the triplet $|t_0\rangle$ and

the doublon states $|d_+\rangle, |d_-\rangle$ the Hamiltonian simplifies to

$$\hat{H} = \begin{pmatrix} 2V & 0 & -2(t-\Delta t) & 0 \\ 0 & 0 & 0 & 0 \\ -2(t-\Delta t) & 0 & U+V & 0 \\ 0 & 0 & 0 & U-V \end{pmatrix}. \tag{3.73}$$

For repulsive interactions we find that $\Delta t < 0$, and therefore density-induced tunnelling enhances the tunnel coupling, which was successfully modelled in [120, 121] by an effectively shallower lattice potential. The opposite behaviour is expected for attractive interactions, where due to the energy gain particles tend to be more localized when a different spin component is present. Density-induced tunnelling was observed with ultracold bosons in a tilted one-dimensional optical lattice [121]. By varying the filling they verified the linear dependence on the density. For fermions the number of particles in a certain spin state is limited to one per lattice site according to Pauli's exclusion principle. Therefore, density-induced tunnelling is in general less relevant for fermionic systems. However, since the interaction integral Δt includes three Wannier functions on the same site, density-induced tunnelling is the off-site interaction term with the highest amplitude. Its relevance is boosted by the fact that we need to compare it to the conventional single-particle tunnelling amplitude t [122], which in our systems is typically much smaller than the on-site interaction U. In Section 6.2.3, I will estimate the relevance of higher order processes for our specific implementation of the bilayer Fermi-Hubbard model.

CHAPTER 4

Setup and Experimental Implementation

The experimental setup that I worked on during the course of my thesis has seen many generations of PhD students by now. Most of the important components had already been in place when I joined the team in 2016, and therefore will only be briefly summarized in this chapter by following the journey of the atoms from the heated potassium reservoir through all the cooling and trapping stages until they are finally loaded into the three-dimensional optical lattice potential. After discussing the main observables that we have access to, I will introduce the recent adaptions to the experiment. To further engineer the optical potential landscape we have set up two superlattices along an in-plane and the out-of-plane direction, respectively. A digital micromirror device (DMD) allows us to create arbitrary optical potentials within the horizontal layers, e.g. to realize a homogeneous Hubbard model.

4.1 Creating an Ultracold Fermi Gas

Alkali atoms whose electronic structure resembles the one of hydrogen are often used for ultracold atom experiments as their electronic transitions are very suitable for laser cooling [123]. In our setup we use the fermionic isotope of potassium, ^{40}K, with atomic number $Z = 19$ and neutron number $N = 21$. With a single valence electron the total angular momentum quantum number of the ground state is given by $J = 1/2$. In combination with a nuclear spin of $I = 4$ the electronic ground state $^2S_{1/2}$ composes of an $F = 9/2$ and an $F = 7/2$ manifold, as shown in Figure 4.1. The eigenenergies of the magnetic hyperfine states $|F, m_F\rangle$ are obtained by exact diagonalization of the hyperfine Hamiltonian in a homogeneous magnetic field $\boldsymbol{B} = B_z \boldsymbol{e}_z$ [124],

$$\hat{H}_{\mathrm{HFS}} = A\hat{\boldsymbol{I}}\hat{\boldsymbol{J}} - \hat{\boldsymbol{\mu}}\boldsymbol{B} = A\hat{\boldsymbol{I}}\hat{\boldsymbol{J}} - (\mu_N g_I m_I - \mu_J g_J m_J)B_z. \tag{4.1}$$

While the $|m_I, m_J\rangle$ basis is an eigenbasis to the magnetic field term, the hyperfine interaction can be rewritten in terms of raising and lowering operators and includes two terms, $\hat{I}_+\hat{J}_-$ and $\hat{I}_-\hat{J}_+$ that both mix basis states with different values of m_I and m_J but the same sum value $m_F = m_I + m_J$. Note that the magnetic quantum number m_F corresponding the projection of the total angular momentum is a good quantum number for all magnetic field strengths, as $[\hat{H}_{\mathrm{HFS}}, \hat{F}_z] = 0$ and therefore it will be used in the following to label the eigenstates. We can differentiate two regimes in the Breit-Rabi diagram shown in Figure 4.1. At low magnetic field strengths, in the so-called Zeeman regime, the energy of all the eigenstates increases

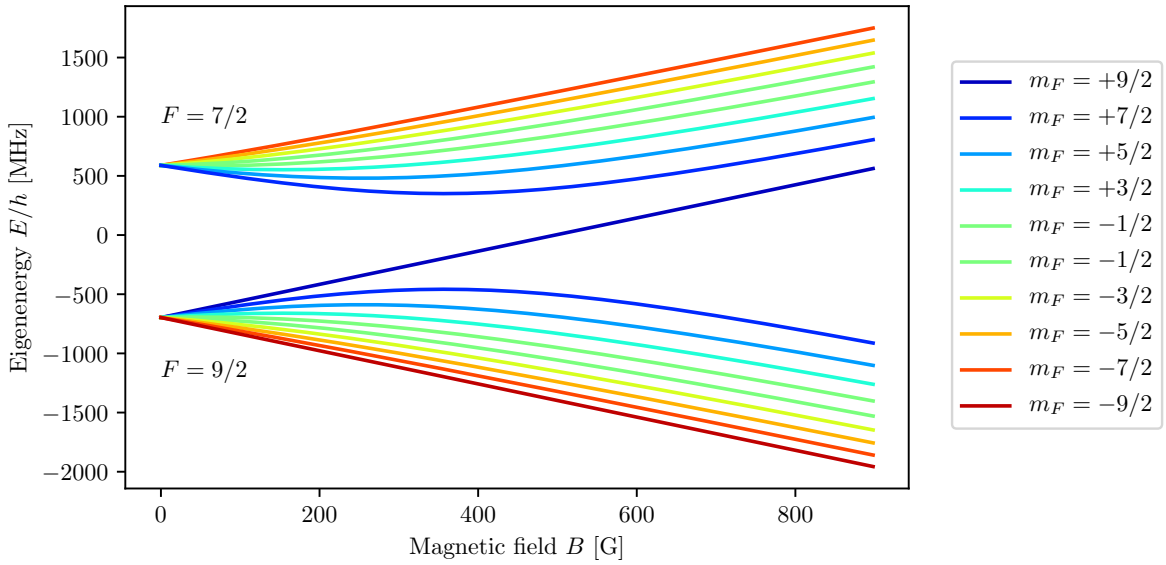

Figure 4.1: Hyperfine structure of ^{40}K in a magnetic field. The energies are referenced to the $^2S_{1/2}$ ground state of ^{40}K. Most of our experimental protocols are concerned with the lowest four states only, which we label according to the magnetic hyperfine quantum number, m_F, which is a good quantum number for all magnetic field strengths. For example, the state $|F = 9/2, m_F = -9/2\rangle$ is abbreviated as $|9\rangle$ $(= |-2m_F\rangle)$ and its energy is denoted as E_9.

linearly with B. As the internal magnetic field with a strength of around A/μ_B still exceeds the external field, the nuclear $\hat{\boldsymbol{I}}$ and electron angular momenta $\hat{\boldsymbol{J}}$ are still coupled to form the total angular momentum $\hat{\boldsymbol{F}}$. Once the external magnetic field reaches the strength of the internal field, the behaviour changes and the eigenenergies increase in parallel. For very strong magnetic fields the eigenstates can be grouped according to their electron angular momentum quantum number $m_J = \pm 1/2$, while the impact of the nuclear magnetic moment on the slope in the Breit-Rabi diagram is negligible since the nuclear magneton is much smaller than the Bohr magneton, $\mu_N \ll \mu_B$.

To implement the spin property of the electron, we identify the lowest two magnetic hyperfine states as the spin-up and -down states,

$$|\uparrow\rangle = |F = 9/2, m_F = -9/2\rangle \equiv |9\rangle \;\text{ and }\; |\downarrow\rangle = |F = 9/2, m_F = -7/2\rangle \equiv |7\rangle\,. \tag{4.2}$$

Throughout this thesis we will employ the term *spin states*, even though we simply refer to two distinct eigenstates of the internal structure of potassium. This pseudo-spin-1/2 system behaves differently when exposed to a real magnetic field. Even though the eigenenergies are different as for a real spin system, the two pseudo-spin states are stable and cannot transform themselves into one another. Therefore, in quantum gas experiments the effect of a magnetic field is simulated by preparing an imbalanced mixture of the two spin components.

One of the benefits of ^{40}K is that its Feshbach resonances, which are essential for modifying the interaction strength between the spin states, lie in the transition region of the Breit-Rabi diagram. This serves a twofold purpose, since firstly we can individually address transitions between any two neighbouring magnetic hyperfine states by Landau-Zener sweeps, see Section 4.2.1. Secondly, the magnetic moments are sufficiently different such that we can manipulate

the relative spin orientation at different lattice sites by applying magnetic field gradients. This is particularly relevant for the detection of magnetic correlations, which plays a crucial role throughout this thesis.

4.1.1 Interaction of Ultracold Neutral Atoms

In the introduction I have motivated the use of ultracold Fermi gases to mimic the behaviour of electrons in solid-state materials. However, neutral atoms clearly do not experience the Coulomb force. Still they interact with each other via collisions, which is modelled by their two-body interaction potential. At short distances when the electron clouds start to overlap the atoms strongly repel each other. This is a consequence of Pauli's exclusion principle, which forces electrons into higher-lying energy states [125]. If the separation of two atoms is much larger than several Bohr radii and electron exchange effects leading to covalent bonding may be neglected, the atoms feel a weak attractive force due to induced dipole-dipole interactions. This so-called van-der-Waals force is caused by vacuum fluctuations of the electric field, which induce a time-dependent dipole moment in a neutral atom. An oscillating dipole moment leads to an electric field, $\boldsymbol{E}^{(1)}_{\text{ind}} \propto 1/r^3$, which quickly decays with distance r. This induced electric field in turn generates an electric dipole moment in another atom, $\boldsymbol{p}^{(2)}_{\text{ind}} \propto \boldsymbol{E}^{(1)}_{\text{ind}} \propto 1/r^3$. The interaction energy of the induced dipole moment in the second atom and the electric field of the first atom amounts to $W = -\boldsymbol{p}^{(2)}_{\text{ind}}\boldsymbol{E}^{(1)}_{\text{ind}} \propto -1/r^6$.

When two colliding particles come close enough such that their thermal de Broglie wavelengths overlap, a classical scattering treatment in terms of particle trajectories and the impact parameter is not sufficient any more [126]. Instead to describe the scattering properties of two ultracold atoms, a quantum-mechanical treatment is necessary which takes the wave-like nature of the atoms into account. Hence, we have to solve the Schrödinger equation with the two-body interaction potential $V(\boldsymbol{r})$, where $\boldsymbol{r} = \boldsymbol{r}_2 - \boldsymbol{r}_1$ is the relative coordinate of the colliding atoms. The eigensolutions are grouped into bound states and scattering states according to the sign of their eigenenergy. By working in the centre-of-mass frame, the two-particle scattering problem is simplified to a one-body problem with relative momentum $\hbar\boldsymbol{k}$ and kinetic energy $E = \hbar^2 k^2/(2m_r)$, where m_r is the reduced mass [127]. The eigensolution to this scattering problem in relative coordinates is a sum of the incident plane wave with the relative momentum pointing along the z-direction[1] and the scattered spherical wave with scattering amplitude $f(\theta)$, which depends on the polar angle θ,

$$\psi(\boldsymbol{r}) \propto e^{ikz} + f(\theta)\frac{e^{ikr}}{r}. \tag{4.3}$$

For the electronic ground state of alkali and alkaline-earth-metal atoms the electronic angular momentum vanishes, $L = 0$. Consequently, the interaction potential is isotropic, i.e. $V(\boldsymbol{r}) = V(r)$ and the relative angular momentum quantum number l is a conserved quantity [124]. Therefore, it is sensible to expand the scattering wavefunction using a partial wave basis, where the quantum number $l = 0, 1, 2, ..$ distinguishes between s-, p- and d-wave scattering events. In spherical coordinates the scattering problem separates into a radial and an angular equation,

[1] without any loss of generality

where the former is given by

$$-\frac{\hbar^2}{2m_r^2}\frac{d^2\phi_l(r)}{dr^2} + V_l(r)\phi_l(r) = E\phi_l(r), \tag{4.4}$$

with the radial wavefunction $\psi_l(r) = \phi_l(r)/r$. The interatomic potential $V_l(r)$ contains the *centrifugal barrier*, $V_l(r) - V(r) = \hbar^2 l(l+1)/(2m_r r^2)$, which vanishes only for s-wave scattering. Higher-partial wave scattering with $l > 0$ may be neglected for ultracold quantum gases, where the collision energy is typically much lower than the centrifugal barrier and hence, resonant interactions with bound states are exponentially suppressed by the barrier height [128]. This has profound consequences, as the relative motion of the colliding particles is coupled to their internal states by quantum statistics. For identical fermions (bosons) the total scattering wavefunction must be antisymmetric (symmetric) with respect to particle exchange. In the absence of spin-orbit coupling the wavefunction factorizes into a spin and spatial part characterizing the internal states and the relative motion of the scatterers, respectively. As the spin wavefunction is always symmetric for identical particles, i.e. particles with the same internal structure, the parity of the spatial part has to be odd (even) for fermions (bosons). The parity of the scattering wavefunction is determined by the angular momentum quantum number and is equal to $(-1)^l$. Therefore, identical fermions (bosons) may only interact via partial waves with odd (even) l. In particular at low enough temperatures where the energy of the scatterers is not sufficient to overcome the centrifugal barrier, identical fermions[2] do not interact with each other. In order to engineer interactions in fermionic quantum gases typically a spin mixture with two different magnetic hyperfine states is implemented.

To identify the impact of the scattering process on the radial wavefunction, it is sufficient to focus on the asymptotic behaviour at a separation r that is larger than the effective range of the potential. It was realized that the partial waves are merely shifted by a phase $\delta_l(k)$ as compared to the incident plane wave, representing free particles [129]. In the limit of low energy scattering $k \to 0$, the thermal de Broglie wavelength is much larger than the effective range of the potential and effectively the scatterers do not resolve the details of the interatomic potential and only the s-wave collision channel is energetically accessible. In this limit the scattering phase shift $\delta_0(k)$ is directly connected to an energy independent parameter, the scattering length a_{sc} [130],

$$a_{\mathrm{sc}} = -\lim_{k\to 0}\frac{\tan\delta_0(k)}{k}. \tag{4.5}$$

For a negative (positive) scattering length the phase of the radial wavefunction advances more (less) quickly, which is equivalent to the case where a particle scatters off an attractive (repulsive) square well potential. Therefore, the scattering length is sometimes interpreted as an effective hard sphere radius [130]. This analogy is also helpful, when thinking about the s-wave scattering cross section, which is given by

$$\sigma = 4\pi a_{\mathrm{sc}}^2 \tag{4.6}$$

in the low energy limit $k \to 0$. It should be noted that for $\delta_0 = \pi/2$ the scattering length diverges. This resonance behaviour is accompanied by a sign change of the scattering length, see

[2] i.e. with the same set of quantum numbers (including m_F)

[130, 131] for more details. Therefore, when increasing the well depth of an attractive two-body potential beyond the resonance position, the phase shift gets larger than $\pi/2$ and the scattering length becomes positive. In [127] it is explained that this effect is related to the energy of the least-bound state of the scattering potential $V(r)$ and the resonance in the scattering length is linked to the appearance of a bound state at $E = 0$. In contrast, purely repulsive potentials do not have bound states and therefore they do not support such a resonance behaviour and the scattering length is always positive [131].

Magnetic Feshbach Resonances When the collision energy of two free atoms matches the energy of a molecular bound state, the scattering is resonantly enhanced. In cold atom systems the resonance condition can typically be tuned by adjusting the strength of an external magnetic field B. Such a magnetically tunable resonance relies on the Zeeman effect, which shifts the energy levels according to the magnetic moment of the respective scattering channels. Neglecting decay of the bound state, the scattering length in the vicinity of a Feshbach resonance can be parametrized by the resonance position B_0 and the width Δ [127],

$$a_{\mathrm{sc}}(B) = a_{\mathrm{BG}}\left(1 - \frac{\Delta}{B - B_0}\right). \tag{4.7}$$

The background scattering length a_{BG} is independent of the involved spin states. For potassium-40 the literature value is $a_{\mathrm{BG}} = 174(7)a_0$ [132]. While the scattering length diverges in the case of resonant coupling to a bound state, the scattering cross section is bound by the maximum of the relative momentum of the scatterers k [133],

$$\sigma(k) = \frac{4\pi a_{\mathrm{sc}}^2}{1 + a_{\mathrm{sc}}^2 k^2} = \begin{cases} 4\pi a_{\mathrm{sc}}^2 & \text{for } k a_{\mathrm{sc}} \ll 1, \\ 4\pi/k^2 & \text{for } k a_{\mathrm{sc}} \gg 1. \end{cases} \tag{4.8}$$

An exhaustive list containing the parameters of both s- and p-wave Feshbach resonance of ^{40}K can be found in the PhD thesis of my colleague Eugenio Cocchi [80]. In Figure 4.2 the scattering length a is shown for the most common spin mixtures of ^{40}K and for the typical magnetic field range used in our experiments.

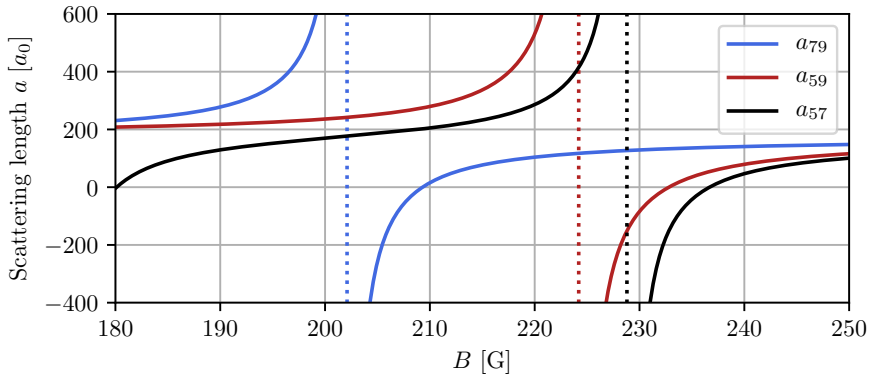

Figure 4.2: Relevant Feshbach resonances of potassium. Feshbach resonances between the lowest three magnetic hyperfine states of the $F = 9/2$ manifold of ^{40}K are plotted according to Equation 4.7. The resonance parameters have been looked up in [80].

4.1.2 Trapping and Cooling to Quantum Degeneracy

In the following I will briefly explain the individual cooling and trapping stages, which are implemented to cool down the potassium atoms to around 100 nK.

Magneto-Optical Trap The journey of creating ultracold atoms starts with a glass ampoule containing solid potassium, which was broken under vacuum in our first experimental chamber several years ago. To reach a sufficient vapour pressure the reservoir is heated to around 60°C. Atoms are evaporated and diffuse throughout the chamber with a velocity that is small enough to directly trap and cool them with a magneto-optical trap (MOT) without the need for a Zeeman slower. Laser cooling relies on the momentum transfer between a near-resonant laser beam and the atomic gas. In the case of red-detuning, $\omega - \omega_0 < 0$, atoms predominantly scatter photons from a beam that is opposing their propagation direction due to the Doppler effect. As a consequence of the spontaneous emission being isotropic, this leads to a net force that slows down the atoms. In a MOT, laser cooling along all three directions is combined with a magnetic quadrupole field that is generated by a pair of coils in anti-Helmholtz configuration. In contrast to magnetic traps, the inhomogeneous magnetic field is not strong enough to trap the atoms with their intrinsic magnetic moment. However, in combination with the three pairs of counter-propagating laser beams with opposite circular polarization the magnetic field gradient close to the centre of the MOT leads to a position dependent force on the atoms if they are displaced from the centre of the intersection region of the laser beams which overlaps with the magnetic field zero. The viscous force slowing down the atoms is counteracted by the random scattering of photons from the near-resonant laser beams. Therefore, in a MOT the equilibrium temperature is bound from below by the *Doppler temperature*, which for potassium is given by

$$T_D = \frac{\hbar\Gamma}{2k_B} = 145\,\mu\text{K}. \tag{4.9}$$

For more information on the basic principle of a MOT see [124].

The setup of the MOT in our experiment is described in detail in [134, 135] and I will only summarize the main aspects in the following. In order to reach sufficiently low temperatures the atoms need to scatter many photons. This is achieved in our experiment by choosing a closed optical transition provided by the D_2 line of potassium at around 767 nm between the $|F = 9/2\rangle$ manifold of the $^2S_{1/2}$ ground state and the $^2P_{3/2}$ excited state with $|F' = 11/2\rangle$. In reality, due to the small hyperfine splitting in the excited state and the finite laser linewidth there is off-resonant excitation to the $|F' = 9/2\rangle$ manifold, which may decay back to the $|F = 7/2\rangle$ ground state manifold. Therefore in addition to the so-called cooling laser operating on the main cooling transition, another laser is necessary to pump atoms back into the cooling cycle. However, as the cooling and the repumping laser are each detuned by 32 MHz from their respective transition frequencies, both contribute to the cooling of the atoms. The final temperature in the MOT is severely limited by random scattering of photons, therefore we need to transfer the potassium atoms into a magnetic trap.

Magnetic Trap For loading the potassium atoms into a magnetic trap they need to be in low-field seeking states, i.e. $m_F g_F > 0$. This is achieved by optically pumping the system on the $|F = 9/2\rangle$ to $|F' = 9/2\rangle$ transition. For this purpose we turn off the MOT quadrupole field

and define a quantization axis by creating a homogeneous bias field along the z-direction. We send σ^+-polarized cooling and repumping light along the quantization axis and end up in a spin mixture of predominantly the $m_F = 9/2$ and $m_F = 7/2$ states. Once the atoms are in the correct magnetic hyperfine states, we quickly turn on a magnetic quadrupole field that is provided by running a much larger current through the MOT coils. Since the MOT coils are mounted on a motorized translation stage, we can consecutively transport them to the science chamber, which is a glass cell with a pressure of around 10^{-11} mbar. This value is considerably lower as compared to the pressure in the MOT chamber, where the background pressure needs to be high enough to load sufficiently many atoms into the MOT. Once the atoms have arrived in the science chamber, they are transferred into a Ioffe-Pritchard trap. For details on the coil design and the evaporative cooling technique see [135, 136]. At the end of the forced radio-frequency (RF) and microwave (MW) evaporation in the Ioffe-Pritchard trap we typically obtain a cloud containing approximately 10.6 million atoms at around 2.9 µK.

Dipole Trap A major drawback of magnetic traps is that the trapping potential depends on the magnetic moment of the atoms and hence on the internal state that we use to emulate the spin property of the electron. Therefore, after the forced evaporation we transfer the atoms from the Ioffe-Pritchard into a crossed-beam dipole trap [136]. The transfer efficiency strongly depends on the position of the horizontal dipole trap, in particular on its z-component, since the vertical beam waist is very small, $w_z = 12.5\,\mu\text{m}$. Furthermore it is beneficial to match the trap depth of the dipole trap to the temperature of the cloud in the Ioffe-Pritchard trap. We consecutively transfer the low-field seeking states to the lowest two magnetic hyperfine states whose Feshbach resonance is located at around 202 G. For the internal state transfer the total magnetic field needs to be in the Zeeman regime, where the energy differences between each two consecutive magnetic hyperfine states are all equal. In this case a Landau-Zener sweep transfers the population from the $+m_F$ to the $-m_F$ state. We carefully adjust the spin mixture to a balanced situation before ramping up the second dipole trap beam, called the dimple. In analogy to the forced evaporative cooling using RF and MW transitions in the magnetic trap, we successively lower the trap depth of the dipole trap to selectively get rid of the hottest atoms. Previously, this evaporation process was performed at magnetic field of around 190 G with repulsive interactions between the lowest two magnetic hyperfine states, see [60] for more details. We typically reached cloud sizes of 110 thousand atoms per spin state at around 10% of the Fermi temperature. The starting point for the bilayer experiments is a band insulator in the optical lattice for which we need a very high density in the centre of the cloud. This is facilitated by using attractive interactions during the lattice loading stage. Furthermore for experiments on the attractive Hubbard model it is beneficial to avoid the abrupt change in interaction energy by already performing the evaporative cooling with attractive interactions. An additional advantage is the absence of the loss channel due to the molecular bound state that is only present for effectively repulsive interactions. With the evaporation at 204 G we typically reach cloud sizes of 70 thousand atoms per spin state at around 9% of the Fermi temperature. For more details see [137].

Optical Lattices At the end of the evaporation in the dipole trap we have reached quantum degeneracy and the atoms are cold enough to be loaded into the three-dimensional optical lattice setup that is shown in Figure 4.3 with typical trap depths on the order of a few µK only. We start by ramping up the vertical lattice that is derived from a Coherent Verdi V-10

and coupled through a polarisation maintaining single-mode photonic-crystal fibre from NKT photonics. At the same time we reduce the dipole trap confinement. During the long ramp time of 3 s we further evaporate hot atoms since the dipole trap confinement in combination with the anti-confinement from the blue-detuned lattice laser creates pockets along the x-direction. The vertical lattice depth decreases exponentially with the distance from the trap centre and at the position of the side pockets at around 220 µm it is not strong enough to trap the atoms against gravity. Therefore the atoms leave the trap along the vertical direction and at the end of the ramp we have lost the hottest atoms, which predominantly occupied the side-pockets. For more details see [60, 80]. This is an important step to reach a cold lattice gas and counteracts the heating caused by non-adiabaticity during the lattice loading [138, 139].

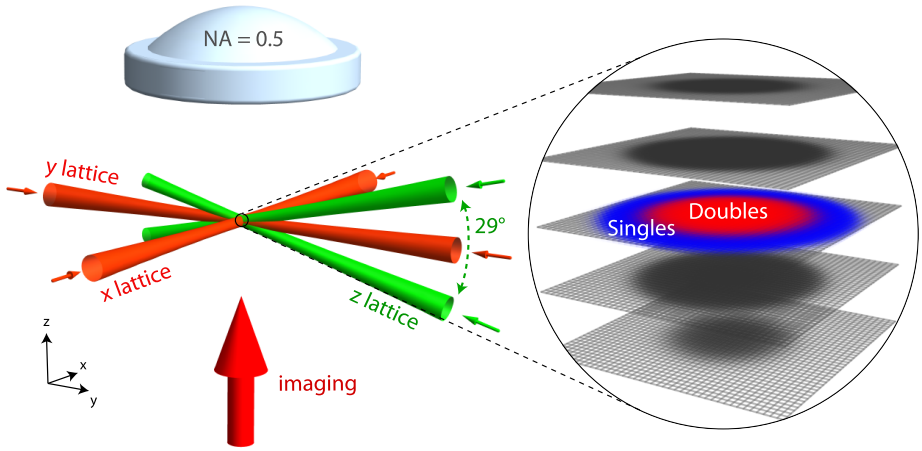

Figure 4.3: Optical lattice setup. Experimental setup of the lattice laser beams that create a stack of two-dimensional layers with a square in-plane lattice structure. Each of theses planes constitutes an independent realization of the two-dimensional Hubbard model. Figure taken from [34].

The vertical lattice separates the three-dimensional cloud into two-dimensional layers as shown in Figure 4.3. The two beams with a wavelength of $\lambda_g = 532\,\text{nm}$ interfere under a half-angle of $\theta_z = 14.5(1)^\circ$, which fixes the lattice spacing to $a_z = 1.064\,\mu\text{m}$. To create a square lattice structure in each of the horizontal planes, we ramp up both the x- and y-lattice with a wavelength of $\lambda_r = 1064\,\text{nm}$ within 500 ms to $6E_{\text{rec}}$. This time has been chosen carefully and is equal to the minimal time that is required to reach global thermal equilibrium within the layer as will be discussed in Section 5.3.6. While previously the light for all infrared lattices was derived from a single 20 W Mephisto Mopa from Innolight, we have changed the laser source for the infrared x-lattice to an Ytterbium-doped fibre laser system (Koheras Adjustik from NKT photonics) with a linewidth reduction to less than 5 kHz. This step was necessary for the implementation of a superlattice along the x-direction, which requires the frequency of the infrared x-lattice to be tuned at will without disturbing the other lattices, see Section 4.1.3 for more details. The Adjustik fibre laser uses a fibre Bragg grating cavity to maintain a single mode laser output over the whole operating range. The wavelength of the Adjustik fibre laser system is coarsely adjustable by thermal tuning of the laser substrate. For locking the laser a fast wavelength modulation with fine control is necessary and is achieved by employing an internal piezo module with a bandwidth of around 20 kHz.

4.1.3 Adding Flavour: Optical Superlattices

We have recently extended our experimental setup by implementing superlattices along the x- and z-direction. This required adding a second optical lattice with a commensurate wavelength along both directions. Furthermore, to obtain full control over the superlattice configuration (compare Figures 2.4 and 2.5) an offset lock was set up for each superlattice to tune the frequency difference of the corresponding lattice lasers.

Intralayer Superlattice

As mentioned above the standard wavelength of both intralayer lattices is $\lambda_r = 1064\,\mathrm{nm}$. To create a superlattice along the x-direction we added a green laser source with $\lambda_g = 532\,\mathrm{nm}$ to the setup. As the distance from the retro-reflecting mirror to the position of the atoms is equal to around 50 cm, the frequency difference that is required for a spatial shift of the optical lattice by one period is given by 300 MHz, see Equation 2.19. For a phase stable superlattice it is hence crucial that both lattice lasers have a small spectral linewidth. This requirement eliminates the use of a commercial green laser source such as the Verdi from Coherent with a spectral linewidth of around 5 MHz. Instead, a monolithic cavity was designed that frequency-doubles the infrared light from a 55 W Mephisto Mopa with a spectral linewidth of approximately 1 kHz over 100 ms [140]. The spectral properties of the frequency-doubled green light are inherited from the infrared laser, in particular the linewidth of the frequency-doubled light is expected to be equal to twice the linewidth of the infrared seed laser. The design and the integration into the experimental setup are described in [141].

In order to reach large enough lattice depths the green laser beam is focussed down by a lens with a focal length of $f = 250\,\mathrm{mm}$ such that the minimum waist position matches the location of the atoms. However, we can not tune the position of this lens, as it is already adjusted for the horizontal dipole trap and the infrared x-lattice. Instead, a regular and a cylindrical telescope are placed into the beam path of the green lattice to match the focus position to the position of the atoms and to tune the beam profile. The optimal beam parameters are found as a compromise between a large lattice depth and a small spatial inhomogeneity of the Hubbard parameters. I will briefly discuss our considerations in the following.

By combining Equations 2.23 and 2.24 one can derive a formula to estimate the lattice depth[3] of the green x-lattice in the centre of the trap

$$V_{\mathrm{x,g}} = \frac{4\sqrt{\gamma}P^{\mathrm{in}}}{\pi\omega_y\omega_z\epsilon_0 c}\cdot \mathrm{Re}\left[\alpha(\lambda)\right], \tag{4.10}$$

which is a function of the power in the incoming beam path, P^{in}, the power ratio $\gamma_{x,g} = P^{\mathrm{refl}}/P^{\mathrm{in}}$ and the two orthogonal beam waists $w_{y,z}$. In addition, we need to know the real part of the atom's polarisability and we use the results from [142] to interpolate the polarisability of potassium-40 for the wavelengths used in our experiment. In SI units we obtain

$$\mathrm{Re}[\alpha(\lambda = 532\,\mathrm{nm})] = -h\cdot 5.97\cdot 10^{-6}\,\frac{\mathrm{m}^2}{\mathrm{sV}^2}, \tag{4.11}$$

$$\mathrm{Re}[\alpha(\lambda = 1064\,\mathrm{nm})] = h\cdot 1.49\cdot 10^{-5}\,\frac{\mathrm{m}^2}{\mathrm{sV}^2}. \tag{4.12}$$

[3] lattice depth in units of Joule

In Figure 4.4 the local lattice depth of the green x-lattice is plotted in units of the corresponding recoil energy as a function of the distance from the trap centre along the y-axis. We assume the local laser intensity to follow a Gaussian behaviour with the width given by the waist in the y-direction. For different values of the vertical beam waist, w_z, the peak intensity is simply scaled by a multiplicative factor. In contrast the waist in y-direction determines the full width at half maximum of the Gaussian shape and if chosen too small will lead to considerable variation of the local lattice depth over the cloud size. This ultimately leads to local variations in the Hubbard parameters, t and U, as both are sensitive to the local lattice depth. The

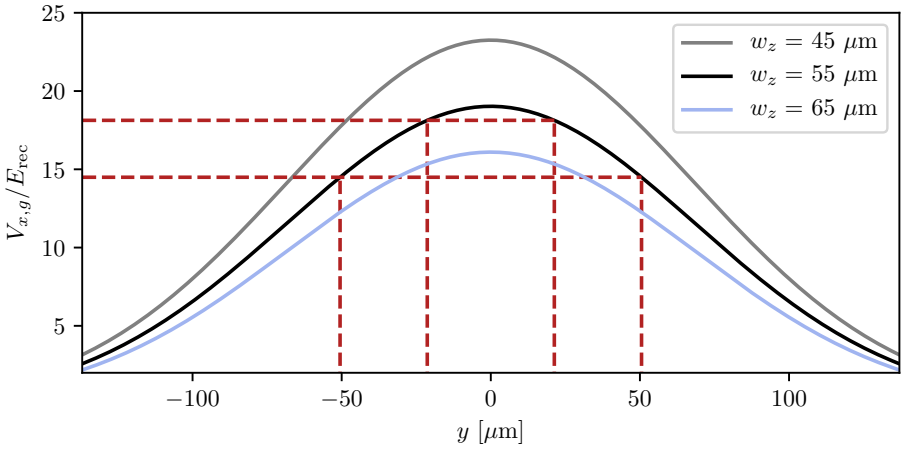

Figure 4.4: Lattice depth variation of the green x-lattice. The lattice depth of the green x-lattice varies as a function of the y-position. The estimate shown is obtained for a power of $P^{\mathrm{in}} = 1\,\mathrm{W}$ in the forward beam, $\gamma_{x,g} = 0.78$ and $w_y = 137\,\mu\mathrm{m}$. The red dashed lines at 21 and 50 µm correspond to a distance of 40 and 95 sites to the trap centre. The corresponding variation in the local lattice depth amounts to 5% and 24%, respectively. Note that this relative variation does not depend on the vertical waist, w_z but on the horizontal one, w_y.

telescope lenses are chosen to produce a cylindrical beam profile with an expected vertical waist of $w_z = 45\,\mu\mathrm{m}$ and $w_y = 138\,\mu\mathrm{m}$ within the plane. With a small camera (Basler acA1300-30gm) we characterise the final beam profile, and obtain $w_z = 55\,\mu\mathrm{m}$ and $w_y = 134\,\mu\mathrm{m}$. More details on the alignment procedure can be found in [77]. In Section 4.3 I explain how we additionally calibrate the horizontal waist w_y via the potential that the atoms experience and we indeed obtain a similar value.

The superlattice configuration is controlled by tuning the frequency of the infrared lattice laser. The frequency variation is minute such that the periodicity of the optical lattice is essentially unchanged. However, the phase is proportional to the frequency difference accumulated over a distance of $L = 50\,\mathrm{cm}$ and hence the position of the potential minima of the infrared lattice will move with respect to the green lattice potential. The main reason for tuning the frequency of the infrared laser is that the absolute position of the lattice sites remain approximately constant, compare Figure 2.4. Furthermore, there are technical reasons for tuning the Adjustik fibre laser whose piezo module has a large bandwidth of around 20 kHz, while the lock of the frequency-doubling cavity would not allow for fast tuning of the wavelength. Even though the frequency stability of both the Mephisto Mopa and the fibre laser are outstanding[4], we lock

[4] e.g. frequency stability of less than 1 MHz/min for the Mephisto laser [140]

their beatnote to an external reference provided by a DDS (AD9914 from Analog Devices), which allows for quickly tuning the frequency of the fibre laser via its piezo module. For more details on the offset lock see [77].

Vertical Superlattice

For implementing an optical superlattice along the vertical direction we needed to overlap an infrared laser with the existing green lattice beam path. The setup including all optical elements is shown and described in [108, 137]. Note that the polarizing beamsplitter cube, which separates the light coming from the fibre coupler into an upper and lower beam path, is not designed for the infrared wavelength, $\lambda_r = 1064\,\mathrm{nm}$. Consequently the power imbalance of the two beams is rather large leading to a strong running-wave component and hence the confinement within the horizontal layers is undesirably tight. Due to the angled lattice configuration, the waist of the vertical lattice beam projected into the horizontal plane is much smaller along the x-direction. Therefore, the confinement of the infrared laser is much tighter along the x-direction. Originally the angled configuration was chosen due to the negligible path length difference of the two interfering beams [60], see Figure 4.3. While this is beneficial for obtaining a high-stability optical lattice, i.e. very little change in the height of the horizontal layers, it is disadvantageous for implementing a superlattice. Even after inserting an anti-reflection-coated glass plate with 5 mm thickness into the upper beam path, the transformation from a symmetric to an asymmetric double-well configuration requires a tuning range of several tens of Gigahertz. The laser source for the additional infrared lattice is the 20 W Mephisto Mopa, which is also used for the y-lattice. Even though it offers to tune its frequency by a piezo-electric transducer with a response bandwidth of up to 100 kHz [140] the tuning range is only ±65 MHz wide, which is way too little for our needs. The thermal tuning range in contrast is much larger, i.e. on the order of 30 GHz. However the thermal response bandwidth of 1 Hz is not sufficient to change the frequency within the course of an experimental cycle. Therefore the superlattice configuration is adjusted by tuning the frequency of the green lattice laser, which is a Verdi-V10 [143]. One of its resonator mirrors is mounted on a piezo-electric actuator containing two stacks of lead zirconate titanate (PZT) material [144] that change the frequency by adjusting the roundtrip length of the cavity. The shorter stack is tuned by the fast PZT input and is suited for small changes in frequency with a fast nominal response bandwidth of 20 kHz. In contrast, the tall stack is controlled by the slow PZT input and allows for a large tuning range of more than 8.2 GHz. Both PZT stacks are controlled independently from one another via two BNC connectors with an input voltage range of 0 to 100 V each. This high voltage is created by a piezo controller[5], which limits the bandwidth performance since the piezo actuator acts as a capacitance and hence forms a low-pass filter in combination with the output impedance of the piezo driver. According to the manual [145] the effective bandwidth may be estimated as

$$\mathrm{BW} = 1/(2\pi \cdot 150\,\Omega \cdot (47\,\mathrm{nF} + C_{\mathrm{PZT}})). \tag{4.13}$$

When connecting the fast (slow) piezo stack whose capacitance is equal to $C_{\mathrm{PZT}} = 25\,\mathrm{nF}$ (450 nF) [137], the bandwidth is limited to 14.7 kHz (2.1 kHz), respectively.

In Figure 4.5 a) and b) we characterize the change in the output frequency as measured

[5] MDT693A Piezo Controller from Thorlabs

by a wavemeter[6] when tuning the etalon temperature and the slow PZT voltage, respectively. Even though the PZT control voltage can be tuned from 0 to 100 V, we have observed an

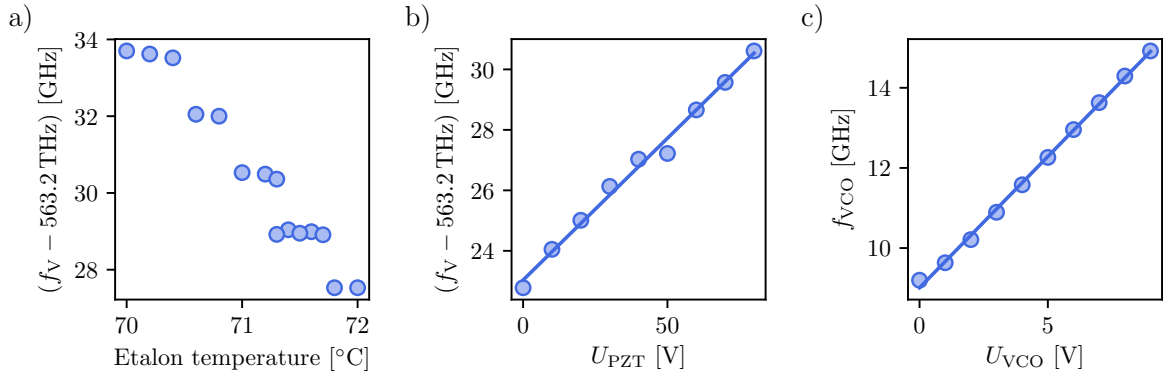

Figure 4.5: Calibration of the Verdi tuning range. a) The etalon temperature changes the frequency of the Verdi and we observe several plateaus with unstable mode-hop regions in between. b) In the unlocked case we directly tune the slow piezo control voltage, U_{PZT} to adjust the superlattice configuration during the course of the experimental sequence. The corresponding gain factor is obtained from a linear fit as $9.4(4) \cdot 10^{-2}\,\mathrm{GHz/V}$. c) In contrast, when locking the frequency of the Verdi via an offset lock to the frequency doubled light from the Mephisto, we tune the VCO which is frequency doubled before mixing it with the beatnote. Consequently, we obtain a scaling factor that is equal to twice the slope inferred from a linear fit to the data shown in c), $2 \cdot \Delta f_{\mathrm{VCO}}/\Delta U_{\mathrm{VCO}} = 1.31(2)\,\mathrm{GHz/V}$.

unstable regime with mode-hops above 80 V. Therefore we typically avoid the large voltage range. As a consequence of the short path length difference, the required frequency tuning range to transform a symmetric into an asymmetric double-well configuration is at least four orders of magnitude larger than the spectral linewidth of either lattice laser forming the vertical superlattice[7]. Therefore, we do not necessarily need an offset lock to control their difference frequency. Instead to adjust the phase relation at the position of the atoms we may directly tune the slow PZT voltage, see Figure 4.5 b). To achieve both the symmetric and a sufficiently asymmetric double-well configuration the absolute frequency of the Verdi is optimized beforehand by tuning the Etalon temperature, see Figure 4.5 a).

To improve the long-term stability of the absolute frequency that is output by the Verdi lattice laser an offset lock was implemented by my colleague M. Gall [137]. This involves frequency-doubling the 1064, nm light that is emitted from the Mephisto with a periodically poled lithium niobate (PPLN) crystal in single-pass configuration. The frequency-doubled light is overlapped with the Verdi to form an optical beat note, which we compare to an external reference provided by a voltage controlled oscillator[8] (VCO). To increase the accessible frequency range we use an upscaling mixer[9], which frequency doubles the VCO signal before mixing it with the high optical frequency beat note. An error signal is obtained by mixing half the power of the downconverted beat signal with its other half that has been delayed by a 15 cm delay line. We obtain both a proportional and an integral regulation signal that are fed

[6] High Finesse WS7
[7] The spectral linewidth of the Verdi is less than 5 MHz over 50 ms [143] and for the Mephisto it is around 1 MHz over 60 s [140].
[8] HMC733 from Analog Devices
[9] HMC264 from Analog Devices

back to the fast and slow PZT input of the Verdi, respectively. For more information on the microwave frequency downconversion and the feedback loop see [137]. To optimize the locking range with respect to the superlattice configuration and to maximize the possible scan range of the Verdi, we tune both the crystal temperature of the Mephisto seed laser and the etalon temperature of the Verdi, respectively. Setting up an offset lock has the additional advantage that we can closely monitor how the frequency difference changes when enforcing a ramp via the VCO control voltage, which allows us to identify mode hops or frequency jumps. Even with the offset lock enabled, the VCO control voltage resulting in a symmetric double-well configuration needs to be regularly optimized.

The offset lock allows us to scan the frequency by up to 6 GHz within 100 ms. As compared to the experimental timescales of the microscopic tunnelling processes this ramp duration is rather long and precludes sudden changes in the optical lattice potential seen by the atoms. However for the experiments presented within this thesis we only need to shift the frequency of the green lattice laser when its power is not used on the atoms. Therefore, we are not severely limited by the ramp duration. The limited frequency tuning range is more problematic, as the symmetric and asymmetric double-well configurations are roughly 60 GHz apart when tuning the frequency of the green laser[10]. To be able to realize both limiting cases of the superlattice configuration within a single experimental cycle a second Mephisto laser was installed (Mephisto (S) with 500 mW), whose only purpose is to realize the fully asymmetric double-well lattice. Therefore it is detuned by around 30 GHz from the original infrared lattice laser [108, 137].

4.2 Detection and Observables

The detection is at the heart of every experimental cycle. In our setup we use absorption imaging to read out the density distribution of the atoms and from this we can further infer properties of the gas such as its temperature. In the following, I will explain the basics of absorption imaging, its implementation into our setup and how we avoid averaging over several horizontal layers with different total atom number. Depending on the specific experiment, it is beneficial to obtain either the density distribution of both spin components individually (without doubles), or to access the full density sector, by separating the signals from singly and doubly occupied sites of one spin component only. Both schemes will be discussed in the following.

4.2.1 Landau-Zener Sweeps

While radio-frequency (RF) and microwave (MW) transitions have already been used for the evaporative cooling in the magnetic trap, they also play a pivotal role for the detection, and therefore, I will briefly explain how to change the internal state of the atoms with high fidelity by so-called Landau-Zener sweeps. As for the evaporation, the RF field is generated by a small coil with five windings and a diameter of around 4 cm. It is glued on top of the Ioffe Pritchard coils in close proximity to the atoms [135].

At large magnetic field strengths of around 200 G, the transition energies between each two consecutive magnetic hyperfine states differ by around 2 MHz and are hence sufficiently different to selectively address individual transitions between magnetic hyperfine states with a linear frequency sweep. The chosen pulse parameters are a sweep width of $\Delta_{\mathrm{RF}} = 175\,\mathrm{kHz}$

[10] When adjusting the infrared frequency only half the tuning range is required, compare Figures 2.4 and 2.5.

and a pulse duration of $T_{\mathrm{RF}} = 2\,\mathrm{ms}$. The amplitude envelope of the RF sweeps is shaped by a voltage controlled attenuator (VCA), which is controlled by an arbitrary function generator (Tektronix AFG 3022C). In the first and last 100 µs of the pulse window the VCA control voltage is linearly increased (decreased). This is necessary to obtain a complete state transfer and to avoid non-adiabatic state projections.

4.2.2 Absorption Imaging

For absorption imaging a resonant laser beam is directed onto the atom cloud, which will imprint a shadow onto the beam profile that contains information about the density distribution of the atoms [146]. The optical density (OD) of the sample is defined via the intensity of the imaging beam before and after passing the atoms and is a dimensionless quantity, which is a measure for the light absorption. If the imaging beam propagation direction is parallel to the z-axis, we obtain the optical density as

$$\mathrm{OD} = -\ln\left(\frac{I(x,y)}{I_0(x,y)}\right) = \sigma_0 n(x,y). \tag{4.14}$$

The last equality follows from a comparison to standard Beer's law [124], where σ_0 is the absorption cross section and $n(x,y) = \int n(x,y,z)\mathrm{d}z$ is the column density. For a two-level system interacting with a resonant probe beam, the bare scattering cross section $\sigma_0 = 3\lambda^2/2\pi$ is modified to

$$\sigma(I) = \frac{\sigma_0}{1 + \frac{I}{I_0^{\mathrm{sat}}}}, \tag{4.15}$$

if saturation effects play a role. In addition, the imaging cross section is affected by deviations from the idealized two-level treatment, which are unavoidable in a real experiment. Possible sources are given for example by an imperfect polarization of the imaging beam or the excited level structure leading to deviations from an ideal cycling transition. Following G. Reinaudi et al. [147], we introduce a dimensionless quantity, $\alpha^* \geq 1$, which measures both the reduction in cross section and the increase in saturation intensity $I_{\mathrm{eff}}^{\mathrm{sat}} = \alpha^* I_0^{\mathrm{sat}}$

$$\sigma_{\mathrm{eff}}(I) = \frac{\sigma_0}{\alpha^*}\frac{1}{1 + \frac{I}{I_{\mathrm{eff}}^{\mathrm{sat}}}}. \tag{4.16}$$

If the cross-section depends on the probe intensity, Beer's law gets modified by a high-intensity correction. Integration of

$$\frac{dI}{dz} = -n(x,y,z)\sigma_{\mathrm{eff}}(I)I \tag{4.17}$$

by a separation of variables leads to the density distribution

$$n(x,y) = -\frac{\alpha^*}{\sigma_0}\ln\left(\frac{I(x,y)}{I_0(x,y)}\right) + \frac{I_0(x,y) - I(x,y)}{\sigma_0 I_0^{\mathrm{sat}}}. \tag{4.18}$$

Therefore, to obtain the high-intensity corrected density distribution, one needs to calibrate the factor α^* beforehand. The procedure for this was developed in [147] and the results for our

setup are discussed in [60, 80].

Vertical Imaging Setup Most of our experimental protocols rely on the vertical imaging setup, sketched in Figure 4.6 a), to obtain an *in-situ density* distribution, i.e. in the presence of the optical lattices. It is explained in detail in [60, 80] and was not adapted since. Therefore, I will only summarize the main features.

First the imaging beam is demagnified by a telescope consisting of an achromatic lens with focal length $f = 350\,\mathrm{mm}$ and a first aspheric lens (asphere) within the glass cell. The corresponding demagnification is rather large $M \approx 1/44$, which is relevant for projecting light and thereby creating small spatial potential structures with the digital-micromirror device (DMD), see Section 4.4. To guarantee that we obtain a high-resolution image with the CCD camera, the light scattered by the atoms in the object plane is collected by a second aspheric lens inside the science chamber with the same focal length and an equally large numerical aperture of NA = 0.5. The beam is magnified such that one square pixel with an edge length of 13 µm corresponds to around 1.1 lattice sites. However, as will be discussed later, the point-spread function (PSF), which characterizes the imaging resolution smears out the signal of a single lattice site over several pixels. A slit is placed in the first imaging plane after the atoms, which ensures that only a fourth of the CCD chip is exposed to the imaging beam. The remaining part of the chip serves as the storage region. Hence, using the fast kinetics mode of the Andor iXon 888 camera we can take up to three images in quick succession, see Figure 4.6 a). The 1:1 relay creates another image plane at the position of the CCD chip.

In Figure 4.6 b) we show how to obtain the density distribution of both spin components in a

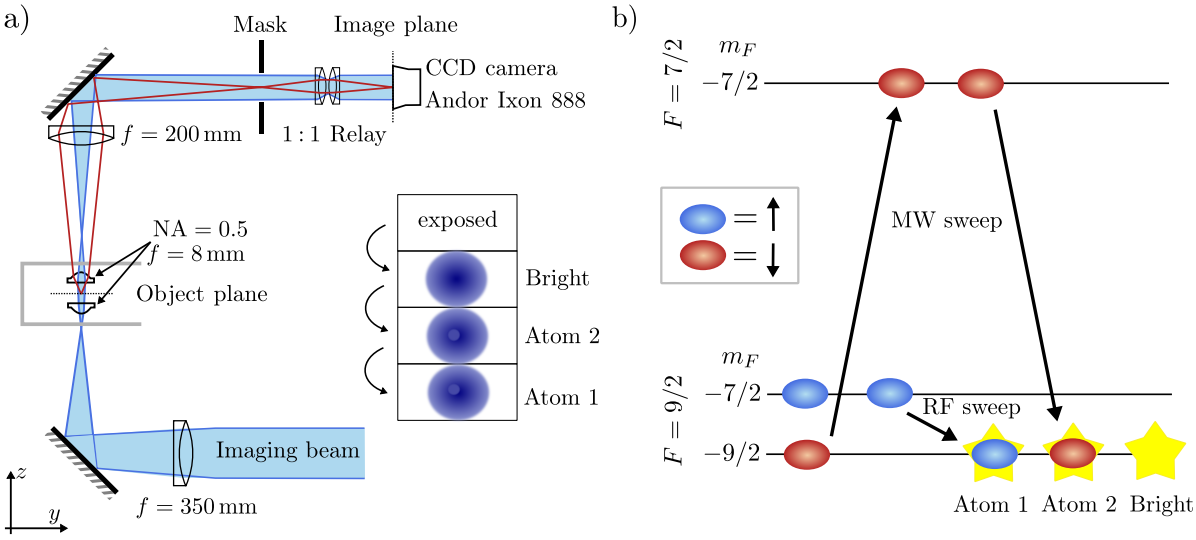

Figure 4.6: Vertical in-situ imaging setup. a) Schematic of the vertical imaging system. Not shown are a line filter to selectively transmit the imaging wavelength to the CCD chip and a quarter-wave plate to minimize interference effects at the position of the atoms by spurious back-reflection [60]. Using the fast kinetics mode of the Andor camera, we can take up to three images in quick succession. This allows us to image for example the density distribution of both spin components in a single realization. b) We utilize a microwave sweep to store one of the spin clouds in a far detuned hyperfine state when imaging the other spin component. This minimizes off-resonant contributions to the absorption imaging signal. This figure was adapted from [137].

single realization.[11] A broad microwave sweep with a width of $\Delta_{\mathrm{MW}} = 1.6\,\mathrm{MHz}$ transfers atoms (red ellipse) residing in the lowest hyperfine state of the $F = 9/2$ ground state manifold to $|F = 7/2, m_F = -7/2\rangle$. Consecutively, the other spin component (blue ellipse), is transferred into the lowest hyperfine state by an RF sweep in order to be imaged on the cycling transition of the D2 line. It is important to depopulate the second lowest hyperfine state as otherwise it contributes to the observed optical density via off-resonant scattering of the imaging light. After having recorded the density distribution of the spin-up component, the spin-down atoms are transferred back into the lowest magnetic hyperfine state by a second MW sweep and imaged in quick succession. If atoms on doubly occupied sites get shelved, both atoms on this lattice site are lost due to spin changing collisions during the MW sweep. The third image ("bright") characterizes the intensity distribution of the imaging light pulse when there are no atoms left to scatter off. In order to calculate the optical densities, the bright image is slightly rescaled to match the intensity of the respective atom image in a region where there are no atoms.

Imaging Resolution The aspheric lenses placed inside the science cell provide a high numerical aperture by requiring a short working distance of 5.92 mm. The numerical aperture, $NA = n \sin\theta$ quantifies the maximum wavevector with half-angle θ that is collected by an optical element with refractive index n. Therefore, it is crucial in determining the diffraction limited resolution. The Rayleigh criterion, for example, yields an estimate on the minimum achievable radius of the Airy disk in the case of incoherent fluorescent imaging. Considering our experimental parameters, we obtain $r_{\mathrm{Airy}} = 1.22\lambda/(2NA) = 0.94\,\mu\mathrm{m}$ as a rough estimate [148].

A more sophisticated approach to determine the imaging resolution of our setup includes the point-spread function (PSF). While I will only quickly summarize the main features, a comprehensive discussion of its impact on absorption imaging may be found in an article by Hung et al. [149]. In simple terms, the PSF smears out the signal of the true in-situ density distribution $n(\boldsymbol{r})$, and therefore the measured density distribution contains contributions from all atoms at position $\boldsymbol{r}$ whose PSF takes on a finite value at position $\boldsymbol{r}'$:

$$n_{\mathrm{meas}}(\boldsymbol{r}') = \int \mathrm{d}\boldsymbol{r} n(\boldsymbol{r}) \mathcal{P}(\boldsymbol{r}' - \boldsymbol{r}). \tag{4.19}$$

The PSF can be determined experimentally via the modulation transfer function (MTF) $\mathcal{M}(\boldsymbol{k}) = |\mathcal{P}(\boldsymbol{k})|$, which quantifies the imaging system's sensitivity at a given spatial frequency $\boldsymbol{k}$ [149]. The MTF in turn can be calculated from the Fourier transform of the density fluctuations if the static density structure factor is approximately constant in reciprocal space. The characterization of our imaging setup in terms of the PSF is presented in detail in the PhD thesis of my colleague J. Drewes [148]. The spatial extent of the Airy-disk-like PSF is quantified by the full width at half maximum, FWHM = 2.5 µm. In Figure 4.7 the PSF is sketched in the CCD pixel array of the vertical imaging camera.

The PSF of our imaging system is not only limited by diffraction [80, 148]. The vertical position of the atoms, fixed by the coils of the Ioffe-Pritchard trap, does not match the exact working distance of the aspheric lenses. As these lenses are mounted within the science chamber we can not easily move them, nor can we move the coils for the magnetic trap. Therefore, the correction of the spherical aberrations does not work as intended and the imaging resolution is slightly worse than expected.

[11] Note that the spin property is encoded in the magnetic hyperfine state.

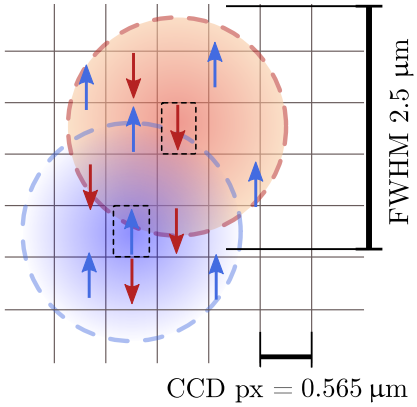

Figure 4.7: Effect of the point-spread function. For our in-situ imaging setup along the vertical direction the resolution limited spot size is larger than the lattice spacing by approximately a factor of five. Individual atoms, represented by the coloured arrows, appear as a resolution limited spot (dashed circles) in the image. This effect is shown only exemplary for both a spin-up and spin-down atom. The grid lines represent the CCD pixel array, therefore, the spins are not necessarily aligned to them. Note that the numbers shown have been scaled down by the magnification $M = 23$ to convert them into the object plane. This allows us to easily compare them to the in-plane lattice spacing, $a = 0.532$ µm.

Lattice Filling As shown in Equation 4.14, we can infer the column integrated density distribution $n(x, y)$ in units of m^{-2} from the imaging beam intensities before and after passing the cloud. In the context of optical lattices it is however more convenient to specify the density in terms of the dimensionless *filling factor*, n. Even though we do not realize a one-to-one mapping of a lattice site to a camera pixel, we can directly obtain the mean filling within the local density approximation from the mean density distribution $\overline{n(x, y)}$ by multiplying it with the area of a single lattice site

$$n = a^2 \, \overline{n(x, y)}. \tag{4.20}$$

Note that the spin property is encoded in the magnetic hyperfine state of the atom, therefore we selectively address a certain spin component when imaging the whole cloud while the imaging beam is off-resonant for the other magnetic hyperfine states. Therefore, the maximum filling (per spin state) in one layer according to the single-band approximation of the Hubbard model is equal to one. This convention will be used throughout this thesis.

4.2.3 Radio-Frequency Spectroscopy Resolving the Interaction Strength

Within the single-band approximation of the Fermi Hubbard model, a lattice site may be occupied by either a single spin-up or spin-down atom (*singles*) or by two particles with opposite spin, i.e. in different magnetic hyperfine states (*doubles*). Of course, the lattice site can also be empty. However, since empty sites do not show up in absorption imaging we can only infer their occurrence indirectly, if we have separately quantified the filling of singles and doubles.

To distinguish singly from doubly occupied sites we employ radio-frequency (RF) spectroscopy and exploit that the on-site interaction, U, shifts the energy in case two atoms in different magnetic hyperfine states occupy the same lattice site. As the on-site shift is in general not equal in the initial and final state configuration, the resonance frequency for transferring atoms

on doubly occupied sites, is shifted with respect to the bare transition frequency of the singles. In Figure 4.8 a) it is schematically shown how we distinguish the signal from singly and doubly occupied sites on the $|9\rangle \rightarrow |7\rangle$ transition. The optimum frequency to transfer singles is given by

$$\nu_S = \frac{E_7(B) - E_9(B)}{h} \tag{4.21}$$

and therefore, only depends on the total magnetic field strength, B. This can be used to extract the magnetic field at the position of the atoms with high accuracy, as demonstrated in Figure 6.14. In contrast, the resonance frequency for atoms on doubly occupied sites will be shifted according to

$$\nu_D = \nu_S + \frac{U_{57} - U_{59}}{h}. \tag{4.22}$$

The on-site interaction shift depends on the compression of the wavefunction and the combination of hyperfine states in addition to the total magnetic field, see Figure 4.2.

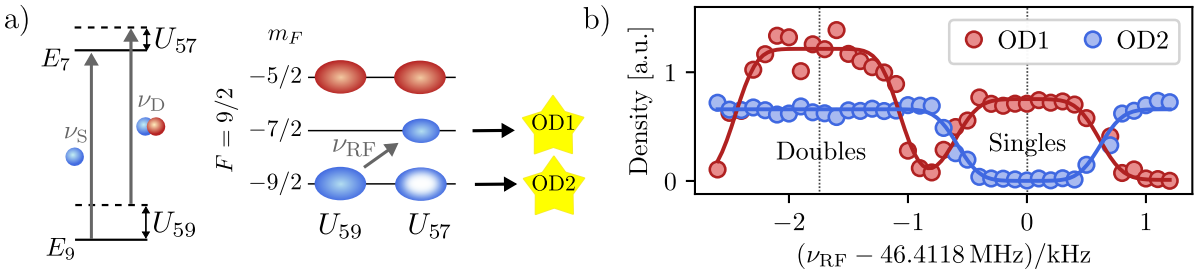

Figure 4.8: RF spectroscopy resolving the interaction strength. a) The transition frequency of the singly occupied sites, ν_S, only depends on the total magnetic field strength through the Zeeman energy of the respective magnetic hyperfine states. In contrast, if an atom is to be transferred from $|9\rangle$ to $|7\rangle$, which shares its lattice site with an atom in the other spin state $|5\rangle$, the transition frequency is shifted by the difference in on-site interaction, $\Delta U = U_{57} - U_{59}$, which is smaller than zero in our case. b) Therefore the doubles get transferred to appear in OD1 at a smaller RF centre frequency than the singles.

To obtain a stable transfer efficiency, we employ a certain pulse shape, where the frequency is swept over the resonance position to realize a Landau-Zener type transfer. This pulse is called the hyperbolic secant (HS1) and is known from nuclear magnetic resonance (NMR) spectroscopy [150].

HS1 Pulse The RF pulse is generated by applying a time-dependent voltage derived from an arbitrary waveform generator (AWG Keysight 33622A) to the RF coil. In the case of the HS1 pulse, the voltage is given by

$$V_{\mathrm{HS1}}(t) = A(t)\cos\left[2\pi\nu(t)\,t\right], \tag{4.23}$$

where the amplitude varies as

$$A(t) = A_0\,\mathrm{sech}\left[C_{\mathrm{trunc}}\left(\frac{2t}{t_{\mathrm{RF}}} - 1\right)\right] \tag{4.24}$$

and the frequency is swept according to

$$\nu(t) = \nu_{\mathrm{RF}} + \frac{\Delta_{\mathrm{RF}}}{2} \tanh\left[C_{\mathrm{trunc}}\left(\frac{2t}{t_{\mathrm{RF}}} - 1\right)\right]. \tag{4.25}$$

In Figure 4.8 b) we show an exemplary RF spectrum, with a sweep width of $\Delta_{\mathrm{RF}} = 1.3$ kHz. The transferred atoms appear in the first image, OD1, and the residuals end up in OD2. We can clearly distinguish two spectral features: If the RF pulse is resonant with the singles, we obtain a peak in OD1 and a corresponding dip in OD2. The fact that no atoms are seen in the second image indicates that atoms on doubly occupied sites are lost during the microwave transfer. The doubles peak is shifted by around 1.8 kHz to the left of the singles peak. Its appearance clearly deviates from the singles peak, as the total atom number detected in OD1 and OD2 is not constant but increases by the amount of doubles, for which one of the atoms is transferred from $|9\rangle$ to $|7\rangle$. Again, this is due to the fact that doubles can only appear in OD1 and not in OD2 because of the loss process during microwave shelving. Note that if the transfer of singles is fully efficient, the ratio of the singles density obtained in OD2 and OD1 should yield the combined efficiency of both microwave pulses.

4.2.4 Radio-Frequency Tomography of a Single Layer

To obtain a quantitative understanding of the 2D Fermi-Hubbard model, we need to avoid averaging over several layers with different local filling factors. Therefore, a crucial step prior to absorption imaging is to select an individual horizontal layer for detection. This is achieved by applying a magnetic field gradient along the z-direction with a strength of 33.3 G/cm. As the magnetic bias field is far from the Paschen-Back regime, the magnetic field gradient shifts the transition frequency between two magnetic hyperfine states according to the local field strength (Zeeman effect).

The vertical gradient is generated by the fast Feshbach coils operated in anti-Helmholtz configuration. The centre of the resulting quadrupole field is not aligned to the atom cloud, meaning that the gradient vector is not perpendicular to the individual 2D layers. Therefore to obtain a constant transfer efficiency within a layer for a given radio-frequency, we need to shift the magnetic field zero in x-direction with the offset coils of the Ioffe trap and in y-direction with a pair of elliptical coils until the magnetic field is constant within each layer respectively [60, 80].

Resolving the horizontal layers with a spacing of $a_z = 1.06\,\mu$m is extremely difficult, as the transition frequency between $|3\rangle$ and $|5\rangle$ differs only by around 640 Hz between neighbouring layers. Therefore, to obtain a stable transfer efficiency, all fluctuations in the total magnetic field should accumulate to around 50 Hz at most. The differential slope in the Breit-Rabi diagram amounts to $(\partial E_{|3\rangle} - \partial E_{|5\rangle})/\partial B = h \cdot 181\,\mathrm{Hz/mG}$. Therefore, the required magnetic field stability between different realizations is on the order of 10^{-4} G. For this purpose a μ-metal shielding is installed around the science chamber. Furthermore, the large bias field is created by the slow Feshbach coils, which feature a large inductance of 2.3 mH. Hence, they are designed to operate at large currents with a small noise level. The downside is the relatively long ramp time that is necessary to change the magnetic bias field. To further optimize the stability, there is a twofold current regulation scheme. The slow part consists of a current transducer (Danfysik STH 600), which measures the current that is output by the power supply (Delta Elektronika SM 60-100), and then converts it into a voltage which is compared to the control voltage from

the respective analogue channel. The slow feedback is, however, not enough to suppress 50 Hz noise and higher harmonics thereof. Therefore, there is an additional fast feedback loop, which consists of a second current transducer (LEM ITN 600 S) and a bandpass filter transmitting frequencies between 20 Hz and 3 kHz. The error signal is not fed back to the power supply, but to an active load element, which is connected in parallel to the main coils and which therefore controls the magnetic field strength at the position of the atoms by adjusting its resistance. The coil setup including the current stabilization was already in place when I joined the group, more information can be found in [80].

Even though the peak-to-peak amplitude of the magnetic field noise is reduced significantly by introducing the active load feedback, the signal from the current transducer still shows oscillations with a period of 20 ms [80]. We therefore synchronize the timing of the RF tomography pulse with centre frequency ν_{RF} to the 50 Hz noise of the power line just before the vertical magnetic gradient field is ramped up, see Figure 4.9 a). Upon the rising edge of the *syncline trigger*, the experimental sequence stops for a variable hold time 0...20 ms, which ends at the next rising edge of the 50 Hz noise of the power line. The tomography pulse can be shifted relative to the noise of the power line by varying the consecutive time step, t_{sync}. With this synchronization and a specifically designed RF pulse (SRS) with a fixed frequency and a time window of $t_{\mathrm{RF}} = 3\,\mathrm{ms}$, we could reduce the contributions from neighbouring planes in the RF tomography signal to less than 5% [60, 80]. However, the transfer function was too narrow and therefore, it was not possible to continuously acquire data at the highest transfer efficiency. To improve the stability of the RF tomography signal, we now use the HS1 sweep that we already successfully employed to separate the signals of singly and doubly occupied lattice sites.

HS1 Sweep for Monolayer Tomography The relevant advantage of the HS1 pulse over the previously used SRS pulse is that its frequency is not constant in time but instead it is swept over the resonance frequency of the RF transition. This greatly increases the stability and hence the average efficiency of the transfer. Another advantage of the HS1 pulse is, that its amplitude A_0 does not need careful calibration as in the case of the SRS, which induces Rabi oscillations between the two spin states. The HS1 pulse is however limited in its frequency resolution, which can in principle be improved by increasing the time window t_{RF}.

To further diminish the effect of magnetic field noise, we measure the transition frequency of the whole cloud (without the magnetic gradient) in a time-resolved manner. For this purpose we employ the SRS pulse, which offers a very good resolution both in time and frequency.[12] In Figure 4.9 b) we show how the resonance frequency changes with time. The observed shift in the centre frequency of the RF transfer corresponds to a peak-to-peak amplitude in the magnetic field strength of around 5 mG, which is approximately a factor of two larger than in [80]. We characterize the time-dependent variations of the total magnetic field in terms of 50 Hz and 150 Hz noise, as well as a linear slope γ by employing the fit function

$$\Delta\nu(t) = A_{50\mathrm{Hz}} \sin\left(2\pi \cdot 50\,\mathrm{Hz} \cdot t + \phi_{50\mathrm{Hz}}\right) + A_{150\mathrm{Hz}} \sin\left(2\pi \cdot 150\,\mathrm{Hz} \cdot t + \phi_{150\mathrm{Hz}}\right) + \gamma t. \quad (4.26)$$

We obtain the following fit results

$$A_{50\mathrm{Hz}} = 242(40)\,\mathrm{Hz}, \quad \phi_{50\mathrm{Hz}} = 3.1(2), \quad \gamma = -2.9(2.4)\,\mathrm{Hz/ms} \quad (4.27)$$

[12] In principle a Gaussian pulse with a short time window of around 3 ms should also work. However, as it was not implemented in the python script controlling the AWG, we opted for the more complicated SRS pulse.

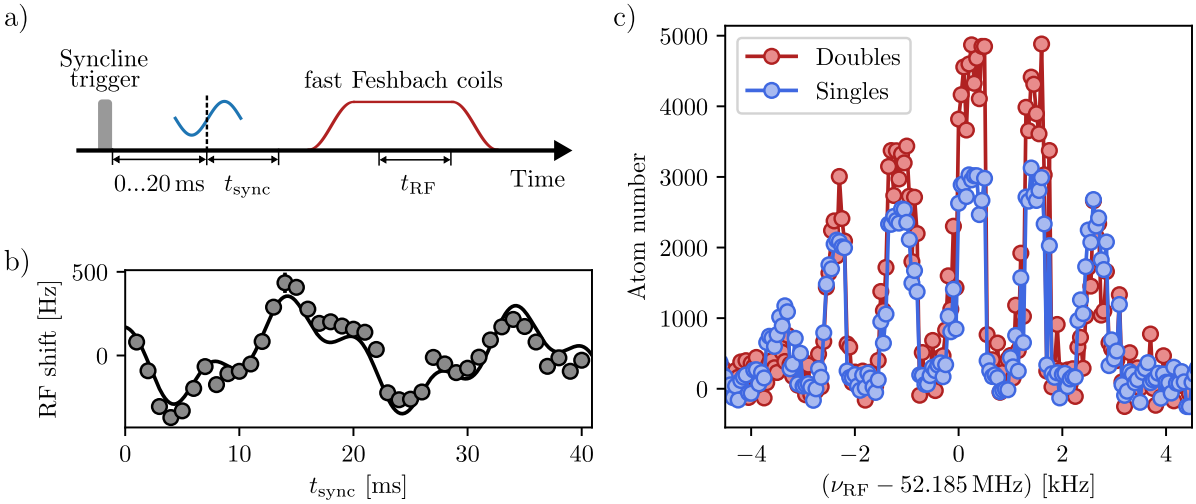

Figure 4.9: Radio-frequency tomography resolving individual horizontal layers. On the rising edge of the syncline trigger the experimental sequence stops and only resumes at the first rising edge of the 50 Hz noise obtained from the power line. This synchronizes the RF tomography pulse relative to the magnetic field noise shown in b) to avoid sudden jumps in the transfer efficiency. An RF tomography spectrum of the whole cloud is shown in c). The HS1 sweep parameters are $t_{\mathrm{RF}} = 14\,\mathrm{ms}$ and $\Delta_{\mathrm{RF}} = 500\,\mathrm{Hz}$.

$$A_{150\mathrm{Hz}} = 110(37)\,\mathrm{Hz}, \quad \phi_{150\mathrm{Hz}} = 1.0(3). \tag{4.28}$$

The linear slope γ that characterises the frequency drift is approximately zero. This is extremely important to check as otherwise the slow Feshbach coils would not be settled during the RF tomography pulse. A drift in the magnetic field would cause sudden jumps in the transfer efficiency since the resonance frequency would change between realizations due to the variable hold time that is added after the syncline trigger has been sent to the clock-interruption circuit, as shown in Figure 4.9 a). Therefore, if the slope does not vanish one has to increase the hold time after the last ramp (before the RF tomography) of the slow Feshbach coils.

We feed forward the fit result to the HS1 waveform by adding a time-dependent phase $\Delta\phi = \int 2\pi\Delta\nu(t)\mathrm{d}t$ to the fast cosine oscillation. This will effectively advance or impede the frequency of the RF sweep to counteract the drift of the magnetic field. Note that so far we have only characterized the field noise and drifts in the absence of the vertical magnetic field gradient that is generated by the fast Feshbach coils. As the quadrupole field changes the total magnetic field at the position of the atoms by only around 1.3 G, it is reasonable to assume, that noise on the fast Feshbach field current will be less problematic. However, we observe that the RF transfer efficiency in the presence of the magnetic gradient depends crucially on the sweep direction, which indicates that the magnetic field experienced by the atoms is not constant over the duration of the pulse. We vary the parameter γ, which adjusts the phase of the RF tomography pulse and find that for $\gamma = 187\,\mathrm{Hz/ms}$ the transfer looks similar for both sweep directions. As the fast Feshbach coils are not water-cooled, this drift might be a thermal effect. Fortunately, by advancing the phase of the tomography pulse correspondingly, we can compensate the field drift. It will not affect the stability of the RF transfer, as the fast Feshbach coils ramp up after the syncline trigger has been sent and therefore, the variable hold time is irrelevant in this case. After completing all the steps as described above, we record a single scan over the whole cloud, where only every second plane is filled, see Figure 4.9 c). We

observe a flat plateau which is around 350 Hz wide and steep flanks, which guarantee that even if all layers were filled, the contribution from neighbouring planes would be negligible.

For reference, I show the full RF schemes that we employ to probe the spin and density sector in Figure 4.10 a) and b), respectively.

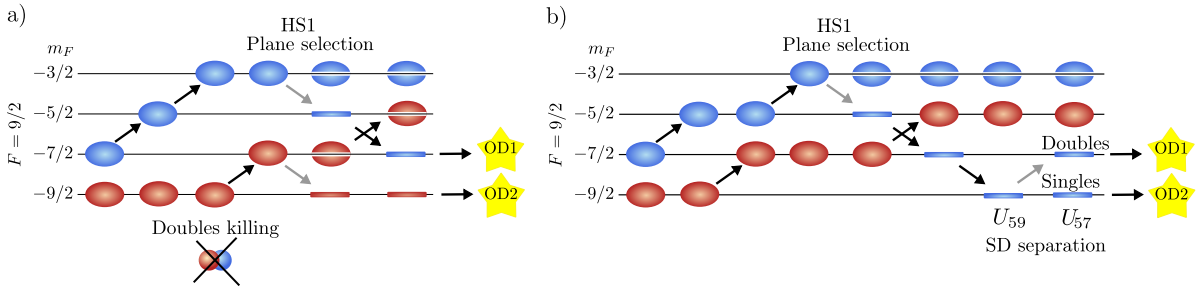

Figure 4.10: Radio-frequency manipulation for detection purposes. We employ both broad Landau-Zener sweeps (black arrows) and narrow HS1 pulses (grey arrows) to manipulate the magnetic hyperfine state of the atoms. The RF tomography pulse takes place at a magnetic bias field of around 213.8 G, where $U_{37} = U_{57}$, and hence, the transfer efficiency for both singly and doubly occupied sites is maximal at the same RF frequency. While the monolayer tomography is relevant for probing both the spin and density sector, shown in a) and b), respectively, the second HS1 sweep to distinguish the contribution from singly and doubly occupied lattice sites is applied only for measurements concerning the full density sector.

4.3 Characterization of the Lattice Potential

In the following I will describe the characterization of the optical lattice potential including both the measurement of the lattice depth as well as the determination of the underlying slowly-varying optical potential due to the Gaussian waist of the laser beams. The latter is relevant in particular when we want to measure the equation of state, which requires mapping a spatial position within a horizontal layer (x, y) to a chemical potential μ.

Lattice Depth Calibration We calibrate the lattice depth by applying a sinusoidal variation to the laser power in the respective lattice beam. This process is called parametric heating and since it preserves the discrete translation symmetry the quasimomentum is conserved[13]. Furthermore, the excitation operator is symmetric with respect to the centre of each lattice site. Therefore, transitions between bands with opposite parity are strongly suppressed. We obtain a quasimomentum resolved spectrum of the resonance by performing adiabatic band mapping after exciting from the lowest to the second excited energy band. From the resonance frequency we can directly infer the lattice depth in the centre of the cloud [60]. For more details on the procedure I refer to [60], while the spectra of the newly added lattices along the x- and z-direction are discussed in detail in [77, 137], respectively. In Section 2.3 we have seen that the full potential generated by the optical lattice beams is not characterized by the lattice depth in the centre alone. The additional, slowly-varying part of the optical lattice potential crucially depends on the beam waists.

[13] The quasimomentum conservation is slightly relaxed by the harmonic confinement, which strictly speaking breaks the discrete translation symmetry.

Beam Waist Determination In order to analyse the inhomogeneous density distribution $n(x, y)$ within a horizontal layer, we need to precisely characterize the slowly varying part of the optical lattice potential, compare Equation 2.29. We measure the trap frequencies $\omega_{x,y}$ by exciting a dipole oscillation along the x, y-direction, respectively. The oscillation is initialized by abruptly turning off an in-plane magnetic field gradient that had been ramped up in 100 ms to displace the centre of the atom cloud.[14] To observe the dipole mode we put a beam block into the setup, which blocks the retroreflection of the lattice beam. The reduced trap confinement is compensated by increasing the power of the respective lattice by a factor of four. When choosing a small enough cloud extent and excitation amplitude, the observed oscillation frequency characterizes the potential $V^{\mathrm{pot}}(x, y)$ close to the trap centre only, where it is well approximated by a second order polynomial. We investigate the impact of the cloud size on the observed oscillation frequency in order to evaluate whether the atoms are probing the harmonic confinement only. Obtaining the correct trap oscillation frequencies is crucial for the potential mapping $V^{\mathrm{pot}}(x, y) \to V^{\mathrm{pot}}(\mu)$ following the local-density approximation. If the measured trap frequency deviates by 1 Hz, the temperature estimate obtained from fitting the equation of state $n(\mu)$ will in turn change by around $0.25t/k_B$. We tune the extent of the cloud in both the x- and y-direction by varying the final power in the dimple beam when handing over to the in-plane lattices. The cloud extent depends approximately linearly on the dimple power. In Figure 4.11 we show the dependence of the trap frequency ω_x on the $1/e^2$-radius of the cloud in x-direction and find a significant dependence. For an increasing cloud size the

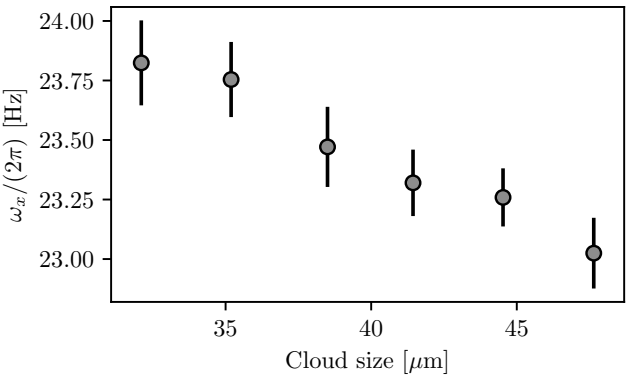

Figure 4.11: Trap frequency investigation. We determine the dependence of the inferred oscillation frequency ω_x on the extent of the atom cloud in the x-direction, which is varied by means of the final dimple confinement during the handover to the three-dimensional optical lattice configuration. The cloud size is given as the $1/e^2$-radius of the density distribution along the x-direction. The standard error on the cloud size is smaller than the marker size. The peak-to-peak oscillation amplitude for the data shown was equal to around 8.5 µm.

atoms experience a larger part of the Gaussian confining potential. This effectively reduces the inferred oscillation frequency. Therefore, we chose to work with the smallest power in the dimple beam, where we still obtain a stable atom number, resulting in a cloud size of around 33 µm. For this cloud extent we did not observe a significant dependence of the oscillation frequency on the peak-to-peak amplitude. Therefore, we stay with an oscillation amplitude of around 8 µm, where the error bars on the oscillation frequency are still reasonably small.

[14] Previously we have displaced the dimple beam to initialize the oscillation. However this scheme suffers from additionally exciting a breathing mode.

In order to calibrate the beam waists of all lattice lasers at the position of the atoms, we measure the x- and y-trap frequencies for various lattice configurations, see Figure 4.12. Note that we always specify the lattice depth in units of the respective recoil energy.

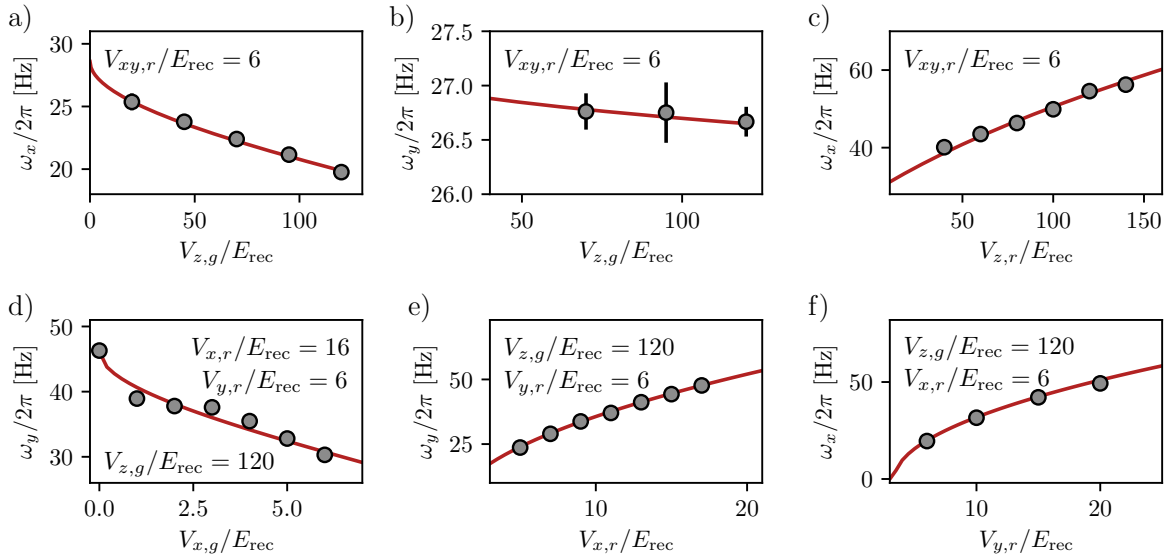

Figure 4.12: Calibration of the lattice beam waists. We measure the trap frequencies along the x- and y-directions, $\omega_{x,y}$, for different lattice configurations. While our experimental data aims at characterising the harmonic part of the slowly-varying potential only, we obtain the beam waists from a comparison to the predicted trap frequency as inferred from a second-order polynomial fit to the the centre region of the full potential given in Equations 4.32 to 4.36.

We compare the experimentally determined (harmonic) trap confinement $\omega_{x,y}$ to the curvature of the full lattice potential $V^{\mathrm{pot}}(x, y)$ close to the trap centre. The slowly-varying part of each individual lattice potential depends on the power ratio in the two (counter-propagating) beams γ, the beam waist w, the propagation direction and the lattice depth V_{latt}. The power imbalance of the interfering beams is measured with a powermeter[15] and the lattice depths are calibrated by parametrically exciting atoms to the second band as described in the previous paragraph. For an accurate determination of the propagation direction of the in-plane lattice beams we measure density correlations in time-of-flight and infer the lattice angles from the position of the antibunching dips that appear due to the Fermi statistics [60]. In the coordinate frame of the vertical camera we specify the propagation direction of the x/y-lattice as the angle $\theta_{x,y}$ relative to the x/y-axis, respectively and we obtain

$$\boldsymbol{e}_{x\text{-latt}} = \begin{pmatrix} \cos\theta_x \\ -\sin\theta_x \\ 0 \end{pmatrix}, \quad \boldsymbol{e}^{\perp}_{x\text{-latt}} = \begin{pmatrix} \sin\theta_x \\ \cos\theta_x \\ 0 \end{pmatrix}, \quad \theta_x = -5.3(3)^\circ, \tag{4.29}$$

$$\boldsymbol{e}_{y\text{-latt}} = \begin{pmatrix} \sin\theta_y \\ \cos\theta_y \\ 0 \end{pmatrix}, \quad \boldsymbol{e}^{\perp}_{y\text{-latt}} = \begin{pmatrix} \cos\theta_y \\ -\sin\theta_y \\ 0 \end{pmatrix}, \quad \theta_y = -0.9(1)^\circ. \tag{4.30}$$

[15] $\gamma_{x,r} = 0.84$, $\gamma_{y,r} = 0.77$, $\gamma_{z,g} = 1.00$, $\gamma_{z,r} = 0.33$, $\gamma_{x,g} = 0.78$

The z-lattice was set up in an angled configuration with two beams that intersect under an angle of $2\theta_z = 29.0(2)^\circ$. We specify the propagation direction for the two interfering beams and note that both orthogonal vectors $\boldsymbol{e}^{\perp}_{z\text{-latt}}$ have a contribution within the xy-plane [80]

$$\boldsymbol{e}_{z\text{-latt}} = \begin{pmatrix} 0 \\ -\cos\theta_z \\ \pm\sin\theta_z \end{pmatrix}, \quad \boldsymbol{e}^{\perp}_{z\text{-latt}} = \left[\begin{pmatrix} 0 \\ \sin\theta_z \\ \pm\cos\theta_z \end{pmatrix}, \begin{pmatrix} 1 \\ 0 \\ 0 \end{pmatrix} \right], \quad \theta_z = 14.5(1)^\circ. \tag{4.31}$$

Since we are only interested in the (anti)confinement that is created within the horizontal xy-plane, the vertical component, which is different for the two z-lattice beams is irrelevant. Combining the knowledge of the lattice beam propagation direction with the general formula for the slowly-varying lattice potential given in Equation 2.29, we obtain the optical potentials for all lattices along the x-, y- and z-direction and for both wavelengths, $\lambda_r = 1064\,\text{nm}$ and $\lambda_g = 532\,\text{nm}$,

$$V^{\text{pot}}_{x,g}(x,y) \simeq V_{x,g} R^{\text{x},g}_{-} e^{-2\left(\frac{x\sin\theta_x + y\cos\theta_x}{w_{\text{x},g}}\right)^2} + \sqrt{V_{x,g}\, E^{x,g}_{\text{rec}}}\, e^{-\left(\frac{x\sin\theta_x + y\cos\theta_x}{w_{x,g}}\right)^2}, \tag{4.32}$$

$$V^{\text{pot}}_{x,r}(x,y) \simeq V_{x,r} R^{x,r}_{+} e^{-2\left(\frac{x\sin\theta_x + y\cos\theta_x}{w_{\text{x},r}}\right)^2} + \sqrt{V_{x,r}\, E^{x,r}_{\text{rec}}}\, e^{-\left(\frac{x\sin\theta_x + y\cos\theta_x}{w_{x,r}}\right)^2}, \tag{4.33}$$

$$V^{\text{pot}}_{y,r}(x,y) \simeq V_{y,r} R^{\text{y},r}_{+} e^{-2\left(\frac{x\cos\theta_y - y\sin\theta_y}{w_{\text{y},r}}\right)^2} + \sqrt{V_{y,r}\, E^{y,r}_{\text{rec}}}\, e^{-\left(\frac{x\cos\theta_y - y\sin\theta_y}{w_{y,r}}\right)^2}, \tag{4.34}$$

$$V^{\text{pot}}_{z,g}(x,y) \simeq V_{z,g} R^{\text{z},g}_{-} e^{-2\left[\left(\frac{x}{w_{z,g}}\right)^2 + \left(\frac{y\sin\theta_z}{w_{z,g}}\right)^2\right]} + \sqrt{V_{z,g}\, E^{z,g}_{\text{rec}}}\, e^{-\left[\left(\frac{x}{w_{z,g}}\right)^2 + \left(\frac{y\sin\theta_z}{w_{z,g}}\right)^2\right]}, \tag{4.35}$$

$$V^{\text{pot}}_{z,r}(x,y) \simeq V_{z,r} R^{\text{z},r}_{+} e^{-2\left[\left(\frac{x}{w_{z,r}}\right)^2 + \left(\frac{y\sin\theta_z}{w_{z,r}}\right)^2\right]} + \sqrt{V_{z,r}\, E^{z,r}_{\text{rec}}}\, e^{-\left[\left(\frac{x}{w_{z,r}}\right)^2 + \left(\frac{y\sin\theta_z}{w_{z,r}}\right)^2\right]}. \tag{4.36}$$

Since we have independently determined the power imbalance γ, the lattice depth in the centre of the trap V_{latt} and the beam propagation direction, the only remaining parameter in the full potential is the beam waist. Hence we obtain an estimate of the beam waists at the position of the atoms by matching the theory expectation of the trap potential provided by Equations 4.32 to 4.36 to the experimentally determined oscillation frequencies. For this purpose we extract the curvature of the full lattice potential[16] that is related to the trap frequency according to $V^{\text{pot}}(x,y) = \frac{m}{2}(\omega_x^2 x^2 + \omega_y^2 y^2)$. The final result for the beam waists of the lattice lasers at the position of the atoms is

$$w_{x,r} = 170\,\mu\text{m}, \;\; w_{y,r} = 162\,\mu\text{m}, \;\; w_{z,g} = 120\,\mu\text{m}, \;\; w_{z,r} = 128\,\mu\text{m}, \;\; w_{x,g} = 137\,\mu\text{m}. \tag{4.37}$$

The simulation matches our experimental results well apart from the green x-lattice, where the deviation is significantly larger than the error bar. There are several things to check for this particular lattice including the propagation direction, which was adjusted by overlapping the forward beam with the one of the infrared x-lattice. However, I imagine the most likely deviation for the data set shown in Figure 4.12 d) to be caused by the superlattice configuration along the x-direction. In the presence of a superlattice the second term of the slowly-varying potential, which quantifies the quantum-mechanical ground state energy (compare Equation

[16] via a second-order polynomial fit close to the trap centre

2.29), does not simply follow as the sum of the individual green and infrared lattice terms, as these potentials do not separate. Instead we need to compute the ground state energy in a superlattice configuration and measure the trap frequency with a well-defined phase relation of the two lattice lasers at the position of the atoms. It is probably beneficial to measure in the symmetric double-well configuration, where the ground state energy is the same for both wells. Another option to generate confinement along the y-direction is to replace the infrared x-lattice with the horizontal dipole trap beam, which however would need to be characterized in terms of its waist and laser power beforehand.

4.4 Digital Micromirror Device

A digital micromirror device (DMD) in combination with a far-detuned laser beam allows us to manipulate the optical potential felt by the atoms in a local manner. The model that we use, a DMD DLP6500 from Texas Instruments, features more than two million micromirrors with a pitch size of 7.56 µm. These tiny mirrors can be tilted around their diagonal axis by an angle of $\pm 12^\circ$ relative to the flat state, and we refer to the "on" and "off"-configuration depending on whether the light is directed towards the atoms or not. We place the DMD in a conjugate image plane of the atoms and demagnify the displayed pattern by the same optics that is used for the vertical high-resolution in-situ imaging.

Optical Setup To achieve strong optical potentials we have upgraded the laser source from a self built grating-stabilized diode laser and a tapered amplifier to a commercial high-power laser system, a Matisse CS (Sirah) pumped by a Verdi V18. If we do not lock the Sirah to its reference cavity the linewidth is specified to be on the order of a few MHz corresponding to a coherence length of around 100 m. With a wavelength of 730 nm the DMD is the laser that is the closest to the D2 transition during the main experimental stage. While this is necessary to obtain a sizeable dipole potential, we have to keep in mind that heating will be more likely to occur. After passing the beam through an acousto-optic modulator for intensity control, the first diffraction order is coupled into an optical fibre, which guides the light to the experiment table. The optical setup starting with the fibre coupler on the experiment table is sketched in Figure 4.13. The purpose of the optical elements is briefly explained in the figure caption. For details on the alignment procedure see [137].

The magnification from the DMD to the object plane is set by the $f = 350$ mm lens and the asphere inside the science cell with $f = 8$ mm and consequently, we expect a demagnification by a factor of around $350/8 \approx 44$. To obtain a more accurate value, the magnification was measured by projecting three circles whose centres are forming an equilateral triangle onto the atom cloud. By varying the separation of the circles we extract the magnification and obtain that the DMD beam is demagnified by a factor of 45.06(12). Consequently, around three DMD pixels, with an edge length of 7.56 µm each, correspond to the lattice spacing of $a = 0.532$ µm. The pointing stability of the DMD beam quantified by the standard deviation measured over several hours is below one lattice site and also the long-term drifts are negligible over the course of a weekend.

Pattern Generation We optimize the pattern generated on the DMD using a CCD camera (Thorlabs DCC1545M), see Figure 4.13. In a first step we display three points with the DMD in order to determine the affine transformation matrix, which provides a mapping between the

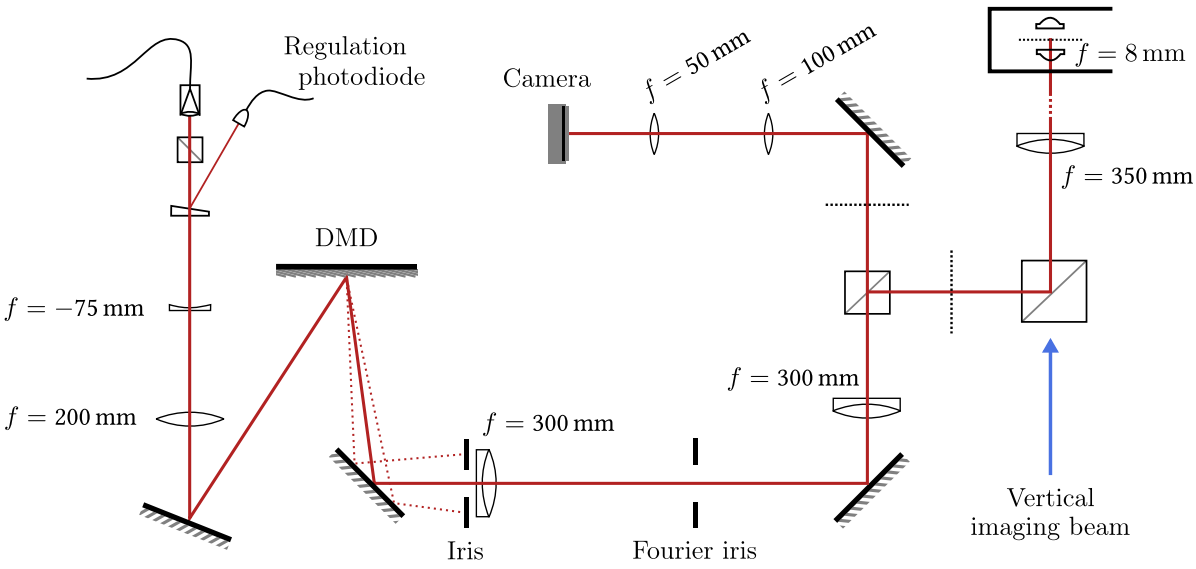

Figure 4.13: Optical setup of the DMD. On the experimental table the polarization of the laser beam is cleaned by a PBS before a small portion of the light is directed to a regulation photodiode. The beam is enlarged by a telescope to cover a large part of the DMD. We filter the light coming from the DMD by a real-space iris, which blocks unwanted diffraction orders that would lead to ghost images [137]. However, ghost images do not appear with either all mirrors on or off, so their appearance is likely connected to the digitalized pattern that is generated by the error diffusion algorithm [151]. The 4F-setup formed by two 300 mm lenses allows us to access the Fourier plane, where another iris is placed to cut off high-frequency noise components. At the first beam splitter cube half of the power is directed onto a CCD camera which is used for optimizing the DMD pattern. A neutral-density filter (not shown) is mounted between the lenses in order not to oversaturate the camera. The black dashed lines mark the (approximate) position of the different image planes. Note however that this sketch is not true to scale. At a second beam splitter cube the DMD beam is overlapped with the vertical imaging light. To be able to create small spatial structures with the DMD at the position of the atoms, the beam is demagnified by a factor of around $350/8 \approx 44$. This figure was adapted from [137].

position on the DMD to the CCD camera. Apart from the translation and the relative rotation angle, we also obtain the magnification from the resulting matrix representation. As expected, 1.37 DMD pixel correspond to one pixel of the CCD camera with a pixel size of 5.2 µm. In a second step we run an optimization loop where the deviation from the desired pattern is fed back to the displayed DMD potential. For the feedback to work properly one has to make sure that the point-spread function of a single (or few neighbouring) DMD pixel(s) is round and small. Otherwise the (local) one-to-one mapping, which does not take the point-spread function into account, will not succeed and the RMS error quantifying the deviation to the target pattern will not converge. Finally, when we have reached the desired potential shape, we need to determine the optical power in the DMD beam that is required to achieve a certain potential depth at the position of the atoms. For this purpose we display the inverted trap potential and tune the laser power. From the special point where the resulting potential seen by the atoms is flat, we obtain the scaling factor, which translates an intensity on the feedback camera to an absolute potential depth. While this in principle concludes the pattern generation, we have implemented an additional feedback loop that improves the displayed DMD potential based on the density distribution of the atoms, instead of the CCD camera.

Atom Density Feedback Optimizing the DMD potential based on the intensity distribution that is seen by the CCD camera suffers from a major drawback namely that any optical element, which is exclusively in the camera feedback path or the main DMD path going to the atoms, might distort the intensity distribution seen by the atoms relative to what is captured by the camera. Therefore we implemented a second feedback loop where we adjust the DMD pattern according to the density of doubly occupied sites, which serves as a sensitive measure of local deviations in the chemical potential μ because the slope in the corresponding equation of state, $n_D(\mu)$, is much larger than for singly occupied sites. In Figure 4.14 a) we show the doubles density summed over two neighbouring layers after the DMD pattern has been optimized based on the camera feedback only. Instead of a flat density distribution that we aimed for, we observe large aberrations.

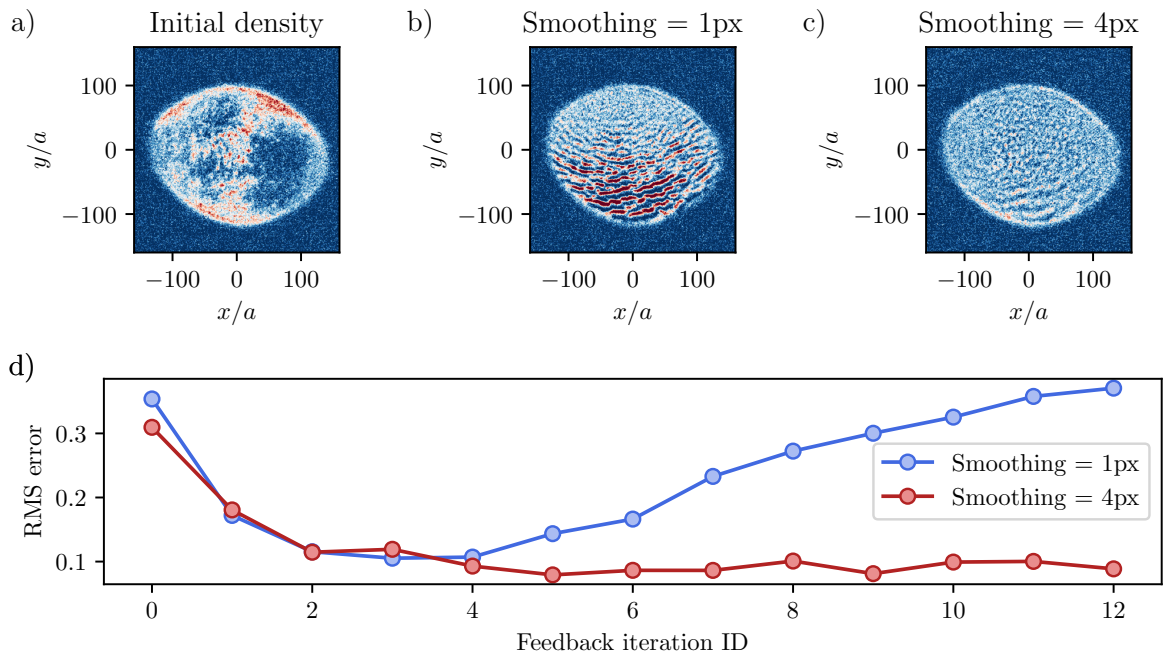

Figure 4.14: DMD atom density feedback. We optimize the intensity pattern that is displayed by the DMD in a feedback optimization loop. The error signal is given by the deviation of the doubles density averaged over 15 realizations from the intended flat distribution. With a sweep width of $\Delta_{\mathrm{RF}} = 2.5\,\mathrm{kHz}$ we obtain the combined signal of approximately two horizontal layers. a) Initially, without applying the atom density feedback, the DMD pattern distorts the density due to large-scale spatial aberrations. b) While the atom feedback clearly improves these features, it also introduces disorder in the potential landscape on a much smaller length scale. c) Applying a Gaussian filter with $\sigma = 4\,\mathrm{px}$ (Andor camera pixel) to the averaged density distribution before feeding it back, reduces the appearance and the amplitude of the small-scale structures. d) We quantify the imperfection in the observed density after each iteration by the RMS error.

For the atom feedback to work properly the affine transformation between the atom and the DMD frame needs to be calibrated carefully. What is however more difficult to achieve is a high quality local point-spread function, which should be small and round at all spatial positions over the extent of the whole cloud. Unfortunately the wavefront is not perfectly planar at the position of the atoms, which might be caused by spherical aberrations as the atoms are not in the exact working distance of the aspheric lenses mounted inside the vacuum system. This

discrepancy from the ideal alignment might be responsible for the fringe pattern appearing predominantly in the lower region of the atom cloud, see Figure 4.14 b). We can reduce the amplitude of the small-scale aberrations that are introduced by the atom density feedback by applying a low-pass filter to the observed density distribution before feeding back the error signal, see Figure 4.14 c).

Disorder The atom density feedback can only improve large-scale structures. At smaller length scales the limited accuracy in mapping the DMD to the atom frame and more importantly the size of the point-spread function preclude a correction of small-scale structures. However, we assume that the finite imaging resolution does not allow high frequency components corresponding to variations in the local chemical potential over a few lattice sites to reach the atoms. Unfortunately, we have observed that the atoms become immobile in the presence of the DMD potential [152] and we have attributed this to disorder in the DMD potential for intermediate length scales ranging from around four to nine lattice sites where neither the imaging resolution nor the atom feedback prevent the appearance of aberrations.

There are several reasons for why the DMD light is more prone to introducing disorder to the potential seen by the atoms than the optical lattice beams. Firstly, the lattice laser beams are focussed down by a single lens with the minimal waist position matched to the atom cloud. Therefore, high frequency (noise) components, which arise due to dust particles or clipping of the beam will be further away from the trap centre. This leads to intrinsic mode-cleaning [60]. However, the DMD beam path shares the high magnification of the vertical in-situ imaging setup and is therefore collimated at the position of the atoms[17]. Secondly, the normal incidence of the DMD beam relative to the surface of the glass cell might lead to interference effects from multiple reflections at the glass cell wall with a thickness of 4 mm. To investigate the relevance of interference effects on the disorder of the DMD potential one could try to broaden the linewidth of the DMD laser to around 45 GHz, where the coherence length is on the order of around 2 mm.

While we still use the DMD to slightly modify the potential or to introduce steep barriers, the intrinsic disorder precludes experiments where the atoms need to be mobile. To further improve the DMD pattern one might try to calibrate the local point-spread function of a DMD pixel at different positions of the atom cloud. Using this knowledge when calculating the error signal for the atom density feedback loop we might reduce the minimal periodicity of spatial intensity variations that can be corrected.

[17] Note that since we need to create spatially extended patterns that cover the whole cloud it is beneficial to place the DMD in the image plane and therefore the DMD beam would always be collimated at the position of the atoms even if it was not for the imaging lenses.

CHAPTER 5

Magnetic Correlations in the Two-Dimensional Fermi-Hubbard Model

Quantum magnetism in the Fermi-Hubbard model has been extensively studied for many decades, in particular the antiferromagnetic phase has been at the heart of research lately [36, 153–156]. The reasons for the continued interest are related to the conjecture by P. W. Anderson [91] that the main features of high-temperature superconductivity are captured by the two-dimensional (2D) Fermi-Hubbard model and the expected phase diagrams, which suggest that high-temperature superconductivity may occur in the regime of strong correlations close to the antiferromagnetic phase [157, 158].

In this Chapter I will explain how we quantify magnetic ordering within a single horizontal layer realizing the two-dimensional (2D) Fermi-Hubbard model. The antiferromagnetic order parameter, the staggered magnetization, is defined in quasimomentum space and peaks at the corners of the Brillouin zone, $\boldsymbol{q}_{\mathrm{AFM}} = (\pi/a, \pi/a)$. Therefore, we employ a scheme that allows for probing the magnetic structure factor at arbitrary quasimomentum $\boldsymbol{q}$, in particular at $\boldsymbol{q}_{\mathrm{AFM}}$. This scheme requires a coherent control over the relative spin orientations between neighbouring lattice sites, which is achieved by applying a magnetic field gradient within the 2D layer. By probing the magnetic correlations at several points in quasimomentum space, we overcome the resolution limit of our absorption imaging setup and are even able to quantify individual spatial spin correlators. Furthermore, the staggered magnetic structure factor serves as a sensitive thermometer and in combination with a global density thermometry it allows for the examination of thermal equilibrium. Parts of this chapter have been published in [159].

5.1 Quantifying Magnetic Order

As discussed in Section 3.2.2, the Fermi-Hubbard model features antiferromagnetic correlations when the on-site interaction U is much stronger than the tunnelling amplitude t. In this limit, the Fermi-Hubbard model maps to the Heisenberg model, which explicitly contains a spin-spin interaction between neighbouring sites, and which considers the spin-1/2 particles to be immobile

$$\hat{H}_{\mathrm{HB}} = J \sum_{\langle i,j \rangle} \hat{\boldsymbol{S}}_i \hat{\boldsymbol{S}}_j, \tag{5.1}$$

where $J = 4t^2/U$ is the superexchange energy scale.[1] This simplified model will help us to gain intuitive insights into magnetic correlations in lattice systems and their quantification.

For $J > 0$, intuitively speaking, the energy is minimized when neighbouring spins align antiparallel and therefore the (semi-)classical Néel state seems to be a sensible guess for the ground state of the Hamiltonian above. The Néel state is defined for bipartite lattices, i.e. lattice structures that may be separated into two disjoint subsystems, where a spin in subsystem A only interacts with spins of subsystem B and vice versa, and is characterized by the spins being polarized in the same direction for a given sublattice and pointing in the opposite direction for the other sublattice. Such a state is considered semi-classical as it does not build up coherence by superposition, the orientation however is quantized unlike the classical case. The Néel state can not be the ground state, as it strongly breaks the SU(2) symmetry, and furthermore it is not even an eigenstate of the Heisenberg (Hubbard) Hamiltonian. The latter can be shown by rewriting the transverse spin operators in Equation 5.1 in terms of raising and lowering operators

$$\hat{H}_{\mathrm{HB}} = J \sum_{\langle i,j \rangle} \left[\hat{S}_i^z \hat{S}_j^z + \frac{1}{2} \left(\hat{S}_i^+ \hat{S}_j^- + \hat{S}_i^- \hat{S}_j^+ \right) \right]. \tag{5.2}$$

By inducing spin flips between neighbouring lattice sites, i and j, the transverse part of the Hamiltonian couples Néel ordered basis states such as $|\uparrow,\downarrow,\uparrow,\downarrow\rangle$ to states with reduced sublattice magnetization, e.g. $|\uparrow,\uparrow,\downarrow,\downarrow\rangle$. For the double-well potential, there are only two spin-balanced basis states, $|\uparrow,\downarrow\rangle$ and $|\downarrow,\uparrow\rangle$, which are coupled by the transverse spin operators to form the spin singlet state as shown in Figure 5.1. This is the ground state with energy $E = -3/4J$, as can be verified by exact diagonalization.

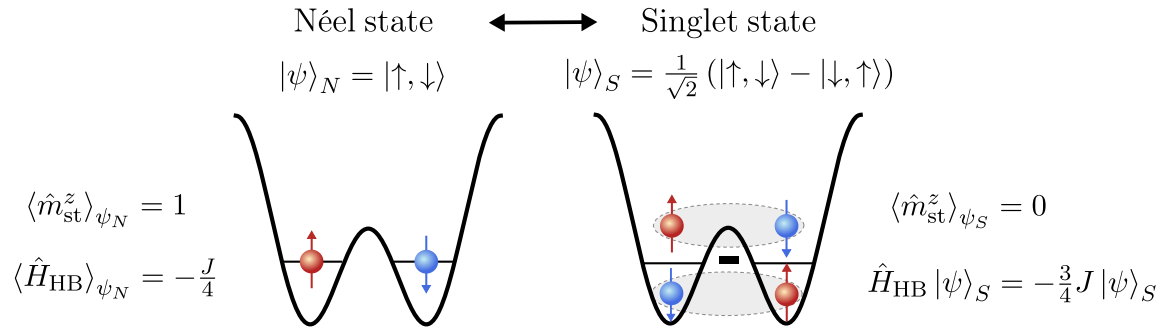

Figure 5.1: Comparison of antiferromagnetic states. The classical Néel state breaks the SU(2) symmetry and is not an eigenstate of the Heisenberg (Hubbard) Hamiltonian. For the double-well potential the expectation value of the energy is given by $(-J/4)$, which is equal to the average energy gain per bond for a larger Néel state. In contrast, the spin singlet state with a total spin of $S = 0$ is the quantum-mechanical ground state. Its energy is reduced by forming a superposition state. The staggered magnetization, $\langle \hat{m}^z_{\mathrm{st}} \rangle$, the order parameter quantifying antiferromagnetic spin alignment, is not suited to describe the magnetic correlations of the spin singlet state, as it vanishes for SU(2) symmetric states.

The quantum-mechanical ground state lowers its energy with respect to the classical Néel ordered state, with energy $(-J/4)$ per bond, by forming a superposition. This effect is often referred to as quantum fluctuations originating from the zero-point motion of spin waves [160, 161], which destroy the perfect Néel order. This is, however, not to be mistaken for a

[1] Note that we have chosen the opposite sign convention as compared to the standard Heisenberg model.

time-dependent mechanism [162]. Instead, the quantum state acquires admixtures with reduced sublattice magnetization by the transverse mixing as discussed above. For a system containing two sites only, spin-balanced basis states with reduced sublattice magnetization do not exist. They only become relevant when the number of lattice sites exceeds two. The impact of these so-called quantum fluctuations on the ground state and its magnetic order increases with the system size and ultimately they oppose long-range magnetic order (LRO). Whether they succeed in rendering LRO impossible critically depends on the lattice dimensionality under consideration and in particular on the coordination number [163].

Typically, the definition of magnetic order parameters builds on (semi-)classical states, such as the Néel state [163]. To (artificially) break the SU(2) symmetry in spin space, which both, the Hubbard and the Heisenberg model possess in the case of a spin-balanced mixture, one needs to introduce a symmetry breaking effective Zeeman field h, see Section 3.3.1. This additional term will lift the SU(2) rotational symmetry by fixing a quantization axis, typically the z-direction, along which the spins align. In the case of spontaneous symmetry breaking, the order parameter for antiferromagnetic alignment, the staggered magnetization $\hat{m}^z_{\mathrm{st}}$, is then defined in the limit of $h \to 0$

$$m^z_{\mathrm{st}} = \lim_{h\to 0} \langle \hat{m}^z_{\mathrm{st}} \rangle = \lim_{h\to 0} \frac{1}{N} \sum_{i=1}^{N} (-1)^i \frac{\hat{S}^z_i}{S}. \tag{5.3}$$

The relevance of this order parameter for our system is however marginal as spontaneous symmetry breaking does not occur in finite lattice systems [163]. Furthermore, for a spin singlet state the staggered magnetization $\langle \hat{m}^z_{\mathrm{st}} \rangle$ vanishes. Therefore one might conclude that the quantum fluctuations, which are necessary for the build-up of SU(2) symmetric superposition states, destroy the magnetic order completely [160]. However, the spin singlet state is in fact strongly correlated in spin space, and therefore a more suitable definition that does not rely on a preferred orientation in spin space needs to be found for spin systems possessing SU(2) symmetry. A common choice is given by [38, 163]

$$\bar{m}_{\mathrm{st}} = \sqrt{\langle (\hat{m}^x_{\mathrm{st}})^2 + (\hat{m}^y_{\mathrm{st}})^2 + (\hat{m}^z_{\mathrm{st}})^2 \rangle} = \sqrt{3 \langle (\hat{m}^z_{\mathrm{st}})^2 \rangle}, \tag{5.4}$$

where the second equality sign requires the state to be SU(2) symmetric. With our experimental quantum simulator we are not able to resolve the occupation of a single lattice site. Therefore, it is not possible to directly measured the staggered magnetization as done in [38]. However, as will be shown in Section 5.3.1, we can measure the magnetic structure factor

$$S^z_{\boldsymbol{q}} = \frac{1}{N} \sum_{i,j=1}^{N} \langle \hat{S}^z_i \hat{S}^z_j \rangle \, e^{i\boldsymbol{q}(\boldsymbol{r}_i - \boldsymbol{r}_j)} = \sum_{j=1}^{N} \langle \hat{S}^z_i \hat{S}^z_j \rangle \, e^{i\boldsymbol{q}(\boldsymbol{r}_i - \boldsymbol{r}_j)} \tag{5.5}$$

at arbitrary quasimomentum $\boldsymbol{q}$. The last equality follows from the discrete translation symmetry in a homogeneous system according to which, it is irrelevant which lattice site, i, is correlated with all other lattice sites j. The staggered magnetic structure factor $S^z_{\boldsymbol{q}_{\mathrm{AFM}}}$ is connected to the antiferromagnetic order parameter via

$$\langle (\hat{m}^z_{\mathrm{st}})^2 \rangle = \frac{1}{N} \frac{S^z_{\boldsymbol{q}_{\mathrm{AFM}}}}{S^2}, \tag{5.6}$$

where the quasimomentum $\boldsymbol{q}_{\mathrm{AFM}} = (\pi/a, \pi/a)$ takes care of the staggered sign $(-1)^i$.

5.2 Quantifying Antiferromagnetic Order with a Finite Resolution

In Section 4.2.2 I have already discussed the finite resolution of our in-situ imaging setup, which precludes us from directly measuring real-space spin correlators defined as

$$C_{ij}^z = \langle \hat{S}_i^z \hat{S}_j^z \rangle - \langle \hat{S}_i^z \rangle \langle \hat{S}_j^z \rangle . \tag{5.7}$$

For a spin-balanced system the expectation value of the z-component of the local spin operator $\langle \hat{S}_j^z \rangle$ vanishes for all sites j. Hence, as expected for an SU(2) symmetric state, there is no net magnetic moment and the second term of C_{ij}^z vanishes. In contrast, magnetic ordering in classical spin systems features localized moments as for example in the Néel state [164] discussed above. The second term is needed in order to only account for proper quantum correlations, since it subtracts an offset such that for a classical state the correlator amounts to $C_{ij} = 0$. In the following I will first discuss the observables quantifying magnetic correlations, which are readily accessible by our spin-resolved imaging technique, i.e. the local moment and the uniform spin structure factor. Then I will explain how to circumvent our limited imaging resolution by probing magnetic order in quasimomentum space, which in particular allows us to measure the staggered magnetic structure factor that is related to the antiferromagnetic order parameter as shown above.

5.2.1 Local Moment

The local moment represents the on-site contribution to the spatial spin correlations C_{ij} and is defined as

$$C_{00} = \frac{1}{N} \sum_{i=1}^{N} C_{ii}^z \equiv C_{ii}^z. \tag{5.8}$$

In a homogeneous system the on-site correlator C_{ii}^z is equal for all sites i. Under the assumption of the single-band approximation, the average particle number on a certain lattice site i in spin state σ is given by

$$n_{i,\sigma} = \langle \hat{n}_{i,\sigma} \rangle = \langle \hat{c}_{i,\sigma}^\dagger \hat{c}_{i,\sigma} \rangle . \tag{5.9}$$

As a consequence of the commutation relations of fermionic creation and annihilation operators, we can apply the occupation number operator several times without changing the result

$$\langle \hat{n}_{i,\sigma}^2 \rangle = \langle \hat{c}_{i,\sigma}^\dagger \underbrace{\hat{c}_{i,\sigma} \hat{c}_{i,\sigma}^\dagger}_{=1-\hat{c}_{i,\sigma}^\dagger \hat{c}_{i,\sigma}} \hat{c}_{i,\sigma} \rangle = \langle \hat{n}_{i,\sigma} \rangle . \tag{5.10}$$

This is intuitively clear, as a lattice site is occupied by at most one particle of a certain spin state due to Pauli's exclusion principle. As a consequence, we may rewrite the local moment in terms of the densities of both spin components

$$C_{00} = \frac{1}{4} \left[\langle \hat{n}_{i,\uparrow} \rangle - \langle \hat{n}_{i,\uparrow} \hat{n}_{i,\downarrow} \rangle + \langle \hat{n}_{i,\downarrow} \rangle - \langle \hat{n}_{i,\uparrow} \hat{n}_{i,\downarrow} \rangle - \big(\langle \hat{n}_{i,\uparrow} \rangle - \langle \hat{n}_{i,\downarrow} \rangle \big)^2 \right] \tag{5.11}$$

$$= \frac{1}{4}\left[s_{i,\uparrow} + s_{i,\downarrow} - \left(\langle \hat{n}_{i,\uparrow}\rangle - \langle \hat{n}_{i,\downarrow}\rangle\right)^2\right], \tag{5.12}$$

where the singles density of spin-up (-down) particles, $s_{i,\sigma}$, is defined as in Equation 3.48. For a spin balanced cloud $\langle \hat{n}_{i,\uparrow}\rangle = \langle \hat{n}_{i,\uparrow}\rangle$ the equation above simplifies to

$$C_{00} = \frac{1}{4}\left(s_{i,\uparrow} + s_{i,\downarrow}\right). \tag{5.13}$$

Therefore, the local moment is a direct measure for the amount of single occupancies, which was to be expected since doubly occupied and empty sites do not contribute to the magnetization of the system as

$$\langle \uparrow\downarrow | \hat{S}^z | \uparrow\downarrow \rangle = \langle 0 | \hat{S}^z | 0 \rangle = 0. \tag{5.14}$$

5.2.2 Uniform Spin Structure Factor

When we acquire the absorption images of both spin components, the signal of an individual atom is smeared out over several pixels by the point-spread-function (PSF), $\mathcal{P}(\boldsymbol{r} - \boldsymbol{r}_i)$, as explained in Section 4.2.2. Therefore, we cannot directly infer the spatial spin correlator C^z_{ij} for arbitrary sites i and j, apart from the special case, $i = j$, which is discussed above. It is however possible to correlate the local density measured by two pixels labelled by the indices k and l,

$$\tilde{C}_{kl} = \langle n(\boldsymbol{r}_k) n(\boldsymbol{r}_l)\rangle = \sum_{i,j} \mathcal{P}(\boldsymbol{r}_k - \boldsymbol{r}_i)\mathcal{P}(\boldsymbol{r}_l - \boldsymbol{r}_j)\,\langle \hat{S}^z_i \hat{S}^z_j\rangle\,, \tag{5.15}$$

which contains contributions from all lattice sites, i and j, whose signal is smeared out by the PSF to the pixels k and l, respectively. The PSF in units of $1/\mathrm{m}^2$ is normalized in real space according to

$$\int \mathcal{P}(\boldsymbol{r} - \boldsymbol{r}_i)\mathrm{d}^2\boldsymbol{r} = 1. \tag{5.16}$$

The discrete version of this normalization condition depends on whether the summation runs over lattice sites or camera pixels and we find that

$$a^2 \sum_j \mathcal{P}(\boldsymbol{r}_j - \boldsymbol{r}_i) = 1 = a^2_{\mathrm{px}} \sum_k \mathcal{P}(\boldsymbol{r}_k - \boldsymbol{r}_i). \tag{5.17}$$

The so-called *summed correlations* correlate each individual pixel l with all other pixels k

$$\sum_{k,l} \tilde{C}_{kl} = \sum_{i,j} C_{ij} \underbrace{\sum_k \mathcal{P}(\boldsymbol{r}_k - \boldsymbol{r}_i)}_{1/a^2_{\mathrm{px}}} \underbrace{\sum_l \mathcal{P}(\boldsymbol{r}_l - \boldsymbol{r}_j)}_{1/a^2_{\mathrm{px}}} = \frac{1}{a^4_{\mathrm{px}}} \sum_{i,j} \langle \hat{S}^z_i \hat{S}^z_j\rangle = \frac{1}{a^4_{\mathrm{px}}} \sum_{i,j} C_{ij}. \tag{5.18}$$

In pixel space we correlate the optical densities and not the dimensionless filling, therefore the additional factor $1/a^4_{\mathrm{px}}$ adjusts the units by converting the optical density into a filling factor per pixel. In the last step we need to account for the size mismatch of a lattice site to a camera pixel by comparing the number of pixels N_{px} to the number of lattice sites N_{sites} that cover a

certain area with fixed size

$$N_{\mathrm{px}} \sum_{l} \tilde{C}_{kl} = \sum_{k,l} \tilde{C}_{kl} = \frac{1}{a_{\mathrm{px}}^4} \sum_{i,j} C_{ij} = N_{\mathrm{sites}} \frac{1}{a_{\mathrm{px}}^4} \sum_{j} C_{ij} \tag{5.19}$$

$$\Rightarrow S_{q=0} = \sum_{j} C_{ij} = a_{\mathrm{px}}^4 \frac{N_{\mathrm{px}}}{N_{\mathrm{sites}}} \sum_{l} \tilde{C}_{kl} = a_{\mathrm{px}}^4 \frac{a^2}{a_{\mathrm{px}}^2} \sum_{l} \tilde{C}_{kl} = a_{\mathrm{px}}^2 a^2 \sum_{l} \tilde{C}_{kl}. \tag{5.20}$$

Here, we he have used that the number of pixels (lattice sites) scales inversely with the size of the respective unit cell. The consequences of this calculation are immense, as it means that we can obtain the uniform spin structure factor even with reduced imaging resolution by performing the correlation analysis in the pixel frame and applying a correction factor $a_{\mathrm{px}}^2 a^2$. The lattice spacing, a, is a well known quantity as we have access to the exact wavelength of the lattice laser. However, the size of a pixel needs rescaling into the object plane, hence the magnification has to be well calibrated. Furthermore, the calculation above implies that the exact shape of the point-spread function does not need to be known. This is however only the case if we sum over a region much larger than the extent of the point-spread function. To reduce the impact of numerical noise from the integration, we typically correlate only pixels whose distance is smaller than the equivalent of seven lattice sites. As the summed correlations depend on the radius of the summation region, the optimal summation point is chosen such that the spin structure factor of an uncorrelated system is equal to the local moment as inferred from the singles density directly. In addition, before running the experiment it is important to optimize the position of the camera along the imaging beam propagation direction, as it affects both the imaging resolution and the magnification. Also, we have observed that the inferred spin correlations greatly deviate if the camera is not in its focus position. For more details on the extraction of the summed spin correlations, I refer the reader to [37, 148].

Results We have measured spin correlations for a spin-balanced cloud in the slowly varying trap potential that is formed due to the Gaussian confinement of the lattice beams. This allows us to sample a broad range of chemical potentials in a single realization. After the green z-lattice has reached its final depth of $120E_{\mathrm{rec}}$, which separates the cloud into two-dimensional pancakes, both in-plane lattices are ramped up to $6E_{\mathrm{rec}}$ within 500 ms to realize the 2D Fermi-Hubbard model with $t/h = 224(6)$ Hz. The on-site interaction between the lowest two hyperfine states $|9\rangle$ and $|7\rangle$ is adjusted to $U/t = 8$, where we expect the antiferromagnetic correlations to be the most prominent. The results are shown in Figure 5.2. The maximum value of the local moment C_{00}, defined in Equation 5.13, is 0.25, as the overall probability to obtain a single occupancy on a lattice site, $s_{i,\uparrow} + s_{i,\downarrow}$, can not exceed unity. Due to the finite interaction strength U/t, there will always be a finite amount of doubles and holes in the lattice even at half-filling. Therefore, the local moment does not reach 0.25. The uniform structure factor contains both on-site and off-site magnetic correlations and is smaller than the local moment owing to the presence of negative nearest-neighbour correlations. While this clearly shows that antiferromagnetic order emerges in our system, the uniform structure factor alone does not yield quantitative information about the correlation length scale and individual spatial spin correlators. Furthermore, with decreasing temperature the amount of off-site correlations will increase and since the individual spin correlators alternate in sign with distance, they partially cancel each other. Therefore, in the zero-temperature limit the uniform structure factor approaches zero [165] and does not serve as a precise thermometer.

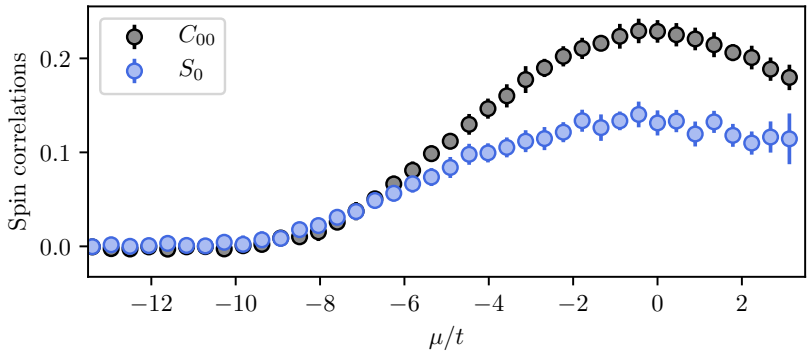

Figure 5.2: Uniform spin structure factor and local moment. Due to the presence of off-site antiferromagnetic correlations, the uniform structure factor is reduced with respect to the local moment, which only quantifies the on-site contribution. The difference is most pronounced around half-filling, $\mu = 0$. The chemical potential is inferred in a local density approximation (LDA) from the precisely calibrated trapping potential [34], compare Section 4.3. These results have been published in [159].

5.3 Coherent Manipulation of Spin Correlations

In the last section we have seen that the autocorrelation analysis of the magnetization does not provide a full characterization of the magnetic order in our system, as we only obtain the integral over the real-space correlation function convolved with the imaging point-spread function. To overcome our optical resolution limit we developed an experimental protocol, which coherently manipulates the spatial spin correlations by imprinting a periodic phase pattern with wavevector $\boldsymbol{k}_{\mathrm{sp}}$ onto the atoms within the two-dimensional layers. This allows us to probe magnetic correlations in quasimomentum space and the observable is the static spin structure factor at arbitrary momentum $\boldsymbol{q} = \boldsymbol{k}_{\mathrm{sp}}$,[2]

$$S^z_{\boldsymbol{q}} = \sum_j \langle \hat{S}^z_i \hat{S}^z_j \rangle \, e^{i\boldsymbol{q}\Delta\boldsymbol{r}_{ij}}. \tag{5.21}$$

In particular this scheme enables us to measure the staggered magnetic structure factor, $S^z_{\pi,\pi}$[3], which is related to the order parameter of the antiferromagnet, see Equation 5.6. Via a discrete Fourier transform we can exploit our precise calibration of the imprinted wavevector to overcome our optical resolution limit and extract information on individual real-space spin correlators.

The following sections summarize the experimental findings published in [159] and add further explanations and discussions. Both the calibration routines and the theoretical description of the coherent manipulation of spin correlations have been developed during my master thesis, therefore more details on these parts can be found in [166].

5.3.1 Theoretical Description of the Coherent Manipulation of Spin Correlations

Probing the uniform structure factor is not ideally suited to characterize antiferromagnetic order, as the real-space spin correlators partially cancel each other. In simple terms, it would be better if we were able to flip the spin on every other lattice site. Effectively, this would

[2] Note that the lattice site index i is arbitrary for a homogeneous system.
[3] For simplicity, we will replace the quasimomentum subscript by the imprinted phase per lattice site $\boldsymbol{q}a$.

transform a chequerboard spin pattern (Néel antiferromagnet) into a spin-polarized state. Consequently, when computing the summed correlations, all off-site correlators would have the same sign and would therefore add up constructively. In the following, I will start by giving a physical intuition about how to manipulate the (relative) orientation of spins in a semi-classical picture. Then, I will explain how the presented scheme acts on the double-well eigenstates and how spin correlations are transformed in a general setting.

Classical Picture In Figure 5.3 the main steps for the manipulation of the spin orientation are depicted. After the atoms have distributed themselves according to the Hubbard parameters, t and U, we freeze the motion within the layers by quickly ramping up the in-plane lattice depths from 6 to $60E_{\mathrm{rec}}$ within 1 ms. Now, the only thing left to manipulate is the internal state of the atoms.

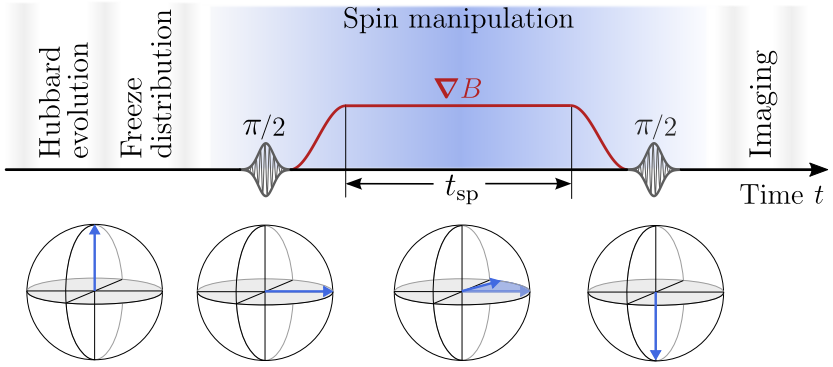

Figure 5.3: Manipulation of the relative spin orientation. Experimental scheme to imprint spatially periodic spin patterns onto fermionic spin-1/2 atoms loaded into an optical lattice potential realizing the 2D Fermi-Hubbard Hamiltonian. After freezing the atomic motion, a Ramsey-type sequence is applied, which is composed of two $\pi/2$ RF pulses enclosing the evolution in a magnetic field gradient ∇B_z for a variable time t_{sp}. The same scheme is employed to probe the static magnetic structure factor at arbitrary quasimomentum. This figure was adapted from [159].

The initial $\pi/2$-pulse rotates the spin vector into the equatorial plane of the Bloch sphere, where it will precess according to the local Larmor frequency, which is proportional to the energy difference of the two spins states $|\uparrow\rangle = |7\rangle$ and $|\downarrow\rangle = |9\rangle$. Therefore, in a magnetic field gradient atoms occupying sites i and j will pick up a relative phase that is given by

$$\phi_{ij} = 2\pi\gamma_{\uparrow,\downarrow} \int \nabla B_z \cdot (\boldsymbol{r}_i - \boldsymbol{r}_j)\mathrm{d}t, \quad \gamma_{\uparrow,\downarrow} = \frac{1}{h}\frac{\partial E_7 - \partial E_9}{\partial B_z}. \tag{5.22}$$

The relative phase between neighbouring sites can be tuned either by the magnetic gradient strength or the duration t_{sp}. For a relative phase of $\phi_{ij} = \pi$, antiparallel spins on lattice sites i and j will change their relative orientation to parallel. If we let them precess for twice as long, the imprinted phase difference will amount to $\phi_{ij} = 2\pi$ and consequently the relative orientation will match the initial configuration. In the last step, we flip back the spin vectors into the measurement (z-)basis by applying a second $\pi/2$-pulse.

Quantum Mechanical Description So far we have neglected that atoms are quantum-mechanical objects and hence will form superposition states to conform to the SU(2) symmetry of the

Hubbard Hamiltonian. While the main principle of operation of the spin manipulation scheme depicted in Figure 5.3 stays the same, there are some peculiarities and I will therefore discuss the impact on the eigenstates of the double-well in the following. For more details, I kindly refer to [166].

When we freeze the motion by quickly ramping up the power in the in-plane lattices, in the quantum-mechanical description we project on the eigenstates of the Hubbard Hamiltonian for $U/t \to \infty$, see Table 3.1. It is unnecessary to consider the $|d_+\rangle$ and $|d_-\rangle$ states, as doubly occupied sites are neither affected by the $\pi/2$-pulses nor by the evolution in the magnetic field gradient. Furthermore, in the experiment we remove all doubles after freezing as they do not contribute to magnetic correlations. Without loss of generality, I choose the x-axis of the Bloch

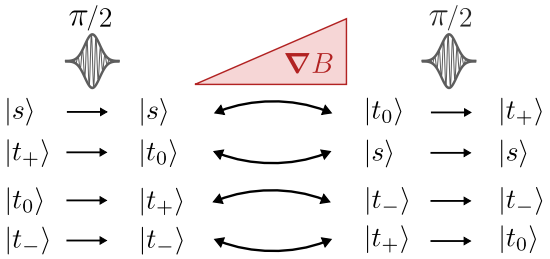

Figure 5.4: Spin manipulation on the double-well. Evolution of the double-well eigenstates for $U/t \to \infty$. The magnetic field gradient breaks the SU(2) symmetry by inducing singlet-triplet oscillations between $|s\rangle$ and $|t_0\rangle$. The oscillation between the $|t_+\rangle$ and $|t_-\rangle$ states occurs at a considerably higher frequency. However, it does not play a role as the number of triplet states has to be equal in the beginning, in order to conform to SU(2) symmetry.

sphere as the rotation axis of both $\pi/2$-pulses and I will explain in the following that it is irrelevant around which axis we rotate due to the SU(2) spin symmetry. If we investigate the effect of the initial $\pi/2$-pulse on the double-well eigenstates, we observe that the singlet state $|s\rangle$ and the triplet state $|t_-\rangle = 1/\sqrt{2}\,(|\uparrow,\uparrow\rangle - |\downarrow,\downarrow\rangle)$ remain unchanged, while the former was to be expected since the singlet state is SU(2)-symmetric, the latter is linked to the choice of the rotation axis[4]. In contrast, the population of $|t_0\rangle$ is mapped onto $|t_+\rangle = 1/\sqrt{2}\,(|\uparrow,\uparrow\rangle + |\downarrow,\downarrow\rangle)$ and vice versa. In the magnetic field gradient the SU(2) spin symmetry is broken as the singlet and triplet populations periodically exchange $|s\rangle \leftrightarrow |t_0\rangle$. If the relative phase between the two sites of the double-well is $\phi_{12} = \pi$, the singlet is fully mapped onto the triplet state. A similar oscillation occurs between the other two triplet states $|t_+\rangle$ and $|t_-\rangle$, however, at much higher frequency. We can not observe this oscillation in a spin-balanced system, since the occupation of all the triplet states is equal for an SU(2) symmetric initial state. Therefore the occupation probabilities of $|t_+\rangle$ and $|t_-\rangle$ will remain constant. As the evolution in the magnetic gradient is described by a Larmor precession around the z-direction on the Bloch sphere, only the x- and y-components of the spin operator have rotated. Therefore, the remaining task is to map the time-evolved spins back into the measurement basis with the second $\pi/2$-pulse. Atoms that were in a singlet configuration initially, end up in the spin-polarized triplet state $|t_+\rangle$. Note that in contrast to the classical case described above the rotation axis of both $\pi/2$-pulses is irrelevant for this measurement as we will always obtain a spin polarized state with some (irrelevant) phase between $|\uparrow\uparrow\rangle$ and $|\downarrow\downarrow\rangle$, if atoms are in the triplet state $|t_0\rangle$ at the end of the singlet-triplet oscillations in the magnetic field gradient.

[4] If we chose the rotation axis to be parallel to the y-axis, the roles of $|t_+\rangle$ and $|t_-\rangle$ would be interchanged.

For a larger system size, the time evolution is better understood in the Heisenberg picture, as all the operators (spin rotations) factorize for the different lattice sites. First, we assume that our initial state is SU(2) symmetric and hence [166]

$$\left\langle \hat{S}_i^x \hat{S}_j^x \right\rangle (0) = \left\langle \hat{S}_i^y \hat{S}_j^y \right\rangle (0) = \left\langle \hat{S}_i^z \hat{S}_j^z \right\rangle (0) =: \left\langle \hat{S}_i^0 \hat{S}_j^0 \right\rangle . \tag{5.23}$$

In this case, the initial $\pi/2$-pulse has no effect since the Hubbard Hamiltonian commutes with the total spin operators $\sum_i \hat{S}_i^{x,y,z}$ and therefore any eigenstate is fully invariant under rotations in spin space [167]. We can visualize this on the Bloch sphere. Since the spin correlations are isotropic on the Bloch sphere before applying the $\pi/2$-pulse, a rotation will not change the amount of spin correlations in any direction. In the experiment we check whether initially the state conforms to the SU(2) symmetry by measuring spin correlations both with the first $\pi/2$-pulse on and off.

The time evolution of the local spin operator $\hat{\boldsymbol{S}}_i$ can be considered as a precession around the magnetic field direction with a locally varying Larmor frequency ω_i,

$$\begin{pmatrix} \hat{S}_i^x \\ \hat{S}_i^y \\ \hat{S}_i^z \end{pmatrix} (t) = \begin{pmatrix} \cos(\omega_i t) & \sin(\omega_i t) & 0 \\ -\sin(\omega_i t) & \cos(\omega_i t) & 0 \\ 0 & 0 & 1 \end{pmatrix} \begin{pmatrix} \hat{S}_i^x \\ \hat{S}_i^y \\ \hat{S}_i^z \end{pmatrix} (0), \tag{5.24}$$

where $\omega_i = (E_7 - E_9)/\hbar$. The differential precession breaks the SU(2) spin symmetry as mentioned before. This becomes clear, when looking at the time evolution of the spin correlators

$$\left\langle \hat{S}_i^x \hat{S}_j^x \right\rangle (t) = \cos\left[\left(\omega_i - \omega_j\right) t\right] \left\langle \hat{S}_i^0 \hat{S}_j^0 \right\rangle = \left\langle \hat{S}_i^y \hat{S}_j^y \right\rangle (t), \tag{5.25}$$

$$\left\langle \hat{S}_i^z \hat{S}_j^z \right\rangle (t) = \left\langle \hat{S}_i^0 \hat{S}_j^0 \right\rangle . \tag{5.26}$$

While the longitudinal spin correlations are left unchanged, the x- and y- correlators oscillate in time and for $\phi_{ij} = \left(\omega_i - \omega_j\right) t = \pi$, we recover the classical result, where the respective spin correlator C_{ij} flips its sign. Note that for $\phi_{ij} = \pi/2$ the transverse spin correlations seem to vanish, they are however rotated into the cross-correlators $\langle \hat{S}_i^x \hat{S}_j^y \rangle (t)$, which were zero in the initial state. Furthermore, it becomes clear, why the rotation axis of the second $\pi/2$-pulse is irrelevant. As the transverse correlators oscillate in phase, they are always equal and therefore, the RF pulse will always map back the full time-evolved spin correlations into the measurement z-basis. When computing the autocorrelation of the magnetization after applying the spin manipulation scheme, we therefore measure the static magnetic structure factor

$$\sum_j \cos\left[\left(\omega_i - \omega_j\right) t\right] \left\langle \hat{S}_i^0 \hat{S}_j^0 \right\rangle = \sum_j e^{i\boldsymbol{q}\left(\boldsymbol{r}_i - \boldsymbol{r}_j\right)} \left\langle \hat{S}_i^0 \hat{S}_j^0 \right\rangle = S_{\boldsymbol{q}} \tag{5.27}$$

at arbitrary momentum $\boldsymbol{q} = 2\pi\gamma_{\uparrow,\downarrow} \int \nabla_{xy} B_z \mathrm{d}t$. Since the spatial spin correlator only depends on the distance of the two lattice sites i and j, we find that in particular $\langle \hat{S}_i^z \hat{S}_j^z \rangle = \langle \hat{S}_j^z \hat{S}_i^z \rangle$. Consequently the structure factor is purely real and we may replace the cosine with the exponential in the equation above.

5.3.2 Calibration Routine: Imprinting Spin Patterns

The calibration routine for imprinting spin patterns onto the atom cloud starts with the two $\pi/2$-pulses. The envelope of the RF pulses in the time domain is described by a Gaussian with a full width at half maximum of 50 µs. This corresponds to a transfer function that is 20 kHz wide. Since the RF frequency is not swept but stays constant for the duration of the pulse, it is important to regularly check that the RF pulse is operating on resonance. In particular, the resonance frequency of the second pulse should not depend on the time t_{sp} during which the spins evolve in the magnetic field gradient. Otherwise the total magnetic field needs more settling time before starting the spin manipulation scheme. Once the frequency is adjusted, the amplitudes of both $\pi/2$-pulses are calibrated consecutively. Starting with a spin-polarized cloud the optimum amplitude is found when the final atom numbers after applying the RF pulse are equal. Note that the atom number recorded in OD2 must be corrected by the MW efficiency to account for relative detection losses between the two spin components $N_{\uparrow}$ and $N_{\downarrow}$. In Figure 5.5, we show the relative atom number of both spin components to account for fluctuations in the total atom number. We fit both curves with a sinusoidal function to obtain the crossing point, which yields the correct amplitude for a $\pi/2$-pulse.

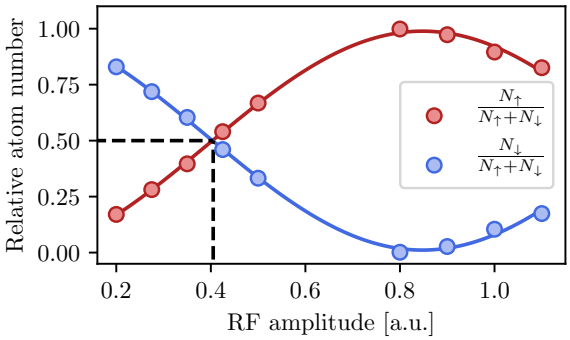

Figure 5.5: Amplitude calibration of the $\pi/2$-pulses. From a sinusoidal fit to the relative atom numbers, we extract the crossing point indicated by the black dashed lines. For this particular RF amplitude we obtain a balanced spin mixture after applying the pulse and hence we have found the $\pi/2$-pulse amplitude.

The differential precession on the Bloch sphere between neighbouring sites is achieved by applying an in-plane magnetic field gradient that is generated by two small coils. At the position of the atoms, they produce a gradient that is pointing approximately along either of the two diagonals within the xy-plane, respectively. Originally, they were implemented to compensate small residual magnetic field gradients and are therefore not water-cooled. Hence, care has to be taken that the applied currents are small enough. In order to calibrate both the amplitude and the angle of the imprinted wavevector we start with a spin-polarized cloud. Since we do not want to apply the monolayer RF tomography scheme, we need to compensate the residual vertical magnetic field gradient. This is described in detail in my Master thesis [166]. As far as we know, this vertical gradient is mostly caused by the slow Feshbach coils, however the two small gradients coils also have a small out-of-plane component. Therefore, the vertical gradient should be compensated for the final currents through the in-plane gradient coils. With the vertical gradient compensated, we can vary the time t_{sp} and observe the change in the periodicity of the imprinted spin spiral pattern, see Figure 5.6 a)-c). Note that it is extremely

relevant to check that the two gradient coils ramp up (and down) equally fast. Otherwise the direction of the total imprinted wavevector, which is proportional to $\int \nabla B_z(t)\mathrm{d}t$, changes as a function of hold time and it would not be possible to measure along the diagonal of the first Brillouin zone without readjusting the currents of the gradient coils [166]. We set the ramp time to 20 ms to solve this problem.

In Figure 5.6 we show typical images of the observed contrast in the singles densities,

$$M(x,y) = \frac{s_\uparrow(x,y) - s_\downarrow(x,y)}{s_\uparrow(x,y) + s_\downarrow(x,y)} \tag{5.28}$$

for different wavevector amplitudes. Owing to the discrete nature of the lattice, the wavevector

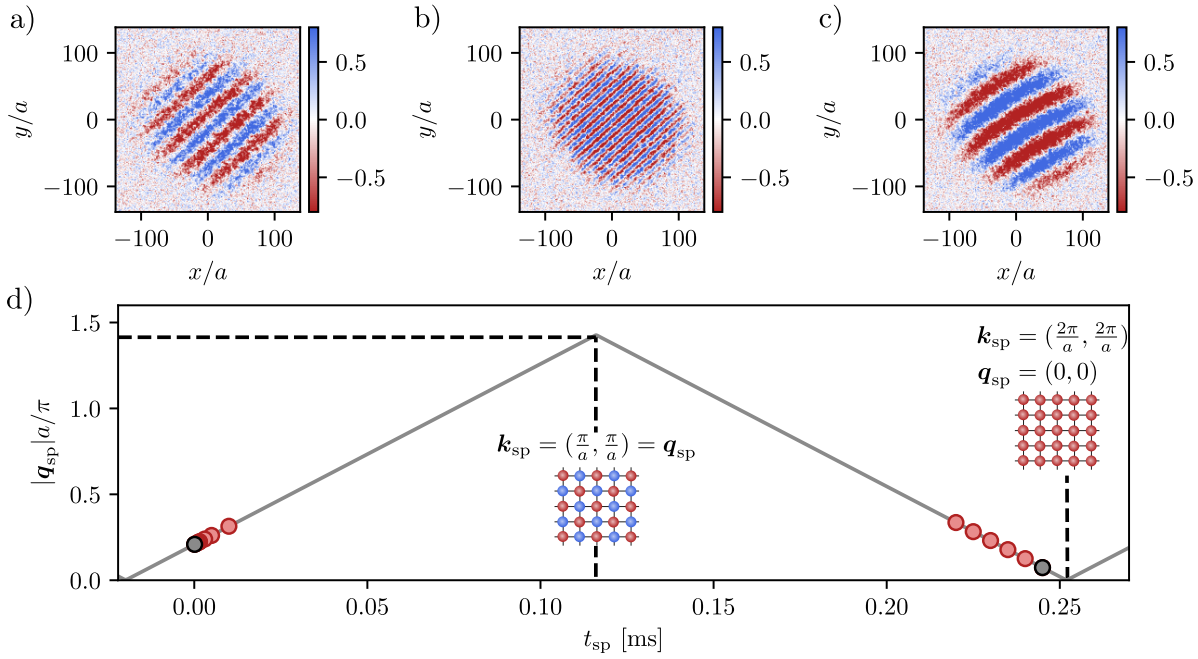

Figure 5.6: Imprinting spin patterns onto a spin-polarized cloud. The magnetic field gradient is ramped up to $|\nabla B_z| = 0.64\,\mathrm{G/cm}$, except for a), where $|\nabla B_z| = 0.1\,\mathrm{G/cm}$. a), b) Contrast $M(x,y)$ for spin patterns observed at different gradient strengths, and $t_{\mathrm{sp}} = 0.1\,\mathrm{ms}$. c) Observed spin pattern with small wavevector after Bragg reflection. The contrast is still high, suggesting that single-particle coherence is maintained. d) We plot the magnitude of the extracted wavevector $|\boldsymbol{q}_{\mathrm{sp}}|$ versus the duration t_{sp} of the spin evolution in the magnetic field gradient. Due to the resolution limit of our imaging setup, we can only infer the imprinted wavevector if the periodicity of the fringe pattern is large enough. A combined fit (solid grey line) provides a precise calibration to imprint spin patterns with arbitrary wavevectors along the diagonal of the first BZ and to extract the turning points t_{sp}^{π} and $t_{\mathrm{sp}}^{2\pi}$, highlighted by the two black dashed lines. This data has been published in [159].

$\boldsymbol{k}_{\mathrm{sp}}$ that monotonically grows with the spin evolution time t_{sp} is equivalent to a wavevector $\boldsymbol{q}_{\mathrm{sp}}$ within the first BZ. From the Fourier transformation of $M(x,y)$ we extract both the magnitude and the direction of the wavevector $\boldsymbol{q}_{\mathrm{sp}}$. Our optical resolution allows us to resolve spin patterns with wavevectors up to $|\boldsymbol{q}_{\mathrm{sp}}| \approx 2\pi/(5a)$. When the imprinted wavevector $\boldsymbol{k}_{\mathrm{sp}}$ crosses the boundary of the first BZ, it effectively gets Bragg-reflected [159]. Therefore, for evolution times $t_{\mathrm{sp}} > 220\,\mathrm{ms}$, we again observe spin patterns. However, the wavevector $|\boldsymbol{q}_{\mathrm{sp}}|$ decreases as we approach the 2π-point, $\boldsymbol{k}_{\mathrm{sp}} = (2\pi/a, 2\pi/a)$, which cannot be distinguished from the initial

spin polarized state apart from some residual magnetic field curvature, see Figure 5.6 c). Note that the direction of the imprinted spin pattern varies rapidly around the desired value if we do not match the diagonal of the 2D in-plane lattice structure perfectly. This characteristic allows for an accurate alignment of the direction to the lattice diagonal with superb precision of less than one degree. From a combined fit to the observed evolution of the x- and y-components of the spiral wavevector at small and large times, we obtain the turning points, t_{sp}^{π} and $t_{\mathrm{sp}}^{2\pi}$, for which a relative phase of π (2π) is imprinted between neighbouring lattice sites.

If the camera position was adjusted to its focus position before running the calibration of the spiral wavevector, one can determine the magnification of the vertical imaging setup by comparing the maximal wavevector amplitude extracted from the combined fit to the theoretical expectation, which is given by the length of the lattice diagonal.

The remaining task before one can use the spin spiral technique to coherently manipulate spin correlations is to cancel all in-plane magnetic field gradients as they would cause the transverse spin correlators to oscillate even before the spin spiral has started and thereby they would change the correlations that we measure. By turning the initial $\pi/2$-pulse on or off we can check whether the transverse correlations have changed with respect to the z-correlations, which are unaffected by magnetic field gradients.

5.3.3 Measurement of the Staggered Structure Factor

As shown on page 89 f., when applying the spin spiral technique to our experimentally prepared state, we probe the magnetic order at the arbitrary wavevector $\boldsymbol{q} = \boldsymbol{k}_{\mathrm{sp}}$. The (local) spin structure factor characterizes the Fourier spectrum of the spatial magnetic correlations in a certain region of the trap. I will start by discussing the special case where the nearest-neighbour phase that we imprint is equal to π. In this case the autocorrelation analysis yields the staggered magnetic structure factor, $S_{\pi,\pi}$. Intuitively speaking, the imprinted spin pattern matches the existing antiferromagnetic order, and we probe our system "on resonance", which is why we obtain a large increase in signal strength. In Figure 5.7 we compare the staggered to the uniform structure factor, which was recorded as in previous work [37] without manipulating the spins. Due to the Gaussian confinement of the lattice beams, we sample a broad range of chemical potentials in a single realization, which we infer using the local density approximation (LDA) from the precisely calibrated trapping potential. As a reference, we show the measured local moment, which is maximal at half-filling, $\mu = 0$.

As discussed before the uniform structure factor is smaller than the local moment due to the negative sign of the nearest-neighbour correlator. In contrast, the staggered spin structure factor is observed to exceed the local moment by more than the mismatch between the local moment and the uniform structure factor since all spatial correlators add up constructively. This asymmetry with respect to the local moment clearly indicates the presence of beyond-nearest-neighbour AFM spin correlations [159]. As the staggered spin structure factor is a sensitive measure for the emerging spin order, it serves as a precise thermometer even when the density degree of freedom is essentially frozen. By direct comparison to calculations using numerical linked-cluster expansion (NLCE) for the staggered structure factor at half-filling and $U/t = 8.2(5)$ [93], we deduce a local (spin) temperature of $k_B T_s = 0.57(3)t$ at half-filling. The global density temperature $k_B T_d = 0.63(3)t$, obtained from fitting NLCE data to the singles' density profiles, yields a similar result.

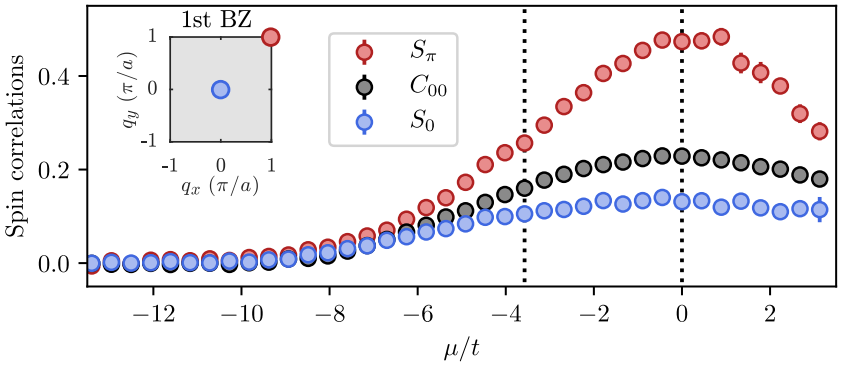

Figure 5.7: Staggered and uniform spin structure factor. We record both the uniform (blue) and staggered (red) spin structure factor as a function of the chemical potential μ. For comparison, we also show the local magnetic moment, C_{00}, as obtained from the mean singles density (black). The data was taken with $t = 224(6)\,\mathrm{Hz}$ and $U/t = 8.2(5)$. The two dashed lines highlight the centres of the potential bins used for Figure 5.9. These results have been published in [159].

5.3.4 Decoherence of the Evolution

To investigate the effect of dephasing and decoherence on the spin correlations, we add a variable hold time of length t_{hold} directly after freezing the in-plane lattices to $60E_{\mathrm{rec}}$ and quantify the amount of spin correlations by both the uniform and staggered spin structure factor, see Figure 5.8. The local moment does not depend on the duration of the hold time. We can only access the pure z-correlations if both $\pi/2$-pulses are off, which limits us to measuring the uniform structure factor. With an exponential decay constant of $\mathrm{T1}^* = 9.3(2.8)\,\mathrm{s}$, the signal loss of the longitudinal spin correlators as quantified by the spin structure factor S_0^z is negligible. The transverse xy-correlations are accessed when only the second $\pi/2$-pulse is turned on (blue data points). In this case, we observe a severe decrease in spin correlations, which can be partially averted by adding a spin echo π-pulse after half the hold time (red data points). It is surprising that the dephasing has such a large impact. This might indicate that the atoms still experience a finite gradient during the hold time. Since the in-plane gradient is typically cancelled over several consecutive time steps, in general it only works for the specific times that were chosen for the calibration and when adding hold time one would have to check whether a small gradient is introduced by this. The exponential decay times of the staggered structure factor are larger as compared to the uniform structure factor, which is unexpected as both quantify the decay of the transverse correlations. However it should be pointed out that the fitted decay times depend on the local moment that we decided to fix to the experimentally determined value. If the coherent manipulation of spin correlations was not fully efficient, we would underestimate the staggered structure factor, which would in turn reduce the extracted exponential decay constant. It is also possible that there is a relative mismatch between the magnetic structure factors as obtained via an autocorrelation analysis and the average filling, as the detection fudge factor enters quadratically and linearly, in the respective cases. Furthermore, if the camera was not in its focus position, the magnification that enters only the calculation of the magnetic structure factors would be wrong.

From this analysis we can conclude that in general the first $\pi/2$-pulse is beneficial, as the transverse spin correlators are more prone to dephasing. By turning on the initial $\pi/2$-pulse, the mean of the transverse and longitudinal spin correlations is measured. Furthermore, it appears to be sensible to implement the spin manipulation scheme at an early stage in the experimental

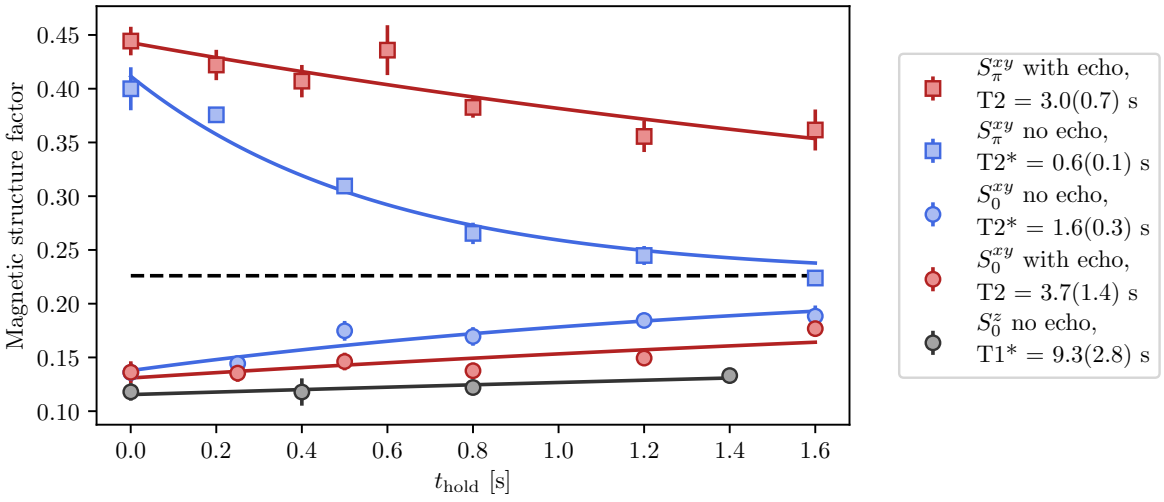

Figure 5.8: Decoherence and dephasing of magnetic correlations. Uniform (circles) and staggered (squares) spin structure factor at half-filling as a function of the hold time in the deep detection lattice configuration. The error bars quantify statistical deviations in terms of the standard deviation around half-filling. The black dashed line indicates the local moment C_{00} as extracted from the singles density. By adding a π-pulse after half of the hold time we realize a spin echo and therefore quantify the decoherence without being affected by dephasing (red data points). In contrast, the full decoherence of the transverse correlators leads to a much faster decay (blue data points).

sequence. Once the spin correlations have been mapped back into the measurement z-basis by the second $\pi/2$-pulse, they are safe from dephasing and even the decoherence effect is minimal. As the time in the deep lattice up to the spin spiral scheme can easily be kept well below 100 ms the effect of decoherence and dephasing is minimal.

5.3.5 Individual Spatial Spin Correlators

In order to infer the individual spatial spin correlators C_{ij}, we need to measure the spin structure factor for various values of the quasimomentum and then perform a Fourier decomposition. As indicated in the inset of Figure 5.9 a), we decided to probe the magnetic order along the diagonal of the first BZ, where $\boldsymbol{q} = (q, q)$. At half-filling, the structure factor exhibits a minimum at $q = 0$ and peaks at $\boldsymbol{q}_{\mathrm{AFM}} = (\pi/a, \pi/a)$, as expected. We observe a qualitatively similar q-dependence of the structure factor away from half-filling, the build-up of spin correlations is however suppressed [159]. Note that at the time we took this data we could not invert the direction of the in-plane gradient. Therefore, the data shown in the interval $q \in [-\frac{\pi}{a}, 0]$ corresponds to an imprinted wavevector with $k_{\mathrm{sp}} \in [\frac{\pi}{a}, \frac{2\pi}{a}]$. As the spin structure factor is purely real, we expect the data to be symmetric in reciprocal space $S(\boldsymbol{q}) = S(-\boldsymbol{q})$. Deviations from this behaviour would indicate that the evolution on the Bloch sphere on the timescale of the spin manipulation t_{sp} is not fully coherent. In particular, as the two data points at $q = 0$, corresponding to no gradient evolution and the longest time $t_{\mathrm{sp}}^{2\pi}$, coincide, the spin spiral rotation is fully efficient at least up to $t_{\mathrm{sp}}^{2\pi}$.[5] The structure factor that we obtain for $qa = \pi/2$ is special as we expect it to be equal to the local moment if the correlations are short-ranged, i.e. only nearest and

[5] If the gradient direction changes (slightly) as a function of evolution time t_{sp} and only matches the lattice diagonal at the 2π-calibration point, we would not obtain the full signal at the π-point, even though the

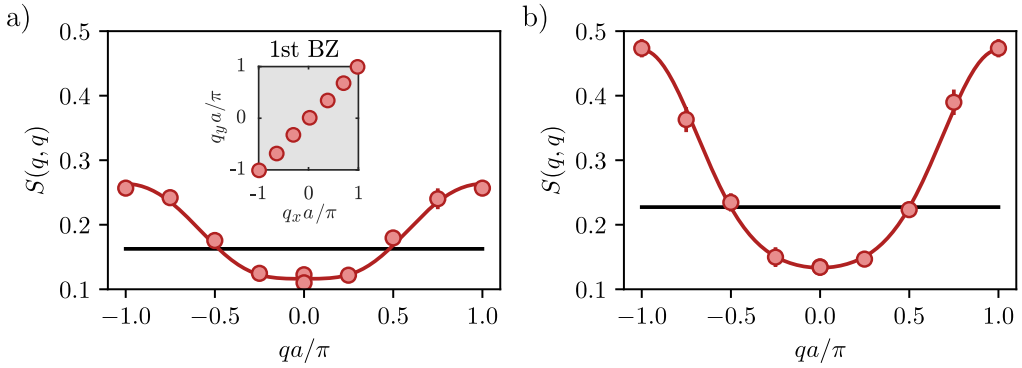

Figure 5.9: Spin structure factor versus quasimomentum. Spin structure factor (circles) and local moment (solid black line) recorded along the diagonal of the first Brillouin zone at a) low filling $\mu = -3.6t$ and b) at half-filling $\mu = 0$, respectively. We plot the fit using the Fourier series given in Equation 5.30 (solid red line). These results have been published in [159].

next-nearest neighbour correlations are significant. The four nearest-neighbour correlators with strength C_{01} vanish at this particular point, while the next-nearest neighbour correlators cancel each other, as two of them still carry the (initial) positive sign, while the other two have flipped their sign. Indeed we observe that the experimentally determined spin structure factor $S(\frac{\pi}{2a}, \frac{\pi}{2a})$ approximately matches the local moment for both fillings presented in Figure 5.9.

Correlation Length Scale In the following, we estimate the length scale over which the AFM correlations extend in our system. At half-filling, the Hubbard model with strong repulsive interactions can be mapped onto the Heisenberg model [85] where the magnitude of spin correlations decays exponentially with a characteristic spin correlation length ξ. Additionally, in a homogeneous system the spatial spin correlators C_{ij} of the unperturbed spin state depend on the distance $d = |\boldsymbol{r}_{ij}|/a$ only. Therefore, at half-filling we obtain

$$|C_{ij}| \equiv |C_d| \propto e^{-da/\xi}, \tag{5.29}$$

which we use to model $S(q,q)$ according to Equation 5.27. Under the assumption of the exponential decay of the spatial spin correlators with distance, we fit the spin structure factor as a function of quasimomentum q at half-filling and obtain $\xi = 0.43(3)a$.

Fourier Decomposition Furthermore, recording the spin structure factor as a function of q provides access to the individual spatial spin correlators C_{ij}. The value of the correlation length deduced at half-filling suggests that spin correlators with $d \geq \sqrt{8}$ do not significantly contribute to the measured spin structure factor. Rewriting $S(q,q)$ along the diagonal of the first BZ as a Fourier series, we obtain

$$S(q,q) \approx \sum_{n=0}^{3} f_n \cos(nqa), \tag{5.30}$$

measurement at $t_{\mathrm{sp}}^{2\pi}$ matches the uniform structure factor.

with $f_0 = C_{00} + 2C_{11}$, $f_1 = 4C_{01} + 4C_{12}$, $f_2 = 2C_{12} + 4C_{02}$, and $f_3 = 4C_{12}$. Using the independent measurement of the local moment C_{00} from the density profile we are able to extract all higher-spin correlators C_d up to a distance of $d = \sqrt{5}$ from the first four Fourier components of the measured structure factor. Note that we do not assume the spatial spin correlators to be governed by an exponential decay. The first three spin correlators are shown in Figure 5.10 as a function of the chemical potential. We compare the nearest-neighbour correlator C_{01} to data from NLCE calculations [93] for a temperature interval of $k_B T_s = [0.54, 0.6]t$. We observe a small deviation for all chemical potentials, which might indicate that there is a relative mismatch between the density and spin correlation results or that we are slightly colder than expected. The next-to-nearest-neighbour correlator C_{11} is observed to contribute significantly to the measured spin structure factor and possesses a positive sign as expected. The obtained values of C_{02} and C_{12} are not shown, because they are mostly consistent with zero within the 1σ error.

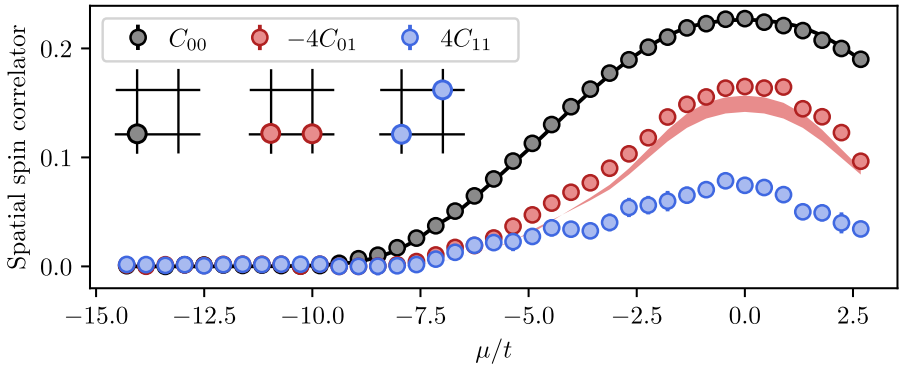

Figure 5.10: Fourier decomposition into spatial spin correlators. Extracted spin correlators as a function of the chemical potential. The red and black shadings show NLCE data of the nearest-neighbour correlator and the local moment for a temperature interval $k_B T/t = 0.54$ to 0.6. These results have been published in [159].

5.3.6 Local Spin Thermometry

Thermometry in strongly interacting fermionic lattice systems is especially difficult at low temperatures when the density degree of freedom is essentially frozen, e.g. in the Mott insulator regime for strong repulsion. In contrast, the staggered spin structure factor is a sensitive measure of the emerging spin order with respect to temperature. Hence the coherent manipulation of spin correlations offers a novel probe for the local temperature of the lattice gas, and is even suited to characterize out-of-equilibrium systems. This is achieved by comparing the temperature T_s inferred from the measured staggered structure factor at half-filling to the temperature T_d obtained from fitting NLCE data [34, 93] to the singles' density profile.

A crucial step in the preparation of our Fermi-Hubbard simulator is the handover from the dipole trap to the square lattice configuration, which unfortunately is never perfectly adiabatic. One of the dominant limitations is the density redistribution, as it strongly affects the global thermalization timescale, which becomes increasingly slow the larger the lattice depth gets [59]. Therefore, dynamics are an integral part of optical lattice experiments and in the following we will investigate the loading process into the two in-plane lattices to obtain a timescale for global thermalization. Figure 5.11 shows the measured temperatures T_s and T_d as a function of

the duration t_{load} within which the in-plane lattice depth is increased from $0E_{\mathrm{rec}}$ to $6E_{\mathrm{rec}}$ using a sine-squared ramp shape. The two independent thermometers agree well for loading times larger than 0.5 s, where both increase linearly with a slope of $0.18(5)t/\mathrm{s}$. We interpret this as genuine heating caused by light-induced scattering of the in-plane lattice beams.[6] To further support this, we compare this slope to the background heating rate $0.37(5)t/\mathrm{s}$, obtained by holding the equilibrated cloud at the final lattice depth. Under the assumption that residual heating is proportional to the integrated intensity of the lattice beams seen by the atoms [169], we expect the heating rate when holding to be twice as large as the one during lattice loading (sine-squared ramp shape). Our data supports this interpretation and we conclude that the main source of heating is related to the in-plane lattices. The linear increase in the spin temperature T_s over the full range of t_{load} suggests that the spins are in local equilibrium for all our measurement data. At short quench times, the density temperature deviates from

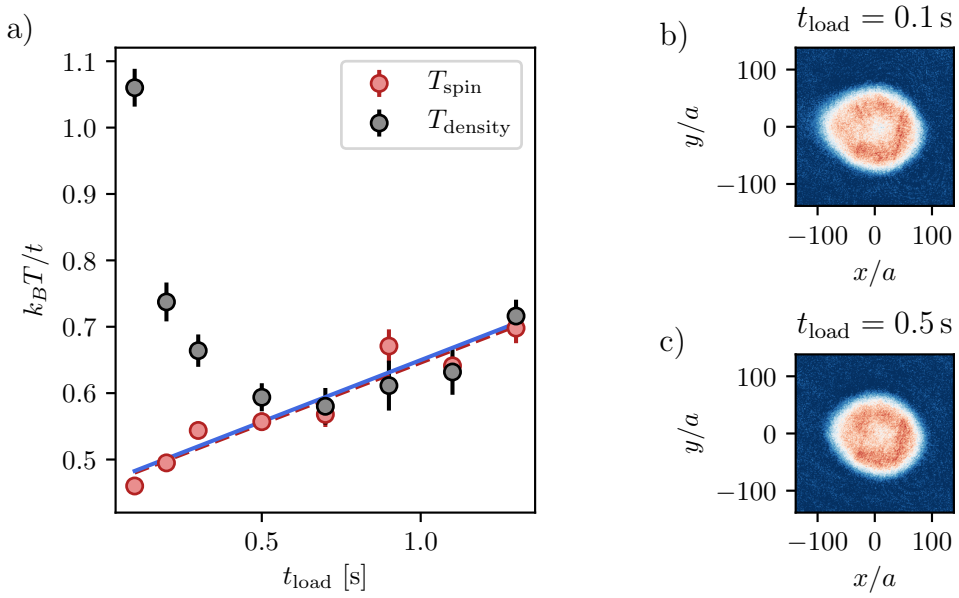

Figure 5.11: Equilibration in the spin and density sector. a) We show the density temperature T_d and the spin temperature T_s as a function of the duration t_{load}. The data suggests that density and spin degrees of freedom reach thermal equilibrium for $t_{\mathrm{load}} > 0.5\,\mathrm{s}$. The red dashed line is a linear fit to T_s, which we compare to an extrapolation using half the heating rate measured by holding at the final lattice depth (blue solid line). b), c) Averaged density profiles at $t_{\mathrm{load}} = 0.1\,\mathrm{s}$ and $t_{\mathrm{load}} = 0.5\,\mathrm{s}$ suggest that equilibration is related to density redistribution towards the trap centre. These results have been published in [159].

the linear trend. Since T_d is extracted from the entire density profile, we conclude that the cloud has not reached global equilibrium. This is reflected in the density redistribution shown in Figure 5.11 b) and c), which occurs as a consequence of the slight change in the harmonic confinement when handing over the atoms from the dipole trap to the three-dimensional lattice configuration. Therefore, to obtain a cold cloud in thermal equilibrium it is crucial to match the

[6] In principle, intensity or phase noise of the lattice lasers is also a possible source for heating [168]. This effect should however be minimal in our case, as we had exchanged the RF source of both AOM driver boxes from a VCO module to a Marconi 2024 Signal Generator with significantly reduced linewidth and less prominent sidebands.

trap confinement as well as possible in order to minimize the time that the atoms are exposed to the residual heating. Note that the density temperature in a system that is not in global equilibrium is not a meaningful quantity, and we only show it in Figure 5.11 to determine the critical timescale, where the two thermometers start to deviate from each other. With this equilibration study we confirm that the spin correlation results presented above are obtained from a thermalized cloud with a reliable temperature estimate for arbitrary filling. We conclude that residual heating in our system caused by the lattice lasers does not only destroy spin correlations of entangled states, but is also reflected in the global density temperature, which is mostly determined by the slope of the equation of state in the wings of the cloud. Furthermore, we have observed that the timescale for global thermalization, which is on the order of 500 ms, is considerably longer compared to the local equilibration timescale in the spin sector.

CHAPTER 6

Magnetic Correlations in the Bilayer Fermi-Hubbard Model

In the past decades the research with strongly-correlated fermions in optical lattices has mostly focussed on the two-dimensional (2D) Fermi-Hubbard model, due to the anticipated connection to high-T_c superconductivity observed in the cuprates [170]. In particular, recent experimental advances pushing the resolution limit down to a single site have fuelled the investigation of the 2D Fermi-Hubbard model. Real materials, however, are rarely two-dimensional, but instead compose of several coupled layers. Therefore, we have extended our experimental setup by implementing a superlattice along the vertical lattice direction. This allows us to precisely control the tunnel coupling, $t_\perp$, between a pair of neighbouring layers. The strength of this additional tunnelling process has been predicted to drive a crossover from a Mott insulating phase with antiferromagnetic correlations within the layer to a band insulating state, where interplanar singlets form along the vertical bonds. This competition in the magnetic ordering has been studied theoretically by various techniques including DMFT, DCA and DQMC [42, 48, 49].

In this chapter I will explain the main steps to prepare a bilayer lattice system including the characterization of the Hubbard parameters. We detect magnetic intralayer correlations with the technique that was introduced in Chapter 5. To access the interlayer spin correlator, we implemented a similar protocol along the vertical direction. By inducing singlet-triplet oscillations and subsequently merging the two layers [59] we were able to quantify magnetic ordering along the vertical bonds and could thus complete our toolbox for the characterization of magnetic correlations in the bilayer Fermi-Hubbard model. Parts of this chapter have been published in [171].

6.1 Experimental Sequence to Prepare a Bilayer System

In the following, I will explain the fundamental steps for preparing a bilayer system close to half-filling with repulsive interactions starting after the evaporative cooling in the dipole trap.

6.1.1 Preparation of a Single-Band Band Insulator

In order to prepare a band insulating state in the long-wavelength vertical lattice, we need a high filling factor n close to unity. For this reason, the handover from the dipole trap

to the in-plane lattices takes place at a moderate attractive interaction, $U_{79} = -1.724(1)t$. Furthermore, the loading scheme of the vertical lattices is optimized to obtain a large atom number in a single layer by reshaping the cloud with the help of the long-wavelength lattice to occupy only every other layer of the short-wavelength lattice.

Second Plane Loading Scheme A schematic showing the laser powers for the relevant beams of the second plane loading scheme is presented in Figure 6.1. When turning on the infrared z-lattice to around $V_{z,r} = 60E_{\mathrm{rec}}$ within 200 ms, prior to the long ramp up of the short-wavelength lattice, the atom cloud at the end of the dipole trap evaporation is separated into several horizontal layers with a distance of $\Delta_z = 2a_z = 2.12\,\mu\mathrm{m}$. In the next step, the short-wavelength lattice depth is increased to $V_{z,r} = 120E_{\mathrm{rec}}$ in 3 s and since the vertical superlattice is in the asymmetric configuration we obtain a clean transfer of the atoms to every other plane of the short-wavelength lattice. The handover between the vertical lattices was optimized by introducing an asymmetric ramp shape[1] to both the long-wavelength z-lattice and the dimple beam of the dipole trap. Consequently, the atoms are held longer in the planes defined by the infrared lattice until the green lattice has reached a sufficient amount of power.

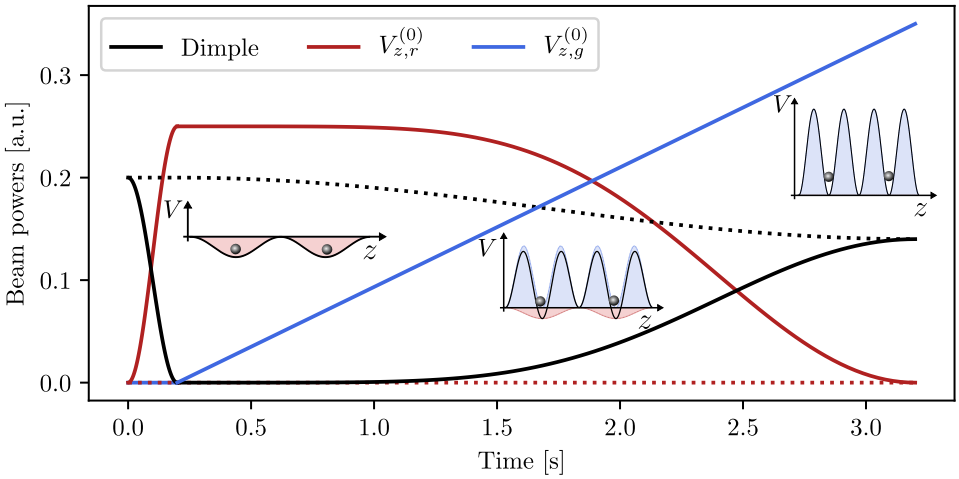

Figure 6.1: Second plane loading schematic. The solids lines indicate the beam powers for the second plane lattice loading scheme, which is completed when every other plane of the short-wavelength lattice is occupied. Without this scheme (dotted lines) the atoms are directly transferred from the dipole trap to the short-wavelength lattice and hence, all planes with a spacing of $\Delta_z = a_z$ are occupied. The small insets show the lattice potential along the z-direction and the resulting occupation in case of the second plane loading scheme.

This protocol is advantageous as we do not throw away the atoms residing in every other plane, but instead the atom cloud is reshaped along the vertical direction by the long-wavelength lattice beforehand. Figure 6.2 visualizes the redistribution of atoms over the horizontal layers as a consequence of the second plane loading scheme. By applying the monolayer tomography we resolve the occupation of individual layers with a narrow RF pulse with a width of $\Delta_{\mathrm{RF}} = 500\,\mathrm{Hz}$. Without the second plane loading scheme (dotted lines in Figure 6.1), all lattice planes of the short-wavelength lattice are occupied and therefore the spacing amounts to $\Delta_z = a_z$ only. While, with the second plane loading scheme enabled, we observe that only every other plane is

[1] The ramp shape is a sine to the power of six.

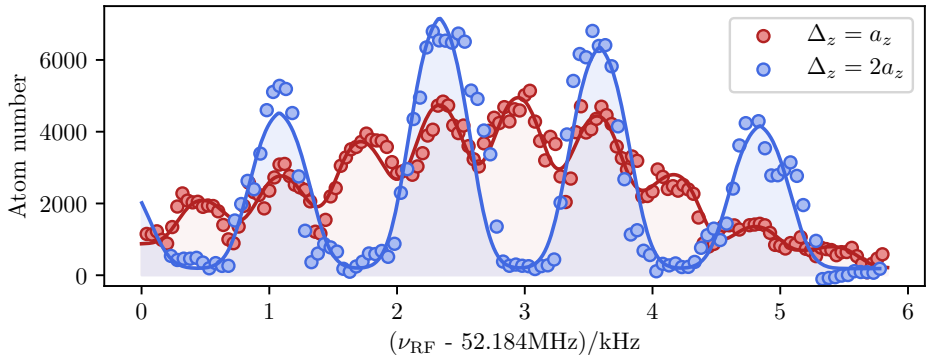

Figure 6.2: RF tomography resolving the horizontal layers. Using a narrow RF transfer in combination with a magnetic field gradient, we resolve the total atom number of individual horizontal layers and observe, that, with the second plane loading scheme enabled (blue data points), only every other plane is occupied. The sequence schematics corresponding to the two cases shown are given in Figure 6.1 as the solid and dotted lines, respectively. The data represents a single scan of the centre frequency of the RF tomography pulse with a spacing of 50 Hz, where data points within a window of 100 Hz have been averaged. The solid lines show the result of a fit consisting of several flat-top line shapes with an equally large spacing and are meant as a guide to the eye.

occupied, which does not only increase the spacing to $\Delta = 2a_z$, but also significantly increases the atom number in the occupied layers.

Characterization of the Band Insulator in the Harmonic Trap Once the atom cloud has been separated into several independent layers by the vertical z-lattice, both infrared in-plane lattices are ramped up to $V_{xy,r} = 6E_{\mathrm{rec}}$ in 500 ms. They create a square lattice structure within the plane, thus realizing the two-dimensional Hubbard model. Freezing the motion of the atoms at this point and comparing their density distribution to the theoretically predicted density equation of state $n(\mu)$, allows us to characterize how close we are to the band insulating regime in the centre of the harmonic trap.

Having precisely calibrated the trap potential $V(x, y)$ in Section 4.3, we can bin the density distribution of a single horizontal layer $n(x, y)$, as shown in Figure 6.5 a) and d), into equipotential regions and fit the density equation of state simulated with DQMC in combination with LDA to the resulting data $n(\mu)$. Figure 6.3 shows the binned density $n(\mu)$ averaged over 10 realizations selected out of a total of 30 data sets.

From the fit to the DQMC theory data, we obtain the temperature T and the global chemical potential μ_0, which together determine the maximum achievable doubles filling in the centre of the harmonic trap. This is a relevant quantity as it characterizes how close we are to a band insulating state. The Hubbard interaction parameter U was calibrated beforehand by performing RF spectroscopy (see Section 6.2.2) and is fixed to $U_{79} = -1.72t$ for the fitting procedure. In addition, the fit of the density equation of state provides us with the individual detection fudge factors for singly and doubly occupied sites, σ_S and σ_D. They account for atom loss processes, e.g. light-assisted collisions, as well as imperfections in the RF and MW transfer pulses and in the (calibration of the) absorption imaging. The resulting fit parameters corresponding to the data shown in Figure 6.3 are

$$k_B T/t = 1.97(6), \quad \mu_0/t = 6.03(6), \quad \sigma_D = 0.483(8), \quad \sigma_S = 0.806(18). \tag{6.1}$$

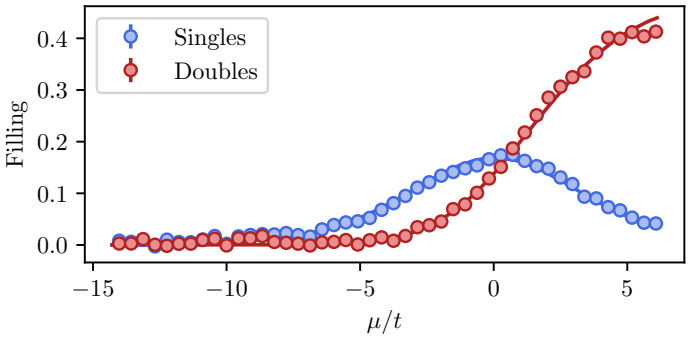

Figure 6.3: Initial state characterization in the harmonic trap. We resolve the density within a single layer of the vertical lattice of our initial state in the harmonic trap. The solid lines indicate the DQMC theory data that was fitted to our experimentally determined density distribution in the harmonic trap under the assumption of the local density approximation. Since the interaction strength is fixed the free fit parameters are the temperature T, the global chemical potential μ_0 and the individual detection fudges for singly and doubly occupied sites. The error bars represent the standard error that results from binning the filling in steps of $\Delta\mu = 100\,\mathrm{Hz}$.

The total filling per spin state in the centre of the trap potential amounts to $n = 0.906(16)$. However, the on-site interaction is still set to slightly attractive and the sudden switch to a strong repulsive interaction as necessary for the bilayer experiment will decrease the filling. Furthermore, the size of the region as defined by the DMD potential, which is discussed in the next section, will also affect the quality of the initial band insulating state.

Potential Reshaping with the DMD In order to separate the high filling region in the centre of the trap from a low filling reservoir we employ a digital micromirror device (DMD), which allows for arbitrary shaping of the potential landscape by adding a repulsive optical potential, see Section 4.4. The spatial separation is important for splitting the band insulator as it involves switching the on-site interaction U from attractive to repulsive, which would increase the cloud size and hence lower the filling in the centre. The DMD potential also defines the core region, where we analyse the spin correlations after splitting the single-band band insulator into a bilayer system.

Without the DMD potential, the combined trap geometry in the centre of the three-dimensional optical lattice is approximated by a harmonic potential, as visualized by the blue line in the upper left and right part of Figure 6.4. To separate the high filling core, the DMD applies a repulsive potential to the region defined by $500\,\mathrm{Hz} \leq V_{\mathrm{latt}}(x, y)/h \leq 3500\,\mathrm{Hz}$ and indicated by the black dotted lines, which pushes atoms outwards, while at the same time creating a steep barrier at the boundary of the core region. A sketch of the DMD potential along the x-direction as well as the combined potential of the optical lattices and the DMD light is shown in the upper right of Figure 6.4 as the red and black solid line, respectively.

In order to facilitate the density redistribution, the DMD potential is ramped up in the same time step as the in-plane lattices, followed by a hold time of 100 ms to ensure that the density is stationary. The motion in the vertical direction is frozen by the short-wavelength z-lattice for the whole duration as shown in the middle panel of Figure 6.4. To analyse the density distribution at this point, we quickly increase the lattice depth of the in-plane lattices, which freezes the motion also within the plane. This allows us to turn off the DMD potential, as the

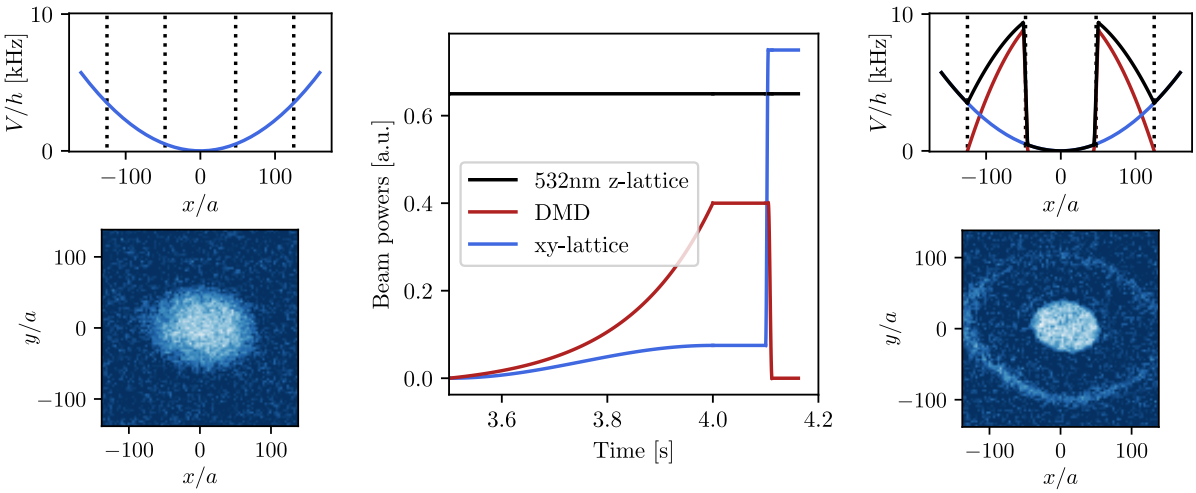

Figure 6.4: Loading the band insulator with the DMD. In the upper row we show how the potential in the three-dimensional lattice configuration (blue solid line) is altered when applying a repulsive DMD potential (red line) to the region indicated by the black dotted lines and defined by $500\,\mathrm{Hz} \leq V_{\mathrm{latt}}(x,y)/h \leq 3500\,\mathrm{Hz}$. The black solid line represents the sum of both terms. Note that the potentials shown represent only sketches, whereas when creating the DMD potential for the experiment, we employ the lattice potential beyond the quadratic approximation as explained in Section 4.3. The false-colour images in the lower row show the density distribution of doubly occupied sites in the three-dimensional optical lattice configuration (left) and after ramping up the DMD potential (right) as sketched in the middle panel.

atoms cannot move any more and to proceed to the detection part. The lower left and right image in Figure 6.4 visualize how the density of doubly occupied sites is altered by adding the DMD potential and we can clearly identify the region that is depleted by the repulsive DMD light pushing atoms much further out.

In the following we want to further investigate the effect of the DMD potential on the density, in particular within the core region of the trap $V_{\mathrm{latt}}(x,y)/h \leq 500\,\mathrm{Hz}$. For this purpose we analyse the density distribution averaged according to the underlying lattice potential $V_{\mathrm{latt}}(x,y)/h$ within equipotential bins with a spacing of 100 Hz. In the top (bottom) row of Figure 6.5 we separately show the results for the distribution of doubly (singly) occupied sites.

So far, we have conducted our experiments in a harmonic trapping potential, where we could individually fudge the spin densities when sampling the equation of state beyond the point of half-filling. In contrast, for a homogeneous system this is not possible, since we cannot assign an absolute chemical potential and hence we are unable to differentiate the detection efficiency from a global variation in the filling factor. Instead, we calibrate a mean detection efficiency by fitting the density distribution of the band insulator in the harmonic trap to DQMC theory data, see Figure 6.3 and Equation 6.1. The scaling factors for the density of single and doubly occupied sites fluctuate only slightly over the course of several weeks and common sources for deviations are the detuning of the imaging resonance and the singles-doubles separation RF pulse. We calibrate the detection efficiency before and after each data run.

In Figure 6.5 c) and f) we plot the density distribution shown in the other four subfigures, binned according to the potential map of the initial lattice configuration with $V_{xy,r} = 6E_{\mathrm{rec}}$ and $V_{z,g} = 120E_{\mathrm{rec}}$ and scaled according to the fudge factors given in Equation 6.1. We can infer that the centre region containing around 5600 sites with an average filling of $n = 0.85(1)$,

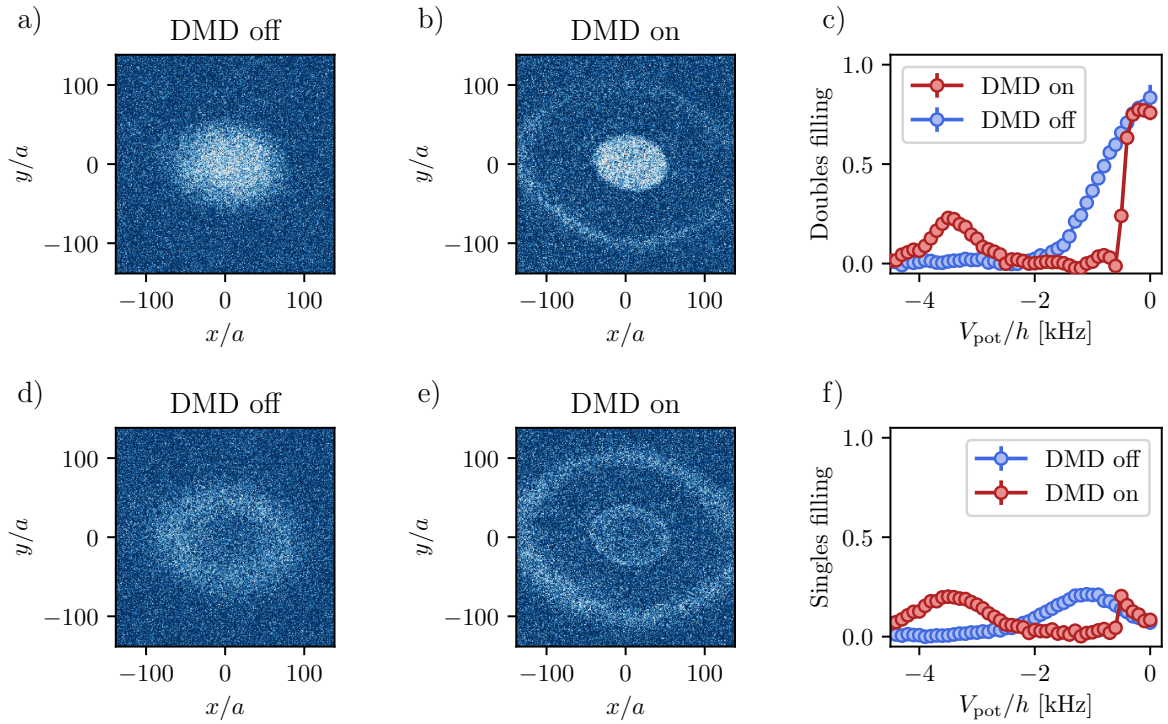

Figure 6.5: Density distribution of the initial state. In the top (bottom) row we show the density distribution of doubly (singly) occupied sites with and without the repulsive DMD potential. A quantitative comparison is obtained from the binned density data in subfigures c) and f). The error bars represent the standard error. The sharp boundary at $V/h = 500\,\mathrm{Hz}$ is clearly visible and the density within the core region is hardly affected by the DMD light.

is separated by a steep potential barrier from the rest of the cloud, which is reflected in the abrupt change in the density when the DMD is on.

The DMD potential is designed to modify only the outer region of the trap, since our aim is to accumulate as many atoms in the centre as possible. Applying a compensation to the centre region is not beneficial, as it would increase the impact of light-assisted collisions, which lead to atom loss. Furthermore, we have realized that the compensation potential, as seen by the atoms, features random disorder on the length scale of several lattice sites, which is disadvantageous when loading the in-plane lattices. Such random speckle might also explain the reduction in doubles density in the centre of the atom cloud when turning on the DMD potential, see Figure 6.5 c).

6.1.2 Splitting the Band Insulator

After the preparation of a band insulating state in the centre of our trap using the DMD, the motion of the atoms is frozen by quickly ramping the lattice depths to $V_{xy,r} = 60E_{\mathrm{rec}}$. Since we later want to split the band insulating initial state into a bilayer lattice by ramping up the short-wavelength vertical lattice, we first need to handover the atoms occupying every other plane of the green z-lattice to the long-wavelength lattice. For this purpose we ramp up the 1064 nm z-lattice to $V_{z,r} = 120E_{\mathrm{rec}}$ within 50 ms and consecutively reduce the power in the 532 nm lattice to zero, see Figure 6.6. For the handover the frequency of the green lattice laser

is detuned by around 5 GHz from the symmetric configuration. Even though this corresponds to a small phase deviation only, due to the high infrared lattice depth, the site offset is still large enough to obtain a clean transfer to the lowest band of the long-wavelength lattice. This was verified by measuring the band occupation after the handover in time-of-flight [137]. As soon as the green z-lattice is off, the frequency of the corresponding laser source is shifted to realize a symmetric double-well configuration, as necessary for the splitting part later on. As a preparation for the fast quench of the interaction strength, the current of the fast Feshbach coils is ramped up and the slow Feshbach coils are ramped down accordingly to keep the total magnetic field at a constant value of around 207 G.

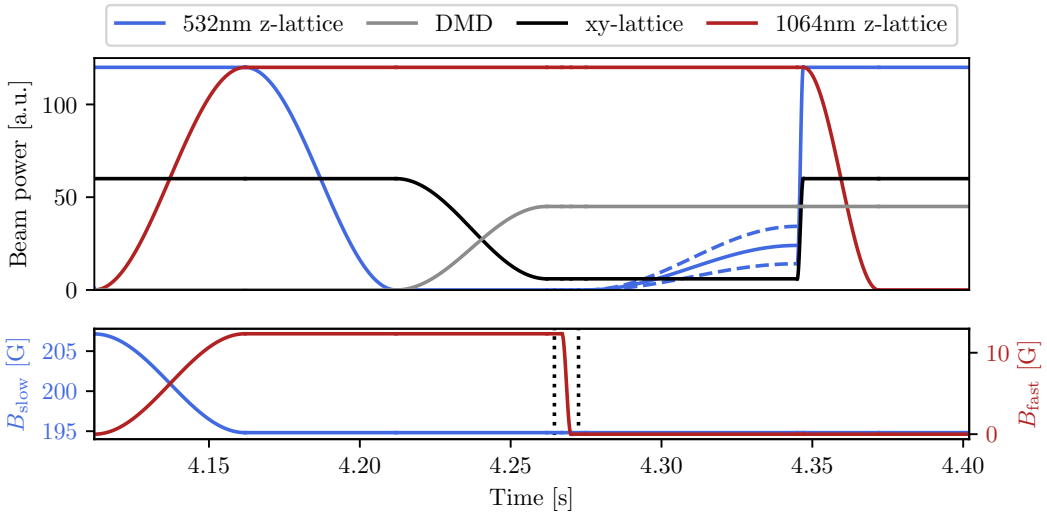

Figure 6.6: Sketch of the experimental sequence to split the band insulator into two horizontal layers. We ramp up the power of the infrared z-lattice from zero to $120E_{\mathrm{rec}}$ when the motion is frozen in all directions. The handover from the short to the long-wavelength lattice is completed once the green z-lattice is turned off. The second DMD potential is designed such that the atoms in the centre of the trap realize the homogeneous Hubbard model. The two dotted lines indicate RF sweeps that exchange the population of the $|5\rangle$ and $|7\rangle$ states as necessary for crossing the Feshbach resonance of the lowest two magnetic hyperfine states located at around 202 G. The single-band band insulator is split into the bilayer lattice configuration by ramping up the short-wavelength lattice in the symmetric superlattice configuration. For the detection part, the motion of the atoms is frozen. The laser power for the optical lattices are given in their respective recoil energy, while the DMD power is given in arbitrary units.

From Attractive to Repulsive Interactions In order to perform the splitting of the single-band band insulator at strong repulsive interactions, we need to cross the Feshbach resonance between the $|7\rangle$ and $|9\rangle$ states located at around 202 G, compare Figure 4.2. We avoid losing double occupancies by moving the occupation of $|7\rangle$ to $|5\rangle$ with a broad RF sweep just before quickly turning off the fast FB coils. The interaction switch is completed, when the population is transferred back from $|5\rangle$ to $|7\rangle$. Since we did not observe any difference in the final doubles fraction, when the interaction switch is performed with the in-plane motion frozen or unfrozen, we decided to ramp down the in-plane lattice depth to $V_{xy,r} = 6E_{\mathrm{rec}}$ already beforehand (see Figure 6.6) to reduce the absolute value of the interaction strength. In order to preserve the high filling in the central part, the DMD is ramped up featuring a barrier with a height of

8 kHz at the boundary of the core region. Furthermore, the DMD potential compensates the strong confinement, mostly imposed by the infrared z-lattice, to achieve an approximately homogeneous central part. Once the interaction strength has been set to strongly repulsive, the green z-lattice is slowly ramped up to a final value of $13E_{\mathrm{rec}} \leq V_{z,g} \leq 28E_{\mathrm{rec}}$, which determines the coupling strength, $t_\perp$, between each two layers emerging from splitting the planes of the long-wavelength lattice. To prepare a SU(2) symmetric state in spin space, it is essential to cancel residual magnetic field gradients in all three directions. Particular care must be taken for the vertical gradient when splitting the band insulator, as it would lead to a spin-imbalance in the horizontal layers. For the detection we freeze the motion by ramping up the power of the in-plane lattices and the green z-lattice within 150 µs.

Single Plane Detection As a consequence of splitting the single-band band insulator into two horizontal layers, the spacing between occupied layers along the z-direction is reduced by a factor of two. Therefore, the detection of the density distribution by the monolayer tomography is more challenging. It is, however, crucial to minimize the contribution of neighbouring planes, since they would partially cancel the signal of the in-plane spin correlations while at the same time increasing the measured density. In order to check whether the density that we detect is contaminated by contributions from neighbouring planes, we measure the density of singly occupied sites for the initial band insulating state in the harmonic trap in two cases, namely with and without the second plane loading scheme that was introduced in Section 6.1.1.

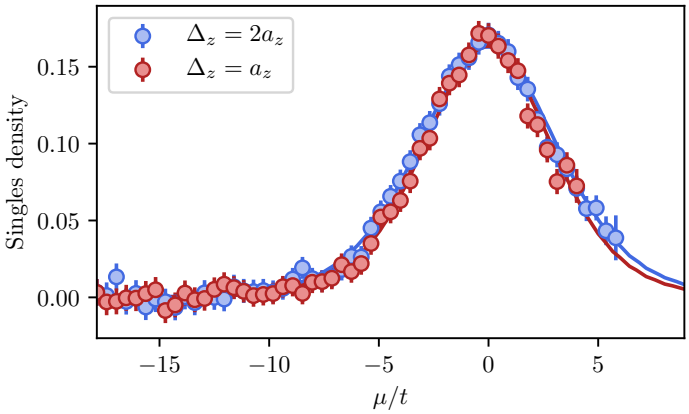

Figure 6.7: Monolayer detection fidelity. We compare the density distribution of singly occupied sites with and without the second plane loading scheme, for reference see Figures 6.1 and 6.2. Without applying the scaling factor σ_{S}, the measured densities coincide and hence we conclude that there are no significant contributions from neighbouring planes even when the spacing between layers amounts to $\Delta_z = a_z$ corresponding to 630 Hz only. Note that as expected the central filling is larger with the second plane loading scheme.

To be able to judge on the contribution of neighbouring planes we apply the exact same HS1 tomography pulse with a sweep width of $\Delta_{\mathrm{RF}} = 500$ Hz in both cases. The resulting equations of state of the singly occupied sites are shown in Figure 6.7 and they coincide with each other within error bars. This is furthermore reflected in the scaling factors that we obtain from the fit to the DQMC theory data

$$\sigma_S = 0.822(16) \quad \text{for } \Delta_z = a_z, \tag{6.2}$$

$$\sigma_S = 0.809(13) \quad \text{for } \Delta_z = 2a_z, \tag{6.3}$$

which agree within errors. Therefore, we conclude that contributions from neighbouring planes are negligible. In addition to the fudge factors, the fit also determines the temperature and the chemical potential in the centre of the trap,

$$k_B T/t = 1.77(4),\ \mu_0/t = 4.50(5) \quad \text{for } \Delta_z = a_z \tag{6.4}$$
$$k_B T/t = 1.98(3),\ \mu_0/t = 5.38(4) \quad \text{for } \Delta_z = 2a_z. \tag{6.5}$$

While with the second plane loading scheme the atom number and in turn the chemical potential in the trap centre is clearly higher, the temperature increases slightly as well. It might be beneficial to perform th handover from the dimple to the infrared z-lattice even slower, compare Figure 6.1, to minimize this increase in temperature.

Symmetry Point of the Vertical Superlattice When we ramp up the green z-lattice in order to split the band insulator, we want the vertical superlattice to be in the symmetric double-well configuration to obtain two equally populated layers. There are several ways to calibrate the symmetry point in the experiment and an overview of the techniques we applied is given in [137]. Here, I will present our most relevant protocol to get an accurate calibration of the symmetry point using the experimental sequence that is presented in Figure 6.6.

When we split the layers of the long-wavelength lattice by ramping up the green z-lattice to $V_{z,g} = 15E_{\text{rec}}$, the double-well that is formed, is strongly coupled, $t_\perp = 3.4t$, where $t = 174\,\text{Hz}$. The on-site interaction between atoms with opposite spins is repulsive $U = 6.8t = 2t_\perp$. We vary the site offset, 2Δ, of the double-well potential along the z-direction by shifting the frequency of the green lattice laser via its slow Piezo input that is controlled by the VCO of the offset lock U_{VCO}. We measure the average site occupation of the left and the right layer in two separate experimental realizations. The result for various superlattice phases is shown in Figure 6.8 and we observe that the atoms predominantly occupy either the left or the right layer when Δ is large as compared to the vertical tunnel coupling $t_\perp$. In between we realize the symmetric double-well configuration, where the initial band insulating state is mostly split into singly occupied sites.

We compare our experimental data for two coupled layers to the expectation for a simple double-well potential, as discussed in Section 3.2.3. The tunnel coupling $t_\perp$ and the interaction strength U are fixed to the values realized in the experiment, see Section 6.2. We find nice agreement if we apply the following scaling between the site offset Δ and the control voltage of the VCO

$$\frac{2\Delta/h}{U_{\text{VCO}}} = 987(41)\frac{\text{Hz}}{\text{V}}. \tag{6.6}$$

Note that apart from the standard detection fudge, no further amplitude scaling was applied to the density data. Nevertheless, we have to treat the quantitative results with caution, since we compare our experimental situation of two strongly coupled layers with a simple double-well potential.

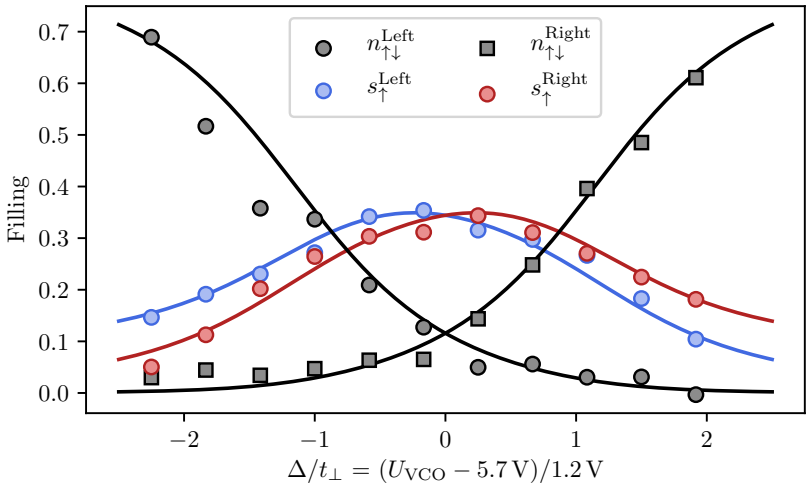

Figure 6.8: Symmetry point of the vertical superlattice. We measure the probability to find a single spin-up particle or a doubly occupied lattice site for both the left and the right layer. The site offset of the double-well potential along the vertical direction is varied by tuning the voltage of the VCO controlling the frequency of the short-wavelength lattice laser. The data shown results from a single measurement, therefore no statistical error bars are given. The solid lines represent the theoretical expectation for a pure double-well potential (compare Figure 3.5) with the only free parameter being the scaling between the site offset Δ and the voltage U_{VCO}.

6.2 Characterization of the Hubbard Parameters

The main features of the superlattice setup along the vertical z-direction have already been described in Section 4.1.3 and extensive information may also be found in the PhD thesis of my colleague Marcell Gall [137]. Therefore, this section mostly focusses on the characterization of the superlattice potential in terms of the interaction strength, U, between particles with opposite spin and the tunnelling amplitude between neighbouring layers, $t_\perp$. The tunnelling amplitude within the layer, t, is inferred from a band structure calculation. In the end of this section, I will also give an estimate on the strength of higher-order effects including density-induced tunnelling and nearest-neighbour interaction.

6.2.1 Vertical Tunnelling Amplitude

The additional parameter that is introduced to formulate the bilayer Fermi-Hubbard model is the vertical tunnelling amplitude, $t_\perp$, between the two layers forming a symmetric double-well along the z-direction. It is calibrated by inducing Rabi tunnel oscillations along the vertical direction. In Figure 6.9 the main stages of the measurement protocol are depicted. Note that the motion in the xy-directions is frozen for the whole sequence. After loading only every second plane of the short-wavelength lattice along z-direction, we ramp up the infrared lattice to form symmetric double-well potentials. Also, as part of the preparation, we reduce the barrier height, however only thus far that the atoms still do not tunnel yet. This step enables us to initialize the Rabi oscillations more quickly by ramping down the green z-lattice depth to the lattice configuration that is to be investigated within 150 µs. After a variable hold time T_{Rabi}, we freeze the motion by ramping up the green z-lattice to $120E_{\text{rec}}$ within 1 ms, while at the same time reducing the infrared z-lattice to zero. We selectively remove the occupation of every

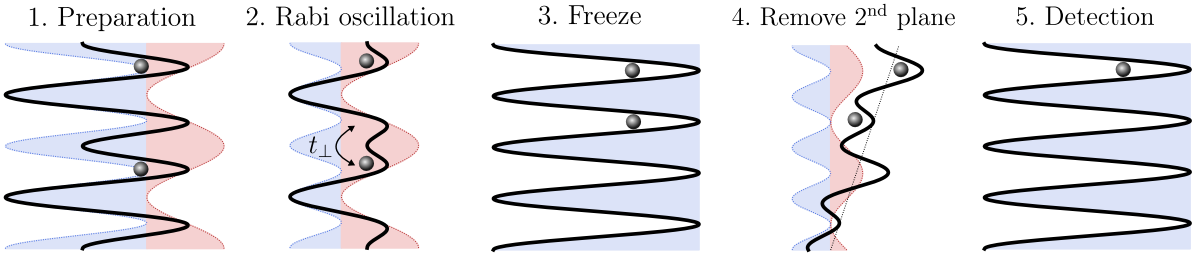

Figure 6.9: Schematic of the protocol to measure Rabi oscillations. We induce Rabi tunnel oscillations along the z-direction by abruptly reducing the barrier height of the double-well potential. After some variable hold time T_{Rabi}, we freeze the motion by quickly ramping up (down) the green (infrared) z-lattice within 1 ms. We ramp up the infrared z-lattice in the asymmetric double-well configuration to selectively remove every second plane with the additional help of a magnetic field gradient. Detection takes place in the short-wavelength vertical lattice only.

second layer by ramping up the infrared lattice in the asymmetric double-well configuration. As compared to the second plane loading, the two in-plane lattices provide additional confinement. Therefore, we need a vertical magnetic field gradient to efficiently remove the occupation without loosing atoms in the planes that we want to keep. This step is crucial since it allows us to resolve the tunnel oscillations between two neighbouring layers by imaging the whole cloud without the need to resolve a single layer using the tomography scheme introduced in Section 4.2.4. In the last step we freeze again the motion in z-direction by increasing the power of the short-wavelength lattice laser and detect the remaining atoms.

Rabi Oscillation Frequency Since the individual double-well potentials do not couple to each other, we may describe the dynamics in the reduced space of a left and right localized Wannier state $|L\rangle$ and $|R\rangle$. Furthermore, since we load a spin-polarized cloud into the lattice, interaction effects may be neglected. The Hamiltonian including a site offset of 2Δ then reads

$$\hat{H} = \begin{pmatrix} \Delta & -t_\perp \\ -t_\perp & -\Delta \end{pmatrix}. \tag{6.7}$$

In the following, I want to relate the observed Rabi oscillation frequency f_{Rabi} to the double-well parameters $t_\perp$ and Δ. The left and right localized states $|L\rangle$ and $|R\rangle$ are not stationary states of the full Hamiltonian including the tunnel coupling $t_\perp$. They are however well suited to express the time evolution of the full wavefunction [124]

$$|\psi\rangle = c_L(T)\,|L\rangle\, e^{-i/\hbar\Delta T} + c_R(T)\,|R\rangle\, e^{+i/\hbar\Delta T}. \tag{6.8}$$

The normalization condition requires the combined probability of being in either the left or the right well to be equal to unity at any instant of time, $|c_L(T)|^2 + |c_R(T)|^2 = 1$.

Starting from the time-dependent Schrödinger equation, we arrive at two coupled first-order differential equations for the time-dependent coefficients

$$i\hbar \begin{pmatrix} \dot{c}_L \\ \dot{c}_R \end{pmatrix} = -t_\perp \begin{pmatrix} c_R e^{2i/\hbar\Delta T} \\ c_L e^{-2i/\hbar\Delta T} \end{pmatrix}. \tag{6.9}$$

By combining these two coupled differential equations, we obtain

$$\begin{pmatrix} \ddot{c}_L \\ \ddot{c}_R \end{pmatrix} - \frac{2i\Delta}{\hbar} \begin{pmatrix} \dot{c}_L \\ -\dot{c}_R \end{pmatrix} + \frac{t_\perp^2}{\hbar^2} \begin{pmatrix} c_L \\ c_R \end{pmatrix} = 0. \tag{6.10}$$

When we prepare a particle in the left well $|\psi(T=0)\rangle = |L\rangle$, which is not an eigenstate of the Hamiltonian, it will oscillate back and forth between the two wells according to

$$|c_R(T)|^2 = \frac{t_\perp^2}{t_{\text{eff}}^2} \sin^2\left(t_{\text{eff}}/\hbar T\right) \text{ and } |c_L(T)|^2 = 1 - |c_R(T)|^2 . \tag{6.11}$$

Therefore, we conclude that the particle performs sinusoidal Rabi oscillations with frequency

$$f_{\text{Rabi}} = 2t_{\text{eff}}/h = 2\sqrt{t_\perp^2 + \Delta^2}/h \tag{6.12}$$

and peak-to-peak amplitude

$$2A_{\text{Rabi}} = \frac{t_\perp^2}{t_\perp^2 + \Delta^2}. \tag{6.13}$$

Data Evaluation In order to observe Rabi tunnel oscillations with a sufficient amplitude in the experiment, it is crucial to be close to the symmetric double-well configuration, compare Figure 6.12 b). Therefore, we need to calibrate the symmetry point of the vertical superlattice before we can observe any tunnel oscillations. In Figure 6.10 the result of a Rabi oscillation including all atoms within the layers is shown for $V_{z,r} = 120E_{\text{rec}}$ and $V_{z,g} = 13E_{\text{rec}}$. Even though the oscillation was recorded for the symmetric double-well potential, the contrast is not perfect, but typically reaches only around 50% for the global cloud. From the in-situ images revealing

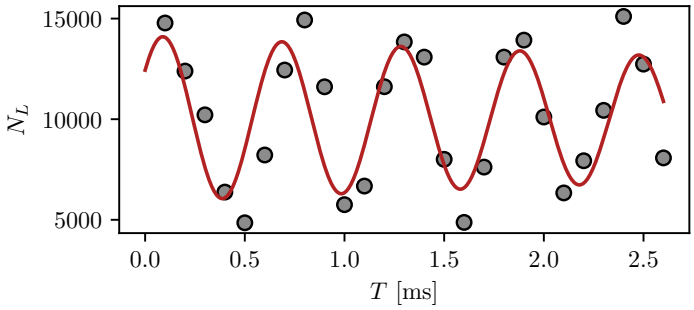

Figure 6.10: Global Rabi tunnel oscillation. Close to the symmetric double-well configuration, the atom number N_L in the left well oscillates with frequency $f_{\text{Rabi}} = 2t_\perp/h$. The contrast reaches at most around 60% due to local dephasing.

the in-plane density distribution it is evident that the tunnel oscillations at different positions within the layer dephase due to a spatial dependence of the tunnel frequency. Therefore, we decided to evaluate the Rabi oscillations locally.

Local Evaluation of Rabi Oscillations To quantify the local dependence of the effective Rabi frequency, we divide the in-situ image into a grid of 8×8 subregions with a size of approximately

10 µm × 10 µm each. In these subregions we separately fit the tunnel oscillations and the local contrast is rather high, which indicates that the regions were chosen small enough and that the different double-wells stacked on top of each other hardly dephase. The latter is explained by the small extent of the cloud in z-direction.

The resulting local fit parameters are shown in Figure 6.11. The amplitude A_{Rabi} reveals the extent of the atom cloud, while the Rabi frequency f_{Rabi} seems to depend mostly on the x-position. This might indicate that the source of the spatial variation are the vertical lattices, since both laser beams forming the optical superlattice enter within the yz-plane (see Figure 4.3) and therefore the waist projected into the xy-plane is smaller in x-direction. Since the

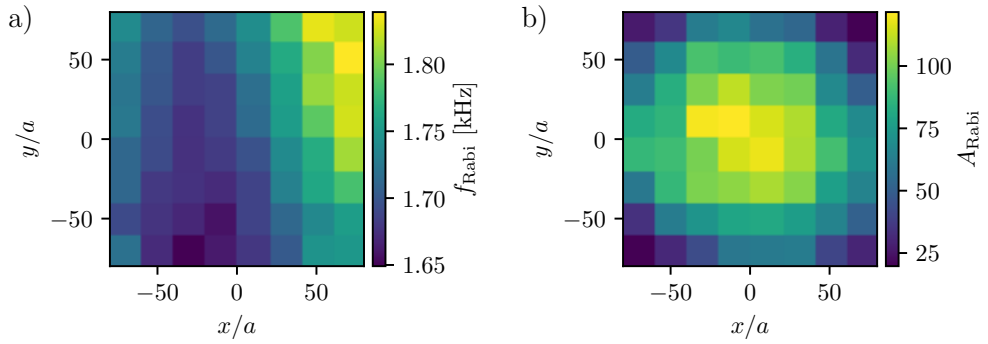

Figure 6.11: Local evaluation of Rabi tunnel oscillations. (a) The Rabi frequency f_{Rabi} depends on the position within the xy-plane and varies by around 5% within the central part of the cloud. (b) The local Rabi amplitude A_{Rabi} reflects the inhomogeneous density distribution in the harmonic trap.

effective tunnel frequency increases to the outside region of the cloud, we attribute the main effect to the blue-detuned short-wavelength lattice, which determines the barrier height. In the centre the barrier height is largest, which would explain a lower oscillation frequency.

The measurement of the effective Rabi frequency provides another tool to calibrate the symmetric double-well configuration, since the oscillation frequency depends on the site-offset and is minimal, when the tilt vanishes. We therefore measure the effective Rabi frequency for different control voltages U_{VCO} of the VCO, which determines the phase of the vertical superlattice. We extract the oscillation frequency in the centre of the cloud $f^{(0)}_{\mathrm{Rabi}}$ as the mean over those four subregions, which are the closest to the centre of mass of the cloud. The dependence on the superlattice phase is shown in Figure 6.12. Under the assumption that the site offset Δ is proportional to the frequency of the offset lock, which is a good approximation close to the symmetric double-well configuration, we fit the effective Rabi frequency using Equation 6.12. Unfortunately, we can shift the superlattice phase by around 0.05π only, therefore the range, where we are able to measure the effective Rabi frequency is limited. Still, we can deduce the symmetry point, which is located at $U_{\mathrm{VCO}} = 5.89(8)\,\mathrm{V}$ and the bare tunnelling amplitude in the centre of the cloud $t^{(0)}_{\perp}$, which is given as half of the oscillation frequency in the symmetric double-well configuration

$$t^{(0)}_{\perp}/h = 846(3)\,\mathrm{Hz}. \tag{6.14}$$

The minute uncertainty on the tunnel amplitude in the central part derives from the confidence interval of the fit, but we should keep in mind that the vertical tunnel amplitude varies by

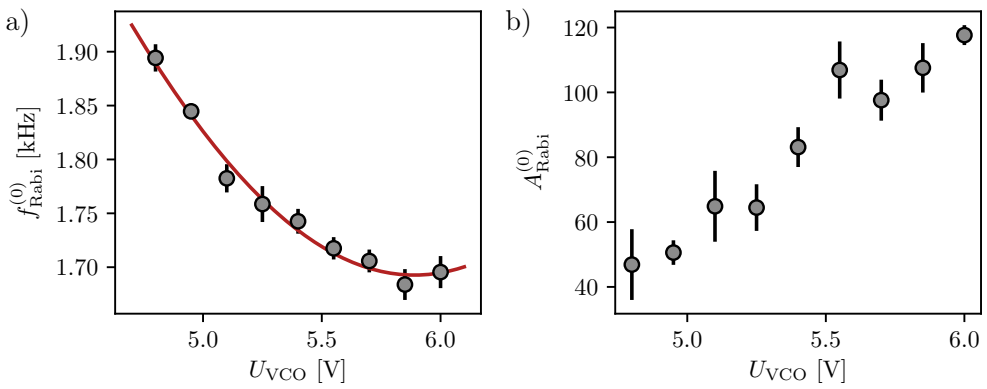

Figure 6.12: Rabi oscillations with finite detuning. We vary the phase of the superlattice around the symmetric double-well configuration at $U_{\mathrm{VCO}} = 5.9\,\mathrm{V}$ and observe how the Rabi frequency f_{Rabi} increases according to Equation 6.12. The red line is a fit to the data assuming that the site offset Δ scales linearly with the control voltage of the VCO. The amplitude increases when approaching the symmetric double-well configuration, as expected.

around 5% over the cloud's extent.

In addition, we obtain a scaling dependence of the site offset on the control voltage. According to Equation 2.22, the site offset 2Δ mostly depends on the long-wavelength lattice depth and the phase of the superlattice potential, but is independent of the short-wavelength lattice depth. For the data set presented, the infrared lattice depth was set to $V_{z,r} = 120E_{\mathrm{rec}}$ and the scaling that we obtain from the fit to the effective Rabi frequency shown in Figure 6.12 a) follows as

$$\frac{2\Delta/h}{U_{\mathrm{VCO}}} = 770(60)\,\frac{\mathrm{Hz}}{\mathrm{V}}. \tag{6.15}$$

Comparison to Numerical Simulation We have repeatedly calibrated the effective tunnel oscillation frequency for different barrier heights, given by $V_{z,g}$, and the results are shown in Figure 6.13. As expected for a quantum-mechanical tunnelling process, the coupling between the two wells decreases exponentially with barrier height.

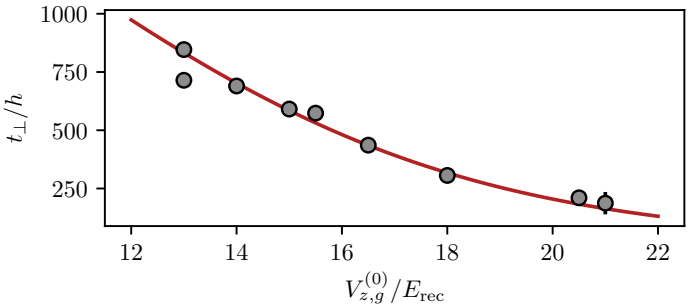

Figure 6.13: Theory comparison for the interlayer tunnelling amplitude. In the experiment, we measure the interlayer tunnelling amplitude by inducing Rabi oscillation between the two layers of a symmetric double-well configuration. From the oscillation frequency in the centre of the cloud we infer the tunnelling amplitude $t_\perp$ and compare it to a numerical simulation of the double-well.

We compare the experimentally determined tunnelling amplitudes to a numerical simulation of a single double-well potential without interactions.[2] A finite difference method was implemented, which discretizes the position in z-direction with a spacing of around $\Delta_z = 0.004 a_z$. Expressing the potential energy in a basis of delta functions is straight forward, the kinetic energy however, contains a second derivative, which effectively couples a position z_n to its neighbouring grid points z_{n+1} and z_{n-1} [172]

$$\frac{d^2\psi(z_n)}{dz^2} \approx \frac{1}{\Delta_z^2}\left[\psi(z_{n-1}) + \psi(z_{n+1}) - 2\psi(z_n)\right]. \tag{6.16}$$

An exact diagonalization of the Hamiltonian yields a set of eigenfunctions and their corresponding eigenenergies. We continue with the two energetically lowest wavefunctions, which are mixed by minimizing the spread of the two resulting Wannier states, which are localized in the left and right well, respectively. In addition, we require the two Wannier states to be orthonormal and to conform to the mirror symmetry of the potential, which fixes the sign of the real-valued Wannier states. With these non-interacting Wannier functions we can not only estimate the tunnelling amplitude between the two wells $t_\perp$, but also investigate how the on-site interaction U and the higher-order corrections V and Δt depend on the double-well potential, which will be discussed later, see Figures 6.16 and 6.17. Note that for a symmetric double-well potential both the inter- and intra-dimer tunnelling amplitudes may also be inferred from the bandwidth and the band separation of the minibands appearing in the superlattice band structure, respectively, compare Figure 3.15.

In Figure 6.13 we compare our experimental results on the interlayer tunnelling amplitude with the numerical simulation of the double-well and find nice agreement. However, we have to keep in mind, that for the calibration of the interlayer tunnelling amplitude we load a single-component Fermi gas into the lattice, which is intrinsically non-interacting. The same is assumed for the simulation. By contrast, in the bilayer experiment the particles will interact repulsively, which slightly broadens the (two-particle) Wannier wavefunction [81]. However, in [82] it was argued that the tunnelling amplitude should not be affected by the broadening of the two-particle Wannier function, as it derives from the single-particle part of the Hamiltonian. Still, intuitively it is clear that an individual spin-down particle will tunnel faster in the presence of a spin-up polarized Mott insulator with strong repulsive interactions as compared to an empty lattice, as effectively the increase in on-site energy reduces the barrier height as seen by the spin-down atom. The opposite effect, i.e. a reduction of the tunnelling amplitude, occurs for strong attractive interactions. This effect is captured by the density-induced tunnelling [121], which is a higher-order process of the local interaction term, see Section 3.4.3. The relevance of this process for our implementation of the bilayer Fermi-Hubbard model will be estimated in Section 6.2.3.

In this paragraph I have only presented the calibration of the intra-dimer tunnelling amplitude of the superlattice potential along the vertical direction. The inter-dimer coupling is expected to be negligible as the barrier height between the double-wells is approximately a factor of three larger than the strongest barrier that we realize within a double-well. As the tunnel coupling through a barrier scales exponentially with its height, the inter-dimer coupling should be strongly suppressed. In addition, the spatial separation of lattice sites between double-wells is larger than within a double-well, which further suppresses t_{inter} with respect to $t_{\text{intra}} \equiv t_\perp$.

[2] This simulation was initially set up by my colleague Marcell Gall.

6.2.2 Interaction Strength

For a simple cubic lattice configuration, where $V_x = V_y \neq V_z$, the interaction strength felt by atoms with opposite spin, may be calculated from the analytic solution for two interacting particles in a harmonic trap [70]. This was already implemented by the earlier generation of PhD students and is discussed in [60, 80]. Therefore, in this case we do not need to probe U directly, but instead it is sufficient to measure the magnetic field to infer the scattering length, which in combination with the knowledge of the lattice depths is enough to calculate the interaction strength. In contrast, for a superlattice configuration the interaction strength is more difficult to predict and we infer it from a narrow RF spectroscopy that resolves the difference in the on-site interaction energy between the initial and the final state. Both techniques and their results will be explained in the following.

Interaction Strength during Lattice Loading It is extremely relevant to obtain an accurate calibration of the interaction strength U when loading the atoms from the dipole trap into the xy-lattices, since it strongly influences the density distribution, in particular the relative occurrence of singles and doubles. Therefore, the detection fudge factors for the densities of singly and doubly occupied sites strongly depend on this interaction parameter, compare Figure 6.3. For the intralayer spin correlations we perform an autocorrelation analysis, where we multiply the magnetization of a single shot with its shifted version and therefore the spin correlation results depend quadratically on the fudge factors. In contrast, the local moment, is proportional to the density and consequently scales linearly with the detection fudge. Hence, if the interaction strength during loading is not accurately known, there will be a mismatch between the local moment and the spin structure factor even if all off-site correlators vanish.

The final lattice depths of the xy-lattice loading stage are $V_x = V_y = 6E_{\mathrm{rec}}$ and $V_z = 110E_{\mathrm{rec}}$. Therefore, we simply need to calibrate the magnetic field during the lattice loading stage and then the interaction strength is calculated as explained above. The total magnetic field strength is obtained from the resonance frequency ν_{RF} of an RF sweep with width $\Delta = 3\,\mathrm{kHz}$ on the $|9\rangle \leftrightarrow |7\rangle$ transition. The sequence schematics is shown in Figure 6.14 a). Starting spin polarized in $|9\rangle$, the RF sweep transfers the population to $|7\rangle$. Applying the microwave detection routine, we obtain the signal of the residual cloud in OD2, which is shown in Figure 6.14 b).

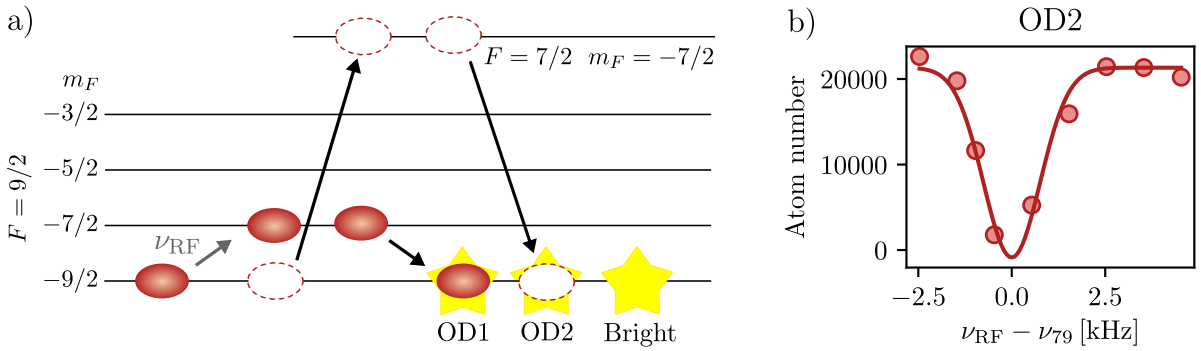

Figure 6.14: Interaction strength calibration during lattice loading. We indirectly measure the total magnetic field B via an RF sweep with width $\Delta = 3\,\mathrm{kHz}$ on the $|9\rangle \leftrightarrow |7\rangle$ transition.

There is a clear dip at 45.6374(1) MHz, which translates to a magnetic field strength of $B = 207.3965(5)\,\mathrm{G}$. At our experimental lattice depths, our simulation suggests an interaction

strength of $U_{79} = -386.1(2)\,\mathrm{Hz}$. With a tunnelling amplitude of $t = 224(6)\,\mathrm{Hz}$ this corresponds to a moderate attractive interaction $U_{79} = -1.72(5)t$.

Interaction Strength in the Bilayer Configuration The interaction during the experimental stage where the band insulator is split into the bilayer lattice configuration needs to be strongly repulsive in order to obtain a sizeable amount of spin correlations. Since we are in a bilayer lattice configuration it is not straight forward to calculate the Hubbard parameter U. We can, however, measure the difference in interaction strength $\Delta U = |U_{79} - U_{59}|$, if we transfer the spin down particles in state $|7\rangle$ to $|5\rangle$, as shown in the sequence schematics in Figure 6.15 a). To achieve this narrow transfer, we apply the same HS1 pulse as for the singles-doubles separation that is part of our detection routine presented in Section 4.2.3, however with a reduced sweep width of $\Delta_{\mathrm{RF}} = 500\,\mathrm{Hz}$. To obtain a stable transfer, we synchronize the HS1 pulse to the power line and optimize the relative delay. It is not possible to calibrate ΔU in

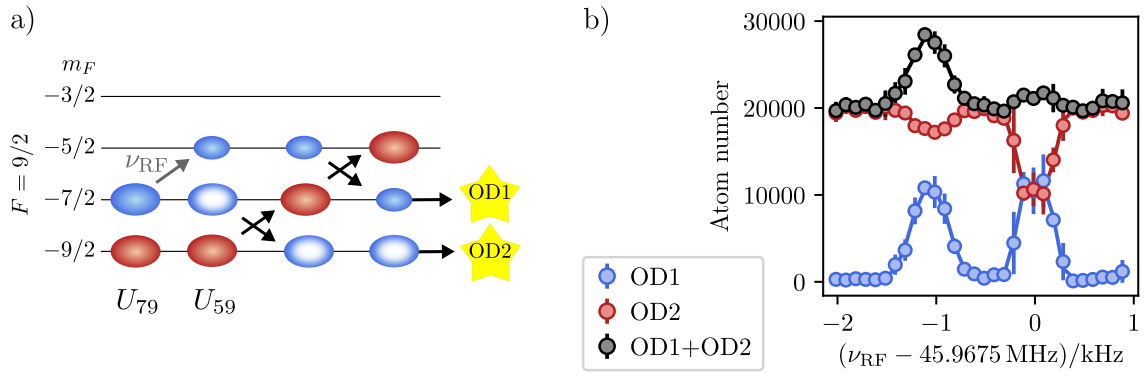

Figure 6.15: Interaction strength calibration in the bilayer configuration. After selectively transferring either the single or double occupancy in the bilayer lattice configuration on the $|7\rangle \leftrightarrow |9\rangle$ transition, the spin states are interchanged such that we obtain the signal of the transferred cloud in OD1 and the residual atom signal in OD2. The microwave routine is identical to the one shown in Figure 6.14 a) and is omitted here.

the lattice configuration used to split the bilayer, since the peak separation would be too small to resolve. Therefore, we increase the xy-lattice depth, which in turn enhances the on-site interaction in either spin mixture. In order not to split all the doubles, which are necessary for the calibration routine, we introduce a small potential tilt to the double-well potential, which hardly alters the wavefunction. Also, it proved to be helpful not to reduce the green z-lattice depth to zero before splitting. In Figure 6.15 b) we separately show the atom number of the transferred (OD1) and residual cloud (OD2), as well as the sum of both for a bilayer lattice configuration with $V_{xy,r} = 60E_{\mathrm{rec}}$, $V_{z,g} = 20E_{\mathrm{rec}}$ and $V_{z,r} = 120E_{\mathrm{rec}}$. The left peak corresponds to the situation, where we transfer doubly occupied sites and the total atom number (black data points) increases, as the doubles are not lost during the microwave sweep. When we transfer singles, they appear in OD1 and therefore, the atom number in OD2 is expected to drop correspondingly, which is the case for the right peak. From the centre frequency of the singles peak, which is independent of the particular lattice configuration, we infer the total magnetic field $B = 194.825\,\mathrm{G}$. At this field a peak separation of 1.07 kHz would also be obtained with a simple cubic lattice configuration of $V_{xy,r} = 60E_{\mathrm{rec}}$, $V_{z,g} = 11.8E_{\mathrm{rec}}$ and $V_{z,r} = 0E_{\mathrm{rec}}$. With this knowledge we can not only infer the difference in interaction strength for different spin mixtures, but also the absolute value of the Hubbard parameter U_{79}, which then only needs

rescaling to account for the in-plane lattice depth. We obtain the interaction strength for an arbitrary z-lattice configuration by rescaling the experimentally determined value according to the change in the Wannier function. The results are shown in Figure 6.16 b). When changing

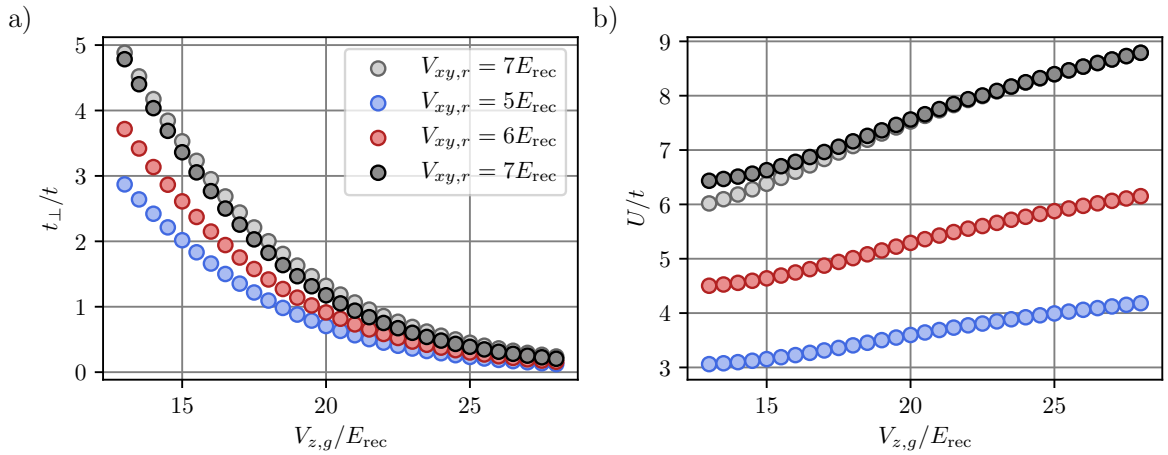

Figure 6.16: Accessible range of Hubbard parameters in the bilayer lattice configuration. The Hubbard parameters $t_\perp$ and U are numerically estimated using a finite difference method introduced on page 114f. As expected, the vertical tunnelling amplitude, $t_\perp$, decreases exponentially with the barrier height, which is proportional to the short-wavelength lattice depth. A knob to tune the on-site interaction strength without changing the magnetic field, is provided by the in-plane lattice depth $V_{xy,r}$, which impacts the extent of the wavefunction. The grey data set estimates the effective tight-binding Hubbard parameters when additionally including higher-order interaction processes, see Section 6.2.3. The legend applies to the whole figure.

the in-plane lattice depth $V_{xy,r}$, the wavefunction gets more or less squeezed, and therefore it serves as a knob to tune the relative strength of the on-site interaction with respect to the interlayer tunnelling amplitude $t_\perp$. However, we only tune the in-plane lattice within a limited range of $V_{xy,r} = [5, .., 7]E_{\mathrm{rec}}$ to avoid higher-order tunnelling processes within the layer and to keep the timescales similar and reasonably short.

6.2.3 Extended Hubbard Parameters

In Figure 6.17 the numerical results for the extended Hubbard parameters Δt and V defined in Section 3.4.3 are shown. For repulsive interactions, density-induced tunnelling as quantified by $\Delta t_\perp$ enhances the tunnelling amplitude in the double-well direction and we therefore compare it to the bare tunnelling amplitude $t_\perp$. For a low barrier height this effect is rather small, however, when increasing the barrier the density-induced tunnelling seems to contribute substantially to the overall coupling strength. This counter-intuitive behaviour is explained by the bare tunnelling amplitude $t_\perp$, which becomes very small at these large barrier heights, compare Figure 6.16 a). The ratio $\Delta t_\perp/t_\perp$ depends on the intralayer lattice depth, since the density-induced tunnelling is an off-site interaction effect, which takes into account the compression of the wavefunction in all spatial dimensions. In contrast, the bare tunnelling amplitude $t_\perp$ does not depend on $V_{xy,r}$ since it follows from a non-interacting calculation for which the Wannier functions in the three directions separate. In Figure 6.16 a) we compare the bare tunnelling amplitude $t_\perp/t$ (black circles) to the effective tunnelling amplitude $(t_\perp + \Delta t_\perp)/t$ (grey circles)

for an in-plane lattice depth with $V_{xy,r} = 7E_{\mathrm{rec}}$. The deviation reaches at most around $0.18t$.

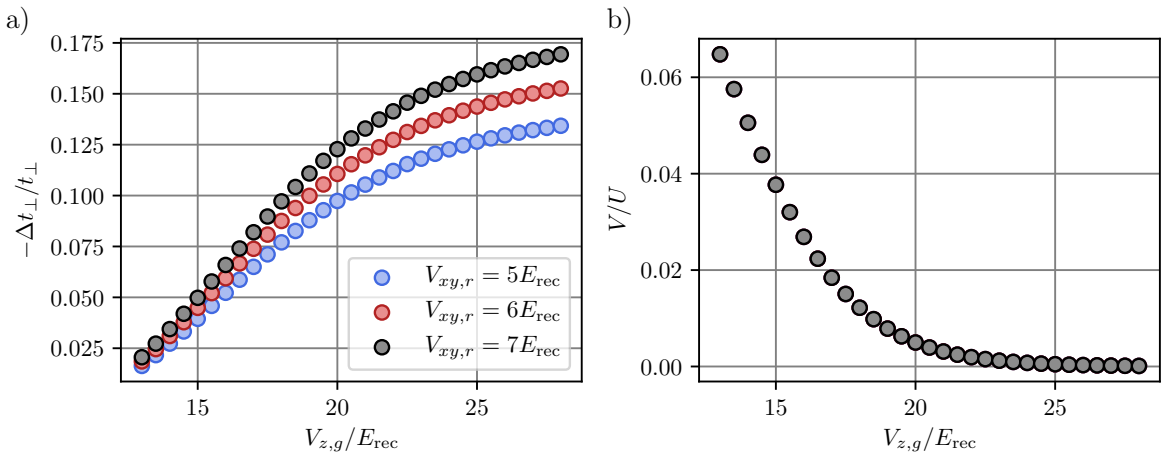

Figure 6.17: Extended Hubbard parameters in the bilayer lattice configuration. The higher-order corrections to the Hubbard interaction term are numerically estimated using the finite difference method introduced on page 114f. The parameter $\Delta t_\perp$ quantifies the amplitude of density-induced tunnelling and directly modifies the bare tunnelling amplitude $t_\perp$, compare Equation 3.73. Therefore its strength needs to be compared to $t_\perp$. In contrast, the interaction parameter V alters the effective interaction shift between singly and doubly occupied sites and consequently has to be compared to U.

The higher-order interaction parameter V comprises several effects, i.e. pair-hopping, nearest-neighbour interaction and spin-flips. On a qualitative level, it follows the behaviour of the bare tunnelling $t_\perp$, since both depend on the overlap of the Wannier states in the left and right well. Therefore, it plays a significant role only for very low barrier heights, where the overlap is largest and the bilayer configuration is well-described by individual double-wells. The interaction parameter V will effectively reduce the on-site interaction strength felt by the atoms to $U - V$, as the expectation value of the energy of the singlet $|s\rangle$ is shifted by $2V$ in contrast to the $|d_+\rangle$ state, which is shifted by V only, compare Equation 3.73. We have already discussed that the on-site interaction depends on the short-wavelength lattice depth due to the compression of the wavefunction. Including the effect of V will further lower the effective interaction in the strongly coupled case, where the barrier is low, compare the black and grey circles in Figure 6.16 b). However, since we will compare our results on magnetic correlations to theory data with a fixed U for all bilayer lattice configurations, the nearest-neighbour interaction is just a small correction on top of the strong U dependence introduced by changing the barrier height.

6.3 Intralayer Spin Correlations in the Bilayer Fermi-Hubbard Model

In the following, I will discuss our results on magnetic intralayer correlations in the bilayer Fermi-Hubbard model. The correlation analysis of the combined spin-up and -down densities as well as the measurement of the local moment is implemented as in Chapter 5, with the slight difference that the atoms do not experience a harmonic trapping potential. Instead we aim at realizing the homogeneous Hubbard Hamiltonian with a constant chemical potential by employing the DMD. Hence, the density as well as the local magnetic structure factor are averaged over the entire central region containing around 5600 lattice sites. We compare

our results to DQMC simulations to obtain an estimate of the spin temperature. Since both horizontal layers show the same amount of magnetic correlations, as we have verified beforehand, the results shown in the following are obtained from one of the layers only.

6.3.1 DQMC Theory Comparison

The DQMC simulations are performed using the Quantum Electron Simulation Toolbox (QUEST)[3] [17]. The bilayer lattice structure is implemented by adding a second orbital for each lattice site. Simulations are performed for a homogeneous lattice with $8 \times 8 \times 2$ sites with 2000 warm-up sweeps and 200000 measurement sweeps, and the number of imaginary time slices is set to 25. The interlayer tunnelling is varied from $t_\perp/t = 0$ to 5.5, while the on-site repulsion is kept at $U/t = 8$. A small but finite doping is introduced by varying the chemical potential over the range of $\mu/t = -2.5$ to 0, which approximately corresponds to a filling factor ranging from $n = 0.4$ to 0.5. The magnetic structure factor is obtained by a finite Fourier transform of the spatial spin correlators [171].

The comparison to the DQMC theory data has to be treated with caution, as it relies on several assumptions, which do not reflect the way we acquire our experimental data. In the following I will discuss the most relevant deviations (to my knowledge).

- The DMD potential, which is designed to create a flat-bottom trap in the centre introduces disorder in the local chemical potential [152]. Due to the finite numerical aperture of the aspheric lens inside the vacuum chamber, which projects the DMD potential onto the atoms, the disorder length scale will be on the order of several lattice sites, and hence much larger than the correlation length of the antiferromagnetic order. As a consequence, locally the lattice potential may still be considered homogeneous, even though we realize a variety of fillings within the central part. Therefore, we do not realize the homogeneous Hubbard model, as we have assumed for the DQMC simulations, but our results will represent an average over locally homogeneous subsystems with varying chemical potential within the layers. Opposing lattice sites of the two horizontal layers should however experience the same DMD disorder and will only be imbalanced in chemical potential if we do not split the single band band insulator in the symmetric double-well configuration. While simulating the effect of potential disorder on the magnetic correlations is difficult with the DQMC method due to the limited system size, real-space functional renormalization group calculations (fRG) might be more suited [51], as much larger system sizes may be realized (several thousands of sites). One of the drawbacks of fRG is that the on-site interaction must be smaller than the bandwidth of the system, which is however approximately fulfilled in our case.

- The interaction strength, U, changes when tuning the interlayer tunnelling amplitude $t_\perp$ via the short-wavelength lattice depth due to the compression of the wavefunction. However, the theory comparison shown in the figures throughout this chapter corresponds to a fixed interaction strength of $U/t = 8$.

6.3.2 Local Moment and its Dependence on the Freezing Timescale

For the detection of intralayer spin correlations in a single layer of the bilayer Fermi-Hubbard model, the sequence sketched in Figure 6.6 already contains all the necessary ingredients. After

[3] Fortran 90/95 package, version 1.44 available from `https://code.google.com/archive/p/quest-qmc/`

ramping up the short-wavelength lattice from zero to a finite value, $13E_{\mathrm{rec}} \leq V_{z,g} \leq 28E_{\mathrm{rec}}$, the atomic density distribution needs to be frozen for the detection part. The timescale for freezing the motion is critical, since we do not want the system to adjust to the change in Hubbard parameters, when quickly increasing the lattice depths. In the previous chapter a freezing timescale of the in-plane lattices of $t_{\mathrm{freeze}} = 1\,\mathrm{ms}$ was sufficiently fast to measure magnetic correlations in the 2D Fermi-Hubbard model with $t = 224\,\mathrm{Hz}$. However, for the implementation of the bilayer Fermi-Hubbard model, we realize interlayer tunnelling amplitudes of up to $t_\perp/h \approx 900\,\mathrm{Hz}$. The largest tunnelling amplitude in any lattice direction determines the critical response time of the atoms. As freezing the in-plane lattices has an effect not only on t, but also on the interaction strength, it also needs to occur faster than the critical timescale, which is given by the vertical tunnelling amplitude in our case. Therefore, we need to be more restrictive on the freezing timescale for all optical lattices when $t_\perp$ is large. In Figure 6.18 b) we plot the local moment C_{00}, which is proportional to the singles filling, as a function of the vertical tunnelling amplitude and investigate the impact of the freezing timescale.

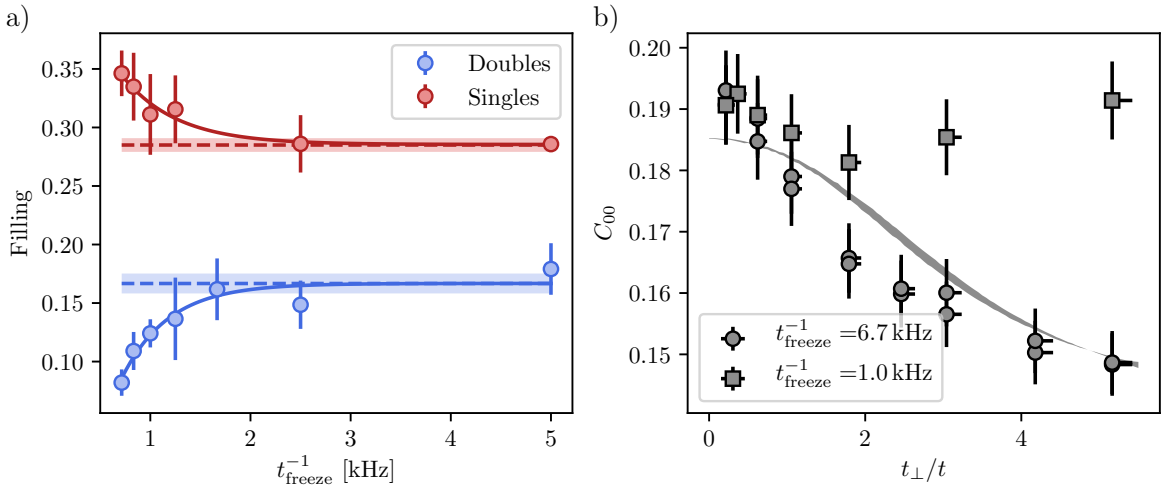

Figure 6.18: Local moment and its dependence on the freezing timescale. a) We investigate the dependence on the freezing timescale for the strongly coupled bilayer lattice configuration, $t_\perp = 5.2t$. The filling of singly and doubly occupied lattice sites suggests an exponential dependence on the inverse of the freezing timescale. The dashed lines and the shaded regions indicate the settling values of the filling as obtained from the exponential fits and the standard error, respectively. b) DQMC theory data (grey shaded region) predicts a monotonic decrease of the local moment when tuning the vertical tunnelling amplitude $t_\perp$ in a bilayer system. Our experimental data with $t_{\mathrm{freeze}} = 1\,\mathrm{ms}$ deviates strongly from the expected behaviour for large $t_\perp$. If the freezing can not be considered instantaneous on experimental timescales, some of the doubly occupied sites are split into single occupancies since the repulsive interaction strength increases when ramping up the lattice depths. With a reduced freezing time of $t_{\mathrm{freeze}} = 0.15\,\mathrm{ms}$, the experimentally determined local moment follows the monotonous behaviour, as expected. Since the standard error of the local moment is tiny, the vertical error bar mostly derives from the uncertainty of the detection fudge. The error bar on the tunnelling amplitude $t_\perp$ takes into account systematic uncertainties in the lattice depth and the vertical superlattice phase, both of which would increase the effective tunnelling amplitude if they deviated from their calibrated values.

We compare our experimental results to DQMC data at $U/t = 8$ and $1.0 \leq k_B T/t \leq 1.4$ and a filling factor of $n = 0.4$ (grey shaded area), which predicts that the local moment decreases monotonically with interlayer tunnelling amplitude. This is expected as we leave the Mott

insulating regime by increasing the tunnelling amplitude. We can qualitatively understand the impact of the freezing timescale in the double-well case. The ground-state composition, starting from an equal mixture of singly and doubly occupied sites at $U = 0$ changes, when introducing interactions and for increasingly strong repulsive interactions the singles fraction increases at the expense of the doubles filling (see Figure 3.3, in particular the inset). When we freeze the motion of the bilayer lattice configuration along all spatial directions, the ratio $U/t_\perp$ is suddenly increased by several orders of magnitude. If the freezing does not happen fast enough as compared to the experimental time scales of the tunnelling amplitude, the ground-state composition can (partially) follow the quench in the lattice depth, and hence the amount of double occupancies reduces, as shown in Figure 6.18 a). While close to the experimental timescale of around 1 kHz we observe a strong dependence of the filling on the duration of the ramp to the detection lattice, the values start to settle off at around 3 kHz. We fit an exponential decay (growth) to the filling of singly (doubly) occupied sites as a function of the inverse freeze duration, which was inspired by the transition probability defined by the Landau-Zener formula.[4]

In Figure 6.18 b) we investigate the effect of the freezing timescale as a function of the interlayer tunnel amplitude, which dictates the critical experimental time scale. At large $t_\perp$, we observe a significant deviation of our experimental data with $t_{\text{freeze}} = 1\,\text{ms}$ from the DQMC theory data. When reducing the time for freezing to $t_{\text{freeze}} = 0.15\,\text{ms}$, the density decreases monotonically with interlayer tunnelling amplitude as expected. However, we still observe a slight discrepancy between theory and experimental data. One likely reason that might explain the deviation in the trend is the on-site interaction strength U, which is fixed at $U/t = 8$ for the theory data, while for our experimental results it decreases from $U/t \approx 9$ to $U/t \approx 6.5$ with the interlayer tunnelling amplitude, as shown in Figure 6.16 b). At very small interlayer coupling, $t_\perp < 1$, the local moment is equal for the differently fast ramps to the detection lattice. While this might indicate, that even the "slow" ramp with $t_{\text{freeze}} = 1\,\text{ms}$ may be considered instantaneous on experimental time scales, it could also be linked to the fraction of doubly occupied lattice sites, which is significantly lower in the regime of the two-dimensional Mott insulator.

Note that also the uniform and the staggered magnetic structure factors deviate from their theory expectation at large $t_\perp$ if the freezing timescale is too slow. This was expected as both are equal to the local moment in the absence of off-site magnetic correlations.

6.3.3 Intralayer Correlation Analysis

When splitting the band insulator into two layers, the repulsive DMD potential is designed to create a flat potential in the centre region. Therefore, we expect to realize the homogeneous bilayer Fermi-Hubbard model with a fixed chemical potential. In a first, *global*, approach, we analyse the magnetic order by averaging over the centre region while generously excluding the edge area. Unfortunately, the DMD light introduces disorder with a length scale of several lattice sites to the potential landscape [152], which leads to large variations in the local density.

[4] However, in contrast to the standard Landau-Zener formula, we expect the filling to level off also in the non-adiabatic regime, which is shown in Figure 6.18 a), and therefore, we decided to plot the settling behaviour for increasingly fast ramps as a function of the inverse ramp duration. The settling values of the filling are given by the overlap of the experimentally prepared state with the respective double-well eigenstate. Another deviation from the scenario described by the Landau-Zener formula is the initial starting configuration of the sweep in the lattice depth, which in our case is not far away from the energy level crossing of the $|d_+\rangle$ and $|s\rangle$ state.

Therefore, in a second, *local* approach, we extract the dependence of the magnetic order on the local singles density, see page 125.

Before discussing our results, I want to mention a few key steps, which are vital to the measurement of intralayer magnetic correlations with our particular setup and which need to be checked regularly. Firstly, it is extremely relevant to focus the camera to the examined atom plane that was selected for the intralayer spin correlation analysis, as this has a direct impact on the point-spread function and hence, the imaging resolution [148]. The focus position is found by moving the camera along the imaging beam direction as the point where the largest wavevectors are collected by the imaging system, see [60, 80] for details. We have empirically found that the position of the camera needs to change by 1 mm, if the centre frequency of the monolayer tomography shifts by around 870 Hz. Secondly, the magnification of our absorption imaging setup needs to be determined accurately as it enters the calculation of the magnetic structure factors. Furthermore, at the end of the splitting procedure, every plane of the short-wavelength vertical lattice is occupied. Therefore, the transfer function of the RF sweep, which selectively transfers an individual layer to a different magnetic hyperfine state, needs to be narrow enough to ensure that the contributions from neighbouring planes are negligible.

Global Evaluation

The spin correlation analysis is implemented as introduced in Chapter 5. In addition, we apply a low-pass filter to the spin densities in Fourier space, with $k_{\mathrm{cut}}/2\pi = 0.22\,\mathrm{a}^{-1}$, which is designed to cut off high-frequency noise, e.g. circular fringes appearing due to small dust particles in the imaging beam path. The resolution limit of our vertical in-situ imaging setup is quantified in terms of the maximum wavevector that is collected, $k_{\mathrm{max}}/2\pi = 0.2\,\mathrm{a}^{-1}$ [80] and the chosen cut-off should always exceed this resolution limit in order not to throw away the actual spin correlation signal. We have observed the intralayer correlations to yield more reproducible values upon introducing the Fourier cut-off.

In Figure 6.19 we plot the local moment together with the uniform and the staggered spin structure factor, as obtained from averaging over the centre region. In the absence of magnetic off-site correlations all three quantities should be equal. However, the local moment is calculated from the singles density directly, while the magnetic structure factors derive from an autocorrelation analysis. Therefore, these quantities scale differently with the detection fudge factors[5] and any error in the determination of the detection fudges or the magnification of the imaging system will imbalance these quantities even if there are no long-range spin correlations. In contrast, the difference between the staggered and uniform spin structure factor does not suffer from this issue and it will reveal without doubt whether off-site correlations are present.

We compare our experimental results to numerical simulations of the bilayer Fermi-Hubbard model using the determinant quantum Monte Carlo (DQMC) method with $U/t = 8$ and $1.0 \leq k_B T/t \leq 1.4$ (see shaded areas in Figure 6.19). The simulation describes a system with a constant filling factor $n = 0.4$. This value was chosen such that the local moment as calculated by DQMC matches our experimental results. The deviation from half-filling is mostly due to imperfections in the initial band insulating state with a typical filling factor of $n = 0.85(1)$ before the splitting takes place. In addition, the effective filling that we need to compare our data to might be further reduced due to the rather large variations in the local chemical potential, as the local moment does not grow linearly with the local filling factor.

[5] The density scales linearly with the detection fudge, while for the calculation of the magnetic structure factors the local densities are multiplied and therefore their scaling is quadratic.

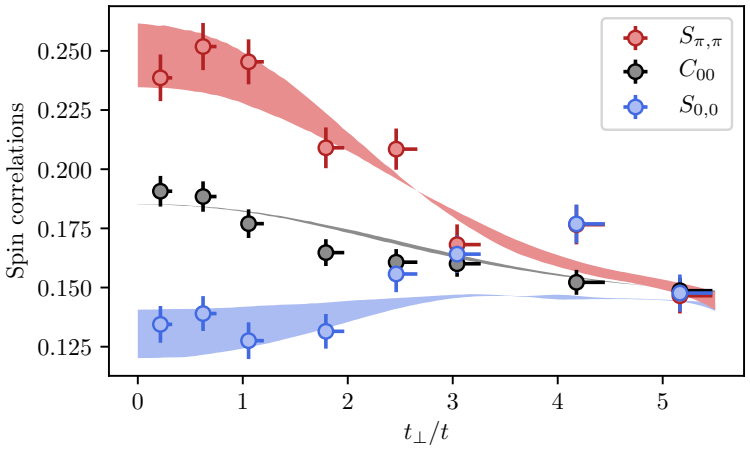

Figure 6.19: Intralayer spin correlations in the bilayer Fermi-Hubbard model. Staggered structure factor (red) and uniform structure factor (blue) versus interlayer tunnelling amplitude $t_\perp$. For comparison, we also show the local magnetic moment (black). The data were taken with $t = 174\,\mathrm{Hz}$ and $U \approx 8t$. The shaded areas are the results of DQMC calculations corresponding to the experimental parameters covering the temperature range $k_B T = 1.0t$–$1.4t$ at filling factor $n = 0.4$. The error bars on the magnetic structure factors denote the standard error of the spin correlation results in the central region of the cloud. The error bars on the local moment C_{00} and the tunnelling amplitude $t_\perp$ are discussed in the caption of Figure 6.18. These results have been published in [171].

All three magnetic correlators shown in Figure 6.19 agree well with the experimental data. At the temperatures reached in our experiment we do not expect long-range correlations. This is reflected in the fact that the distances of the staggered and uniform structure factors to the local moment are equal, which indicates nearest-neighbour correlations only, see Equation 5.30. We observe that the antiferromagnetic intralayer correlations disappear for increasing coupling $t_\perp$ between the two-dimensional layers [171]. In particular, for very large values of $t_\perp$ the homogeneous and staggered structure factors approach the local moment and agree within errors, which directly implies that within the layer there are only on-site spin correlations. This result is in contrast to the three-dimensional Hubbard model, where due to the larger coordination number the relative strength of quantum fluctuations is suppressed, and therefore, a phase transition occurs at finite temperature, below which the system exhibits long-range order [114]. However, increasing $t_\perp$ does not simply add a new dimension for the atoms to move, but also breaks the isotropy in the tunnelling amplitude. It has been predicted in several publications including [43, 51, 113, 117] that increasing the interlayer coupling, $t_\perp$, beyond the intralayer tunnelling amplitude, t, drives the formation of singlets across the bonds between the two layers at the expense of reducing magnetic correlations within the layers. We have experimentally verified this by observing that the difference between the staggered and the uniform magnetic structure factor, which quantifies magnetic order within the horizontal layer, decreases monotonically with the interlayer coupling strength and completely vanishes in the strong coupling limit. Furthermore, the local moment quantifies the occurrence of single occupancies, which are an important prerequisite for the superexchange process that is responsible for the antiferromagnetic correlations in the Mott insulator at low $t_\perp$. The reduction in the local moment when increasing the vertical coupling strength indicates that the superexchange process does not dominate the magnetic properties in the strong coupling limit.

Local Evaluation

Due to the large variations in the local chemical potential introduced by the DMD light, the average singles density is not constant within the central region. The characteristic length scale of the disorder potential is on the order of four to nine lattice sites, as everything beyond should be taken care of by the atom feedback loop (see Section 4.4) and smaller structures are prohibited by the limited numerical aperture of the lower aspheric lens within the science cell (see Figure 4.6). Histograms of the local moment evaluated pixel by pixel in the centre region of the trap are shown in Figure 6.20 for different vertical tunnelling amplitudes. As the variations in the chemical potential do not depend on the interlayer tunnelling amplitude, $t_\perp$, the width of the distribution is a measure of the insulating nature of the corresponding many-body state. The relative width is the smallest at large $t_\perp$, indicating that the state is the most insulating in this regime.

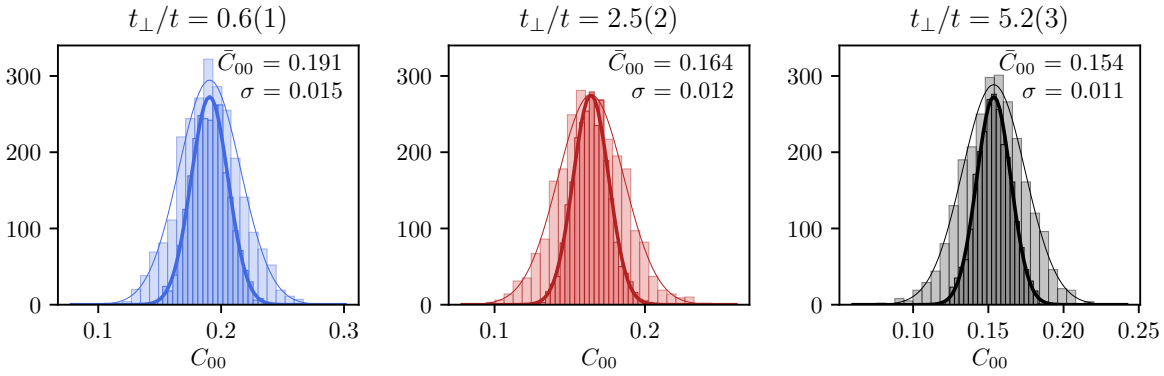

Figure 6.20: Histograms of the local moment. We evaluate the density in the centre region without applying any filter to the images (faint colour histogram) and investigate how the width of the distribution changes (darker colour) when applying a Gaussian low pass filter with an RMS width of $\sigma = 2\,\mathrm{px}$ corresponding to around $\sigma = 2.1a$. For each histogram around 90 realizations were combined. The fit results of the normal distribution corresponding to the darkly coloured lines are given as an inset.

The faintly coloured histograms represent the raw density data without averaging over different realizations and without smoothing. Therefore, their width is affected by both the imaging noise, e.g. shots noise of the camera or fringes, and the DMD disorder. Assuming that the imaging shot noise is present on much shorter length scales than the DMD disorder potential, we aim to disentangle these two effects by applying a Gaussian filter with RMS width of $\sigma = 2\,\mathrm{px}$ corresponding to about 2.1 lattice sites[6]. The absolute width reduces by 0.01 for all three graphs shown in Figure 6.20. Using the DQMC method, we can simulate the local moment as a function of the chemical potential, see Figure 7.1 b). This allows us to estimate the RMS disorder amplitude that is felt by the atoms to around $\sigma_\mu = 0.65t$. This number appears small as compared to the on-site interaction, which should in principle limit the effect of the disorder. However, the finite temperature and a filling of $n = 0.4$ only, strongly reduce the insulating nature and therefore the density response is larger than naively expected.

Furthermore, the local evaluation of magnetic correlations allows us to correlate the local density of singly occupied sites (local moment) with the amount of off-site correlations. However,

[6] As the DMD disorder is mostly constant over time, in contrast to imaging noise, another approach would be to average over different realizations instead of smoothing the density data.

to observe the trend shown in Figure 6.21, we need to apply a Gaussian filter with an increased width of $\sigma \approx 6.4a$. We compare to DQMC theory data with a density n between 0.4 and 0.5.

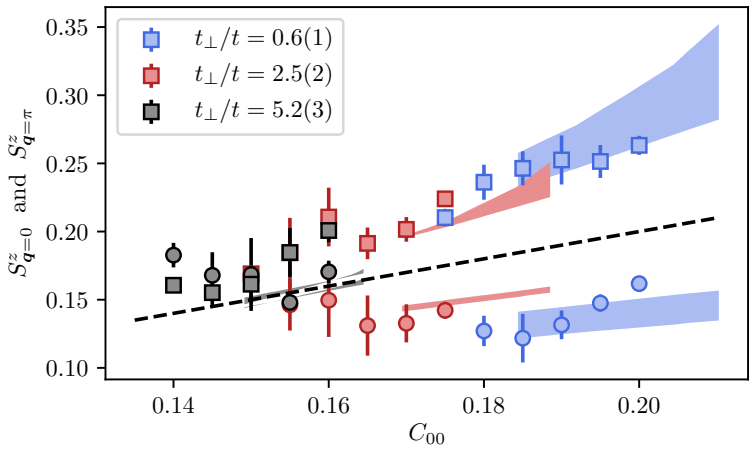

Figure 6.21: Local evaluation of the magnetic structure factor. We apply a Gaussian low pass filter with an RMS width of $\sigma = 6\,\mathrm{px}$ corresponding to around $\sigma = 6.4a$ to the 2D map of both the local moment and the magnetic structure factor before binning the data. The squares (circles) represent the staggered (uniform) structure factor, with the error bar given as the standard deviation of the (filtered) magnetic structure structure factor evaluated in regions where the local moment is within a certain bin of width $\Delta C_{00} = 0.005$. The dashed line indicates the expectation for purely on-site magnetic correlations, hence, where $S^z_{\boldsymbol{q}} = C_{00}$ for any wavevector $\boldsymbol{q}$.

For the largest vertical tunnelling amplitude shown, we do not expect to observe off-site magnetic correlations, and indeed, our experimental data for the uniform and staggered magnetic structure mostly agree within errors. However, they both deviate from the local moment, which is indicated by the dashed line and which is lower for almost all data points with $t_\perp/t = 5.2(3)$. The approximately linearly increasing trend, as expected from DQMC data, is clearly visible on the staggered magnetic structure factor, although the slope seems lower.

There are several possible explanations for the deviations that we observe in Figure 6.21 at large $t_\perp$ (black data points). As discussed above, the experimental timescales in this case are extremely fast. This implies a reduced upper bound on the freezing timescale and as discussed above if the freezing occurs too slowly we will overestimate the amount of singles and hence the local moment. Unfortunately we can not easily reduce the time for freezing further in order to check whether it has a significant effect. However, it is also possible that we systematically overestimate the magnitude of the magnetic structure factors for all values of $t_\perp$, for example due to errors in the magnification, the detection fudge factors or the summation point of the spin correlations. These, error sources would however drag down both the uniform and the staggered structure factor, which would render them asymmetric around the local moment for medium and small $t_\perp$. This would in turn indicate that the spin spiral does not properly rotate all the spin correlators, which however can not be linked to decoherence since we verified that $S^z_{\boldsymbol{q}=2\pi} = S^z_{\boldsymbol{q}=0}$.

6.4 Interlayer Spin Correlations in the Bilayer Fermi-Hubbard Model

To complement the investigation of magnetic order in the bilayer Fermi-Hubbard model, this section will focus on the determination of the interlayer spin correlations. Measuring the spin-resolved occupation of both coupled layers is not possible in a single realization, therefore the autocorrelation analysis presented in the previous chapter is not feasible. Instead, the general idea is to adiabatically remove the barrier along the vertical direction and hence transform the double-well potential into a single well [173]. According to the quantum adiabatic theorem [53], the eigenstates of these two extreme cases are connected smoothly to each other, if the system has enough time to adapt to the change in the Hamiltonian. In particular, the spin singlet ground-state of the double-well potential transforms to a double occupancy with both particles in the lowest band of the single well [153]. In simple terms, the measurement of the interlayer spin correlations therefore simplifies to the determination of the doubles filling in a single layer.

In this section, I will discuss the implementation of this so-called merging procedure and explain how to extract the spin correlator along the vertical lattice direction.

6.4.1 Merging along the Double-Well Direction

To detect the interlayer spin correlations we employ a scheme that was successfully implemented in the group of T. Esslinger [59, 153] to measure the singlet-triplet imbalance in both dimerized and anisotropic cubic two-dimensional lattices. A similar technique was already applied in 2010 to a bosonic system [173].

In Figure 6.22 the protocol is shown that allows us to measure the overlap of our experimentally prepared state with the double-well ground state. After having split the long-wavelength lattice layer into two coupled planes by ramping up the green z-lattice, we quickly freeze the motion within the planes by ramping to $V_{xy,r} = 30E_{\mathrm{rec}}$ within 1 ms. This projects the wavefunction onto the double-well eigenstates if the ramp is fast enough. Next, we remove the barrier of the double-well potential by slowly ramping down the green z-lattice to zero within 20 ms. This step is called merging and was previously used to detect the left-right imbalance by switching to an asymmetric double-well configuration prior to detection [174, 175]. In the symmetric case, however, there is no distinction between left and right sites. Instead the ground state of the double-well, which is a spin-singlet state for fermions, is mapped onto the two-particle ground state of the underlying long-wavelength lattice well. Hence, by detecting the amount of double occupancies averaged over the two in-plane directions, we obtain the ground state overlap of our experimentally prepared state. In contrast, the spin triplet states require one particle to occupy a higher band after merging, and will be detected as single occupancies as their spatial wavefunction is antisymmetric and hence they do not experience an on-site energy shift, $U = 0$.

After slowly merging the vertical double-well potential, we further increase the in-plane lattice depth to its final value, $V_{xy,r} = 60E_{\mathrm{rec}}$. At this point we could in principle proceed to the detection part, however, we hand over the atoms to the short-wavelength vertical lattice to facilitate the separate detection of singly and doubly occupied lattices sites.

Handover to the Short-Wavelength Lattice It is preferable to transfer the atoms from the long- to the short-wavelength vertical lattice, where due to the smaller lattice spacing the wavefunction is squeezed more tightly. Consequently, the on-site interaction is stronger, which facilitates the distinction of singly and doubly occupied sites. In Figure 6.23 we compare the resonance position of the doubly occupied sites as obtained from RF spectroscopy for the

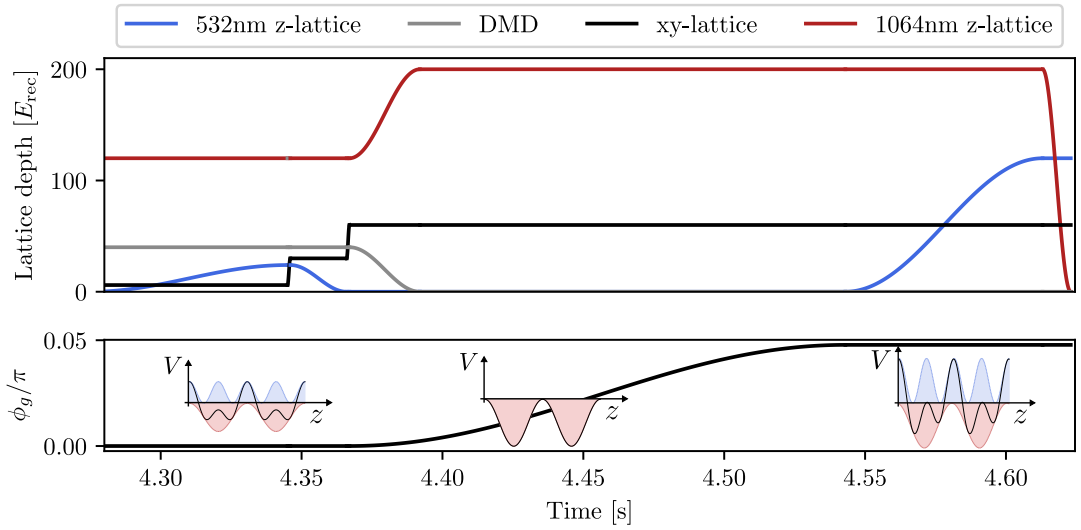

Figure 6.22: Schematic of the experimental sequence to merge the bilayer lattice. After splitting the initial band insulating state into a bilayer lattice configuration, the xy-lattice depth is quickly increased to $30E_{\mathrm{rec}}$ to freeze the motion within the layers. Consecutively, the symmetric double-well along the vertical direction is transformed to a single well by slowly turning off the green z-lattice. The phase of the vertical superlattice ϕ_g is adjusted to facilitate the transfer to the short-wavelength lattice, for detection purposes. The laser powers for the optical lattices are given in their respective recoil energies while the DMD power is given in arbitrary units.

infrared and the green vertical lattice. In the lattice configuration that is routinely used for detection, i.e. $V_{xy,r} = 60E_{\mathrm{rec}}$ and $V_{z,g} = 120E_{\mathrm{rec}}$, the singles and doubles peak (red data points) are separated by around 1.8 kHz, which is easily resolvable by an RF sweep with $\Delta_{\mathrm{RF}} = 1.3$ kHz. For the infrared z-lattice, we try to compensate the larger lattice spacing by increasing the lattice depth to $V_{z,r} = 200E_{\mathrm{rec}}$, however, the separation is still only on the order of a few hundred Hz and we can not resolve the transfer of doubly occupied sites with the standard sweep width.

To facilitate the transfer to the short-wavelength lattice after merging, we ramp the infrared z-lattice to $V_{z,r} = 200E_{\mathrm{rec}}$, see Figure 6.22. Furthermore, it is crucial to shift the frequency of the Verdi, once the short-wavelength lattice has been turned off, to adjust the phase of the vertical superlattice for the handover. Note that we exploit the whole range of the offset lock for this purpose, therefore the ramp has to be sufficiently slow. Once the frequency of the Verdi lattice laser has been adjusted, the green z-lattice is slowly ramped up to $V_{z,g} = 120E_{\mathrm{rec}}$, followed by turning off the infrared z-lattice. In Figure 6.24 we show the amount of singly and doubly occupied sites that end up in every other plane of the short-wavelength lattice after the handover has taken place. It is evident from the data that the superlattice configuration needs to be sufficiently asymmetric, at least $\phi_g \approx 0.04\pi$. However, even when properly adjusting the superlattice configuration according to Figure 6.24, the handover was not fully efficient, but we lost around 15% of the doubles signal, while the number of singles remained approximately constant.[7] It was only later that we realized that there are no losses if we perform the handover at a smaller depth of the vertical long-wavelength lattice, e.g. $V_{z,r} = 120E_{\mathrm{rec}}$.

[7] This was quantified by imaging the whole cloud without applying the monolayer tomography and the singles-doubles spectroscopy, once in OD1 without the MW and once in OD2 with the MW transfer.

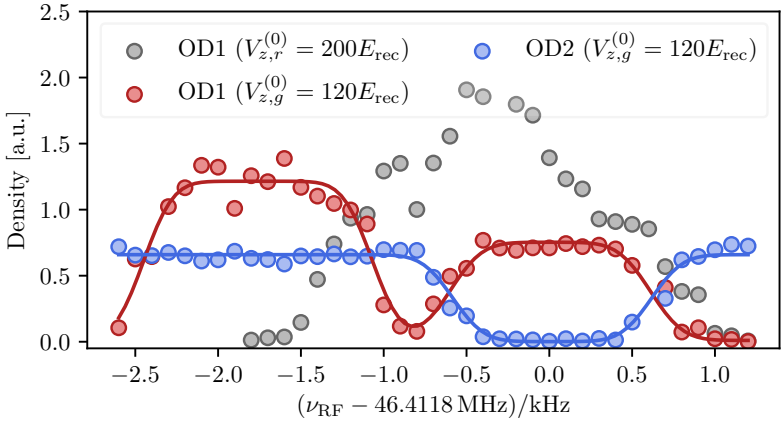

Figure 6.23: Comparison of the singles-doubles separation in the green and in the infrared vertical lattice. We separate singly and doubly occupied sites with an RF sweep of width $\Delta_{\mathrm{RF}} = 1.3$ kHz. The transferred atoms appear in the first image, OD1, and the residuals end up in OD2. In the short-wavelength vertical lattice, the doubles peak is shifted by around 1.8 kHz to the left of the singles peak. In contrast, for the long-wavelength lattice the separation is reduced to only a few hundred Hz. Therefore, it is much more difficult to obtain a clean and stable transfer of only doubly occupied sites and we are not able to resolve the singles and doubles peak with the standard sweep width of $\Delta_{\mathrm{RF}} = 1.3$ kHz.

While the interlayer correlation results from directly merging the double-well were still taken in the short-wavelength lattice with the loss process in the doubles filling, we opted for the detection in the infrared z-lattice for the singlet-triplet oscillation experiment, presented in Section 6.4.2. To separate the signals of singly and doubly occupied lattice sites in the infrared z-lattice, we had to reduce the width of the RF sweep by nearly a factor of two to $\Delta_{\mathrm{RF}} = 700$ Hz. The resulting RF spectroscopy signal is shown in Figure 6.25. The transferred atoms appear in OD1 and the residuals in OD2. Even though the peaks corresponding to the transfer of either

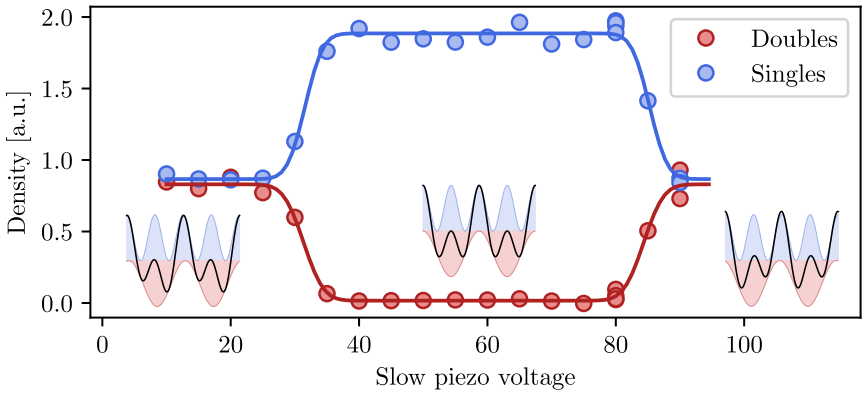

Figure 6.24: Dependence on the superlattice phase for the handover. We vary the endpoint of the ramp of the superlattice phase ϕ_g, see lower panel of 6.22, and observe that if we ramp up the short-wavelength lattice too close to the symmetric double-well configuration we split all the doubles into singles. Note that for the data set presented, we did not use the offset lock of the vertical superlattice, but instead we directly tuned the voltage of the slow Verdi piezo to increase the accessible range.

singly or doubly occupied sites (blue data points) are not clearly discernible, we still claim to fully separate the two contributions as the amount of singles in the residual data (red points) is not reduced at the resonance position of the doubles peak. However, as the window with a high transfer efficiency is only around 300 Hz wide, magnetic field drifts of merely 1 mG will already greatly affect the transfer. Therefore, the centre frequency of the sweep needs much more frequent adjustment.

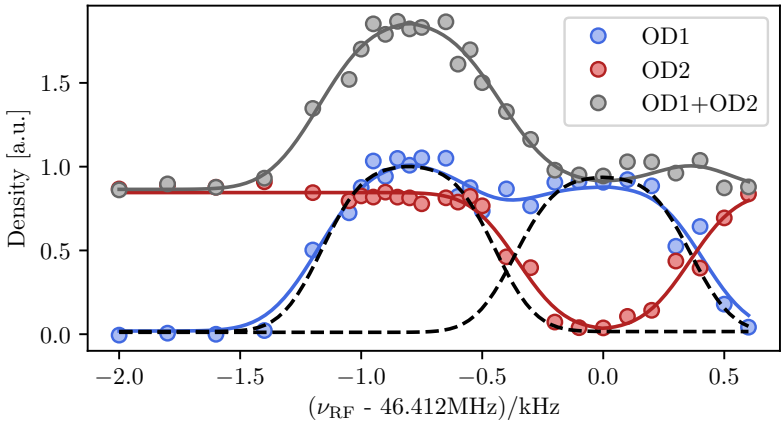

Figure 6.25: Singles-doubles separation in the long-wavelength vertical lattice. In the infrared z-lattice even for the maximum lattice depth of $V_{z,r} = 200E_{rec}$, the singles and doubles peak are separated by around 800 Hz only. We set the sweep width to $\Delta_{RF} = 700$ Hz to obtain a rather flat plateau of around 300 Hz, where the transferred amount of doubles is constant and contains a negligible contribution from singly occupied lattice sites. We reconstruct the individual doubles and singles peaks (black dashed lines) by subtracting the constant offset from a Gaussian fit to the sum signal OD1+OD2 and by inverting the singles dip visible in OD2, respectively.

Energy Eigenstates During Merging

I have already argued in simple terms that during the adiabatic removal of the barrier between the two horizontal layers, the double-well ground state is mapped onto the ground state of a single site, i.e. both particles occupying the lowest band. In the following, I want to investigate the eigenstates of the initial and final configuration in more detail. In particular, as the mirror symmetry of the double-well potential is conserved during merging, so are both the spatial and spin symmetry of the wavefunction. Therefore, these symmetries serve as an indicator to connect the eigenstates in the two limiting cases. Furthermore, I will discuss the on-site interaction shift in the final state, which decides whether we detect a single or a double occupancy with the narrow RF spectroscopy.

In Section 3.2 and in particular in Table 3.1, I have already investigated the double-well Hamiltonian and its eigenstates in detail. For fermions the ground state is a spin-singlet with a spatially symmetric wavefunction. In case of strong repulsive interactions the gap to the threefold degenerate triplet energy is given by the superexchange constant $J = 4t_\perp^2/U$. The spatial wavefunction of the spin triplet states is antisymmetric, and hence they do not experience an interaction shift mediated via s-wave collisions, $E_3 = 0$. The other two states, E_4 and E_2, hardly contribute at low temperatures, see Figure 6.26.

In the ground state of two (interacting) fermions in a single-well, both particles occupy

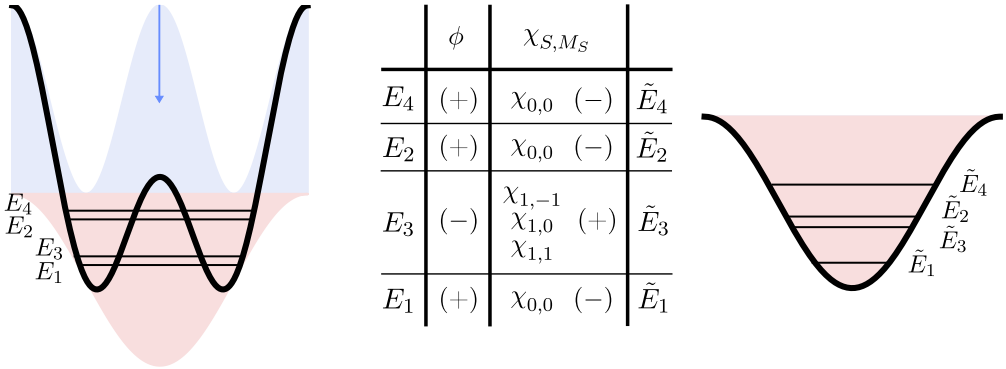

Figure 6.26: Sketch of the energy eigenstates during merging. When merging the double-well potential into a single site by ramping down the short-wavelength lattice (faint blue), the eigenenergies transform smoothly from E_i to $\tilde{E}_i$. The symmetry of both, the spatial (ϕ) and the spin (χ) wavefunction are conserved. The second lowest energy eigenstate is a spin triplet and hence, threefold degenerate.

the lowest (*ground*) band,[8] $|{\uparrow\downarrow}, 0\rangle_{ge}$. If we are able to spectroscopically separate the double occupancy in the ground band of a single well, from the other eigenstates, we indirectly measure the ground state probability of our experimentally prepared state projected on individual double-wells. We therefore need to calculate the on-site interaction shift for the eigenstates of a single well including higher bands.

On-Site Interaction in the Presence of Higher Bands For large enough lattice depths we may approximate a localized state in an optical lattice by the eigensolutions of the harmonic oscillator potential, which are the Hermite-Gaussian polynomials [176]

$$\phi_n(z) = \frac{1}{\sqrt{2^n n!}} \cdot \left(\frac{m\omega}{\pi\hbar}\right)^{1/4} \cdot e^{-\frac{m\omega z^2}{2\hbar}} \cdot H_n\left(\sqrt{\frac{m\omega}{\hbar}} z\right), \qquad n = 0, 1, 2, ... \tag{6.17}$$

Using this approximate solution we can estimate the on-site interaction felt by atoms in two arbitrary bands, a and b. Note that even though the corresponding eigenfunctions $\phi_a(x)$ and $\phi_b(x)$ might be orthogonal, they will in general still experience an on-site energy

$$U_{ab} \propto \int_{-\infty}^{\infty} |\phi_a(z)|^2 |\phi_b(z)|^2 \mathrm{d}z, \tag{6.18}$$

if there is a finite overlap of their probability densities [177]. The on-site interaction energy for two atoms in arbitrary bands in units of the standard Hubbard on-site shift $U_{00} \equiv U$ follows as

$$\frac{U_{ab}}{U_{00}} = \frac{\int_{-\infty}^{\infty} |\phi_a(z)|^2 |\phi_b(z)|^2 \mathrm{d}z}{\int_{-\infty}^{\infty} |\phi_0(z)|^4 \mathrm{d}z}. \tag{6.19}$$

If we insert the definition of the Hermite-Gaussian polynomials, we find that the relative interaction strength U_{ab}/U is independent of the experimental parameters such as the mass m and the eigenfrequency ω, which represents the lattice depth in the harmonic approximation. The numerical values are given in Figure 6.27.

[8] Due to Pauli's exclusion principle this is only possible for two particles with *opposite* spin.

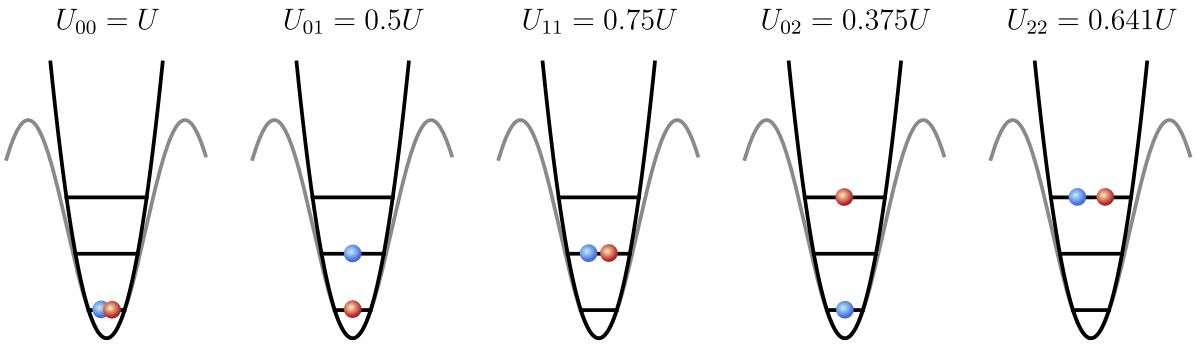

Figure 6.27: Band-dependent on-site energy. If the lattice depth is large enough, here $V = 60E_{\mathrm{rec}}$, the localized states of an optical lattice potential (grey) are well approximated by the lowest harmonic oscillator states $n = 0, 1, 2$ (black). Atoms residing in different band combinations experience a band-dependent on-site energy shift (not shown), which is given in units of $U_{00} \equiv U$. Note that for two atoms with opposite spin, which reside in different bands, the spatial wavefunction has to be properly antisymmetrized according to the spin-statistics theorem. This drastically affects the on the on-site interaction (see main text).

However, a proper many-body state has to conform to the spin-statistics theorem, and therefore the states $\phi_{ab}(z) = \phi_a(z) \otimes \phi_b(z)$ and $\phi_{ba}(z) = \phi_b(z) \otimes \phi_a(z)$ will get mixed to form a symmetric $(+)$ and an antisymmetric $(-)$ spatial wavefunction

$$\phi_{ab}^{\pm}(z) = \frac{1}{\sqrt{2}} \left(\phi_a(z) \otimes \phi_b(z) \pm \phi_a(z) \otimes \phi_b(z) \right), \quad \text{for } a \neq b. \tag{6.20}$$

There is a peculiarity about the on-site energy shift experienced by two atoms, which are in a superposition state of two different bands. If we consider both the symmetric and the antisymmetric superposition of two atoms in different bands a and b, we will find that the on-site interaction is given by

$$\frac{U_{ab}^{\pm}}{U} = \frac{\int_{-\infty}^{\infty} |\phi_{ab}^{\pm}(z)|^2 \mathrm{d}z}{\int_{-\infty}^{\infty} |\phi_0(z)|^4 \mathrm{d}z} = \frac{1}{2} \frac{\int_{-\infty}^{\infty} (2 \pm 2) |\phi_a(z)\phi_b(z)|^2 \mathrm{d}z}{\int_{-\infty}^{\infty} |\phi_0(z)|^4 \mathrm{d}z} = \begin{cases} 2U_{ab}/U & \text{for } \phi_{ab}^{+}, \\ 0, & \text{for } \phi_{ab}^{-}. \end{cases} \tag{6.21}$$

While the symmetric superposition seems to experience an enhancement in on-site energy by a factor of two, the antisymmetric superposition does not have any on-site energy shift at all. This was expected, since two ultracold fermions interact via s-wave collisions only, which requires a spatially symmetric wavefunction [178].

This effect may also be understood using the Fock state description for a single site. For this purpose we employ a set of basis states $\{|\uparrow\downarrow, 0\rangle_{ab}, |\uparrow, \downarrow\rangle_{ab}, |\downarrow, \uparrow\rangle_{ab}, |0, \uparrow\downarrow\rangle_{ab}\}$[9] where the first (second) entry specifies the occupation of the lower (higher) lying band with index a (b), as indicated by the subscript. In a multi-band description of the Hubbard model for a single site, the contact interaction does not only lead to an on-site energy shift, but extended Hubbard parameters have to be considered, such as a spin flip process [178], which couples the two Fock states $|\uparrow, \downarrow\rangle_{ab}$ and $|\downarrow, \uparrow\rangle_{ab}$. The Hamiltonian in the restricted space, where the two particles

[9] Similar to the description of the double-well (see Equation 3.24) we choose the ordering of the fermionic creation operators in the basis state definition as $\hat{c}_{b\downarrow}\hat{c}_{b\uparrow}\hat{c}_{a\downarrow}\hat{c}_{a\uparrow}|0\rangle$.

reside in different bands, is given by[10]

$$\begin{pmatrix} U_{ab} & -U_{ab} \\ -U_{ab} & U_{ab} \end{pmatrix}. \tag{6.22}$$

By diagonalising this matrix we obtain the same result as above, namely that the on-site energy vanishes for the triplet states. In Table 6.1 we summarize the results for the lowest four states of a single well, including the on-site energy, the symmetries of the wavefunction and the state description in second quantization.

Eigenenergy	$\lvert\phi\rangle$	$\lvert\chi_{S,M_S}\rangle$	$\lvert\psi\rangle$
$\tilde{E}_1 = \hbar\omega + U_{00}$	ϕ_{00} $(+)$	$\lvert\chi_{0,0}\rangle$ $(-)$	$\lvert\uparrow\downarrow, 0\rangle_{01}$
$\tilde{E}_2 = 3\hbar\omega + 2U_{01}$	ϕ_{01}^{+} $(+)$	$\lvert\chi_{0,0}\rangle$ $(-)$	$\frac{1}{\sqrt{2}}\left(\lvert\uparrow,\downarrow\rangle_{01} - \lvert\downarrow,\uparrow\rangle_{01}\right)$
$\tilde{E}_3 = 3\hbar\omega$	ϕ_{01}^{-} $(-)$	$\lvert\chi_{1,-1}\rangle$ $(+)$	$\lvert\downarrow,\downarrow\rangle_{01}$
		$\lvert\chi_{1,0}\rangle$ $(+)$	$\frac{1}{\sqrt{2}}\left(\lvert\uparrow,\downarrow\rangle_{01} + \lvert\downarrow,\uparrow\rangle_{01}\right)$
		$\lvert\chi_{1,1}\rangle$ $(+)$	$\lvert\uparrow,\uparrow\rangle_{01}$
$\tilde{E}_4 = 5\hbar\omega + U_{11}$	ϕ_{11} $(+)$	$\lvert\chi_{0,0}\rangle$ $(-)$	$\lvert 0, \uparrow\downarrow\rangle_{01}$

Table 6.1: Eigenstates of two interacting fermions in a single well. We approximate the eigenenergies of a single deep well by the harmonic oscillator levels, the ground (0) and the first excited (1) band. The spatial symmetry and the spin wavefunction match the corresponding eigenstate in a double-well potential, compare Table 3.1 and Figure 6.26.

From the analysis of the on-site interaction we can draw the following conclusion: The ground state of the double-well, $|\psi_1\rangle$ is mapped to a double occupancy in the lowest band of the single well with an on-site shift of $E_{\text{int}} = U_{00} = U$. The spin triplet state $|t_0\rangle$ features an antisymmetric spatial part. The symmetry is conserved during the merging process, hence it will be transformed to ϕ_{01}^{-}, for which the on-site energy shift vanishes. Therefore, we will detect particles that are in the triplet state in the initial double-well configuration as singles after merging. The same holds for the other two triplet states $|t_+\rangle$ and $|t_-\rangle$, which also possess a spatially antisymmetric wavefunction. For strong repulsive interactions the remaining two states of the double-well are gapped by the on-site energy as they mostly contain doubles. Therefore, it is unlikely that they are populated, at least in the case of low $t_\perp$. The on-site energy shift corresponding to the initial $|d_-\rangle$ state is $E_{\text{int}} = 2U_{01} = U$ and hence, we would detect it as a double, while for the highest energy state considered $E_{\text{int}} = U_{11} = 0.75U$ the energy shift is reduced and we should observe an additional peak in the spectrum. This is however not the case and hence, we assume that the excited states $|\psi_2\rangle$ and $|\psi_4\rangle$ do not play a significant role. Therefore, we can conclude that we are able to distinguish the double-well ground state from the triplet states by selectively detecting single and double occupancies after merging.

[10] In our case, pair hopping may be neglected as the band separation of the lowest two bands is much larger for a single site than for a double-well.

Data Analysis and Results

In the following, I will briefly explain how we analysed the density obtained after merging along the vertical direction and how to extract an estimate on the amount of spin correlations within the double-well. More details may be found in the PhD thesis of my colleague M. Gall [137].

Our aim is to calculate the interlayer spin correlator, C_z, which quantifies magnetic correlations between opposing sites of the two bilayer planes, labelled as $m = \{1, 2\}$. It is defined as an average over the in-plane directions

$$C_z = -\frac{1}{N}\sum_{i=1}^{N}\left[\langle \hat{S}^z_{1i}\hat{S}^z_{2i}\rangle - \langle \hat{S}^z_{1i}\rangle \langle \hat{S}^z_{2i}\rangle\right]. \tag{6.23}$$

The ground state of the double-well potential approaches the spin singlet state, $|s\rangle$, in the $U/t_\perp \to \infty$ limit. For this state the spin correlator assumes its maximum value

$$C_z = -\langle s|\hat{S}^z_1\hat{S}^z_2|s\rangle = \frac{1}{4}. \tag{6.24}$$

However, as we learnt in the last section, the merging protocol accesses the ground state overlap, which is proportional to the singlet fraction only in the $U/t_\perp \to \infty$ limit. In general, even the ground state contains a finite double admixture in form of the $|d_+\rangle$ state. Therefore, if we estimate the vertical spin correlator C_z via the ground state fraction from the merging procedure, we would overestimate the amount of spin correlations, as the doubles do not possess magnetization and hence

$$C_z = -\langle d_+|\hat{S}^z_1\hat{S}^z_2|d_+\rangle = 0. \tag{6.25}$$

To account for the finite doubles admixture of the double-well ground state, we subtract the amount of doubles that are present in either plane before merging from the doubles filling after merging[11]. In Figure 6.28 we show the total doubles filling of both coupled layers before merging, n_D^0, and compare it to the doubles filling after merging, n_D. From the simple estimate, we expect the difference (red shading) to be proportional to the interlayer correlator according to

$$C_z = \frac{1}{4}(n_D - n_D^0). \tag{6.26}$$

The factor 1/4 arises, since we obtain a doubles filling of $n_D - n_D^0 = n_D = 1$ after merging, if each double-well was occupied by a spin singlet state, $|s\rangle$. Figure 6.28 b) shows the measured interlayer correlations as a function of the interlayer tunnel coupling strength. We observe that increasing $t_\perp$ enhances the interlayer correlations, which are a key feature of the band insulator phase. We compare our results to DQMC data and find nice agreement over the investigated range, with minor deviations at very small and very large $t_\perp$. Furthermore, the interlayer correlations show the opposite behaviour to that of the intralayer correlations discussed in Figure 6.19. Therefore, we conclude that by tuning the interlayer coupling, we observe the crossover from the antiferromagnetic Mott insulator to the band insulator at elevated temperatures [171].

[11] In the following section we will see that this is not entirely correct, but it still yields a good estimate.

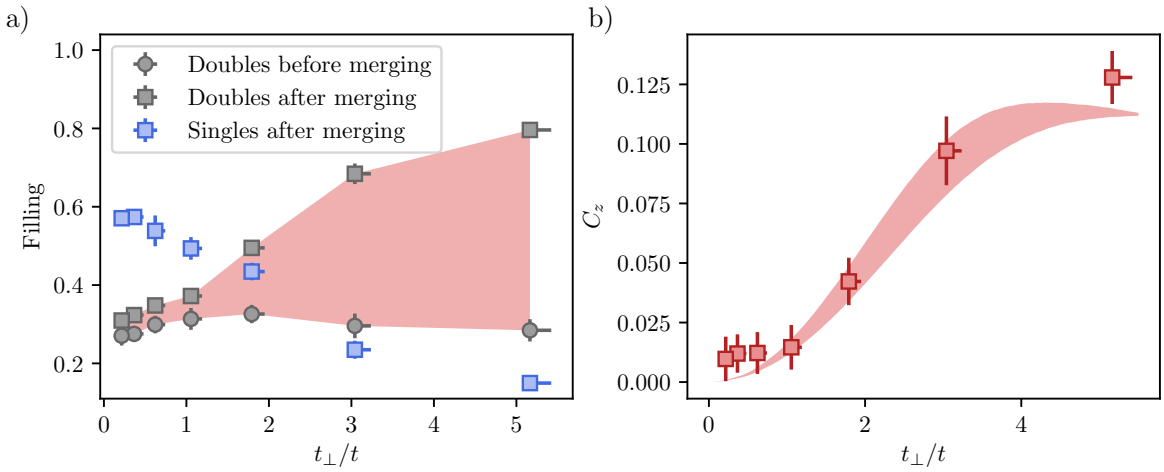

Figure 6.28: Interlayer spin correlations by merging the double-well. a) We plot the singles and doubles filling before and after merging for a single unit cell of the vertical lattice. Note that the "singles filling" after merging also includes sites where two particles occupy different bands (triplets). In b) we plot the interlayer spin correlator, C_z, which is inferred from the difference in doubles filling before and after merging (indicated by the red shaded area in the left plot). We compare the interlayer correlator to DQMC data (shaded area) with $n = 0.42$, $k_B T/t = 1.0t - 1.4t$ and $U/t = 8$. These results have been published in [171].

Investigating the Offset Correlations

So far, we subtracted the amount of doubles that we had in both planes before merging to account for the discrepancy between ground state overlap and antiferromagnetic interlayer correlations. In the following I will investigate whether these offset correlations are indeed related to double occupancies before merging. For this purpose, we implement two additional RF sweeps, which transfer the population from $|m_F = -7/2\rangle$ to $|m_F = -3/2\rangle$ to get rid off the double occupancies. Since the RF sweeps change the combination of magnetic hyperfine states, the on-site interaction strength changes, see Figure 4.2. Therefore, they have to take place when the many-body state cannot react to this change in U. This is achieved by quickly freezing the motion along all lattice directions by ramping the lattice depths to $\{V_{xy,r}, V_{z,g}\} = \{30, 110\}E_{\mathrm{rec}}$ directly after splitting, which projects onto the strongly interacting Hubbard eigenstates, $\{|s\rangle, |t_0\rangle, |d_-\rangle, |d_+\rangle\}$. The two additional sweeps are inserted after freezing, and we consecutively merge two neighbouring z-lattice planes by ramping down the short-wavelength lattice to zero. In Figure 6.29 we show the effect on the filling of both singly and doubly occupied sites after merging. We do not apply the RF tomography scheme to resolve the filling of a single layer, which reduces the measurement time. On the contrary, the data can only provide a qualitative assessment, as we average over several layers with different filling. There is a significant discrepancy in the amount of doubles, if $t_\perp/t > 2$. This matches the expectation from a single double-well potential, where the admixture of the $|d_+\rangle$ state to the ground state quickly decreases as a function of $U/t_\perp$, see Figure 3.3. For the largest value of $t_\perp$, the on-site interaction is on the order of $U/t_\perp \approx 1.5$, and the corresponding doubles contribution (at half-filling) is around 30%. This nicely matches our results on the difference in doubles filling with and without doubles removal. In contrast, for low interlayer coupling the effective on-site interaction $U/t_\perp$ is large and therefore the ground state overlap with the $|d_+\rangle$ nearly vanishes. Even though, it is not ideal to compare the bilayer

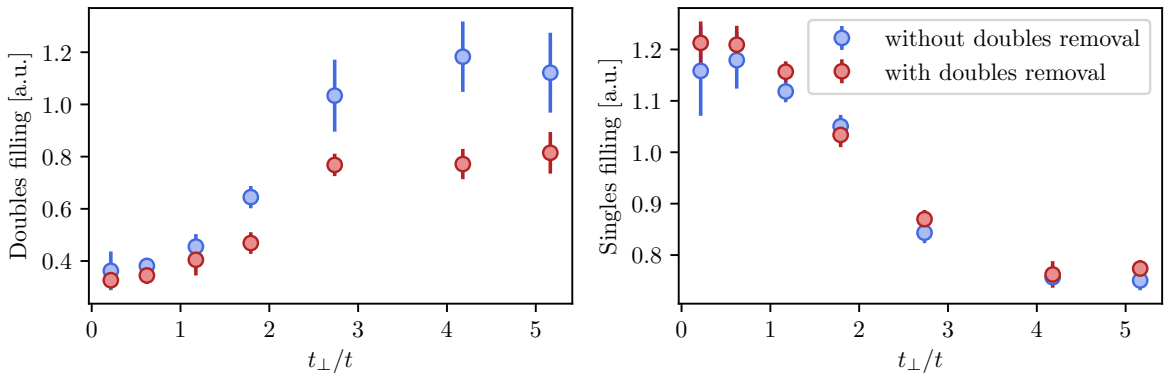

Figure 6.29: Effect of the removal of double occupancies. We investigate the filling of doubles (a) and singles (b) after merging without applying the RF tomography scheme. If we remove the double occupancies before merging the double-well, the doubles filling changes drastically for large $t_\perp/t > 2$, while it is essentially unchanged for weak interlayer coupling. The legend applies to the whole figure. The error bars represent the standard deviation including around six repetitions.

lattice to the double-well at low $t_\perp$, we find also experimentally that the doubles filling after merging is hardly affected by the removal of the doubles, if $t_\perp/t < 1$. As expected, the singles filling after merging is not affected by the removal of double occupancies before merging. This is reasonable as only the triplet states of the double-well potential, which do not possess a doubles admixture, merge to a single occupancy.

I conclude that the doubles fraction before merging only significantly affects the inferred interlayer correlator for large values of $t_\perp$. The inaccuracy in the previous reasoning was to assume that for $U > T$ all doubles that are present before merging stem from the double-well ground state. While this is indeed a reasonable assumption for large $t_\perp$, where the experimentally prepared state has a large overlap with the double-well eigenstates, this assumption fails at small $t_\perp$, where the double-well is essentially uncorrelated. Therefore, subtracting the initial doubles filling n_D^0, as done in Figure 6.28, was unjustified at small $t_\perp$, as they would not merge to doubles. This in turn means that in the discussion so far we have overlooked another source contributing to the offset correlations in particular at low interlayer coupling, since it is unphysical to obtain interlayer spin correlations when there is negligible tunnel coupling along the double-well direction.

6.4.2 Interlayer Correlations via Singlet-Triplet Oscillations

From the last section it still remains unclear why we observe a significant amount of doubles for low interlayer coupling after merging. Therefore, in this part I will start by investigating how a state that is uncorrelated along the double-well direction is represented in the double-well basis.

Interlayer Correlations versus Singlet Fraction

There are two aspects about the procedure presented in the last paragraph that complicate the measurement of the interlayer correlations: We have shown experimentally that the finite amount of double occupancies in the state that is prepared by splitting the bilayer will increase the amount of doubles that we measure after merging. However, even when setting this aside, there remains one problem, namely that we measure the singlet fraction and deduce the vertical

spin correlator from it. In general there are two cases, where the system does not exhibit any spin correlations along the vertical direction, even though there is a finite probability to occupy the singlet state: Either the temperature is much larger than the superexchange energy scale, $T \gg J = 4t^2/U$ and therefore the singlet and triplet states will be equally populated, or the correlations form along another bond that is more strongly coupled, e.g. for $t_\perp \ll t$. In the following, I will focus on the latter scenario and study a four site plaquette with strong coupling along the x-direction and negligible tunnelling along the perpendicular, z-direction, as sketched in Figure 6.30. At low temperature and strong repulsive interactions, I expect the ground state

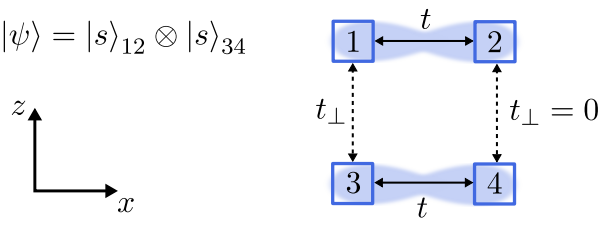

Figure 6.30: Spin correlations in contrast to singlet fraction. The approximate ground state for strong repulsive interactions, $U \gg t$, and negligible perpendicular tunnelling, $t_\perp$, is the direct product of two singlets oriented along the x-direction. While we do not expect to observe correlations along the perpendicular bond, in general a finite amount of singlet fraction will be observed. In the particular case shown, the overlap with a singlet along the vertical bond is $|\langle s_{13}|\psi\rangle|^2 = 0.25$.

to show antiferromagnetic correlations along the two bonds that are parallel to the x-direction,

$$|\psi\rangle = \frac{1}{\sqrt{2}}(|\uparrow,\downarrow\rangle_{12} - |\downarrow,\uparrow\rangle_{12}) \otimes \frac{1}{\sqrt{2}}(|\uparrow,\downarrow\rangle_{34} - |\downarrow,\uparrow\rangle_{34}) \tag{6.27}$$

$$= \frac{1}{2}\left[|\uparrow,\uparrow\rangle_{13}|\downarrow,\downarrow\rangle_{24} + |\downarrow,\downarrow\rangle_{13}|\uparrow,\uparrow\rangle_{24} - |\uparrow,\downarrow\rangle_{13}|\downarrow,\uparrow\rangle_{24} - |\downarrow,\uparrow\rangle_{13}|\uparrow,\downarrow\rangle_{24}\right]. \tag{6.28}$$

For simplicity, the finite doubles admixture is neglected. I compute the reduced density matrix of the subsystem including sites 1 and 3 in the basis $\{|\uparrow,\uparrow\rangle_{13}, |\downarrow,\downarrow\rangle_{13}, |\uparrow,\downarrow\rangle_{13}, |\downarrow,\uparrow\rangle_{13}\}$ by performing a partial trace

$$\rho_{13} = \mathrm{Tr}_{24}|\psi\rangle\langle\psi| = \frac{1}{4}\begin{pmatrix} 1 & 0 & 0 & 0 \\ 0 & 1 & 0 & 0 \\ 0 & 0 & 1 & 0 \\ 0 & 0 & 0 & 1 \end{pmatrix}. \tag{6.29}$$

This reduced density matrix describes a mixed state with equal probabilities for obtaining the singlet or either of the three triplet states[12]

$$\rho_{13} = 0.25 \cdot [|s\rangle\langle s| + |t_0\rangle\langle t_0| + |t_+\rangle\langle t_+| + |t_-\rangle\langle t_-|]. \tag{6.30}$$

[12] Density matrices of the singlet and triplet state are given by

$$|s\rangle\langle s| = \frac{1}{2}\begin{pmatrix} 0 & 0 & 0 & 0 \\ 0 & 0 & 0 & 0 \\ 0 & 0 & 1 & -1 \\ 0 & 0 & -1 & 1 \end{pmatrix}, \quad |t_0\rangle\langle t_0| = \frac{1}{2}\begin{pmatrix} 0 & 0 & 0 & 0 \\ 0 & 0 & 0 & 0 \\ 0 & 0 & 1 & +1 \\ 0 & 0 & +1 & 1 \end{pmatrix}.$$

Therefore I have shown that a state with perfect singlet correlations along the x-direction, may be described along the z-direction by equal probabilities for the singlet and the three triplet states. As shown in Table 6.2, for negligible tunnel coupling along the vertical lattice direction, the spin correlator of the corresponding bond vanishes, as expected. Hence, a finite singlet fraction, as quantified by merging the double-well into a single well, does not imply a finite spin correlator.

	$\lvert s\rangle$	$\lvert t_0\rangle$	$\lvert\uparrow,\uparrow\rangle$	$\lvert\downarrow,\downarrow\rangle$	$\lvert t_+\rangle$	$\lvert t_-\rangle$
$\langle\hat{S}_1^x\hat{S}_2^x\rangle$	$-\frac{1}{4}$	$+\frac{1}{4}$	0	0	$+\frac{1}{4}$	$-\frac{1}{4}$
$\langle\hat{S}_1^y\hat{S}_2^y\rangle$	$-\frac{1}{4}$	$+\frac{1}{4}$	0	0	$-\frac{1}{4}$	$+\frac{1}{4}$
$\langle\hat{S}_1^z\hat{S}_2^z\rangle$	$-\frac{1}{4}$	$-\frac{1}{4}$	$+\frac{1}{4}$	$+\frac{1}{4}$	$+\frac{1}{4}$	$+\frac{1}{4}$

Table 6.2: Spin correlations on the double-well. The spin singlet state is SU(2) symmetric by its own, therefore the three correlators are equal. In contrast, the triplet states need to be weighted equally to conform to SU(2) symmetry. If in addition all four states are equally populated, the spin correlations vanish along all directions in spin space. This is for example the case, if the temperature is much larger than the superexchange constant or if the tunnel coupling is much stronger along a different lattice direction, as sketched in Figure 6.30.

Principle of Singlet-Triplet Oscillations

In the last section it has become clear that a system containing an equal amount of the singlet and each triplet state does not possess spin correlations. Only if the number of singlets exceeds the amount of triplets, we will find antiferromagnetic correlations. Therefore, we implemented an experimental scheme, which induces oscillations between the singlet, $|s\rangle$, and the triplet state, $|t_0\rangle$, in order to access their imbalance via the oscillation amplitude [153, 173]. The protocol is explained in detail in the PhD thesis of D. Greif [59], and I will only summarize the main important aspects in the following.

The principle of singlet-triplet oscillations (STO) relies on the ability to rotate a singlet into a triplet state and vice versa, by applying a magnetic field gradient. This effect was already successfully exploited for the coherent manipulation of spin correlations in Chapter 5 with an in-plane magnetic field gradient. In contrast, to extract the interlayer spin correlator, we need to apply the gradient along the vertical direction. If there is a differential energy shift for the two spin states, i.e. if the slopes in the Breit-Rabi diagram are not the same, then the degeneracy of $|\uparrow,\downarrow\rangle$ and $|\downarrow,\uparrow\rangle$ is lifted[13]. Consequently, these two basis states will acquire different time evolution phase factors, which will ultimately rotate a singlet into a triplet state and vice versa. If we start from a singlet state $|s\rangle$ along the vertical double-well direction at time $t_{\mathrm{STO}} = 0$, the state evolves in the presence of a magnetic field gradient $\nabla_z B_z$ that was suddenly turned on[14] according to

$$|\psi(t_{\mathrm{STO}})\rangle = \frac{1}{\sqrt{2}}\left[|\uparrow,\downarrow\rangle\, e^{-\frac{i}{2\hbar}(\Delta E_\uparrow - \Delta E_\downarrow)t_{\mathrm{STO}}} - |\downarrow,\uparrow\rangle\, e^{\frac{i}{2\hbar}(\Delta E_\uparrow - \Delta E_\downarrow)t_{\mathrm{STO}}}\right], \tag{6.31}$$

[13] In addition the magnetic field gradient breaks the SU(2) symmetry.

[14] The experimental timescales in the frozen lattice configuration are rather long, therefore this is not a very restrictive requirement.

where $\Delta E_\uparrow = \gamma_\uparrow \nabla_z B_z a_z$. After a certain time $t_{\mathrm{STO}} = t_\pi$, neighbouring sites have acquired a relative phase of π in the equatorial plane of the Bloch sphere,

$$\frac{\Delta E_\uparrow - \Delta E_\downarrow}{\hbar} t_\pi = \pi \tag{6.32}$$

and consequently the singlet state has transformed into the $|t_0\rangle$ state. By making use of $\sqrt{2}\,|\uparrow,\downarrow\rangle = |t_0\rangle + |s\rangle$ and $\sqrt{2}\,|\downarrow,\uparrow\rangle = |t_0\rangle - |s\rangle$, we can express the time-evolved state as

$$|\psi(t_{\mathrm{STO}})\rangle = \cos\left(\frac{\Delta E_\uparrow - \Delta E_\downarrow}{2\hbar} t_{\mathrm{STO}}\right)|s\rangle + i \sin\left(\frac{\Delta E_\uparrow - \Delta E_\downarrow}{2\hbar} t_{\mathrm{STO}}\right)|t_0\rangle\,. \tag{6.33}$$

Therefore, we conclude that a magnetic field gradient oriented along the double-well direction rotates the singlet state $|s\rangle$ into the triplet state $|t_0\rangle$ and vice versa. If initially only the singlet state is populated, we expect to observe singlet-triplet oscillations (STO) with full contrast. In general, the STO amplitude is proportional to the amount of excess singlets in the system.[15] In the limiting case, when there is an equal mixture of singlet and triplet states initially, the amplitude of the STO signal vanishes, which is the indicator for an uncorrelated bond.

To observe these oscillations in the populations induced by the vertical gradient, we consecutively merge the double-well similar to Section 6.4.1 in order to differentiate singlet and triplet states by their on-site interaction shift in the final state.

Observable in the STO Measurement Before proceeding to the implementation of the STO scheme into our experimental setup, I will review in the following that by measuring the imbalance of singlet and triplet states we indeed access the transverse spin correlator [59, 69], $C_z^\perp$, which typically is defined as the sum of the xx- and yy-correlators

$$C_z^\perp = \langle \hat{S}_1^x \hat{S}_2^x \rangle + \langle \hat{S}_1^y \hat{S}_2^y \rangle = \frac{1}{2}\left\langle \hat{c}_{1\downarrow}^\dagger \hat{c}_{1\uparrow} \hat{c}_{2\uparrow}^\dagger \hat{c}_{2\downarrow} + \hat{c}_{1\uparrow}^\dagger \hat{c}_{1\downarrow} \hat{c}_{2\downarrow}^\dagger \hat{c}_{2\uparrow} \right\rangle. \tag{6.34}$$

For this purpose we need to define two operators creating either the singlet or the triplet state along the double-well direction[16]

$$|s\rangle = \hat{s}^\dagger |0\rangle = \frac{1}{\sqrt{2}}\left(\hat{c}_{2,\downarrow}^\dagger \hat{c}_{1,\uparrow}^\dagger - \hat{c}_{2,\uparrow}^\dagger \hat{c}_{1,\downarrow}^\dagger\right)|0\rangle\,, \tag{6.35}$$

$$|t_0\rangle = \hat{t}_0^\dagger |0\rangle = \frac{1}{\sqrt{2}}\left(\hat{c}_{2,\downarrow}^\dagger \hat{c}_{1,\uparrow}^\dagger + \hat{c}_{2,\uparrow}^\dagger \hat{c}_{1,\downarrow}^\dagger\right)|0\rangle\,. \tag{6.36}$$

Then the corresponding observables, the singlet fraction n_S and the triplet fraction n_T, follow from the general definition of the occupation number in second quantization as

$$n_S = \langle \hat{s}^\dagger \hat{s} \rangle = \frac{1}{2}\left\langle \hat{n}_{2\downarrow}\hat{n}_{1\uparrow} + \hat{n}_{2\uparrow}\hat{n}_{1\downarrow} - \hat{c}_{2\uparrow}^\dagger \hat{c}_{1\downarrow}^\dagger \hat{c}_{1\uparrow}\hat{c}_{2\downarrow} - \hat{c}_{2\downarrow}^\dagger \hat{c}_{1\uparrow}^\dagger \hat{c}_{1\downarrow}\hat{c}_{2\uparrow} \right\rangle, \tag{6.37}$$

$$n_T = \langle \hat{t}_0^\dagger \hat{t}_0 \rangle = \frac{1}{2}\left\langle \hat{n}_{2\downarrow}\hat{n}_{1\uparrow} + \hat{n}_{2\uparrow}\hat{n}_{1\downarrow} + \hat{c}_{2\uparrow}^\dagger \hat{c}_{1\downarrow}^\dagger \hat{c}_{1\uparrow}\hat{c}_{2\downarrow} + \hat{c}_{2\downarrow}^\dagger \hat{c}_{1\uparrow}^\dagger \hat{c}_{1\downarrow}\hat{c}_{2\uparrow} \right\rangle. \tag{6.38}$$

[15] In principle, also an excess of triplet states could be detected this way. This is, however, not relevant for this thesis.

[16] Fermionic ordering $\hat{c}_{2\downarrow}\hat{c}_{2\uparrow}\hat{c}_{1\downarrow}\hat{c}_{1\uparrow}|0\rangle$.

If we now compare the definition of the transverse spin correlator $C_z^{\perp}$ with the singlet and triplet fractions, we obtain the final relation [59, 69]

$$C_z^{\perp} = -\frac{n_S - n_T}{2}. \tag{6.39}$$

For an SU(2) symmetric state the spin correlators are equal [166]

$$\langle \hat{S}_i^x \hat{S}_j^x \rangle = \langle \hat{S}_i^y \hat{S}_j^y \rangle = \langle \hat{S}_i^z \hat{S}_j^z \rangle \,, \tag{6.40}$$

therefore the interlayer correlator in the z-basis of the spin follows as

$$C_z = -\frac{n_S - n_T}{4}. \tag{6.41}$$

This is the quantity that will be computed in the following to compare the results of the STO measurement to the interlayer correlations inferred by directly merging the double-well potential.

Implementation of the Singlet-Triplet Oscillations

The main ingredient for the implementation of the singlet-triplet oscillations is the vertical magnetic field gradient, which we generate by the fast Feshbach coils connected in anti-Helmholtz configuration. This creates a quadrupole field with the magnetic field zero located somewhere below the atom cloud and slightly shifted in the xy-direction. Therefore, the magnetic field gradient will obtain a finite in-plane component, which we do not compensate, as it will only lead to minor dephasing within the layer.

After splitting the single-band band insulator, we quickly freeze the motion along all directions within 150 µs, see Figure 6.31 and consecutively remove the double occupancies by spin-changing collisions as they do not contribute to spin correlations. At this point, with the motion frozen, we ramp up the current I_{STO} generating the magnetic quadrupole field within 1 ms. To observe the oscillations in the population of singlets, we decided to scan the strength of the magnetic field gradient instead of the hold time. This minimizes the impact of time-dependent field drifts.[17] The atoms experience the full gradient strength over a hold time of 20 ms. After ramping down the current, we merge the double-well into a single site. If the vertical bond is occupied by two atoms in the spin singlet state, $|s\rangle$, they are both mapped to the lowest band of the merged lattice, see Figure 6.31. In contrast, for a triplet state, the spatial wavefunction of the two atoms has to remain antisymmetric during the merging procedure, i.e. one of the atoms has to end up in the first excited band of the merged lattice. Due to the isotropic character of the s-wave scattering potential, the on-site interaction shift vanishes in this case. We resolve the on-site interaction shift by a narrow RF pulse, see Figure 6.25. The doubles filling after merging is shown in the top row of Figure 6.32 for varying interlayer tunnel coupling strength. We apply a sinusoidal fit without damping to the double occupancy where both the frequency and phase are fixed by the results for large $t_{\perp}$. In principle, it is not necessary to sample a full period of the oscillation, as we can infer the difference in singlet and triplet filling from the two

[17] In contrast, for the measurement of intralayer correlations, the time is varied. As the dissipated power scales quadratically with current, but only linear in time, it is in general more sensible to scan the time if the coil is limited by the power it may dissipate. This is, however, not a problem for the measurement of the interlayer correlations.

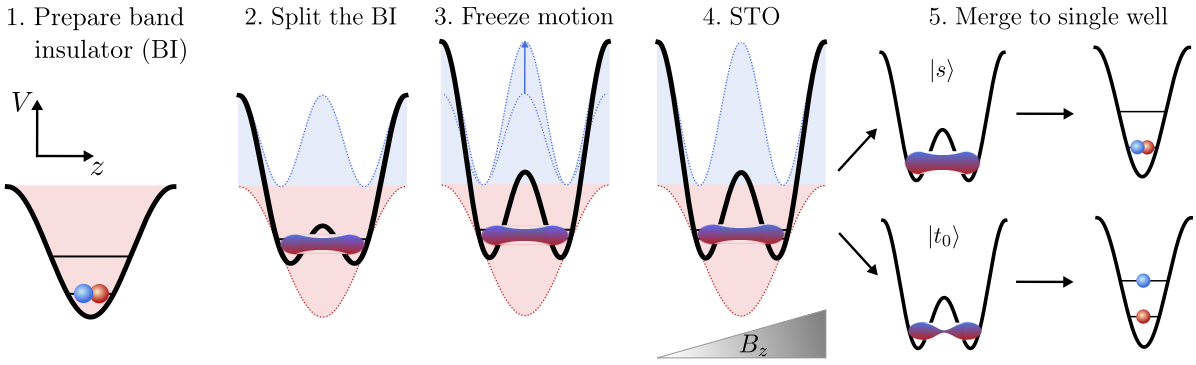

Figure 6.31: Experimental scheme for the detection of singlet-triplet oscillations. We start by preparing a band insulator in the lowest band of the long-wavelength lattice, which is split by ramping up the short-wavelength lattice. After freezing the motion along both the vertical and the in-plane directions (latter not shown), we remove double occupancies. Consecutively, the magnetic field gradient $\nabla_z B_z$ is ramped up and induces singlet-triplet oscillations (STO). After a hold time t_{STO}, the short-wavelength lattice is slowly turned off within 40 ms. This merges the double-well into a single site and enables us to differentiate between singlet and triplet states according to their distinct shift of the on-site energy in the final state.

extreme cases, where the doubles filling after merging is minimal/maximal. However, the result from a sinusoidal fit is much more reliable, as we do not have to calibrate and readjust the π-point of the oscillation. Note that atoms, which are in the triplet state $|t_0\rangle$ at the end of the STO, seem to get lost. Therefore, the singles filling after merging is approximately constant and does not show oscillations as we would have expected. Since we have verified that the atoms are completely lost from the trap, it might be that they are transferred to higher energy bands, which become untrapped at some point in the detection scheme.

For low interlayer coupling strength the doubles filing after merging does not oscillate. This is a clear indicator for vanishing interlayer spin correlations. Nevertheless, the offset at $I_{\mathrm{STO}} = 0$, represents singlet bonds. However, since there are as many triplet bonds, $|t_0\rangle$, in the system, the spin correlations cancel each other, see Equation 6.41. When the tunnel coupling in the double-well direction exceeds the one within the layer, pronounced oscillations are visible in the doubles filling after merging, see Figure 6.32 b) and c). While the amplitude of the STO (faint blue area) increases with the ratio $t_\perp/t$, signalling enhanced spin correlations, the amount of triplet states decreases significantly (faint red area). Therefore, evaluating spin correlations along the double-well direction by simply measuring the singlet fraction overestimates the interlayer correlator, C_z mostly at low $t_\perp$.

In Figure 6.32 d) we compare the increase in singlet bonds starting from the uncorrelated regime at $t_\perp \approx 0$ to the reduction in the triplet state, $|t_0\rangle$. As the quantum many-body state has to conform to SU(2) symmetry before starting the singlet-triplet oscillations, the occupation of the triplet states $|t_+\rangle$ and $|t_-\rangle$ is expected to be equal to the $|t_0\rangle$ state. The total reduction of the triplet states is mirrored by an increase in the ground state fraction including the contributions from $|s\rangle$ and $|d_+\rangle$. However, the relative occurrence of $|d_+\rangle$ and $|s\rangle$ is determined by the interplay of the on-site interaction and the kinetic energy and precludes the determination of the interlayer correlator by the triplet reduction alone. Therefore, we need the additional measurement of the singlet fraction at $I_{\mathrm{STO}} = 0$ to determine the interlayer correlator.

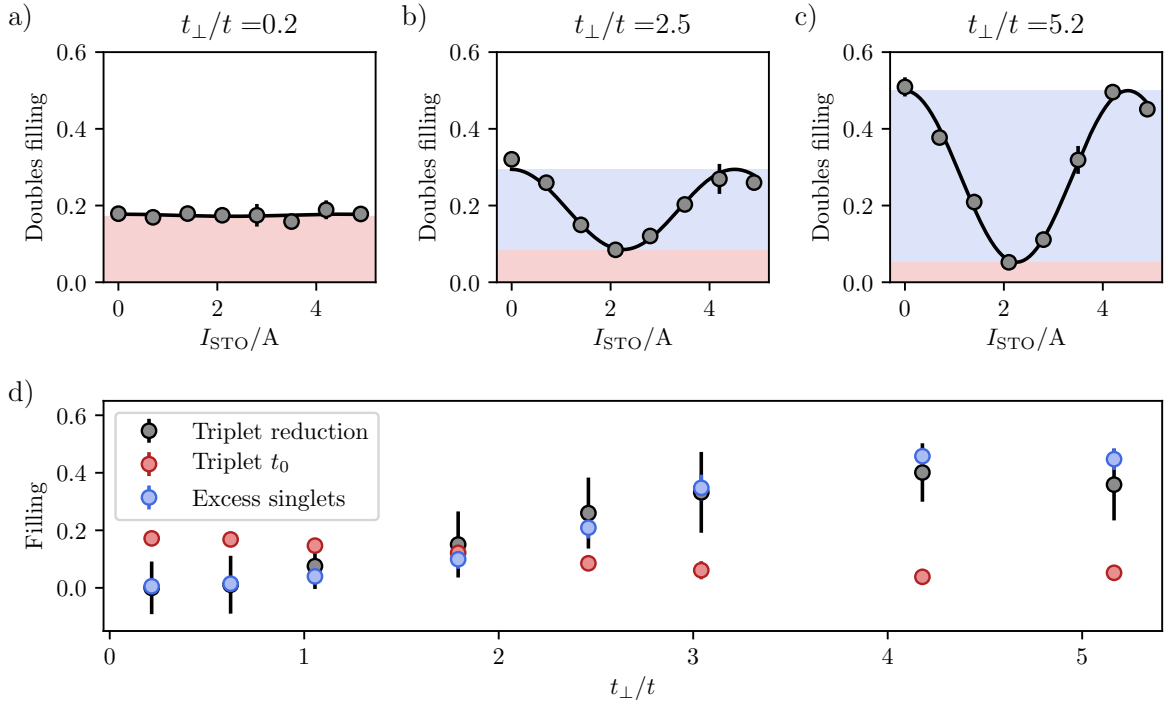

Figure 6.32: Analysis of the singlet-triplet oscillations. We investigate the doubles filling after merging for varying interlayer coupling strength, $t_\perp$. For low $t_\perp$, the number of singlet and triplet states are equal, see Equation 6.30, therefore, we do not observe singlet-triplet oscillations. In contrast, when increasing the coupling strength within the double-well, the number of singlet (and doublon) bonds grows at the expense of the triplet states, as the state tries to minimize its kinetic energy. For each realization, we average the local doubles filling within the central region over several thousand individual double-well potentials and obtain a tiny standard error on the mean filling for each realization. The error bars in a) - c) represent the standard deviation of around three repetitions. From the singlet-triplet oscillations we infer the amount of excess singlets, which is proportional to the interlayer correlator, compare Equation 6.41, as well as the reduction in triplet states for increasingly strong coupling along the double-well direction. The error bars in d) are deduced from the 95% confidence interval of the STO fit parameters.

Dependence on the Freezing Timescale After preparing the bilayer lattice configuration at a certain interaction strength U/t and tunnel amplitudes $t_\perp/t$, we want to quickly freeze the density distribution, see Figure 6.31. If the ramp to the deep lattice configuration is only slightly adiabatic, we do not project onto the double-well eigenstates as intended, but instead the quantum many-body state will adjust to the increased interaction strength, which enhances the singlet contribution of the ground state, $|\psi_1\rangle$, compare Figure 3.3. Therefore, if we freeze the distribution too slowly, we will overestimate the amount of interlayer spin correlations.

For the data presented so far, the motion has been frozen as quickly as the PID regulation in combination with the discretized ramp of the laser powers allows, which is approximately 150 µs. The maximum tunnelling amplitude realized along the vertical direction is $t_\perp/h \approx 900\,\mathrm{Hz}$. In Figure 6.33 we investigate the effect of the freezing time on the STO signal and observe that the amplitude of the oscillation (excess singlets) increases significantly with t_{freeze}. The increase in STO amplitude is directly related to the singlet fraction, which is given by the doubles

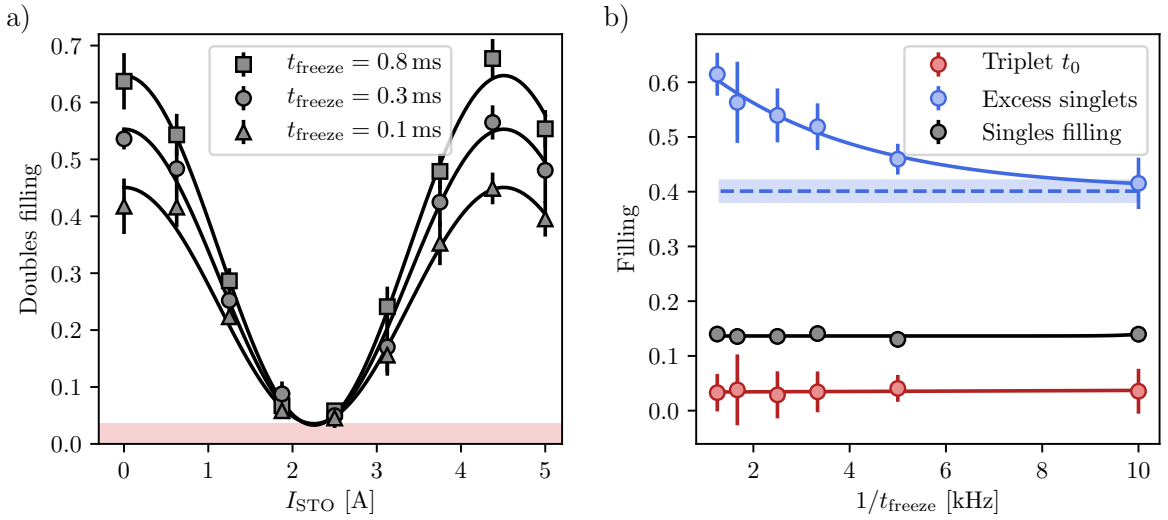

Figure 6.33: Dependence on freezing timescale. a) For $t_\perp/t = 5.2$, we investigate the dependence of the STO amplitude on the time, t_{freeze}, during which we freeze the motion both within and in between the layers. Note that the absolute values are not comparable with the STO data presented so far, as the detection was performed in the green z-lattice and we lost some of the doubles after merging during the handover. The trend in the STO amplitude should however, not be affected by this loss process. b) While the filling of triplet states is not affected by the freezing time, we observe an exponential decay (solid blue line) of the singlet probability with inverse freezing timescale, compare Figure 6.18 a). The dashed line and the blue shaded region indicate the settling value of the singlet filling as obtained from the exponential fit and its standard error, respectively.

filling after merging at $I_{\mathrm{STO}} = 0$. In contrast, the triplet fraction, $|t_0\rangle$, does not depend on the freezing timescale at all. This was to be expected, as all the triplet states do not change their composition as a function of $U/t_\perp$ and therefore, their occupation probability does not depend on t_{freeze}. Unfortunately, it is not possible to infer the interlayer spin correlator merely from (the reduction in) the triplet fraction as a function of $t_\perp$, since both the singlet and doublon fraction grow when coupling the double-well more strongly, while only the singlet state contributes to the increase in interlayer spin correlations.[18] Choosing the optimum time scale for freezing the density distribution is further complicated by the risk of populating higher bands when increasing the lattice depth too quickly. If higher bands were excited during the ramp up[19], we would expect the singlet fraction, which we measure by merging along the double-well direction, to decrease as the ground state overlap is reduced. Therefore, we are not able to disentangle the effects from the imperfect non-adiabaticity of the ramp and the probability to excite higher bands. In contrast, when detecting the filling directly after freezing the density distribution along all directions, see Figure 6.18, the doubles filling would decrease when exciting higher bands, while the opposite behaviour was observed when increasing the ramp speed to the detection lattice. Hence, we conclude, that for all the freezing times investigated, the probability to excite higher bands is negligible. Therefore the fastest ramp speed was chosen.

[18] The reduction in triplet fraction quantifies the increase in the overlap of the experimentally prepared state with the double-well ground state.

[19] Note that only bands with the same parity may be excited when ramping up the lattice depth due to the even parity of the excitation.

Lifetime of the Singlet-Triplet Oscillations In the following, we will investigate how the STO amplitude decreases over time. For recording the long-term behaviour, we apply a magnetic gradient strength of around 0.7 G/cm generated by a fast Feshbach current of $I_{\mathrm{STO}} = 2.3\,\mathrm{A}$ and scan the hold time, see Figure 6.34.

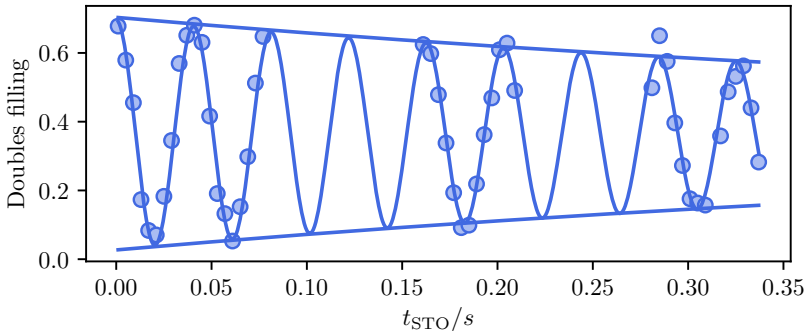

Figure 6.34: Lifetime of the singlet-triplet oscillations. Singlet-triplet oscillation for long oscillation times, t_{STO}, in a deep double-well bilayer lattice with $[V_{xy,r}, V_{z,g}, V_{z,r}] = [30, 33, 120]\,E_{\mathrm{rec}}$ and a magnetic field gradient strength of around 0.7 G/cm. We fit an exponentially damped sinusoidal function and obtain a time constant of $\tau_{\mathrm{STO}} = 0.7(2)\,\mathrm{s}$.

We fit an exponentially damped sinusoidal function to extract the time constant of the decay, $\tau_{\mathrm{STO}} = 0.7(2)\,\mathrm{s}$. The uncertainty on the fit parameter seems quite large considering that the fit reproduces our data nicely. A likely explanation is the limited sample region as we take data to around half the $1/e$-time only. The exponential decay is most likely related to local dephasing, as our signal is averaged over several thousand individual double-well potentials. Therefore, if there is an in-plane component of the magnetic field gradient or magnetic field curvature, the STO frequency will vary locally [59]. In principle, also the photon scattering induced by lattice lasers limits the coherence time of entangled states, see supplementary material of [169]. To separate the effects of dephasing and decoherence a π-pulse may be added in the middle of the STO evolution time. However, as the signal loss over our experimental timescale is very small, we did not investigate this further. For the data presented in Figures 6.32 and 6.35, we chose $t_{\mathrm{STO}} = 20\,\mathrm{ms}$, and hence expect a signal loss of around 3% only.

Results and Discussion According to Equation 6.41, the interlayer correlator may be inferred from the singlet-triplet oscillations as a fourth of the peak-to-peak amplitude. In Figure 6.35 the experimental results obtained from directly merging the double-well potential (blue data points) are compared to the STO data (red). While the general trend looks very similar for the two detection protocols, there are some systematic deviations, which I will discuss in the following. The earlier data where the double-well was directly merged was taken at slightly higher total density, $n = 0.42$ as compared to $n = 0.4$. This however, can not explain the finite offset from zero at low interlayer tunnel coupling. As we have discussed before, it is not possible to properly infer the interlayer correlator merely from the singlet fraction after merging, in particular, when the atoms are uncorrelated along the double-well direction. Therefore, a deviation in particular at low $t_\perp$ was to be expected. If we calculate C_z via the STO amplitude, we find that at low $t_\perp$ the interlayer correlations indeed vanish. At high $t_\perp$, our data suggests a larger amount of spin correlations than the DQMC theory comparison, while for intermediate coupling strength the opposite trend is observed. These opposing deviations might be linked to

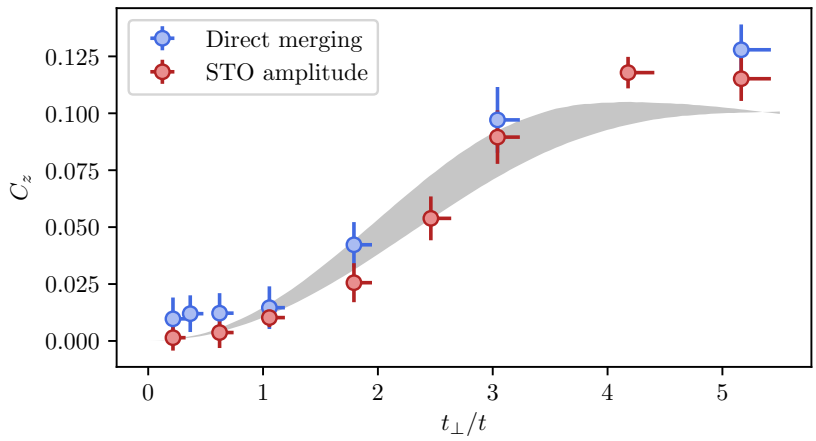

Figure 6.35: Comparison of the interlayer correlation results. We compare the interlayer correlator as inferred from the STO measurement to the results obtained by directly merging the double-well. The grey shaded area represents DQMC theory data with $n = 0.4$, $k_B T/t = 1.0t - 1.4t$ and $U/t = 8$. The error bars on the interlayer correlator inferred from the STO measurement follow from the 95% confidence interval of the fitted peak-to-peak amplitude.

the finite freezing timescale, which is limited in the experiment to around 150 µs. If freezing the density distribution occurs too slowly, we will overestimate the spin correlator. In Figure 6.18 we have seen that we are particularly sensitive on this freezing time if the tunnelling amplitude along the double-well direction is large. From the exponential fit to the STO amplitude for $t_\perp/t = 5.2$, shown in Figure 6.33, we estimate the deviation to the instantaneous ramp to amount to around 4% only. However, since the settling behaviour of the STO amplitude was only investigated for the largest tunnel coupling, I did not take its effect into account for the data presented in Figure 6.35.

Due to the narrow RF sweep that needs to resolve the on-site interaction shift (see Figure 6.25), we are very sensitive to magnetic field drifts. In general, fluctuations around the optimal RF centre frequency will decrease the number of doubles that we detect, and in turn the inferred spin correlator will be reduced. Therefore, it would be beneficial to transfer the atoms to the short-wavelength lattice, where the separation of the spectral features is significantly larger. This, as we figured out after the data was taken is possible even without transfer losses, if the long-wavelength lattice depth is chosen small enough.

To conclude, we have measured magnetic correlations between the two coupled layers of a bilayer lattice configuration, which complements the characterization of the intralayer spin correlations discussed above. The significant increase in singlet bonds along the vertical direction is a signature of the bilayer band insulator phase, and we observe that in the strongly coupled regime on average nearly every second double-well is occupied by a singlet state.

CHAPTER 7

Compressibility in the Bilayer Fermi-Hubbard Model

In the previous chapter we have observed that the tunnel coupling between two Hubbard layers induces a crossover from a state with antiferromagnetic correlations within the layer to a band insulating state of singlets forming along the vertical bonds. In the case of the well-known band insulator in a simple cubic lattice configuration, where each lattice site is occupied by two fermions, the lowest band of the optical lattice is fully filled and the large band gap in combination with Pauli's exclusion principle guarantees a strong insulating character at low temperatures. In contrast, the bilayer band insulator phase occurs at half-filling in the case of strong interlayer coupling and therefore the underlying physical picture of the insulating nature is slightly different, as I will discuss in detail in this chapter.

The compressibility is a thermodynamic variable that quantifies the response of the density of a system when exerting an external pressure. Therefore, it is a suitable observable to quantify the insulating character of a certain state independent of its physical origins. We show both experimentally and by performing DQMC calculations that the bilayer Fermi-Hubbard system with intermediate repulsive interactions is the most insulating at strong interlayer coupling. While we obtain a clear signature in the thermodynamic variable, the microscopic understanding is more complicated and I will investigate the relevant microscopic states and their energies by comparing to an isolated double-well system.

This chapter is organized as follows. First I will present the DQMC predictions on the compressibility of a bilayer Fermi-Hubbard system. These results will be discussed and compared to the limiting case of a double-well potential to obtain a more intuitive picture. The experimental scheme for measuring the compressibility relies on a magnetic field gradient that is applied within the plane in order to quantify how reluctant the atoms are to adjusting their density to the tilt in the potential landscape.

7.1 Definition of the Compressibility for Quantum Gases in Optical Lattices

The compressibility is known from standard thermodynamics as the rate of change of a system's volume with pressure. Its definition differentiates between the isothermal and the adiabatic

compressibility [179]. We will focus on the isothermal compressibility

$$\kappa_T = -\frac{1}{V}\left(\frac{\partial V}{\partial p}\right)_{T,N}, \tag{7.1}$$

where both the temperature T and the total particle number N are kept constant during the relaxation/compression. Since clouds of fermionic atoms are typically confined in a harmonic potential, the pressure is not uniform but instead increases to the trap centre. This stabilizes the cloud against the trap confinement that tries to squeeze the cloud. In thermal equilibrium and for vanishing magnetization the Gibbs-Duhem relation simplifies to

$$N d\mu = V dp. \tag{7.2}$$

In this case the pressure may be inferred from the integral over the density equation of state

$$p(\mu) = \int_{-\infty}^{\mu} n(\mu')d\mu', \tag{7.3}$$

where $n = N/V$. This enables us to rewrite the isothermal compressibility in terms of the density and the chemical potential, quantities that we readily access in our system [80, 108],

$$\kappa_T = -\frac{1}{V}\left(\frac{\partial V}{\partial \mu}\frac{\partial \mu}{\partial p}\right)_{T,N} = -\frac{1}{nV}\left(\frac{\partial V}{\partial \mu}\right)_{T,N} = -\left(\frac{\partial (1/n)}{\partial \mu}\right)_{T,N} = \frac{1}{n^2}\left(\frac{\partial n}{\partial \mu}\right)_{T,N}. \tag{7.4}$$

For the remainder of this thesis, we define the compressibility as

$$\kappa = \left(\frac{\partial n}{\partial \mu}\right)_{T,N} \tag{7.5}$$

without the prefactor that references the density response to the local density. Note that as a consequence, the compressibility will be particle-hole symmetric $\kappa(\mu) = \kappa(-\mu)$.

7.2 DQMC Simulation of the Compressibility

As for the spin correlation results presented in Chapter 6, we employ the Quantum Electron Simulation Toolbox (QUEST) [17] to obtain DQMC theory data for the compressibility. For the simulation, the chemical potentials of both layers are fixed to be equal, and we assume a spin-balanced mixture throughout this chapter,

$$\mu_{\uparrow 1} = \mu_{\downarrow 1} = \mu_{\uparrow 2} = \mu_{\downarrow 2} \equiv \mu. \tag{7.6}$$

Following the definition given in Equation 7.5, the compressibility of the bilayer Fermi-Hubbard model is obtained by repeating the simulation of the total filling factor (proportional to the local density) for varying chemical potential μ and performing a numerical derivative on the equation of state $n(\mu)$[1]. This requires a fine sampling of the chemical potential μ and we chose a spacing of $\Delta\mu = 0.25t$. Since the difference in the filling factor when simulating the bilayer

[1] In principle, we could have investigated the density response upon introducing a chemical potential difference between the layers. This however would have required to measure the density of both layers, which effectively

system at $T/t = 1$ as two 4×4, 6×6 or 8×8 grids amounts to less than one percent, we decided to speed up the calculations and decreased the system size for the DQMC compressibility simulations to 6×6, as compared to the spin correlation data, where a larger grid of 8×8 was used. Note that this conclusion strongly depends on the chosen temperature, and in general larger systems have to be considered when simulating colder temperatures, where correlations extend over several lattice sites. We perform 20000 measurement sweeps for each data point and the number of imaginary time slices is set to 25. The total filling factor of an individual spin component comprises contributions from doubly and singly occupied lattice sites. While the singles filling is connected to the local moment C_{00} (see Equation 5.13), the doubles filling is extracted from the DQMC results as the lowest order of the density-density correlation function

$$n = \langle \hat{n}_\uparrow \hat{n}_\downarrow \rangle + s_\uparrow = \langle \hat{n}_\uparrow \hat{n}_\downarrow \rangle + 2C_{00}. \tag{7.7}$$

We exploit the full particle-hole symmetry as discussed in Section 3.3.2 to infer the probability of singly and doubly occupied sites above half-filling $\mu > 0$ from the probabilities below half-filling according to

$$s_\uparrow(\mu) = s_\uparrow(-\mu), \tag{7.8}$$

$$\langle \hat{n}_\uparrow \hat{n}_\downarrow \rangle (\mu) = \langle (1 - \hat{n}_\uparrow)(1 - \hat{n}_\downarrow) \rangle (-\mu). \tag{7.9}$$

This significantly reduces the computation time.

In Figure 7.1 a) and b) we separately plot both contributions to the equation of state, i.e. doubles and singles, for varying tunnel coupling $t_\perp$ between the layers. At $t_\perp = 0$, where

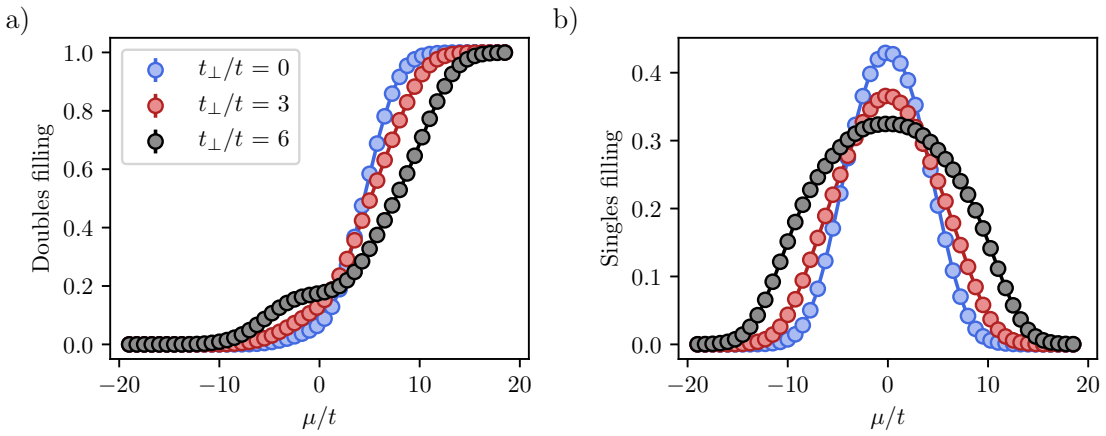

Figure 7.1: DQMC results for the filling of singly and doubly occupied sites. DQMC results for the filling factor in a bilayer system with a repulsive on-site interaction, $U/t = 7$, at a temperature of $k_B T/t = 1$. We distinguish the contributions of doubly-occupied sites (a) and singly-occupied sites of one spin component (b). The legend applies to the whole figure.

the two layers completely decouple from each other, the simulations match the results of the two-dimensional Hubbard model, as expected: For an intermediate repulsive on-site interaction $U/t = 7$ and at low temperature $k_B T/t = 1$, as chosen in Figure 7.1, the system near half-filling is close to the Mott insulating regime and most sites are occupied by a single spin. This changes

doubles the amount of experimental data.

when introducing a finite tunnel coupling between the layers. The additional tunnelling channel effectively reduces the significance of the on-site repulsion and drives the system away from the Mott insulating behaviour as apparent from the reduction in the singles filling. In Figure 7.2 we show both the total density equation of state for either of the two spin components, as well as the compressibility κ, which we obtained as the derivative of a third-order polynomial fit to the total density $n(\mu)$. Surprisingly, the bilayer system near half-filling is the most insulating for large tunnel coupling $t_\perp$, as indicated by the minimum in the compressibility.

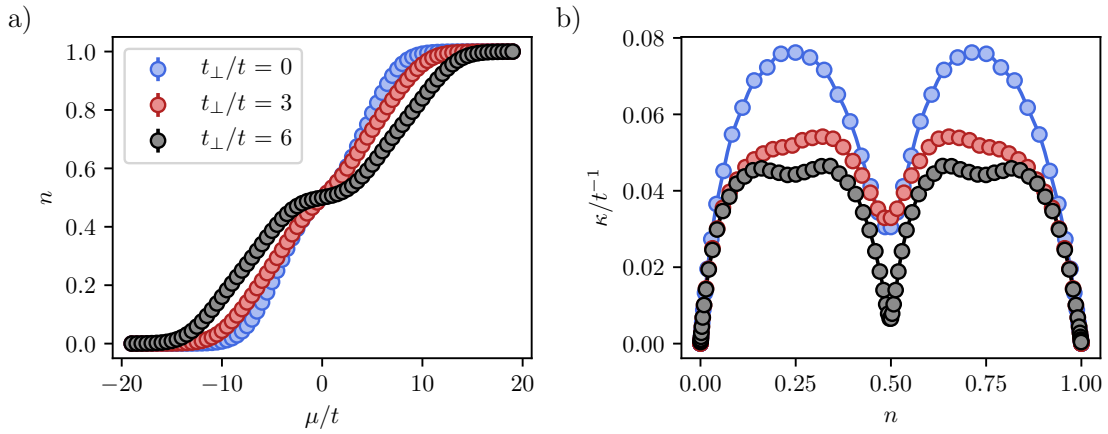

Figure 7.2: DQMC results for the equation of state and the compressibility. a) DQMC results for the total filling factor n in a bilayer configuration with repulsive on-site interaction $U/t = 7$ at a temperature of $k_B T/t = 1$. b) The compressibility is inferred from the equation of state by a third-order polynomial fit over a chemical potential range of $\Delta\mu = 1.5t$. The error bars on the density only contain the statistical error from the DQMC code and are not visible in the figure, since $\delta n_{\text{stat}}/n \approx 10^{-4}$. The legend applies to the whole figure.

7.2.1 Bilayer Fermi-Hubbard Model at Low Filling

Introducing a finite tunnel coupling between the layers for strong repulsive interactions does not only significantly reduce the compressibility at half-filling, the bimodal distribution is also modified for higher and lower chemical potentials as shown in Figure 7.2 b). In particular, two small dips appear at quarter and three-quarter filling, signalling the opening of additional charge gaps within the upper and lower Hubbard band, respectively. These dips are the more prominent, the larger both the on-site interaction and the interlayer tunnelling amplitude, which is emphasized in Figure 7.3. For $2t_\perp > U \gg t$, the charge gaps at quarter and three-quarter filling are predominantly interaction driven, similar to the Mott gap of the 2D Fermi-Hubbard model at half-filling.

We can estimate the charge gap by considering the microscopic states involved. Deep in the bilayer band insulator regime and for strong repulsive interactions, all double-well bonds get occupied by the state

$$|\psi\rangle_\sigma = \frac{1}{\sqrt{2}} \left(|\sigma, 0\rangle + |0, \sigma\rangle\right) \tag{7.10}$$

up to quarter filling. Note that the corresponding spatial wavefunction is symmetric, hence it

minimizes the kinetic energy in the vertical direction, $E_{|\psi\rangle_\sigma} = -t_\perp$. To avoid forming double occupancies the spins do not delocalize within the layer and at quarter filling[2] one can think of this state, as a Mott insulator that is smeared across two neighbouring planes. If we now intend to fill more particles into the bilayer system, the on-site interaction will compete with the delocalization energy $t_\perp$. If the latter is significantly stronger, then we will continue to fill states with a symmetric superposition of the left and right lattice sites, $|\psi\rangle_\sigma$, at the expense of forming double occupancies

$$|\psi\rangle_\uparrow \otimes |\psi\rangle_\downarrow = \frac{1}{2}\left(|\uparrow,\downarrow\rangle - |\downarrow,\uparrow\rangle + |\uparrow\downarrow,0\rangle + |0,\uparrow\downarrow\rangle\right). \tag{7.11}$$

By comparing to the discussion of the double-well eigenstates in Section 3.2, we can identify this state as the ground state of two fermions in a double-well potential at $U = 0$. Whereas when introducing repulsive interactions the amount of doubles will decrease (see Table 3.1) and the approximate energy of the interacting two-particle state will increase according to $E \approx -2t_\perp + U/2$. The approximate eigenenergy[3] reflects that we obtain the delocalization energy of $t_\perp$ for both particles and have to pay $U/2$, since the probability to form a double occupancy is 50%. Therefore, we expect that the two peaks forming either the bonding or antibonding band are separated by $\Delta\mu = U/2$. In Figure 7.3 we show the compressibility for

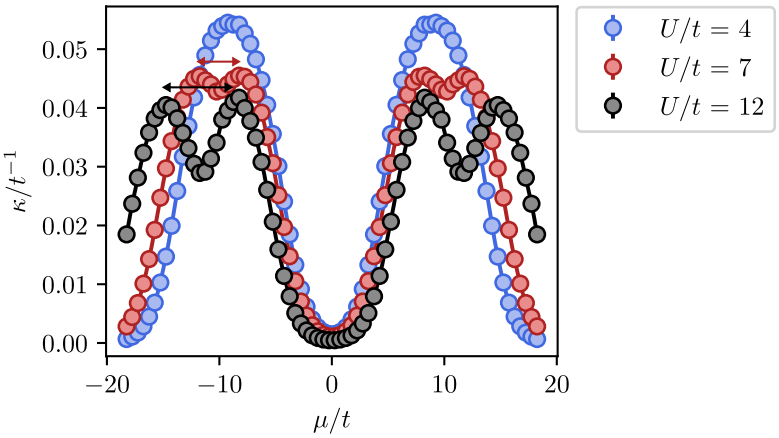

Figure 7.3: DQMC results for the compressibility for varying interaction strength. Compressibility $\kappa(\mu)$ for $t_\perp/t = 8$ and varying interaction strength U. The arrows indicate the value $U/2$ for the respective data set.

increasing repulsive interaction and observe how the additional "Mott" dips at quarter and three-quarter filling get more prominent. Using arrows, we indicate the expected distance of $U/2$, which nicely matches the DQMC results.

The analogy of the state at quarter filling to the Mott insulator of the 2D Fermi-Hubbard model can be extended even beyond the charge sector. In Figure 7.4, we show the amount of antiferromagnetic spin correlations within the layer quantified by the difference of the staggered structure factor to the local moment for the whole range of the filling factor n. For decoupled layers and at $U/t = 7$ and $T/t = 1$, we predominantly obtain spin correlations at

[2] i.e. one particle per vertical double-well

[3] We may also obtain this estimate on the energy by performing a Taylor expansion of E_1 around $U = 0$, compare Table 3.1.

half-filling, where the amount of singly occupied sites is largest. Upon introducing the tunnel coupling $t_\perp$ between the layers, this peak disappears and instead we find antiferromagnetic spin correlations at quarter and three quarter filling. This signals that the finite amplitude of the intralayer tunnel coupling, t, still leads to delocalization within the layer, at least in the form of second-order tunnelling events. Therefore, the spins that are smeared out over the double-well due to the large interlayer tunnelling amplitude, order antiferromagnetically within the layer.

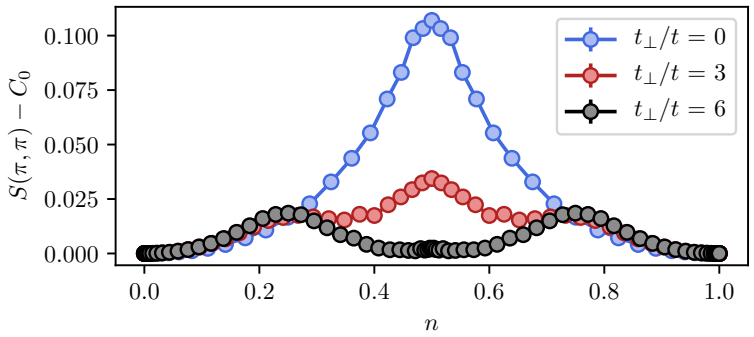

Figure 7.4: DQMC results for antiferromagnetic spin correlations. The difference of the staggered magnetic structure factor to the local moment is plotted versus the filling factor n for a single horizontal layer at $U/t = 7$ and $T/t = 1$. We observe that the intralayer spin correlations at half-filling for two decoupled layers continuously decrease with the tunnel coupling $t_\perp$, until they completely vanish in the regime of the bilayer band insulator. We still observe spin correlations in this case, however, at quarter and three quarter filling.

Summarising the discussion above, we have seen that the bilayer lattice configuration offers new intriguing states, by adding yet another energy scale, $t_\perp$, which competes with the on-site interaction and the delocalization energy within the layer. If both U and $t_\perp$ are large, additional charge gaps appear at quarter and three-quarter filling. The physical intuition will be helpful for the following discussion of the half-filled bilayer lattice, which is the more relevant case for the comparison to our experimental data.

7.2.2 Bilayer Fermi-Hubbard Model at Half-Filling

In Figure 7.1 we have seen that the amount of singles at half-filling decreases with the interlayer tunnel coupling $t_\perp$. Still, the compressibility is lowest in the strongly coupled regime and we draw the conclusion that the insulating nature of the bilayer band insulator phase is very different from the one of the Mott insulator, which relies on the large repulsive interaction energy favouring singly occupied sites over doubles and holes. In contrast, for the band insulating phase at large $t_\perp$, we instead observe an increase in the number of doubles and holes. This can be understood in an intuitive picture: since the dominant energy scale of the bilayer band insulator is the tunnelling amplitude, the most important goal of the particles is to reduce their kinetic energy. For the double-well potential the reduction in the kinetic energy is the largest for an equal amount of $|s\rangle$ and $|d_+\rangle$, as in this case the intrinsic density fluctuations are the most dominant (compare Figure 3.3). In conclusion, the bilayer band insulator minimizes its energy by delocalizing the particles along the double-well direction, which works best at half-filling. Therefore, if we apply a potential gradient along any lattice direction, the atoms will oppose the density redistribution in order to preserve the energy gain from tunnel delocalization. In

the following, I will investigate why the compressibility is lowest in the band insulating regime by comparing to the double-well case and identifying the relevant microscopic states.

Double-Well Comparison Already in the discussion away from half-filling we have seen that for a strong tunnel coupling in the vertical direction, the particles mostly delocalize within the double-well. Therefore a comparison to the exactly solvable double-well physics is reasonable. The main idea is to compute the mean density of a symmetric double-well potential as a function of the chemical potential, which we discretize in steps of $\Delta\mu = 0.25t$ as for the DQMC calculation. From the density equation of state, we can derive the compressibility either analytically or numerically. The thermal average of an operator $\hat{O}$ is given by

$$\langle \hat{O} \rangle = \frac{1}{Z} \operatorname{Tr}\left(e^{-\beta(\hat{H}-\mu\hat{N})} \hat{O} \right) \tag{7.12}$$

with the grand canonical partition function

$$Z = \operatorname{Tr}\left(e^{-\beta(\hat{H}-\mu\hat{N})} \right). \tag{7.13}$$

To obtain the mean density, we trace over all 16 eigenstates including the spin-polarized ones of the two-site Fermi-Hubbard model in the single-band approximation. In Figure 7.5 we compare the compressibility of the double-well system to the DQMC results for a $6 \times 6 \times 2$ bilayer lattice configuration. Surprisingly, the qualitative behaviour is quite similar and even the numerical values are close. In particular when comparing the corresponding false-colour maps in the lower row, we do not observe a significant deviation in the general trend. However, the approximation of a bilayer lattice by a single double-well potential consistently underestimates the compressibility, since it does not account for the finite bandwidth W of the bilayer system. Instead, the double-well description considers flat bands and therefore the charge gap is larger for all parameters U and $t_\perp$ considered.

The compressibility is a thermodynamic variable that quantifies the (macroscopic) density response of a many-body state when exposed to a potential gradient. To obtain a thorough understanding of the insulating (or metallic) nature of a system we need to identify its relevant microscopic states and processes. By comparing the results in Figure 7.5 a) and b), we have observed that the double-well calculation reproduces the key features of the compressibility in a bilayer system as predicted by DQMC calculations. We will therefore investigate the microscopic properties of a double-well in the following. The ground state energy E_1 of two interacting fermions in a double-well is given in Table 3.1 and the corresponding state is a spin singlet with contributions both from singly occupied sites as well as doubles and holes, $|s\rangle$ and $|d_+\rangle$, respectively. If we apply a strong enough in-plane gradient, the mean density per double-well will change, and the corresponding microscopic states are $\frac{1}{\sqrt{2}}\left(|\uparrow\downarrow,\uparrow\rangle + |\uparrow,\uparrow\downarrow\rangle\right)$ and $\frac{1}{\sqrt{2}}\left(|0,\downarrow\rangle + |\downarrow,0\rangle\right)$, with energies $-t_\perp + U$ and $-t_\perp$, respectively.[4] Therefore, the charge gap for an in-plane gradient may be approximated as

$$E_{\text{gap}} = -t_\perp + U - t_\perp - 2E_1 = \sqrt{16t_\perp^2 + U^2} - 2t_\perp. \tag{7.14}$$

In the two limiting cases of non-interacting particles, $U = 0$, and negligible tunnel coupling,

[4] If we applied the gradient along the vertical direction, the compressibility would likely be even lower, since the relevant microscopic state on the double-well would be $|\uparrow\downarrow, 0\rangle$ with energy U.

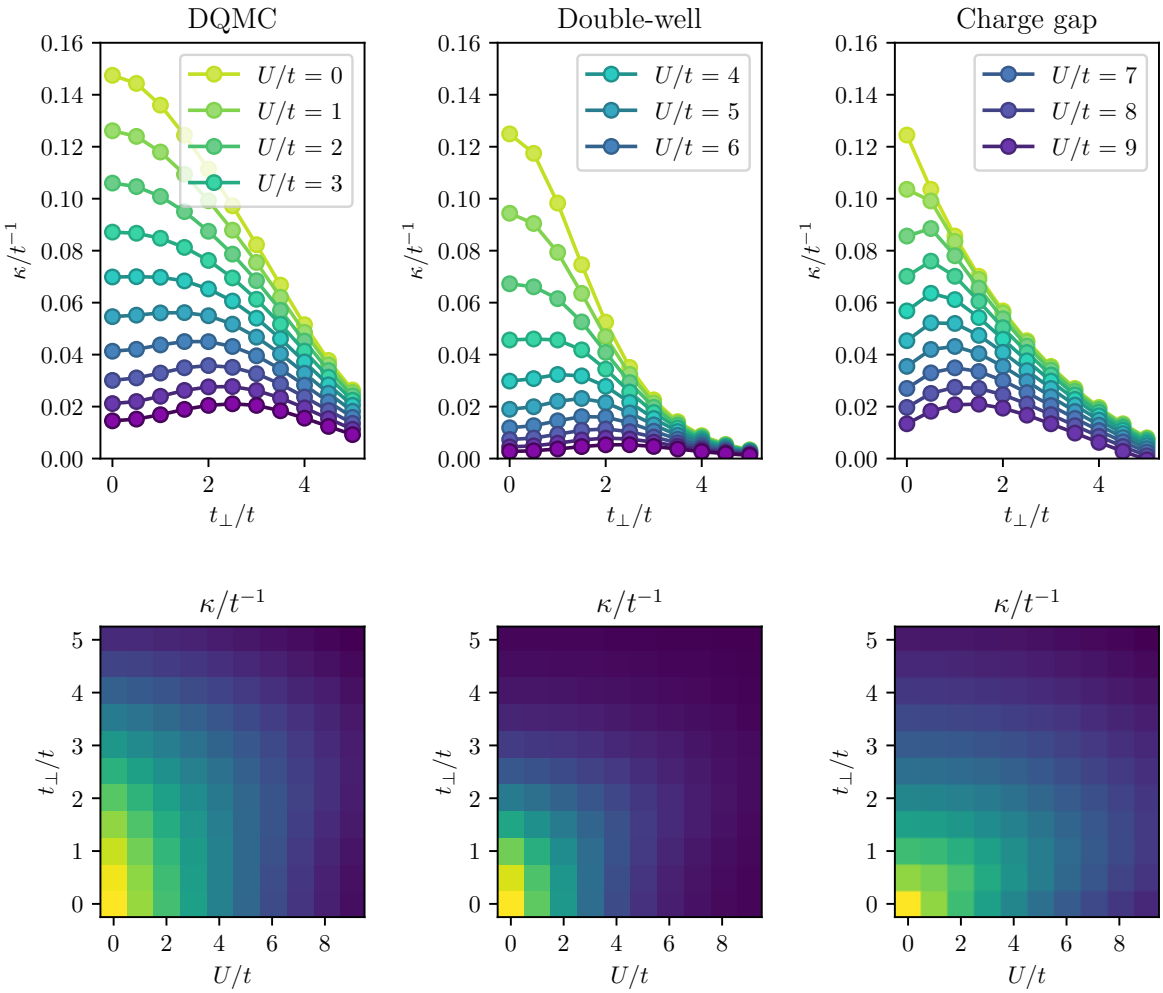

Figure 7.5: Theory comparison of the compressibility. Left column: DQMC results for the compressibility in a bilayer lattice with repulsive on-site interactions $U/t = 7$ at a temperature of $k_B T/t = 1$. The compressibility is inferred from the density equation of state by a third-order polynomial fit, compare Figure 7.2. Middle column: Within the double-well description we compute the mean density in the grand-canonical ensemble and derive the compressibility as for the DQMC data using a numerical derivative on the discretized equation of state. Right column: We estimate the compressibility in a double-well via the approximate formula for the charge gap given in Equation 7.14.

$t_\perp = 0$, we recover the scaling dependence as obtained in Sections 3.3.3 and 3.4.1, namely that the Mott gap is directly given by the on-site interaction energy and that the single particle gap responsible for the bilayer band insulator phase is equal to $2t_\perp$. From this handwavy estimate of the charge gap it is evident that if we realize a strongly coupled band insulator at an intermediate repulsive interaction strength, the compressibility has to be lower than in the uncoupled regime, $t_\perp \approx 0$, as both the kinetic and the interaction energy oppose the density redistribution in a potential gradient. Unfortunately, we can not directly compare the charge gap estimate to the compressibility. Instead, we assume an exponential dependence of the compressibility on the charge gap and after adjusting the coefficients we obtain the result shown in the third column of Figure 7.5. Even though neglecting the finite temperature does

seem to have a significant effect on some of the features of the compressibility in particular at low $t_\perp$ the rough trend as a function of both U and $t_\perp$ is similar to the two cases discussed before. Therefore, we assume that the microscopic picture used to estimate the charge gap given in Equation 7.14, is sensible.

7.3 Measuring the Compressibility in a Homogeneous Hubbard System

Previously we have measured the compressibility within the harmonic trapping potential that appears as a consequence of the finite waist of the lattice laser beams [34]. This confining potential has the advantage that we sample the density equation of state over a broad range of chemical potentials in a single realization. The compressibility, which depends on the local density, is obtained as the numerical derivative $\kappa = \partial n/\partial \mu$. For the realization of the bilayer Fermi-Hubbard model in our experiment, the trap confinement is compensated by the repulsive DMD potential to create a flat core region. Therefore, probing the insulting nature is not as straight-forward and we need to engineer a potential gradient, which serves as the equivalent of an electric voltage applied to a solid-state material.

In principle, it would be sensible to employ a potential gradient generated by optical means, since for a far-detuned laser source the gradient strength is independent of the magnetic hyperfine state. However, the DMD potential introduces disorder in the local potential strength on the order of four to nine lattice sites and as a consequence strongly suppresses the mobility of the atoms if the DMD intensity is too large [152]. Therefore, we decided to employ an in-plane magnetic field gradient instead, even though it suffers from the drawback of introducing a slightly spin-dependent gradient strength. So far we have used magnetic field gradients mostly for their differential effect on the spin state in a frozen lattice configuration, see Chapter 5 and Section 6.4.2. However, if tunnelling is allowed, a magnetic field gradient will lead to density redistribution according to the respective magnetic moment of the atoms, which is given by the slope in the Breit-Rabi diagram, see Figure 4.1. For the measurement of the compressibility we will make use of this (slow) density redistribution in order to quantify how easily the atoms adjust to a tilt in the potential landscape while being in the bilayer lattice configuration for different values of $t_\perp$.

7.3.1 Experimental Sequence

For probing the compressibility in the bilayer Fermi-Hubbard model we slightly modify the experimental sequence shown in Figure 6.6, which was used to create the bilayer Hubbard system and to measure magnetic intralayer correlations. Firstly, we ramp up the current of the two gradient coils in parallel with the depth of the short-wavelength z-lattice, which splits a single layer into the coupled bilayer system. It is not problematic to expose the atoms to the in-plane magnetic field gradient already before the bilayer lattice has reached its final configuration, since we expect the compressibility to be lowest for small barrier heights and therefore it is unlikely that the atoms will redistribute much. We hold the atoms at a fixed gradient strength in the bilayer lattice realizing a broad range of tunnelling amplitudes from $t_\perp/t \approx 0$ to 5 until we quickly freeze the density distribution in all three directions within approximately $t_{\mathrm{freeze}} = 150\,\mu\mathrm{s}$. At this point we can remove the in-plane magnetic field gradient, as the atoms are not able to tunnel any more. In order to prevent the two coils, which are not

water-cooled, from overheating we removed the ramps for the spin spiral part, as we are not interested in measuring spin correlations anyway. Instead, to infer the compressibility of the bilayer system we need to measure the density equation of state by separately detecting the contributions from singly and doubly occupied lattice sites.

Gradient Strength In order to obtain a quantitative estimate of the compressibility from the density distribution of the atoms, we need to know the strength of the potential gradient. Since we employ the same coils as for the spin spiral technique, we can make use of the precise calibration of the gradient strength with the atoms, see Figure 5.6. If we run the spin spiral at a magnetic bias field of $B = 191.4\,\mathrm{G}$, the difference between the π- and the 2π-point for neighbouring sites is $\Delta t_\pi = 0.129s$[5]. At this field, the differential slope of the lowest two magnetic hyperfine states (compare Figure 4.1) is

$$\Delta\gamma = \frac{\partial E_{|7\rangle} - \partial E_{|9\rangle}}{h\partial B} = -1.4\,\frac{\mathrm{kHz}}{\mathrm{mG}} + 1.24\,\frac{\mathrm{kHz}}{\mathrm{mG}} = 160\,\frac{\mathrm{Hz}}{\mathrm{mG}}. \tag{7.15}$$

The relative phase between nearest neighbours along the diagonal of the in-plane lattice, is twice the phase between nearest neighbours along either of the two lattice directions. Therefore, the gradient strength is given by

$$2\pi\Delta\gamma|\nabla B_z|a_{\mathrm{diag}}\Delta t_\pi \stackrel{!}{=} 2\pi. \tag{7.16}$$

The spacing between sites along the diagonal is $a_{\mathrm{diag}} = 780.8\,\mathrm{nm}$, which is larger than the expectation for a square lattice $\sqrt{2}a = 752\,\mathrm{nm}$ due to our slightly angled lattice configuration. Finally, the gradient strength for $\Delta I_{\mathrm{Retro}} = 17.2\,\mathrm{A}$ and $\Delta I_{\mathrm{Stage}} = 5.115\,\mathrm{A}$ leads to a difference in the magnetic field strength between neighbouring sites of

$$|\nabla B_z| \cdot a = |\nabla B_z| \cdot 532\,\mathrm{nm} = 0.033\,\mathrm{mG}. \tag{7.17}$$

The advantage of creating a potential gradient using magnetic fields is that it varies more smoothly over the extent of the cloud as compared to a gradient generated by optical means, such as a spatial light modulator. On the other hand, this approach suffers from the weakness that the gradient strength felt by the atoms depends on the magnetic hyperfine state. Since we only detect atoms in the $|7\rangle$ state, the maximum possible gradient strength that they experience is given by

$$|\nabla V| = \frac{0.033\,\mathrm{mG}}{532\,\mathrm{nm}} \cdot 1.24\,\frac{\mathrm{kHz}}{\mathrm{mG}} = 77\,\frac{\mathrm{Hz}}{\mu\mathrm{m}}. \tag{7.18}$$

This, however, slightly underestimates the gradient strength felt by doubly occupied lattice sites. Under the assumption that the doubles do not split up when applying the magnetic field gradient, they experience a gradient strength that is around 6% larger.

Settling Behaviour of the Density Redistribution In order to determine the slope in the density due to the in-plane gradient, our fitting routine consists of two steps. First, we obtain

[5] Note that we cannot simply take the time of the π-point itself, since the phase evolution when the current of the gradient coils is ramped up and down would be included in this time, and hence we would overestimate the time that is needed at the full gradient.

the direction of the in-plane gradient, which slightly deviates from the intended lattice diagonal, by fitting a plane to the two-dimensional density distribution. In a second step, we bin the density along this predetermined gradient direction and obtain the rate of change of the density from a one-dimensional linear fit, see Figure 7.8 c) and f). For both parts of the analysis we do not use the full centre region defined by the steep DMD barrier, but instead we exclude those parts of the peripheral region, where the atoms do not follow the linear trend. The reason for these deviations is likely given by the DMD potential, which increases in intensity when moving away from the trap centre and which suppresses the mobility of the atoms due to disorder. Even after restricting the region of interest, we still fit the slope in the density over around 50-60 lattice sites along the direction of the magnetic field gradient.

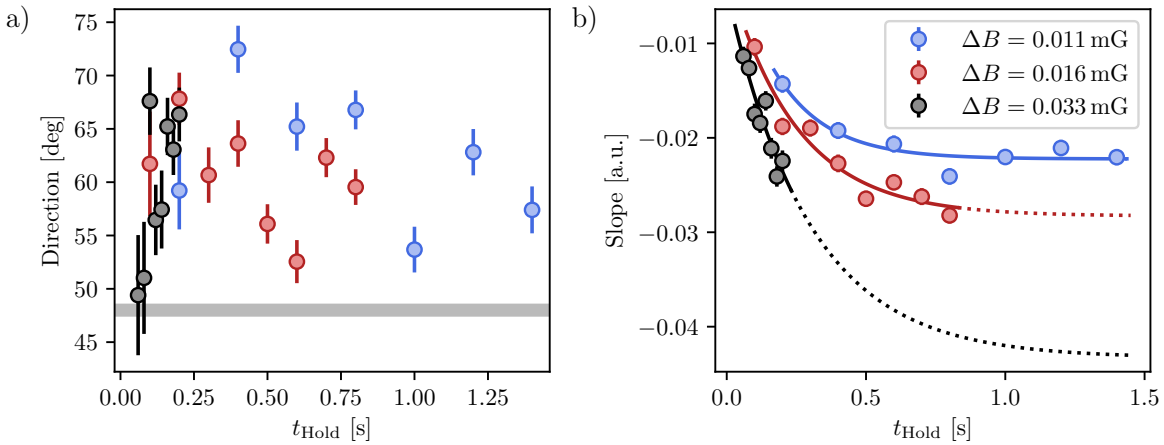

Figure 7.6: Settling behaviour of the density gradient. While the gradient direction (a) is mostly independent of the hold time, we observe an exponential settling behaviour in the slope of the total density (b). We extrapolate the exponential decay (dotted line) to indicate the settling value for the slope. Under the assumption that the exponential time constant scales roughly linearly with the gradient strength, we also fit the dataset with the largest gradient. Still this extrapolation only serves as a rough guess. The grey shaded region in (a) represents the direction of the lattice diagonal, which is what we aimed for. The legend applies to the whole figure and specifies the gradient strength as the difference in magnetic field over a distance of $a = 532\,\mathrm{nm}$.

To obtain a reliable estimate on the compressibility, we have to ensure that the density distribution has settled according to the applied in-plane gradient. The density response is the larger, the stronger the gradient. On the one hand, we are aiming for the largest signal strength, on the other hand, however, we are limited by the dissipated power of the coils as they are not water cooled. This restricts the maximum hold time for a certain coil current. In Figure 7.6 we investigate the settling behaviour of the density response for different magnetic field gradient strengths. For the maximum gradient strength, $\Delta B = 0.033\,\mathrm{mG}$, the density has not settled at all. Therefore, we need to reduce the current and the final parameters are $\Delta B = 0.013\,\mathrm{mG}$ and $t_{\mathrm{Hold}} = 1\,\mathrm{s}$.

Note that the ratio of the settling values of the slope in the density for the lower two gradient strengths in Figure 7.6 b) does not match the expectation inferred from the applied magnetic field gradients. It seems that the density follows less the stronger the gradient. We take this effect into account by rescaling the observed slope with the mismatch of the expected to the observed ratio in the density slope.

Furthermore, the direction of the density gradient does not match the lattice diagonal, as intended, but deviates by around ten degree. To investigate the source of this discrepancy, we change the amount of light that is sent to the DMD, see Figure 7.7. Interestingly enough, the slope in the density is unaffected by changing the power of the compensation potential, however the direction increases linearly with the optical DMD power. The DMD potential is designed to

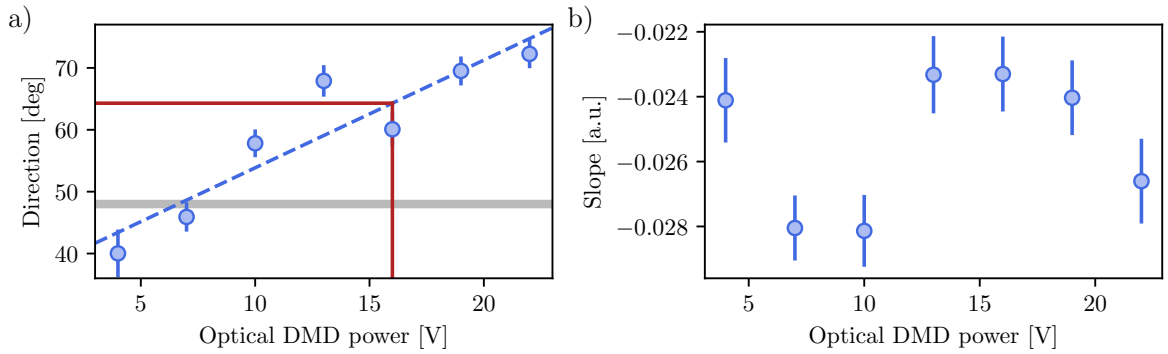

Figure 7.7: Effect of over/undercompensating the harmonic trap. We tune the optical power in the DMD beam quantified by the voltage that is detected by the regulation photodiode to investigate the effect of over/undercompensating the harmonic trap confinement on both the direction and the amplitude of the resulting slope in the density. The grey line indicates the in-plane direction that we expected to match. The red lines mark the situation, where we took the final data shown in Figure 5.11.

create a homogeneous lattice potential in the core region, and therefore mostly compensates the strong confinement along the x-direction generated by the infrared z-lattice. A possible reason that might explain why the DMD potential does not perfectly cancel the harmonic confinement of the lattice lasers, is given by the alignment process. The DMD is typically aligned to the centre of the cloud in the three-dimensional optical lattice configuration with $V_{xy,r} = 6E_{\mathrm{rec}}$ and $V_{z,g} = 120E_{\mathrm{rec}}$, while the infrared z-lattice is aligned to the centre of the imaging frame. Typically there is a significant discrepancy in the position along the x-axis for these two cases and therefore the centre of the DMD anti-confinement was likely misplaced with respect to the centre of the trap confinement. When adding up a parabola and an inverted parabola whose centres are shifted with respect to each other, the resulting potential is a straight line, which might be the cause for the deviation in the observed gradient direction. For future experiments, this problem may easily be circumvented by aligning the infrared z-lattice in the same way as the DMD, i.e. to the centre of the cloud in the three-dimensional optical lattice configuration.

7.3.2 Discussion and Results

Having optimized the evaluation of the density slope for a setting, where we expect the bilayer system to be the least insulating, we have measured the compressibility for varying strength of the interlayer tunnel coupling. In the upper and lower row of Figure 7.8 we show the evaluation steps for a large and an intermediate tunnel amplitude, $t_\perp = 5.2t$ and $t_\perp = 1.8t$, respectively. The mean density is close to, but slightly below half-filling, which is larger than what we would expect when splitting a single-band band insulator with an initial filling of $n = 0.85(1)$ into two equally filled layers. This might indicate that the layer, which we probe, has a higher average filling than the correlated neighbouring layer. When subtracting the mean filling, the difference in the slope of the density distribution is already discernible, see Figure 7.8 b) and e).

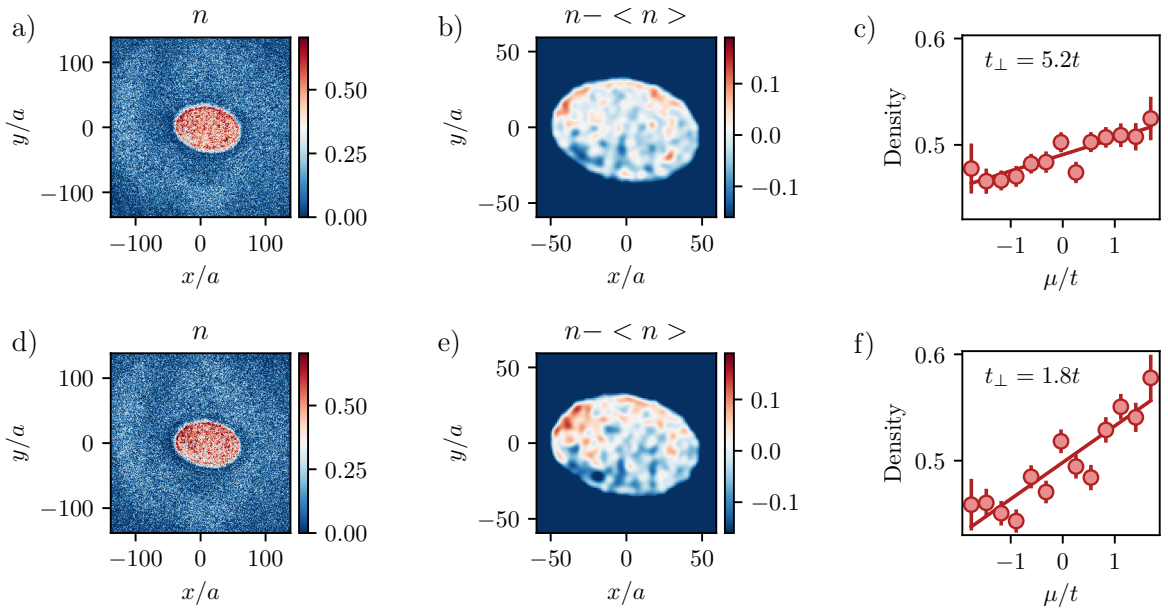

Figure 7.8: Density distribution in the band insulating and intermediate bilayer regime. We show the total density (left column), the deviation from the mean density in the centre region (middle column) and how the density varies as a function of the chemical potential within the plane (right column), both for the band insulating regime $t_\perp = 5.2t$ (top row) and for an intermediate coupling strength $t_\perp = 1.8t$ (bottom row) of a coupled bilayer system. For each interlayer tunnel coupling, we combine the data of around 80 individual realizations. We have applied a Gaussian filter with $\sigma = 2a$ to the density deviation data $n - \langle n \rangle$ in order to facilitate detecting the difference in the density slope by naked eye. The error bars on the binned density in c) and f) represent the standard error resulting from binning the density in steps of $\Delta\mu/h = 50\,\mathrm{Hz}$.

From a linear fit to the density binned according to the expected chemical potential map of the in-plane gradient, see subfigures c) and f), we obtain the compressibility in units of t^{-1}, where $t/h = 174\,\mathrm{Hz}$, which is shown in Figure 7.9 as a function of the interlayer tunnelling amplitude. We compare our experimental results to DQMC calculations at $U/t = 7$ and $k_B T/t = 1.0..1.4$. To account for the varying density within the centre region, we average the theory data for the compressibility over $\mu/t = -1.75$ to $\mu/t = 1.0$.

The atoms seem to suggest a lower compressibility than expected by DQMC theory data. We should however keep in mind that apart from the statistical error shown in Figure 7.9, our results are also affected by several systematic uncertainties on, for example, the interaction strength, the detection fudges and most importantly the gradient strength felt by the atoms. In particular, the interaction strength is not constant over the investigated range of vertical tunnelling amplitudes, see Figure 6.16 b). Also, we should keep in mind that the density of the two coupled layers might be different, which would increase the inferred compressibility only in the intermediate to strong coupling regime. Furthermore, the disorder introduced by the DMD potential might reduce the mobility of the atoms and thereby affect the inferred compressibility.

When comparing our results on the compressibility in the bilayer Fermi-Hubbard model close to half-filling in the crossover regime from a Mott insulator to the bilayer band insulator to the simulations presented in Figure 7.2, we realize that the bilayer system remains insulating

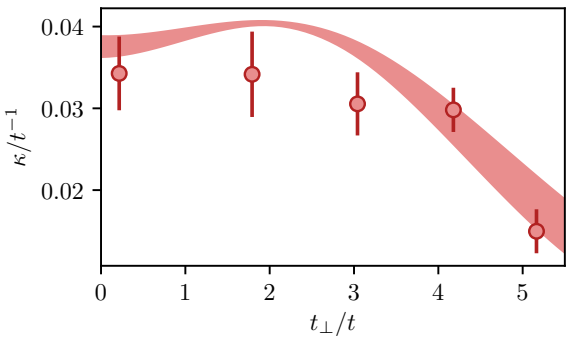

Figure 7.9: Compressibility in the bilayer Fermi-Hubbard model. We have measured the compressibility as a function of the interlayer tunnelling amplitude $t_\perp$ at $U/t \approx 7$. The error bars represent the 95% confidence interval of the corresponding fit parameter. The shaded region shows the DQMC calculations for a temperature range of $k_B T = 1.0t..1.4t$. These results have been published in [171].

over the whole range of interlayer tunnel coupling investigated. However, the physical nature of the state changes drastically. At small interlayer coupling, $t_\perp < t \ll U$, the particles hardly delocalize within the horizontal layer and even less over the double-well. The magnetic order is dominated by localized spins and the insulating behaviour is linked to the repulsive on-site interaction only. In contrast, at strong interlayer coupling, $t_\perp > t$, the energy gain by delocalizing over the double-well is a dominant contribution as $t_\perp$ is on the order of the interaction strength. Therefore, any density redistribution would increase both the kinetic as well as the interaction energy of the prepared state, see discussion in Section 7.2.2 and consequently the repulsive interaction strength together with the delocalization energy of the double-well cause the many-body state to be strongly insulating. For this reason we observe that the bilayer band insulator has a lower compressibility.

In contrast to the standard single-band band insulator, where each lattice site is occupied by two particles, the bilayer band insulator occurs at half-filling and may be thought of as a standard band insulator that is spread out over two (coupled) layers. Both phases aim at the reduction of their kinetic energy, either by only populating the lowest band or the lower miniband of a superlattice band structure. The latter corresponds to a delocalization over the double-well in the singlet configuration and leads to strong magnetic correlations between the coupled layers due to Pauli's exclusion principle even in the non-interacting case.

CHAPTER 8

Conclusion and Outlook

Within the scope of this thesis I have investigated the Fermi-Hubbard model with ultracold potassium atoms in a strongly anisotropic three-dimensional optical lattice configuration with full control over the interaction strength between opposite spins and the tunnelling amplitudes. We have implemented a novel scheme to measure magnetic correlations within a single two-dimensional layer in a locally resolved manner. By coherently manipulating magnetic correlations we probe the antiferromagnetic order at arbitrary quasimomentum. In particular at $q_{\mathrm{AFM}} = (\pi/a, \pi/a)$, we access the *staggered magnetic structure factor*, a quantity that probes the alternating spin pattern "on resonance" and is hence directly linked to the order parameter of the antiferromagnet. With the superb quasimomentum resolution we overcome our limited optical resolution, which by itself precludes the detection of individual spatial spin correlators. Furthermore, the staggered spin structure factor serves as a sensitive *local thermometer* and in combination with the global density thermometry it allows us to identify a non-equilibrium density distribution. We have utilized this to optimize the loading procedure into the in-plane lattices and to characterize the background heating rate in the lattice.

By implementing a superlattice along the vertical direction we have extended our Fermi-Hubbard toolbox. In our most recent project we have realized the *bilayer Fermi-Hubbard* model by splitting a single-band band insulator into two coupled layers. We have characterized the magnetic order within one of the two-dimensional layers by probing both the uniform and the staggered structure factor as before. To measure spin-correlations between horizontal layers we induce coherent singlet-triplet oscillations along the vertical direction followed by an adiabatic mapping to the eigenstates of a single well (*merging*). By tuning the coupling strength between the two layers, $t_\perp$, we have observed the crossover from predominantly antiferromagnetic correlations within the layer at weak coupling to singlet bonds forming along the vertical direction in the strong coupling regime. The corresponding low-temperature phases are given by the two-dimensional antiferromagnet and the bilayer band insulator. In addition the local moment, which is proportional to the singles filling, underlines that the physical nature changes drastically from localized moments when $t_\perp, t \ll U$ to a delocalized state with increased density fluctuations for $t_\perp \approx U \gg t$. Although we find very different behaviour for the weakly and the strongly coupled bilayer configuration, both states are insulating as we have verified by exposing the atoms to an in-plane magnetic field gradient. The lowest compressibility is obtained in the band insulating regime at the strongest interlayer coupling strength that we achieve $t_\perp/t \approx 5$. While we have without doubt found signatures of both the two-dimensional antiferromagnetic Mott insulator and the bilayer band insulator, there is room for improvement, particularly

concerning the preparation of the initial state and the splitting. Both parts will be discussed in the following.

Suggestions for Further Improvements

For the starting point of the bilayer experiment we aim for a single-band band insulator, however, the filling that we reach is on the order of 85%. Instead of merely cutting into the density distribution within the harmonic trap (see Figure 6.5), we could try to squeeze more atoms into the centre region by adjusting the slope of the barrier. If we start to ramp up the power in the DMD beam path with a reduced slope steepness towards the centre region, atoms sitting at the position of the slope might be slowly pushed into the centre and they would get squeezed the more the larger the power of the DMD beam becomes. Another possibility might be to increase the confinement of the dipole trap prior to loading the atoms into the in-plane lattices.

The potential disorder introduced by the DMD light severely limits the flatness that we achieve when splitting the single-band band insulator into the bilayer lattice configuration. We have observed that further reducing the DMD power during the splitting process increases the amount of singles and should thus in turn enhance the amount of spin correlations that we obtain. This suggests that it is beneficial to accept a small harmonic confinement over the extent of the cloud when in turn reducing the disorder on length scales of a few sites. While it would be interesting by itself to further investigate the dependence of magnetic correlations on the disorder strength, there are several possible routes to tackle the disorder problem. First, we could try to improve on the atom density feedback by incorporating the point-spread function in the feedback loop to possibly account for even smaller structures. Second, we could try to get rid off the DMD potential during the splitting process. As the DMD mostly needs to compensate the strong confinement from the running-wave component of the infrared z-lattice beam, it might be sensible to increase its waist along the x-direction. Due to the rather large lattice spacing of 2.13 µm we do not need a lot of power to reach a certain lattice depth in units of the corresponding recoil energy. Therefore we might even reduce the waist by a factor of four without running into power issues for the splitting configuration. However, from the technical standpoint it might be simpler to employ the green z-lattice beam as a source of deconfinement and as for the infrared z-lattice its effect on the potential is strongest along the x-direction. As we only need to reach around $30E_{\mathrm{rec}}$ during splitting we might add a motorized half-wave plate in order to imbalance the power of the two interfering green lattice beams at this particular point in the experimental sequence [137]. This would increase the running wave component and in turn the deconfinement predominantly along the x-direction. In principle it would also be possible to add an additional deconfinement beam for example via the dimple port.

Bilayer Configuration with Vertical Potential Bias

Concerning the measurement of the compressibility in the bilayer Fermi-Hubbard model it would be interesting to complement the investigation presented in this thesis by employing a potential gradient along the vertical direction. This is easily achieved by tuning the phase of the optical superlattice, which will introduce a total site offset of 2Δ, compare Equation 2.22 and Figure 6.8. This tilt is identical for both spin components, which is a clear benefit over the measurement with the in-plane magnetic field gradient. Furthermore, systematic uncertainties could be reduced as we can calibrate the potential energy offset by inducing Rabi

oscillations between the two layers and the disorder should be less problematic since both layers experience the same optical (disorder) potential. On the downside we have to measure the full density sector in both layers, which might increase the required acquisition time. Introducing a potential bias between the two horizontal layers also offers the prospect of investigating new physics. K. Bouadim et al. have presented determinant quantum Monte Carlo (DQMC) calculations of the self-doped bilayer Fermi-Hubbard model, where one layer is particle-doped and the other one hole-doped with respect to half-filling [44]. They have found signatures of d-wave pairing, however at temperatures about an order of magnitude smaller than the ones currently realized in our experiment.

Entropy Cooling

Another incentive of implementing the superlattice along the vertical direction was to reach low entropy states by preparing a band insulator and adiabatically splitting it into two layers. A band insulator is an ideal starting point as its density of states vanishes due to the large energy gap to the higher bands and therefore theoretically it features a vanishing entropy [180]. However, we do not observe an increase in the amount of intralayer correlations as compared to the study of the two-dimensional Fermi-Hubbard model and consequently we can not identify a significant cooling effect. While this might be connected to the disorder that is introduced by the DMD potential, another bottleneck of this approach is given by the creation of the initial band insulating state as discussed above. Entropy cooling within a layer was successfully employed in [180] and a low entropy band insulator was achieved through entropy redistribution. However, in our case this scheme suffers from the larger system size of several thousand lattice sites and as the redistribution takes time the system heats up due to nonadiabaticities [139]. Therefore it might be beneficial to investigate cooling schemes where the contact between the reservoir and the investigated system is maximised. One of the early proposals suggests to employ a Bose-Einstein condensate covering the whole extent of the fermionic cloud as a heat reservoir [181]. Another approach that is feasible for our experiment involves the redistribution of entropy between two layers along the vertical direction, where one layer acts as the entropy reservoir for the other one. This scheme was suggested by A. Kantian et al. and they expect that the entropy in a single layer may be reduced by up to an order of magnitude [182]. In a bosonic system a similar scheme was successfully implemented with an in-plane bichromatic superlattice [169]. Introducing a potential energy offset leads to a spatially alternating appearance of Mott insulators and superfluid regions, where the latter act as the high-entropy reservoir.

Topology and Floquet Engineering

In addition to entropy cooling, the superlattice that was recently implemented along one of the in-plane lattice directions offers a broad range of new projects. For example, it allows us to realize the one-dimensional Su-Schrieffer-Heeger (SSH) model, which is one of the simplest paradigmatic models with a symmetry-protected topological phase. By combining the superlattice potential with sharp potential boundaries defined by the DMD beam, we aim at observing topologically protected edge states. Beyond static experiments, the superlattice configuration also offers the possibility of introducing dynamic variations to the potential landscape. In [183] the effect of modulating the site offset was investigated for the two-site Hubbard model and a parameter regime was identified where particles tunnel predominantly in pairs. Enhancing the pair over

the standard single-particle tunnelling is an important prerequisite for the proposal of observing Majorana quasiparticles in a two-leg ladder configuration [184]. This setting could be realized in our experiment by modulating the frequency of the long-wavelength lattice laser that is part of the x-superlattice, e.g. by setting up an AOM in double-pass configuration. While the Floquet engineering of the site offset would suppress the single-particle tunnelling along the x-direction, particles can still tunnel along the y-direction.

η-Pair Condensate via In-Plane Superlattice

Another interesting project involves the preparation of the η-pair state [185], a highly coherent many-body state, which is formed by doubly occupied sites that experience a phase shift of π between neighbouring lattice sites. We have already introduced the η-pair creation operator $\hat{\eta}^\dagger$ in Equation 3.54 and if applied to an empty double-well system we obtain one of the excited Hubbard eigenstates

$$\hat{\eta}^\dagger |0\rangle \propto |d_-\rangle = \frac{1}{\sqrt{2}} \left(|\uparrow\downarrow, 0\rangle - |0, \uparrow\downarrow\rangle \right), \tag{8.1}$$

where the minus sign indicates the π-phase shift[1]. The pseudospin operators comply with the spin algebra as defined by the commutation relations of their pseudospin components $\hat{\eta}_x$, $\hat{\eta}_y$ and $\hat{\eta}_z$, and at half-filling they all commute with the Fermi-Hubbard Hamiltonian. This leads to the additional pseudo-spin SU(2) symmetry for simple cubic lattice configurations (at half-filling only), which conserves the number of η-pairs and is linked to superfluid correlations [39, 107]. As discussed in [186] the formation of an η-pair condensate is expected to give rise to sharp peaks in the momentum distribution of the fermion pairs,

$$\langle \hat{d}_k^\dagger \hat{d}_k \rangle = \sum_{m,n} e^{i(\boldsymbol{r}_m - \boldsymbol{r}_n)\boldsymbol{k}} \langle \hat{d}_n^\dagger \hat{d}_m \rangle , \tag{8.2}$$

where we have introduced the operator $\hat{d}_m^\dagger = \hat{c}_{m,\downarrow}^\dagger \hat{c}_{m,\uparrow}^\dagger$. The sign of the real-space pair correlator $\langle \hat{d}_n^\dagger \hat{d}_m \rangle$ alternates with the distance between the sites n and m and therefore when realizing an η-condensate the peaks in the momentum distribution will be centred at $\boldsymbol{k} = (\pi/a, \pi/a)$. The correlator $\langle \hat{d}_n^\dagger \hat{d}_m \rangle$ is an interesting quantity by itself as it quantifies off-diagonal long-range order that is linked to the characteristic properties of superconducting states [187]. We can express the real-space correlator in terms of the transverse pseudospin operators,

$$\langle \hat{d}_n^\dagger \hat{d}_m \rangle \propto \langle \hat{\eta}_n^x \hat{\eta}_m^x \rangle + \langle \hat{\eta}_n^y \hat{\eta}_m^y \rangle , \tag{8.3}$$

which do not have a classical analogue. Note that the transverse pseudospin correlators indicate an s-wave superfluid phase of fermion pairs, while the longitudinal z-correlator $\langle \hat{\eta}_n^z \hat{\eta}_m^z \rangle$ links to charge-density wave ordering [104].

A. Kantian et al. have proposed a scheme that aims at creating an η-condensate using ultracold atoms by employing a time-dependent superlattice potential [188]. They start in a band insulating state with attractive interactions, where the doubles occupy only the lower sites of a superlattice potential with a finite tilt, which breaks the pseudospin SU(2) symmetry. As

[1] Note that for an arbitrary number of lattice sites L, the η-pair state at half-filling is defined as $\left(\hat{\eta}^\dagger\right)^{L/2} |0\rangle$ up to a normalization factor.

an intuitive picture, the energy offset between left and right sites introduces a site-dependent chemical potential, which makes it more favourable for doubles to occupy the lower lying sites, while the other sites are empty. This acts in a similar way as a staggered magnetic field term for spin-up and spin-down particles, which would violate the spin SU(2) symmetry. Therefore, in analogy to the spin sector, introducing a finite tilt in the superlattice potential will break the symmetry conserving the number of η-pairs, which is a prerequisite for creating an η-condensate. Energy is pumped into the system by quickly switching the interaction strength to a positive value. By adiabatically removing the long-wavelength lattice the doubles are expected to delocalize over the lattice and build up global coherence. As we are interested in the momentum distribution of the pairs, the detection of an η-condensate would require a short RF pulse to switch the interaction strength from repulsive to attractive followed by a ramp over the Feshbach resonance to associate doubly-occupied lattice sites to deeply bound dimers. Then the momentum distribution may be obtained by the standard time-of-flight technique.

Bibliography

[1] B. Raveau. "Strongly correlated electron systems: From chemistry to physics". In: *Comptes Rendus Chimie* 14.9 (2011), pp. 856–864. DOI: 10.1016/j.crci.2011.06.006.

[2] E. Dagotto, T. Hotta and A. Moreo. "Colossal magnetoresistant materials: the key role of phase separation". In: *Physics reports* 344.1-3 (2001), pp. 1–153. DOI: 10.1016/S0370-1573(00)00121-6.

[3] J. Matsuno et al. "Strongly correlated oxides for energy harvesting". In: *Science and technology of advanced materials* 19.1 (2018), pp. 899–908. DOI: 10.1080/14686996.2018.1529524.

[4] L. J. Dunne, E. J. Brändas and H. Cox. "High-temperature superconductivity in strongly correlated electronic systems". In: *Advances in Quantum Chemistry* 74 (2017), pp. 183–208. DOI: 10.1016/bs.aiq.2016.06.003.

[5] J. G. Bednorz and K. A. Müller. "Possible high T_c superconductivity in the Ba-La-Cu-O system". In: *Zeitschrift für Physik B Condensed Matter* 64.2 (1986), pp. 189–193. DOI: 10.1007/BF01303701.

[6] D. Eichenberger. "Superconductivity and antiferromagnetism in the two-dimensional Hubbard model". PhD thesis. Universtiy of Fribourg, 2008.

[7] P. A. Lee, N. Nagaosa and X.-G. Wen. "Doping a Mott insulator: Physics of high-temperature superconductivity". In: *Reviews of modern physics* 78.1 (2006), p. 17. DOI: 10.1103/RevModPhys.78.17.

[8] D. L. Feng et al. "Electronic Structure of the Trilayer Cuprate Superconductor $Bi_2Sr_2Ca_2Cu_3O_{10+\delta}$". In: *Physical review letters* 88.10 (2002), p. 107001. DOI: 10.1103/PhysRevLett.88.107001.

[9] A. Damascelli, Z. Hussain and Z. Shen. "Angle-resolved photoemission studies of the cuprate superconductors". In: *Reviews of modern physics* 75.2 (2003), p. 473. DOI: https://doi.org/10.1103/RevModPhys.75.473.

[10] *New High-Temperature Superconductors*. The New Superconductors. Selected Topics in Superconductivity. Springer, Boston, MA, 2002. DOI: https://doi.org/10.1007/0-306-47069-1_8.

[11] I. Vishik. "A coexistence that CuO_2 planes can see". In: *Science* 369.6505 (2020), pp. 775–776. DOI: 10.1126/science.aba9482.

[12] S. Zhang. "Auxiliary-Field Quantum Monte Carlo for Correlated Electron Systems". In: *Emergent Phenomena in Correlated Matter Modeling and Simulation, edited by E. Pavarini, E. Koch, and U. Schollwöck (Verlag des Forschungszentrums Jülich), Vol. 3* (2013).

[13] H. Shi and S. Zhang. "Symmetry in auxiliary-field quantum Monte Carlo calculations". In: *Physical Review B* 88.12 (2013), p. 125132. DOI: 10.1103/PhysRevB.88.125132.

[14] S. R. White. "Density matrix formulation for quantum renormalization groups". In: *Physical review letters* 69.19 (1992), p. 2863. DOI: 10.1103/PhysRevLett.69.2863.

[15] S. R. White. "Density-matrix algorithms for quantum renormalization groups". In: *Physical Review B* 48.14 (1993), p. 10345. DOI: 10.1103/PhysRevB.48.10345.

[16] T. Maier et al. "Quantum cluster theories". In: *Reviews of Modern Physics* 77.3 (2005), p. 1027. DOI: 10.1103/RevModPhys.77.1027.

[17] C. Varney et al. "Quantum Monte Carlo study of the two-dimensional fermion Hubbard model". In: *Physical Review B* 80.7 (2009), p. 075116. DOI: 10.1103/PhysRevB.80.075116.

[18] H.-C. Jiang and T. P. Devereaux. "Superconductivity in the doped Hubbard model and its interplay with next-nearest hopping t'". In: *Science* 365.6460 (2019), pp. 1424–1428. DOI: 10.1126/science.aal5304.

[19] M. Qin et al. "The Hubbard model: A computational perspective". In: *arXiv preprint arXiv:2104.00064* (2021). URL: https://arxiv.org/abs/2104.00064.

[20] D. P. Arovas et al. "The Hubbard Model". In: *arXiv preprint arXiv:2103.12097* (2021). URL: https://arxiv.org/abs/2103.12097.

[21] J. P. F. LeBlanc et al. "Solutions of the two-dimensional Hubbard model: Benchmarks and results from a wide range of numerical algorithms". In: *Physical Review X* 5.4 (2015), p. 041041. DOI: 10.1103/PhysRevX.5.041041.

[22] R. P. Feynman. "Simulating physics with computers". In: *Int. J. Theor. Phys.* 21.6/7 (1982), pp. 467–488. DOI: 10.1007/BF02650179.

[23] E. Altman et al. "Quantum simulators: Architectures and opportunities". In: *PRX Quantum* 2.1 (2021), p. 017003. DOI: 10.1103/PRXQuantum.2.017003.

[24] T. W. Hänsch and A. L. Schawlow. "Cooling of gases by laser radiation". In: *Optics Communications* 13.1 (1975), pp. 68–69. DOI: 10.1016/0030-4018(75)90159-5.

[25] M. H. Anderson et al. "Observation of Bose-Einstein condensation in a dilute atomic vapor". In: *science* 269.5221 (1995), pp. 198–201. DOI: 10.1126/science.269.5221.198.

[26] C. C. Bradley et al. "Evidence of Bose-Einstein condensation in an atomic gas with attractive interactions". In: *Physical review letters* 75.9 (1995), p. 1687. DOI: 10.1103/PhysRevLett.75.1687.

[27] K. B. Davis et al. "Bose-Einstein condensation in a gas of sodium atoms". In: *Physical review letters* 75.22 (1995), p. 3969. DOI: 10.1103/PhysRevLett.75.3969.

[28] B. DeMarco and D. S. Jin. "Onset of Fermi degeneracy in a trapped atomic gas". In: *science* 285.5434 (1999), pp. 1703–1706. DOI: 10.1126/science.285.5434.1703.

[29] P. Gillot et al. "The LNE-SYRTE cold atom gravimeter". In: *2016 European Frequency and Time Forum (EFTF)*. 2016, pp. 1–3. DOI: 10.1109/EFTF.2016.7477832.

[30] W. Li. "A boost to Rydberg quantum computing". In: *Nature Physics* 16 (2020), pp. 820–821. DOI: 10.1038/s41567-020-0907-8.

[31] R. Meppelink et al. “Phase contrast imaging of Bose condensed clouds”. In: *Physical review. A, Atomic, molecular and optical physics* 81.5 (2010), p. 053632. DOI: 10.1103/PhysRevA.81.053632.

[32] F. Schäfer et al. “Tools for quantum simulation with ultracold atoms in optical lattices”. In: *Nature Reviews Physics* 2.8 (2020), pp. 411–425. DOI: https://doi.org/10.1038/s42254-020-0195-3.

[33] M. Lu, S. H. Youn and B. L. Lev. “Trapping ultracold dysprosium: A highly magnetic gas for dipolar physics”. In: *Physical review letters* 104.6 (2010), p. 063001. DOI: 10.1103/PhysRevLett.104.063001.

[34] E. Cocchi et al. “Equation of State of the Two-Dimensional Hubbard Model”. In: *Phys. Rev. Lett.* 116 (2016), p. 175301. DOI: 10.1103/PhysRevLett.116.175301.

[35] L. W. Cheuk et al. “Observation of spatial charge and spin correlations in the 2D Fermi-Hubbard model”. In: *Science* 353.6305 (2016), pp. 1260–1264. DOI: 10.1126/science.aag3349.

[36] M. F. Parsons et al. “Site-resolved measurement of the spin-correlation function in the Fermi-Hubbard model”. In: *Science* 353.6305 (2016), pp. 1253–1256. DOI: 10.1126/science.aag1430.

[37] J. H. Drewes et al. “Antiferromagnetic Correlations in Two-Dimensional Fermionic Mott-Insulating and Metallic Phases”. In: *Phys. Rev. Lett.* 118 (2017), p. 170401. DOI: 10.1103/PhysRevLett.118.170401.

[38] A. Mazurenko et al. “A cold-atom Fermi–Hubbard antiferromagnet”. In: *Nature* 545.7655 (2017), pp. 462–466. DOI: https://doi.org/10.1038/nature22362.

[39] D. Mitra et al. “Quantum gas microscopy of an attractive Fermi–Hubbard system”. In: *Nature Physics* 14.2 (2018), pp. 173–177. DOI: 10.1038/nphys4297.

[40] J. M. Tarascon et al. “Preparation, structure, and properties of the superconducting compound series $Bi_2Sr_2Ca_{n-1}Cu_nO_y$ with $n = 1, 2$, and 3”. In: *Physical Review B* 38.13 (1988), p. 8885. DOI: https://doi.org/10.1103/PhysRevB.38.8885.

[41] M. Di Stasio, K. Müller and L. Pietronero. “Nonhomogeneous charge distribution in layered high-T_c superconductors”. In: *Physical review letters* 64.23 (1990), p. 2827. URL: https://doi.org/10.1103/PhysRevLett.64.2827.

[42] D. H. A. Fuhrmann and H. Monien. “From Mott insulator to band insulator: A dynamical mean-field theory study”. In: *Physical Review B* 73.24 (2006), p. 245118. DOI: https://doi.org/10.1103/PhysRevB.73.245118.

[43] S. S. Kancharla and S. Okamoto. “Band insulator to Mott insulator transition in a bilayer Hubbard model”. In: *Physical Review B* 75.19 (2007), p. 193103. DOI: https://doi.org/10.1103/PhysRevB.75.193103.

[44] K. Bouadim et al. “Magnetic and transport properties of a coupled Hubbard bilayer with electron and hole doping”. In: *Physical Review B* 77.14 (2008), p. 144527. DOI: https://doi.org/10.1103/PhysRevB.77.144527.

[45] M. Sentef et al. “Correlations in a band insulator”. In: *Physical Review B* 80.15 (2009), p. 155116. DOI: 10.1103/PhysRevB.80.155116.

[46] H. Hafermann, M. Katsnelson and A. Lichtenstein. "Metal-insulator transition by suppression of spin fluctuations". In: *EPL (Europhysics Letters)* 85.3 (2009), p. 37006.

[47] B. Napitu and J. Berakdar. "Traces of the evolution from Mott insulator to a band insulator in the pair excitation spectra". In: *The European Physical Journal B* 85.2 (2012), pp. 1–10. DOI: https://doi.org/10.1140/epjb/e2011-20679-6.

[48] A. Euverte et al. "Magnetic transition in a correlated band insulator". In: *Physical Review B* 87.12 (2013), p. 125141. DOI: https://doi.org/10.1103/PhysRevB.87.125141.

[49] H. Lee et al. "Competition between band and Mott insulators in the bilayer Hubbard model: A dynamical cluster approximation study". In: *Physical Review B* 89.3 (2014), p. 035139. DOI: https://doi.org/10.1103/PhysRevB.89.035139.

[50] R. Rüger et al. "The phase diagram of the square lattice bilayer Hubbard model: a variational Monte Carlo study". In: *New Journal of Physics* 16.3 (2014), p. 033010. DOI: 10.1088/1367-2630/16/3/033010.

[51] M. Golor et al. "Ground-state phase diagram of the half-filled bilayer Hubbard model". In: *Physical Review B* 90.19 (2014), p. 195131. DOI: https://doi.org/10.1103/PhysRevB.90.195131.

[52] R. Grimm, M. Weidemüller and Y. B. Ovchinnikov. "Optical dipole traps for neutral atoms". In: *Advances in atomic, molecular, and optical physics*. Vol. 42. Elsevier, 2000, pp. 95–170. DOI: https://doi.org/10.1016/S1049-250X(08)60186-X.

[53] F. Gerbier. *Quantum gases in optical lattices*. 2017. URL: http://www.lkb.upmc.fr/boseeinsteincondensates/wp-content/uploads/sites/10/2015/12/OL2017.pdf (visited on 08/01/2021).

[54] F. Gerbier and Y. Castin. "Heating rates for an atom in a far-detuned optical lattice". In: *Physical Review A* 82.1 (2010), p. 013615. DOI: https://doi.org/10.1103/PhysRevA.82.013615.

[55] C. N. Cohen-Tannoudji. "Manipulating atoms with photons". In: *Physica Scripta* (1998). DOI: 10.1238/Physica.Topical.076a00033.

[56] J. H. Denschlag et al. "A Bose-Einstein condensate in an optical lattice". In: *Journal of Physics B: Atomic, Molecular and Optical Physics* 35.14 (2002), p. 3095. DOI: 10.1088/0953-4075/35/14/307.

[57] F. Bloch. "Über die Quantenmechanik der Elektronen in Kristallgittern". In: *Zeitschrift für Physik* 52.7-8 (1929), pp. 555–600. DOI: https://doi.org/10.1007/BF01339455.

[58] U. Schneider et al. "Fermionic transport and out-of-equilibrium dynamics in a homogeneous Hubbard model with ultracold atoms". In: *Nature Physics* 8.3 (2012), pp. 213–218. DOI: https://doi.org/10.1038/nphys2205.

[59] D. G. Greif. "Quantum magnetism with ultracold fermions in an optical lattice". PhD thesis. ETH Zurich, 2013. DOI: 10.3929/ethz-a-010008097.

[60] L. Miller. "Ultracold Fermions in Two-Dimensional Optical Lattices: Quantum Simulation of the Hubbard Model". PhD thesis. University of Cambridge, 2016.

[61] M. C. Gutzwiller. "Effect of Correlation on the Ferromagnetism of Transition Metals". In: *Phys. Rev. Lett.* 10 (1963), pp. 159–162. DOI: https://doi.org/10.1103/PhysRev.134.A923.

[62] J. Hubbard. "Electron correlations in narrow energy bands". In: *Proceedings of the Royal Society of London. Series A. Mathematical and Physical Sciences* 276.1365 (1963), pp. 238–257. DOI: https://doi.org/10.1098/rspa.1963.0204.

[63] J. C. Slater and G. F. Koster. "Simplified LCAO method for the periodic potential problem". In: *Physical Review* 94.6 (1954), p. 1498. DOI: https://doi.org/10.1103/PhysRev.94.1498.

[64] H. Tasaki. "The Hubbard model-an introduction and selected rigorous results". In: *Journal of Physics: Condensed Matter* 10.20 (1998), p. 4353. DOI: 10.1088/0953-8984/10/20/004.

[65] M. Lewenstein et al. "Ultracold atomic gases in optical lattices: mimicking condensed matter physics and beyond". In: *Advances in Physics* 56.2 (2007), pp. 243–379. DOI: https://doi.org/10.1080/00018730701223200.

[66] I. Bloch, J. Dalibard and W. Zwerger. "Many-body physics with ultracold gases". In: *Reviews of modern physics* 80.3 (2008), p. 885. DOI: 10.1103/RevModPhys.80.885.

[67] T. Esslinger. "Fermi-Hubbard Physics with Atoms in an Optical Lattice". In: *Annual Review of Condensed Matter Physics* 1.1 (2010), pp. 129–152. DOI: 10.1146/annurev-conmatphys-070909-104059.

[68] D. Jaksch and P. Zoller. "The cold atom Hubbard toolbox". In: *Annals of physics* 315.1 (2005), pp. 52–79. DOI: https://doi.org/10.1016/j.aop.2004.09.010.

[69] L. Tarruell and L. Sanchez-Palencia. "Quantum simulation of the Hubbard model with ultracold fermions in optical lattices". In: *Comptes Rendus Physique* 19.6 (2018), pp. 365–393. DOI: https://doi.org/10.1016/j.crhy.2018.10.013.

[70] Z. Idziaszek and T. Calarco. "Analytical solutions for the dynamics of two trapped interacting ultracold atoms". In: *Physical Review A* 74.2 (2006), p. 022712. DOI: https://doi.org/10.1103/PhysRevA.74.022712.

[71] Y. Wang, P. Julienne and C. H. Greene. "Few-body physics of ultracold atoms and molecules with long-range interactions". In: *Annual Review of Cold Atoms and Molecules* 3 (2015), p. 77. DOI: https://doi.org/10.1142/9789814667746_0002.

[72] G. H. Wannier. "The structure of electronic excitation levels in insulating crystals". In: *Physical Review* 52.3 (1937), p. 191. DOI: 10.1103/PhysRev.52.191.

[73] S. Kivelson. "Wannier functions in one-dimensional disordered systems: Application to fractionally charged solitons". In: *Physical Review B* 26.8 (1982), p. 4269. DOI: https://doi.org/10.1103/PhysRevB.26.4269.

[74] M. Modugno and G. Pettini. "Maximally localized Wannier functions for ultracold atoms in one-dimensional double-well periodic potentials". In: *New Journal of Physics* 14.5 (2012), p. 055004. DOI: 10.1088/1367-2630/14/5/055004.

[75] U. Bissbort. "Dynamical effects and disorder in ultracold bosonic matter". PhD thesis. Univ.-Bibliothek Frankfurt am Main, 2012. URL: http://publikationen.ub.uni-frankfurt.de/frontdoor/index/index/docId/28591.

[76] N. Marzari et al. "Maximally localized Wannier functions: Theory and applications". In: *Reviews of Modern Physics* 84.4 (2012), p. 1419. DOI: https://doi.org/10.1103/RevModPhys.84.1419.

[77] N. Klemmer. “Ultracold Fermions in an Optical Superlattice”. Master thesis. Rheinische Friedrich-Wilhelms-Universität Bonn, 2020.

[78] P.-I. Schneider, S. Grishkevich and A. Saenz. “Ab initio determination of Bose-Hubbard parameters for two ultracold atoms in an optical lattice using a three-well potential”. In: *Physical Review A* 80.1 (2009), p. 013404. DOI: 10.1103/PhysRevA.80.013404.

[79] T. Busch et al. “Two cold atoms in a harmonic trap”. In: *Foundations of Physics* 28.4 (1998), pp. 549–559. DOI: https://doi.org/10.1023/A:1018705520999.

[80] E. Cocchi. “Analogue Quantum Simulation of the Two-Dimensional Hubbard Model with Ultracold Fermions”. PhD thesis. University of Cambridge, 2016.

[81] S. Zhu and B. Wu. “Interaction effects on Wannier functions for bosons in an optical lattice”. In: *Physical Review A* 92.6 (2015), p. 063637. DOI: 10.1103/PhysRevA.92.063637.

[82] M. Kremer et al. “Interaction-induced effects on Bose-Hubbard parameters”. In: *Physical Review A* 96.6 (2017), p. 063611. DOI: 10.1103/PhysRevA.96.063611.

[83] C. Foot and M. Shotter. “Double well potentials and quantum gates”. In: *American Journal of Physics* 79.7 (2011), pp. 762–768. DOI: 10.1119/1.3583478.

[84] A. Bergschneider. “Strong correlations in few-fermion systems”. PhD thesis. Ruperto-Carola University of Heidelberg, 2017. DOI: 10.11588/heidok.00023328.

[85] A. Auerbach. *Interacting electrons and quantum magnetism*. Springer Science & Business Media, 2012.

[86] I. Dimitrova et al. “Enhanced superexchange in a tilted mott insulator”. In: *Physical review letters* 124.4 (2020), p. 043204. DOI: 10.1103/PhysRevLett.124.043204.

[87] S. Trotzky et al. “Time-resolved observation and control of superexchange interactions with ultracold atoms in optical lattices”. In: *Science* 319.5861 (2008), pp. 295–299. DOI: 10.1126/science.1150841.

[88] R. Cava et al. “Bulk superconductivity at 36 K in $La_{1.8}Sr_{0.2}CuO_4$”. In: *Physical review letters* 58.4 (1987), p. 408. DOI: 10.1103/PhysRevLett.58.408.

[89] C. Chu et al. “Superconductivity at 52.5 K in the Lanthanum-Barium-Copper-Oxide System”. In: *Science* 235.4788 (1987), pp. 567–569. DOI: 10.1126/science.235.4788.567.

[90] R. Jördens et al. “A Mott insulator of fermionic atoms in an optical lattice”. In: *Nature* 455.7210 (2008), pp. 204–207. DOI: 10.1038/nature07244.

[91] P. W. Anderson. “The resonating valence bond state in La_2CuO_4 and superconductivity”. In: *science* 235.4793 (1987), pp. 1196–1198. DOI: 10.1126/science.235.4793.1196.

[92] J. Hirsch and S. Tang. “Antiferromagnetism in the two-dimensional Hubbard model”. In: *Physical review letters* 62.5 (1989), p. 591. DOI: 10.1103/PhysRevLett.62.591.

[93] E. Khatami and M. Rigol. “Thermodynamics of strongly interacting fermions in two-dimensional optical lattices”. In: *Physical Review A* 84.5 (2011), p. 053611. DOI: 10.1103/PhysRevA.84.053611.

[94] S. Chiesa et al. “Magnetism and pairing of two-dimensional trapped fermions”. In: *Physical review letters* 106.3 (2011), p. 035301. DOI: 10.1103/PhysRevLett.106.035301.

[95] W. S. Bakr et al. "A quantum gas microscope for detecting single atoms in a Hubbard-regime optical lattice". In: *Nature* 462.7269 (2009), pp. 74–77. DOI: 10.1038/nature08482.

[96] P. T. Brown et al. "Bad metallic transport in a cold atom Fermi-Hubbard system". In: *Science* 363.6425 (2019), pp. 379–382. DOI: 10.1126/science.aat4134.

[97] C. S. Chiu et al. "String patterns in the doped Hubbard model". In: *Science* 365.6450 (2019), pp. 251–256. DOI: 10.1126/science.aav3587.

[98] P. T. Brown et al. "Probing dynamical quantities in the 2D Fermi-Hubbard model with quantum gas microscopy". PhD thesis. 2019. URL: https://www.proquest.com/docview/2307397401.

[99] T. Roscilde. "Exploring the grand-canonical phase diagram of interacting bosons in optical lattices by trap squeezing". In: *Physical Review A* 82.2 (2010), p. 023601. DOI: 10.1103/PhysRevA.82.023601.

[100] J. Dobrzyniecki and T. Sowiński. "Simulating Artificial 1D Physics with Ultra-Cold Fermionic Atoms: Three Exemplary Themes". In: *Advanced Quantum Technologies* (2020), p. 2000010. DOI: 10.1002/qute.202000010.

[101] P. T. Brown et al. "Spin-imbalance in a 2D Fermi-Hubbard system". In: *Science* 14.6358 (2017), pp. 1385–1388. DOI: 10.1126/science.aam7838.

[102] M. Gall et al. "Simulating a Mott Insulator Using Attractive Interaction". In: *Phys. Rev. Lett.* 124 (2020), p. 010403. DOI: 10.1103/PhysRevLett.124.010403.

[103] G. Orso et al. "Lattice modulation spectroscopy of strongly interacting bosons in disordered and quasiperiodic optical lattices". In: *Physical Review A* 80.3 (2009), p. 033625. DOI: 10.1103/PhysRevA.80.033625.

[104] A. F. Ho, M. A. Cazalilla and T. Giamarchi. "Quantum simulation of the Hubbard model: The attractive route". In: *Physical Review A* 79.3 (2009), p. 033620. DOI: 10.1103/PhysRevA.79.033620.

[105] P. Schupp. "Quantum symmetry of Hubbard model unraveled". In: *Physics Letters A* 229.1 (1997), pp. 53–58. DOI: https://doi.org/10.1016/S0375-9601(97)00170-9.

[106] S. Zhang. "Pseudospin symmetry and new collective modes of the Hubbard model". In: *Physical review letters* 65.1 (1990), p. 120. DOI: 10.1103/PhysRevLett.65.120.

[107] C. N. Yang and S. C. Zhang. "SO_4 symmetry in a Hubbard model". In: *Modern Physics Letters B* 4.11 (1990), pp. 759–766. DOI: 10.1142/S0217984990000933.

[108] C. F. Chan. "Quantum simulation of strongly-correlated two-dimensional fermions in optical lattices". PhD thesis. Rheinische Friedrich-Wilhelms-Universität Bonn, 2019.

[109] A. Rapp, S. Mandt and A. Rosch. "Equilibration rates and negative absolute temperatures for ultracold atoms in optical lattices". In: *Physical review letters* 105.22 (2010), p. 220405. DOI: 10.1103/PhysRevLett.105.220405.

[110] S. Braun et al. "Negative absolute temperature for motional degrees of freedom". In: *Science* 339.6115 (2013), pp. 52–55. DOI: 10.1126/science.1227831.

[111] S. Braun. "Negative absolute temperature and the dynamics of quantum phase transitions". PhD thesis. Ludwig Maximilian University of Munich, 2014. DOI: 10.5282/edoc.18002.

[112] L. Rademaker et al. “Determinant quantum Monte Carlo study of exciton condensation in the bilayer Hubbard model”. In: *Physical Review B* 88.23 (2013), p. 235115. DOI: 10.1103/PhysRevB.88.235115.

[113] R. T. Scalettar et al. “Magnetic and pairing correlations in coupled Hubbard planes”. In: *Physical Review B* 50.18 (1994), p. 13419. DOI: 10.1103/PhysRevB.50.13419.

[114] R. T. Scalettar. “Magnetism and spin liquid behavior in a two layer Hubbard model”. In: *Journal of low temperature physics* 99.3-4 (1995), pp. 499–504. DOI: 10.1007/BF00752329.

[115] K. Hida. “Quantum Disordered State without Frustration in the Double Layer Heisenberg Antiferromagnet -Dimer Expansion and Projector Monte Carlo Study-”. In: *Journal of the Physical Society of Japan* 61.3 (1992), pp. 1013–1018. DOI: 10.1143/JPSJ.61.1013.

[116] A. Millis and H. Monien. “Spin Gaps and Spin Dynamics in $La_{2-x}Sr_xCuO_4$ and $YBa_2Cu_3O_{7-\delta}$”. In: *Physical review letters* 70.18 (1993), p. 2810. DOI: 10.1103/PhysRevLett.70.2810.

[117] A. Sandvik and D. Scalapino. “Order-disorder transition in a two-layer quantum antiferromagnet”. In: *Physical review letters* 72.17 (1994), p. 2777. DOI: 10.1103/PhysRevLett.72.2777.

[118] L. Wang, K. Beach and A. W. Sandvik. “High-precision finite-size scaling analysis of the quantum-critical point of $S = 1/2$ Heisenberg antiferromagnetic bilayers”. In: *Physical Review B* 73.1 (2006), p. 014431. DOI: 10.1103/PhysRevB.73.014431.

[119] O. Dutta et al. “Non-standard Hubbard models in optical lattices: a review”. In: *Reports on Progress in Physics* 78.6 (2015), p. 066001. DOI: 10.1088/0034-4885/78/6/066001.

[120] D.-S. Lühmann, O. Jürgensen and K. Sengstock. “Multi-orbital and density-induced tunneling of bosons in optical lattices”. In: *New Journal of Physics* 14.3 (2012), p. 033021. DOI: 10.1088/1367-2630/14/3/033021.

[121] O. Jürgensen et al. “Observation of density-induced tunneling”. In: *Physical review letters* 113.19 (2014), p. 193003. DOI: 10.1103/PhysRevLett.113.193003.

[122] O. Jürgensen. “Extended Hubbard models for ultracold atoms in optical lattices”. PhD thesis. Universität Hamburg, 2015.

[123] M. Inguscio and L. Fallani. *Atomic physics: precise measurements and ultracold matter*. OUP Oxford, 2013. DOI: 10.1093/acprof:oso/9780198525844.003.0002.

[124] C. J. Foot et al. *Atomic physics*. Vol. 7. Oxford University Press, 2005.

[125] J. B. Adams. “Bonding Energy Models”. In: *Encyclopedia of Materials: Science and Technology*. Ed. by K. H. J. Buschow et al. Oxford: Elsevier, 2001, pp. 763–767. DOI: https://doi.org/10.1016/B0-08-043152-6/00146-7.

[126] N. Borghini. *Lecture notes on Nonequilibrium Physics*. 2016. URL: https://www.physik.uni-bielefeld.de/~borghini/Teaching/Nonequilibrium/05_09.pdf.

[127] C. Chin et al. “Feshbach resonances in ultracold gases”. In: *Reviews of Modern Physics* 82.2 (2010), p. 1225. DOI: 10.1103/RevModPhys.82.1225.

[128] D. S. Jin and J. Ye. “Polar molecules in the quantum regime”. In: *Phys. Today* 64.5 (2011), p. 27. DOI: 10.1063/1.3592002.

[129] S. S. M. Wong. *Introductory nuclear physics*. Wiley Online Library, 1998, pp. 409–415.

[130] M. Höfer. "A two-orbital quantum gas with tunable interactions". PhD thesis. Ludwig Maximilians Universität München, 2017. DOI: 10.5282/edoc.21221.

[131] T. Volz. "Ultracold Rubidium Molecules". PhD thesis. Technische Universität München, 2007. URL: https://mediatum.ub.tum.de/doc/613042/document.pdf.

[132] T. Loftus et al. "Resonant Control of Elastic Collisions in an Optically Trapped Fermi Gas of Atoms". In: *Phys. Rev. Lett.* 88 (17 Apr. 2002), p. 173201. DOI: 10.1103/PhysRevLett.88.173201.

[133] T. Lompe. "Efimov Physics in a three-component Fermi gas". PhD thesis. Ruprecht-Karls Universität Heidelberg, Germany, 2011. DOI: 10.11588/heidok.00012212.

[134] M. Feld. "Low temperature phases of interacting fermions in two dimensions". PhD thesis. University of Cambridge, 2011. URL: https://www.quantum.uni-bonn.de/publications/thesis-feld.

[135] B. Fröhlich. "A Strongly Interacting Two-Dimensional Fermi Gas". PhD thesis. University of Cambridge, 2011. URL: https://www.quantum.uni-bonn.de/publications/thesis-froehlich.

[136] E. Vogt. "Collective Modes and Polarons in two-dimensional Fermi Gases". PhD thesis. University of Cambridge, 2013. URL: https://www.quantum.uni-bonn.de/publications/thesis-vogt.

[137] M. Gall. "Quantum Simulation of the Bilayer Hubbard Model Using Ultracold Atoms". PhD thesis. Rheinische Friedrich-Wilhelms-Universität Bonn, 2020.

[138] M. Dolfi et al. "Minimizing nonadiabaticities in optical-lattice loading". In: *Physical Review A* 91.3 (2015), p. 033407. DOI: 10.1103/PhysRevA.91.033407.

[139] M. Soni, M. Dolfi and M. Troyer. "Density redistribution effects in fermionic optical lattices". In: *Phys. Rev. A* 94 (6 2016), p. 063404. DOI: 10.1103/PhysRevA.94.063404.

[140] *Mephisto Mopa: Ultra-Narrow Linewidth High-Power CW DPSS Laser, manufacturer's datasheet*. Coherent (2015). URL: https://www.coherent.com/assets/pdf/Mephisto-MOPA-Data-Sheet.pdf.

[141] N. Klemmer. "Cavity design for high-power frequency doubling". Bachelor thesis. Rheinische Friedrich-Wilhelms-Universität Bonn, 2018.

[142] M. Safronova, B. Arora and C. W. Clark. "Frequency-dependent polarizabilities of alkali-metal atoms from ultraviolet through infrared spectral regions". In: *Physical Review A* 73.2 (2006), p. 022505. DOI: 10.1103/PhysRevA.73.022505.

[143] *Verdi Family: Diode-Pumped Solid-State Lasers, High-Power CW Output at 532 nm, manufacturer's datasheet*. Coherent (2011). URL: https://www.coherent.com/assets/pdf/Verdi-Family-Data-Sheet.pdf.

[144] *Wavelength Control and Locking with Sub-MHz Precision*. Coherent. URL: https://www.coherent.com/assets/pdf/Wavelength_Control_and_Locking_with_Sub-MHz_Precision.pdf.

[145] *MDT693A/MDT694A Piezo Controllers, Operating Manual*. Thorlabs. URL: https://www.thorlabs.de/thorproduct.cfm?partnumber=MDT693A.

[146] T. Pyragius. "Developing and building an absorption imaging system for Ultracold Atoms". In: *arXiv preprint arXiv:1209.3408* (2012). URL: https://arxiv.org/abs/1209.3408.

[147] G. Reinaudi et al. "Strong saturation absorption imaging of dense clouds of ultracold atoms". In: *Opt. Lett.* 32.21 (2007), pp. 3143–3145. DOI: 10.1364/OL.32.003143.

[148] J. H. Drewes. "Ultracold quantum gases in three-dimensional optical lattice potentials". PhD thesis. Rheinische Friedrich-Wilhelms-Universität Bonn, 2020.

[149] C.-L. Hung et al. "Extracting density–density correlations from in situ images of atomic quantum gases". In: *New Journal of Physics* 13.7 (2011), p. 075019. DOI: 10.1088/1367-2630/13/7/075019.

[150] M. Garwood and L. DelaBarre. "The Return of the Frequency Sweep: Designing Adiabatic Pulses for Contemporary NMR". In: *Journal of Magnetic Resonance* 153.2 (2001), pp. 155–177. DOI: 10.1006/jmre.2001.2340.

[151] C. F. Chan. *Light shaping techniques in exploring strongly-correlated ultracold fermions.* First year report, Rheinische Friedrich-Wilhelms-Universität Bonn. 2016.

[152] J. Fleper. "Long-range disorder in the non-interacting one-dimensional Fermi-Hubbard model". Master thesis. Rheinische Friedrich-Wilhelms-Universität Bonn, 2020.

[153] D. Greif et al. "Short-range quantum magnetism of ultracold fermions in an optical lattice". In: *Science* 340.6138 (2013), pp. 1307–1310. DOI: 10.1126/science.1236362.

[154] R. A. Hart et al. "Observation of antiferromagnetic correlations in the Hubbard model with ultracold atoms". In: *Nature* 519.7542 (2015), pp. 211–214. DOI: 10.1038/nature14223.

[155] L. W. Cheuk et al. "Quantum-gas microscope for fermionic atoms". In: *Physical review letters* 114.19 (2015), p. 193001. DOI: https://doi.org/10.1103/PhysRevLett.114.193001.

[156] M. Boll et al. "Spin- and density-resolved microscopy of antiferromagnetic correlations in Fermi-Hubbard chains". In: *Science* 353.6305 (2016), pp. 1257–1260. DOI: 10.1126/science.aag1635.

[157] T. Yanagisawa. "Antiferromagnetism, Superconductivity and Phase Diagram in the Two-Dimensional Hubbard Model - Off-Diagonal Wave Function Monte Carlo Studies of Hubbard Model III -". In: *Journal of the Physical Society of Japan* 88.5 (2019), p. 054702. DOI: https://journals.jps.jp/doi/10.7566/JPSJ.88.054702.

[158] M. M. T. Yanagisawa and K. Yamaji. "Phase Diagram and Mechanism of Superconductivity in Strongly Correlated Electrons". In: *Journal of Superconductivity and Novel Magnetism* 33 (2020), pp. 2355–2359. DOI: https://doi.org/10.1007/s10948-020-05487-1.

[159] N. Wurz et al. "Coherent manipulation of spin correlations in the Hubbard model". In: *Phys. Rev. A* 97 (2018), p. 051602. DOI: 10.1103/PhysRevA.97.051602.

[160] D. Poilblanc. "Entanglement Hamiltonian of the quantum Néel state". In: *Journal of Statistical Mechanics: Theory and Experiment* 2014.10 (2014), P10026. DOI: 10.1088/1742-5468/2014/10/p10026.

[161] B. Schmidt and P. Thalmeier. "Frustrated two dimensional quantum magnets". In: *Physics Reports* 703 (2017), pp. 1–59. DOI: 10.1016/j.physrep.2017.06.004.

[162] C. Lhuillier and G. Misguich. "Frustrated quantum magnets". In: *High magnetic fields*. Springer, 2002, pp. 161–190. DOI: 10.1007/3-540-45649-X_6.

[163] J. Richter, J. Schulenburg and A. Honecker. "Quantum magnetism in two dimensions: From semi-classical Néel order to magnetic disorder". In: *Quantum Magnetism*. Springer, 2004, pp. 85–153. DOI: 10.1007/BFb0119592.

[164] F. Kolley et al. "Entanglement spectroscopy of SU(2)-broken phases in two dimensions". In: *Physical Review B* 88.14 (2013), p. 144426. DOI: 10.1103/PhysRevB.88.144426.

[165] W. Zimmermann, R. Frésard and P. Wölfle. "Spin and charge structure factor of the two-dimensional Hubbard model". In: *Physical Review B* 56.16 (1997), p. 10097. DOI: 10.1103/PhysRevB.56.10097.

[166] N. Wurz. "Imprinting Spin Spirals into an Ultracold Fermi Gas". Master thesis. Rheinische Friedrich-Wilhelms-Universität Bonn, 2016.

[167] F. Essler et al. *The One-Dimensional Hubbard Model*. Cambridge University Press, 2005. DOI: 10.1017/CBO9780511534843.

[168] H. Pichler, A. Daley and P. Zoller. "Nonequilibrium dynamics of bosonic atoms in optical lattices: Decoherence of many-body states due to spontaneous emission". In: *Physical Review A* 82.6 (2010), p. 063605. DOI: 10.1103/PhysRevA.82.063605.

[169] B. Yang et al. "Cooling and entangling ultracold atoms in optical lattices". In: *Science* 369.6503 (2020), pp. 550–553. DOI: 10.1126/science.aaz6801.

[170] S. Kancharla et al. "Anomalous superconductivity and its competition with antiferromagnetism in doped Mott insulators". In: *Physical Review B* 77.18 (2008), p. 184516. DOI: 10.1103/PhysRevB.77.184516.

[171] M. Gall et al. "Competing magnetic orders in a bilayer Hubbard model with ultracold atoms". In: *Nature* 589.7840 (2021), pp. 40–43. DOI: 10.1038/s41586-020-03058-x.

[172] D. Ninno, G. Cantele and F. Trani. "Real-space grid representation of momentum and kinetic energy operators for electronic structure calculations". In: *Journal of Computational Chemistry* 39.20 (2018), pp. 1406–1412. DOI: 10.1002/jcc.25208.

[173] S. Trotzky et al. "Controlling and detecting spin correlations of ultracold atoms in optical lattices". In: *Physical Review Letters* 105.26 (2010), p. 265303. DOI: 10.1103/PhysRevLett.105.265303.

[174] J. Sebby-Strabley et al. "Preparing and probing atomic number states with an atom interferometer". In: *Physical Review Letters* 98.20 (2007), p. 200405. DOI: 10.1103/PhysRevLett.98.200405.

[175] S. Fölling et al. "Direct observation of second-order atom tunnelling". In: *Nature* 448.7157 (2007), pp. 1029–1032. DOI: 10.1038/nature06112.

[176] C. Cohen-Tannoudji et al. *Quantum mechanics*. Vol. 1. John Wiley & Sons, 1977.

[177] W. S. Bakr et al. "Orbital excitation blockade and algorithmic cooling in quantum gases". In: *Nature* 480.7378 (2011), pp. 500–503. DOI: 10.1038/nature10668.

[178] X. Wang, Q. Zhou and S. D. Sarma. "Mott-insulating phases and magnetism of fermions in a double-well optical lattice". In: *Physical Review A* 84.6 (2011), p. 061603. DOI: 10.1103/PhysRevA.84.061603.

[179] P. Attard. *Thermodynamics and statistical mechanics: equilibrium by entropy maximisation*. Elsevier, 2002.

[180] C. S. Chiu et al. "Quantum State Engineering of a Hubbard System with Ultracold Fermions". In: *Phys. Rev. Lett.* 120 (2018), p. 243201. DOI: 10.1103/PhysRevLett.120.243201.

[181] T.-L. Ho and Q. Zhou. "Squeezing out the entropy of fermions in optical lattices". In: *Proceedings of the National Academy of Sciences* 106.17 (2009), pp. 6916–6920. DOI: 10.1073/pnas.0809862105.

[182] A. Kantian, S. Langer and A. J. Daley. "Dynamical disentangling and cooling of atoms in bilayer optical lattices". In: *Physical review letters* 120.6 (2018), p. 060401. DOI: 10.1103/PhysRevLett.120.060401.

[183] S. Bauer. "Enhancing Pair Hopping in a Floquet-Engineered Two-Site Hubbard Model". Bachelor thesis. Rheinische Friedrich-Wilhelms-Universität Bonn, 2020.

[184] N. Lang and H. P. Büchler. "Topological states in a microscopic model of interacting fermions". In: *Physical Review B* 92.4 (2015), p. 041118. DOI: 10.1103/PhysRevB.92.041118.

[185] C. N. Yang. "η pairing and off-diagonal long-range order in a Hubbard model". In: *Phys. Rev. Lett.* 63 (1989), pp. 2144–2147. DOI: 10.1103/PhysRevLett.63.2144.

[186] A. Rosch et al. "Metastable superfluidity of repulsive fermionic atoms in optical lattices". In: *Physical review letters* 101.26 (2008), p. 265301. DOI: 10.1103/PhysRevLett.101.265301.

[187] H. Fan and S. Lloyd. "Entanglement and off-diagonal long-range order of an η-pairing state". In: *Journal of Physics A: Mathematical and General* 38.23 (2005), p. 5285. DOI: 10.1088/0305-4470/38/23/014.

[188] A. Kantian, A. Daley and P. Zoller. "η condensate of fermionic atom pairs via adiabatic state preparation". In: *Physical review letters* 104.24 (2010), p. 240406. DOI: 10.1103/PhysRevLett.104.240406.

List of Figures

List of Tables